ABSTRACT

Title of Thesis: BRINGING NEW CHEMISTRY TO GUANOSINE HYDROGELS

Songjun Xiao, Doctor of Philosophy, 2020

Thesis Directed By: Professor Jeffery T. Davis, Department of Chemistry and Biochemistry

Molecular self-assembly is a powerful method to construct functional materials such as supramolecular hydrogels. Hydrogels contain mostly water but show solid-like rheology. Nucleosides and nucleotides contain rich recognition information, which opens up opportunities for gelator design. Hydrogels derived from these natural products have seen a resurgence in the past decade due to the high biodegradability and biocompatibility. Guanosine (G **1**) and its analogs are powerful supramolecular hydrogelators. The structural basis for most guanosine hydrogels is $G_4 \bullet M^+$ quartet with K^+ being the best metal to stabilize such a structure. These hydrogen-bonded macrocycles further stack to form 1D G-quadruplex that traps water to give hydrogels. Guanosine hydrogels have been used for applications such as bioactive molecule trap and release, environmental remediation, sensing and cell culture.

While the H-bonded G-quadruplex is critical for gelation, G **1** can be synthetically modified to introduce new functions. The work presented here is focused on G-quartet

hydrogels made from synthetic guanosine analogs. Guanosine analogs containing sulfur on 8- and 5′-position are purified and their hydrogelation properties in water were examined. The resulting hydrogels can potentially be applied to environmental remediation.

Substitution of 5′-OH in G **1** into a hydrazine group in HG **2** significantly improves the hydrogelation properties. The resulting HG **2** KCl hydrogel can be used to non-covalently bind anionic dyes and covalently trap toxic electrophiles such as acrolein.

A binary mixture of G **1** and HAG **15** forms a stable hydrogel with KCl. The hydroxamic acid group in HAG **15** serves as a pH-switchable group that can be applied as a carboxylic acid substitute in hydrogelator design. Furthermore, the hydrogel serves as a supramolecular siderophore and binds Fe^{3+} to generate patterns on the gel surface. The surface can be erased with a reducing agent and rewritten with Fe^{3+}.

BRINGING NEW CHEMISTRY TO GUANOSINE HYDROGELS

by

Songjun Xiao

Thesis submitted to the Faculty of the Graduate School of the
University of Maryland, College Park, in partial fulfillment
of the requirements for the degree of
Doctor of Philosophy
2020

Advisory Committee:
Professor Jeffery T. Davis, Chair
Professor Daniel E. Falvey
Associate Professor Paul J. Paukstelis
Assistant Professor Myles B. Poulin
Associate Professor Amy J. Karlsson

Acknowledgements

There are many people in my graduate school journey that I would like to thank. First, I want to thank Prof. Jeff Davis for giving me the opportunity to work in the lab. I couldn't have achieved anything without your patience, help and support. Thank you for imparting me your knowledge and wisdom. I have learned so much from you as an advisor and you inspired me to become a more independent chemist and also a better person. Thank you for bringing the group to ISMSC in Cambridge and for the punting on the Cam river was particularly enjoyable.

Thank you to my committee members, Prof. Falvey, Prof. Paukstelis, Prof. Poulin and Prof. Karlsson, for providing new perspectives for my project and helping me throughout my PhD career. Special thanks to Prof. Bryan Eichhorn for filling in on my candidacy exam and saving me from trouble and to Dr. Amy Karlsson for all the encouragement and career suggestions.

Working on an interdisciplinary project, I greatly benefited from the help and support of the staff at UMD. Thank you Dr. Yinde Wang, Dr. Fu Chen, Dr. Yiu-Fai Lam and Dr. Daoning Zhang for your help with NMR experiments. Thank you to Dr. Yue Li for the tremendous help with mass spectrometry and career advices. Thank you Dr. Wonseok Hwang, Katchen Lachmayer and Prof. Lawrence Sita for your help with rheology. Thank you Dr. Paul Paukstelis for your help with all the amazing 3D-printing experiments. Thank you to Dr. Richard Ash of the geology department for teaching me about ICP-MS. Thank you Rishvi and Dr. Peter Zavalij for PXRD and single-crystal data. Thank you Dr. Wen-An Chiou at the Nanocenter for the SEM images.

Thank you to my labmates in the Davis Group for keeping me accompanied and helping me get through graduate school. To Taylor and Gretchen, thank you for helping me get started on this interesting hydrogel project and providing invaluable insights to my projects. To Keith and Deiaa, thank you for being great labmates and all the research discussions. To Allison, thank you for making lab work enjoyable and always asking great questions. To Prof. Mike Shi, thank you for telling me about your life story at ISMSC and it is my great pleasure to know you. To Tao, Mitchell, Michael, Luke, Sabrina, Soumya, thank you for making the lab so much fun.

Thank you to Dr. Jeff Davis, Dr. Monique Koppel and Dr. Lee Friedman for giving so much care to me as a TA and teaching me your own teaching philosophies.

My research at UMD was funded by "Separations and Analysis Program, Chemical Sciences, Geosciences, and Biosciences Division, Basic Energy Sciences, US Department of Energy (Grant # DE-FG02-98ER14888). I was also supported by the University of Maryland Graduate Student Summer Research Fellowship from the UMD Department of Chemistry and Biochemistry, the University of Maryland Jacob Goldhaber Travel Grant and International Conference Student Support Award. Thank you for the support.

Many thanks to my family and friends. To my parents, Guishan Xiao and Yuzhu Wang, thank you for giving me a life and caring for me. To the rest of my family, thank you for the support throughout the years. To Dr. Christine Piggee, thank you for being a great neighbor and for your great advices for career and life. To Jingwen Guan, Di Zhuang, Bo Yu and Mingfei Zhang, thank you for being great friends and traveling with me. I couldn’t have survived without your support and love. To all my friends in

the chemistry department, thank you for your support and it was absolutely a pleasure to know you. To my roommates and landlord, thank you for making my life outside of work so much fun. Last but not least, to Yanxi Li, thank you for keeping me accompanied and for being a great partner!

Table of Contents

List of Figures

Chapter 1: Hydrogels Containing Self-assembled Macrocycles and Cages

1.1 Summary

Molecular self-assembly is ubiquitous in Nature, especially in living organisms and it is a powerful tool to construct functional materials. Nucleosides contain extensive hydrogen bonding sites that can form complex higher-order structures.[1] Of all naturally occurring nucleobases, guanine (G) has the richest recognition sites, which can form G-C triple base pairing in nucleic acids or ribbon structures with another guanine molecule.[2] In the presence of a templating cation, however, guanines self-assemble into macrocyclic G-quartets (**Figure 1.1**).[2] The planar cycles further stack to form G-quadruplex structures, which can give rise to fibers that promote the formation of hydrogels.[2]

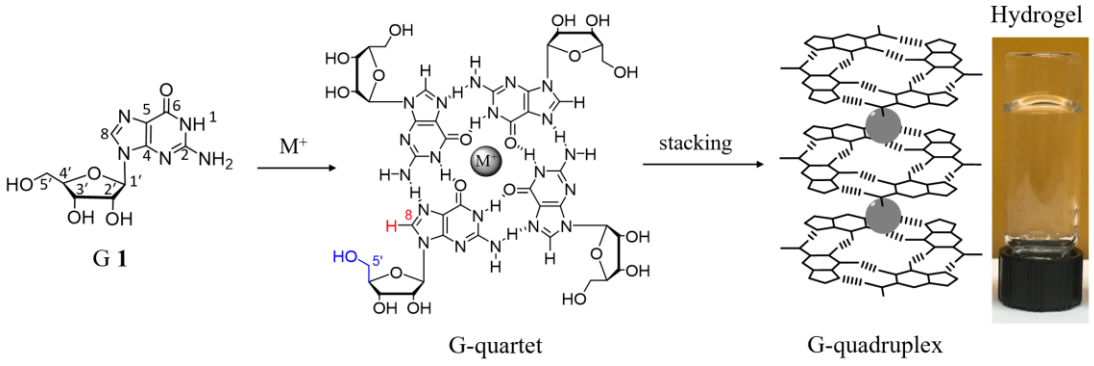

Figure 1.1: G **1** and its analogs in water can self-assemble, in the presence of a cation, to give a G-quartet hydrogel.

While guanine hydrogels were discovered in 1910,[3] there has been a resurgence of such systems due to the accessibility of guanine analogs, their biocompatibility and

ease to synthesize.[4] Guanosine (G **1**) has a highly modifiable periphery (ribose and C8 position) that does not alter G-quartet formation. In this thesis "*Bringing New Chemistry to Guanosine Hydrogels*", we focus on the 5′- and 8- modification of G **1** (**Figure 1.1**). Guanosine hydrogels are used as a model system to bring some new functional groups into the realm of supramolecular hydrogels.

1.2 Thesis organization

This thesis is organized into six separate chapters. **Chapter 1** provides an introduction of hydrogels that contain macrocycles and cages, with emphasis on the self-assembled macrocyclic hydrogels. Of all these macrocyclic hydrogels, G-quartet systems, which are the main theme of this thesis, will then be reviewed in detail. In **Chapter 2** we describe the synthesis and self-assembly properties of four novel 5′- and 8-modified sulfur-containing analogs. Methods to trigger gelation were either tested or proposed in this chapter. **Chapters 3 and 4** are focused on the hydrogelation of 5′-hydrazinoguanosine (HG **2**) with KCl and the applications of the resulting hydrogel. We found that HG **2** forms a G-quartet based hydrogel with only 0.25 eq KCl. The resulting assemblies were used to non-covalently bind an anionic dye, naphthol blue black and also covalently bind propionaldehyde via hydrazone formation.[5] **Chapter 4** is the continuation of the studies carried out in **Chapter 3**, and we utilized HG **2** KCl hydrogels for the remediation of carcinogenic α,β-unsaturated carbonyls from the gas and aqueous phase. The absorption was achieved via the formation of a covalent adduct.[6] In **Chapter 5**, a hydroxamic acid containing guanosine analog, HAG **15**, was found to form G-quartet hydrogels with equimolar G **1** and KCl.[7] We demonstrate that

hydroxamic acid functionality serves as a pH switchable group in the hydrogel and binds a cationic dye upon raising the pH. The HAG **15** containing hydrogel is also a supramolecular siderophore and binds Fe^{3+} to give a red color, which was used for surface patterning by hand or using a 3D-printer. Finally, **Chapter 6** contains supporting information for **Chapters 2-5**, synthetic procedures and spectra for guanosine/inosine analogs and anti-cancer screening results of various synthetic analogs from NCI-60 tests, which were carried out by the National Cancer Institute. In **Figure 1.2** we show a list of compounds discussed in **Chapters 2-6**.

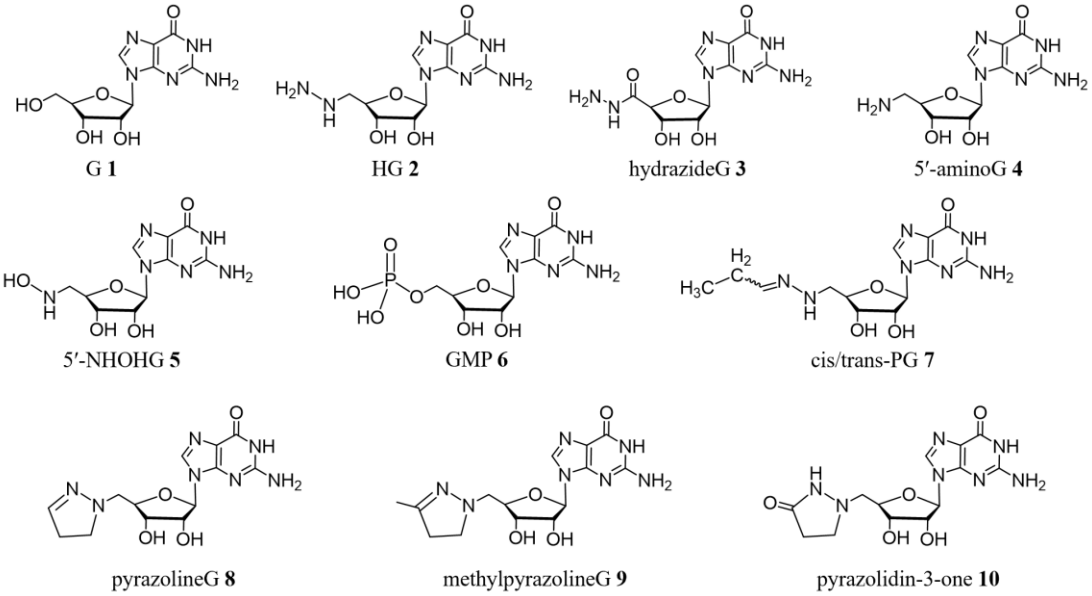

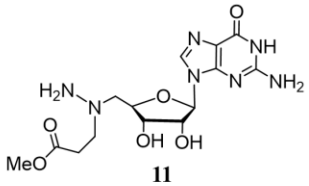

11

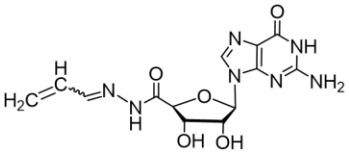

cis/trans-acylhydrazone **12**

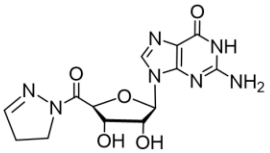

cyclic acylhydrazone **13**

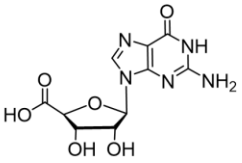

CAG **14**

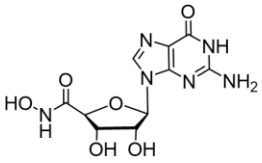

HAG **15**

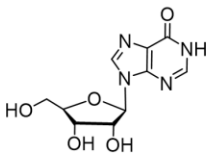

inosine **16**

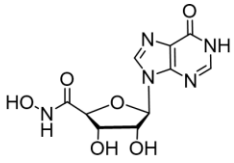

HAI **17**

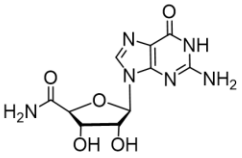

amideG **18**

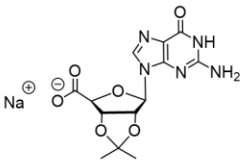

ipG **19**

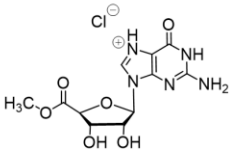

esterG **20**

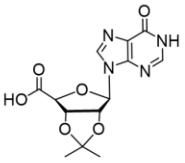

ipI **21**

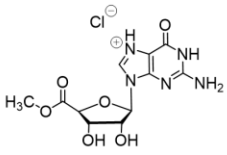

esterI **22**

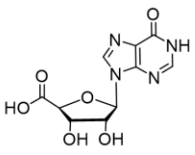

CAI **23**

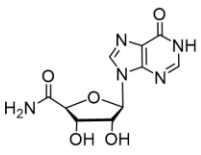

amideI **24**

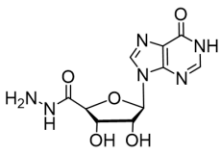

hydrazideI **25**

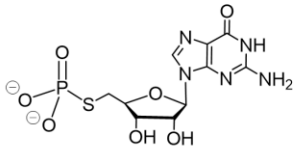

thiophosphoG **26**

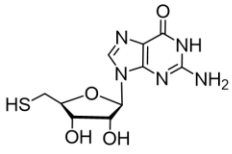

5′-SHG **27**

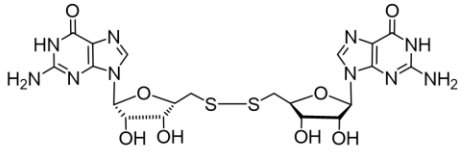

5′-disulfideG **28**

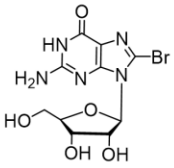

8-BrG **29**

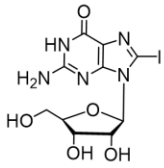

8-IG **30**

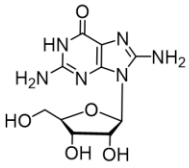

8-aminoG **31**

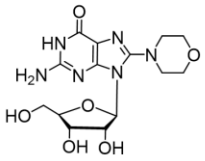

8-morpholinoG **32**

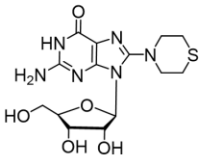

8-thiomorpholinoG **33**

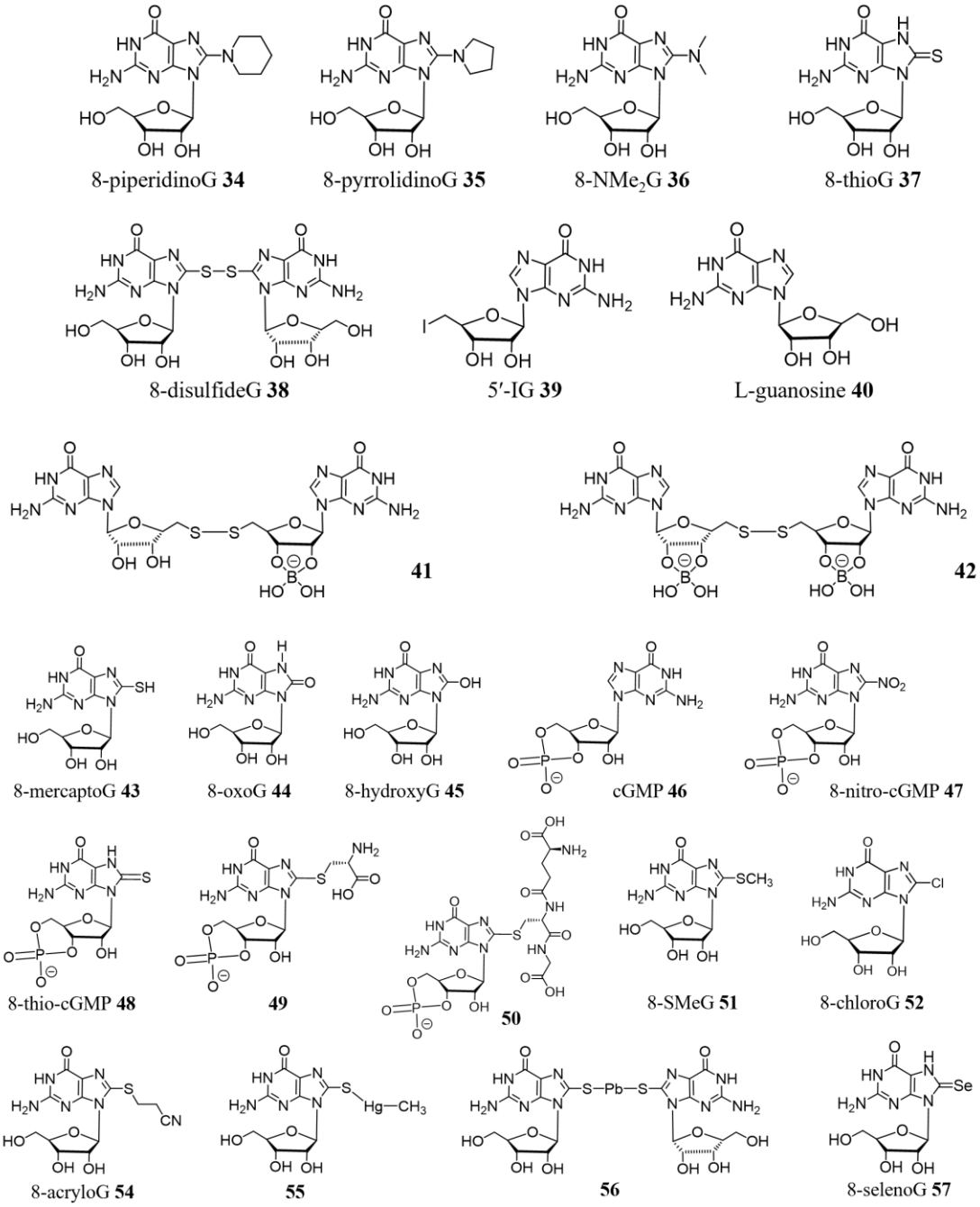

Figure 1.2: A list of guanosine analogs discussed in **Chapters 2-6**.

1.3 Introduction of supramolecular hydrogels

A gel is defined the IUPAC as a "(n)on-fluid colloidal network or polymer network that is expanded throughout its whole volume by a fluid".[8] Based on the definition, there are two phases in a gel: a continuous solid phase of 3D-network and a continuous solution phase consisting of solvent. Generally speaking, a gel behaves like a solid while most of the material is made of a liquid. A gel made with water is called a hydrogel while those containing organic solvents are called organogels. This thesis focuses on hydrogels, since water is the solvent of life and hydrogels are commonly applied to biomedical applications.[9–11]

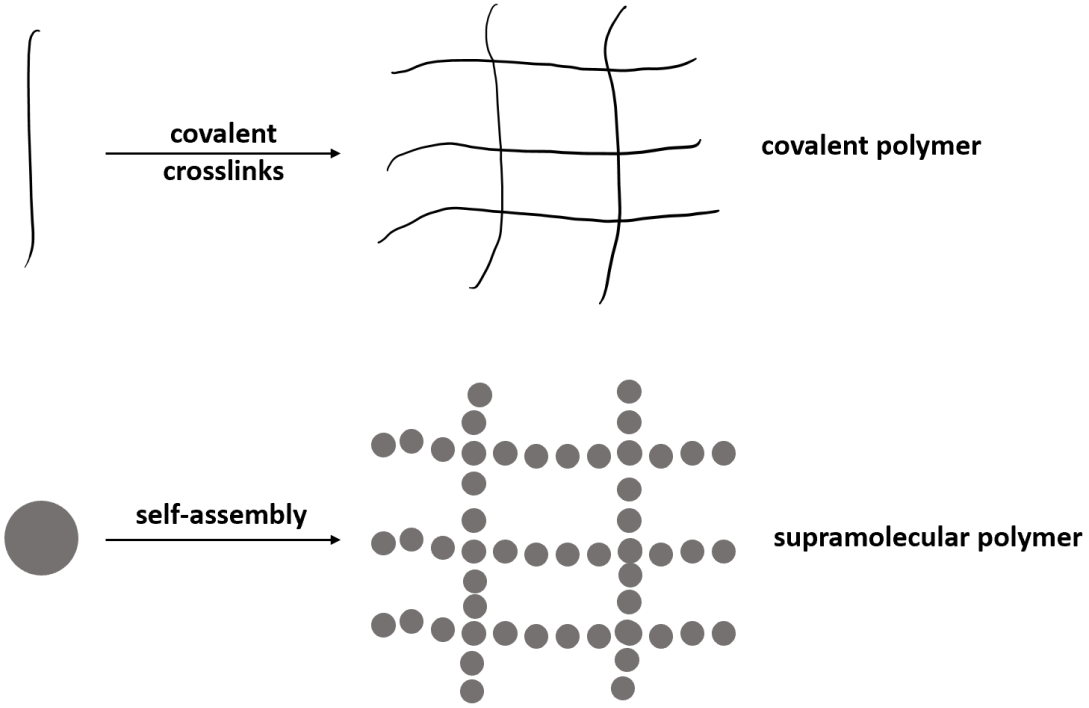

Figure 1.3: (top) Covalent network formed from entanglement and crosslinking of covalent polymers. (bottom) Supramolecular polymer network formed from the self-assembly of small molecules.

Based on the types of interactions that are responsible for the formation of crosslinks in the network, a hydrogel can be further categorized into physical hydrogel and supramolecular hydrogel.[12] For a physical hydrogel, the network is held together by covalent bonds (**Figure 1.3**). Such a hydrogel is generally more robust and can shrink or swell depending on the environment. However, the network in a physical hydrogel is usually hard to break down, which limits its biodegradability. On the other hand, supramolecular hydrogels, made from self-assembly of low molecular weight building block, are mainly held together via non-covalent interactions including hydrogen bonding, ion-dipole interactions, π-π stacking, electrostatic interactions, van der Waals interactions, etc.[13] These non-covalent forces are weak interactions, which make supramolecular hydrogels more responsive to external stimuli, such as pH, light, mechanical force, etc. Supramolecular hydrogels are often biodegradable and biocompatible, which make them ideal candidates for biomaterials. This chapter describes some recent developments on supramolecular hydrogels, with a focus on systems containing self-assembled macrocycles, which often have interesting recognition and stimuli-responsiveness.

1.4 Macrocycles in supramolecular hydrogels

There has been a surge of interest in supramolecular hydrogels, since these materials often exhibit phase change in response to external stimuli.[14] Such stimuli-responsiveness often arises from the non-covalent nature of the crosslinks. One common method to introduce stimuli-responsiveness to hydrogels is to use covalent macrocycles, which can form host-guest complexes and crosslink the polymeric

network.[15,16] Non-covalent interactions, such as hydrogen bonding, ion-dipole interactions, hydrophobic interactions and electrostatic interactions, are formed between the host macrocycle and the guest. Due to the higher aqueous solubility, cyclodextrins and cucurbiturils are amongst the most commonly used hosts in supramolecular hydrogels, which have found applications in adhesives, drug delivery, and artificial muscles (**Figure 1.4**).[15,17–19] On the other hand, although not critical for gelation, crown ethers are frequently incorporated into polymeric hydrogel networks. Such hydrogels are used for sensing and remediation of toxic metal ions, owing to the unique cation-binding properties of crown ethers.[20–22] More recently, Sessler and coworker incorporated tetraimidazolium boxes into polymeric networks that are used for remediation of anions from water and construct self-healing hydrogels for encoding and transforming information.[15,23] In the past few years, there have been some excellent review articles that summarizes the exciting development of macrocyclic hydrogels.[15,24,25]

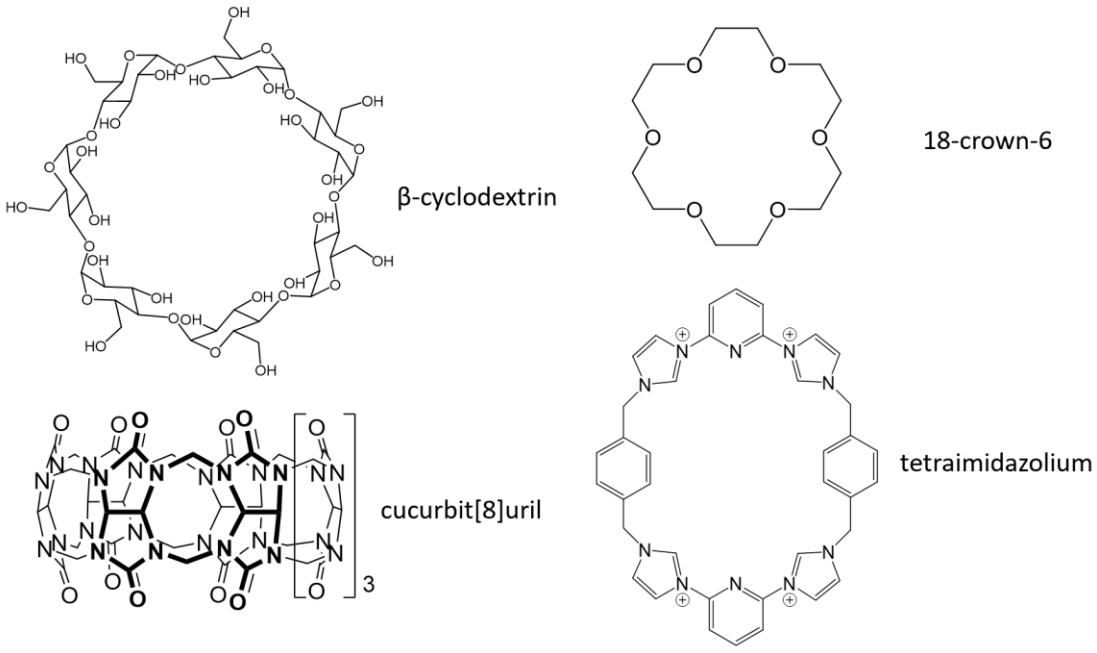

Figure 1.4: Structures of some covalent macrocycles used in hydrogel design.

However, hydrogel systems containing covalent macrocycle do have a few drawbacks. First, the macrocycles are often synthetically challenging and relatively inaccessible and expensive, which limits their practical applications for bulk material construction.[26–28] Also these macrocyclic hosts are often used in combination with a polymeric backbone, which requires extra steps of synthesis;[15] the resulting covalent polymers are generally hard to degrade in a biological system. Self-assembled macrocycles and cages as opposed to covalent macrocycles, however, maintain the capability of crosslinking different strands of polymer and stimuli-responsiveness. Furthermore, while most covalent macrocyclic hosts fail to self-assemble into polymers, non-covalent and dynamic covalent macrocycles can often stack or aggregate to form 1D-supramolecular polymers.[2,29] Such hydrogel systems are highly biodegradable and easy to synthesize, showing promise for design of biomedical materials. Non-covalent

macrocycles are usually more structurally diverse and often contain a modifiable periphery for the introduction of new functions. In the following sections, we focus on the development of hydrogel systems containing self-assembled macrocycles and cages, in hope of providing some insight and generalized design principles for the preparation of stimuli-responsive hydrogels.

1.5 Hydrogels containing dynamic covalent macrocycles

Dynamic covalent bonds are covalent bonds that are labile and exchangeable under appropriate conditions.[30,31] Such interactions are intermediate in strength between a covalent bond and a non-covalent bond. Disulfides, acylhydrazones and thioesters are among the most common linkages used to construct dynamic covalent systems.[32] Dynamic disulfide macrocycles are well developed in literature for making synthetic receptors.[33] Before moving from purely covalent into purely non-covalent macrocycles, it is interesting and necessary to discuss the hydrogel assembly containing dynamic covalent macrocycles that have intermediate strength.

Otto and coworkers developed a disulfide-containing system as a rare example of a dynamic covalent macrocycle to generate a supramolecular hydrogel (**Figure 1.5**).[34] They conjugated an oligopeptide to an aromatic dithiol to maximize the interaction between each monomer **59**. Under oxidizing conditions in water, dithiol form macrocyclic disulfides with different numbers of repeating units. They discovered that different types of physical agitation can cause drastically different product distribution.[35] Under shaking, a macrocyclic hexamer **60** predominates and further stacks to form fibers. The resulting fibers are short and only gave a solution. Upon

irradiation using UV-light, however, the disulfides form thiol radicals and exchange to form a linear polymeric disulfide network, which maintained the original folding. Macroscopically, the solution turns into a hydrogel after irradiation for 3 days.

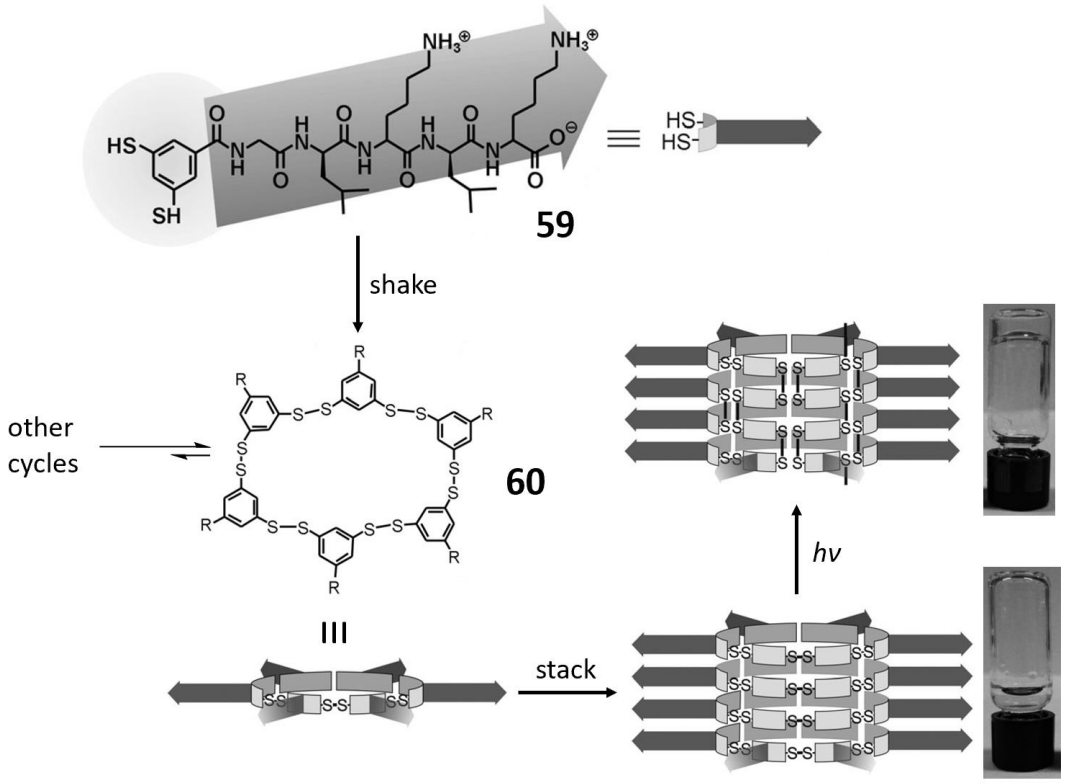

Figure 1.5: Dithiol **59** is oxidized and forms hexameric macrocycle **60** under shaking. **60** stacks to form columns that are covalently trapped to give a hydrogel after irradiation with light.[34] Reprinted with permission from John Wiley & Sons.

The Otto group continued to develop an azobenzene disulfide system from monomers **61** and **62** (**Figure 1.6**).[36] The monomers contain carboxylic acid groups for potential recognition of metal ions while having an azobenzene core for potential π-π stacking and responsiveness to light. Initial oxidation of monomer mixture gave a solution containing a mixture of different macrocycles (**63-65**). Addition of Mg^{2+} ions instead gave a self-standing hydrogel, which consists exclusively of the **65** macrocycle

based on HPLC-MS. Addition of other cations fails to induce gelation. A crystal structure of **65**•$Ca_2(H_2O)_{15}$ was also obtained to provide structural insight into gelation (**Figure 1.7**). X-ray analysis shows that the stacks of **65** are connected by Ca^{2+} ions via coordination to carboxylates and interlayer hydrogen bonding. The resulting hydrogel is responsive to multiple stimuli, such as heat, UV-light, mechanical forces and reducing agents. This work is a great demonstration that thermodynamic drives, such as metal-ligand interaction, can influence the outcome of a dynamic covalent mixture.

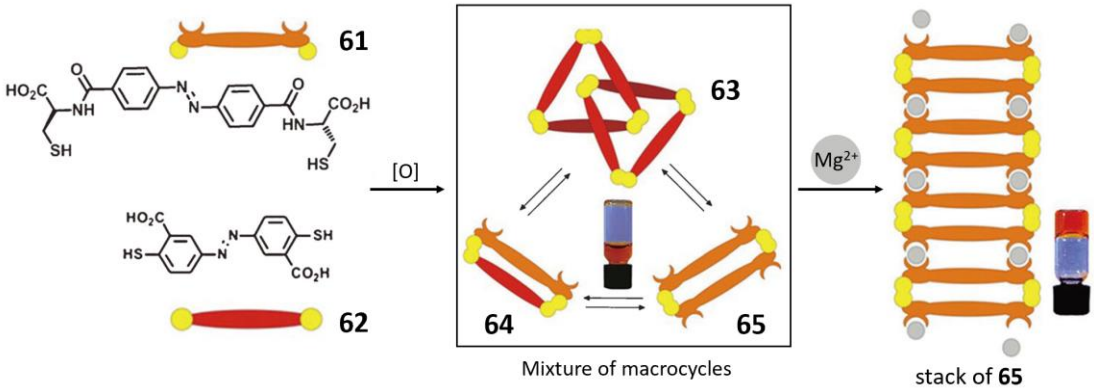

Figure 1.6: Dithiols **61** and **62** form solution mixture of macrocycles **63-65** upon oxidation. Addition of Mg^{2+} shifts the equilibrium completely to macrocyclic **65**. The **65** formed non-covalent stacks and gave a self-standing hydrogel.[36] Reprinted with permission from John Wiley & Sons.

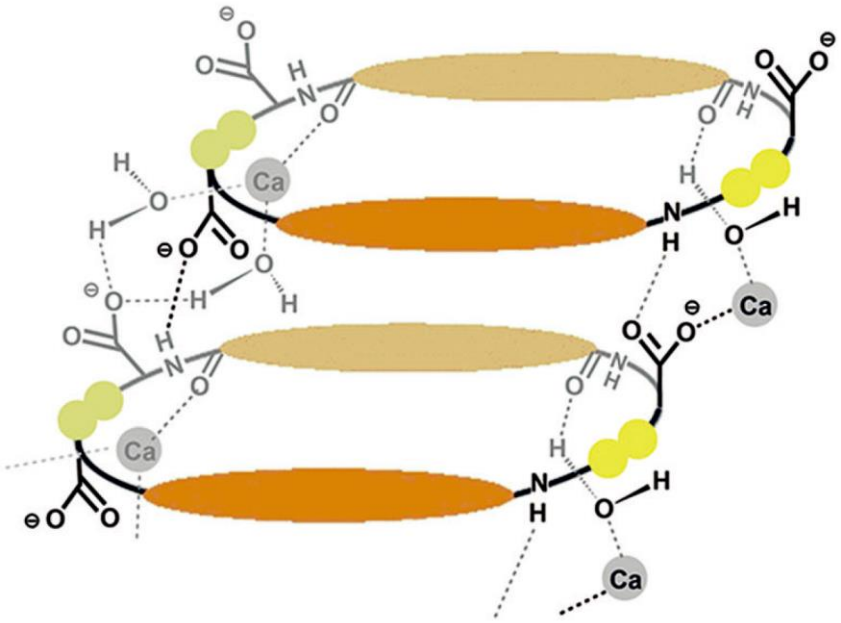

Figure 1.7: A crystal structure of **65**•$Ca_2(H_2O)_{15}$ shows a stack of **65** with interlayer crosslinks from Ca^{2+} coordination and H-bonding.[36] Reprinted with permission from John Wiley & Sons.

1.6 Hydrogels containing non-covalent metal-organic macrocycles and cages

Coordination driven self-assembly has been utilized to construct metallocycles and cages.[37] Depending on the geometry of the ligands and directionality of metal core, a wide variety of 2D and 3D structures can be produced from small building blocks.[38] Such metallocycles are often prepared in organic solvents and hydrophobic, limiting their applications in aqueous environments. One strategy to generate hydrogels is to conjugate solubilizing polymers on the periphery of the core assembly, thus increasing solubility in water while maintaining the self-assembly properties. Stang and coworkers prepared discrete rhomboids from di-Pt(II) complex **67** and dicarboxylates **66**/**68**, which have complementary shapes (**Figure 1.8**).[39] With a PEG chain attached, the organic metallocycle can self-assemble to give micelles in water. Increasing the

concentration of metallocycles in the water, on the other hand, gave a white hydrogel. The authors proposed that hydrophobic interactions and π-π stacking between macrocycles are critical for gelation. This work demonstrates the first example of hydrogels containing metallo-organic macrocycles.

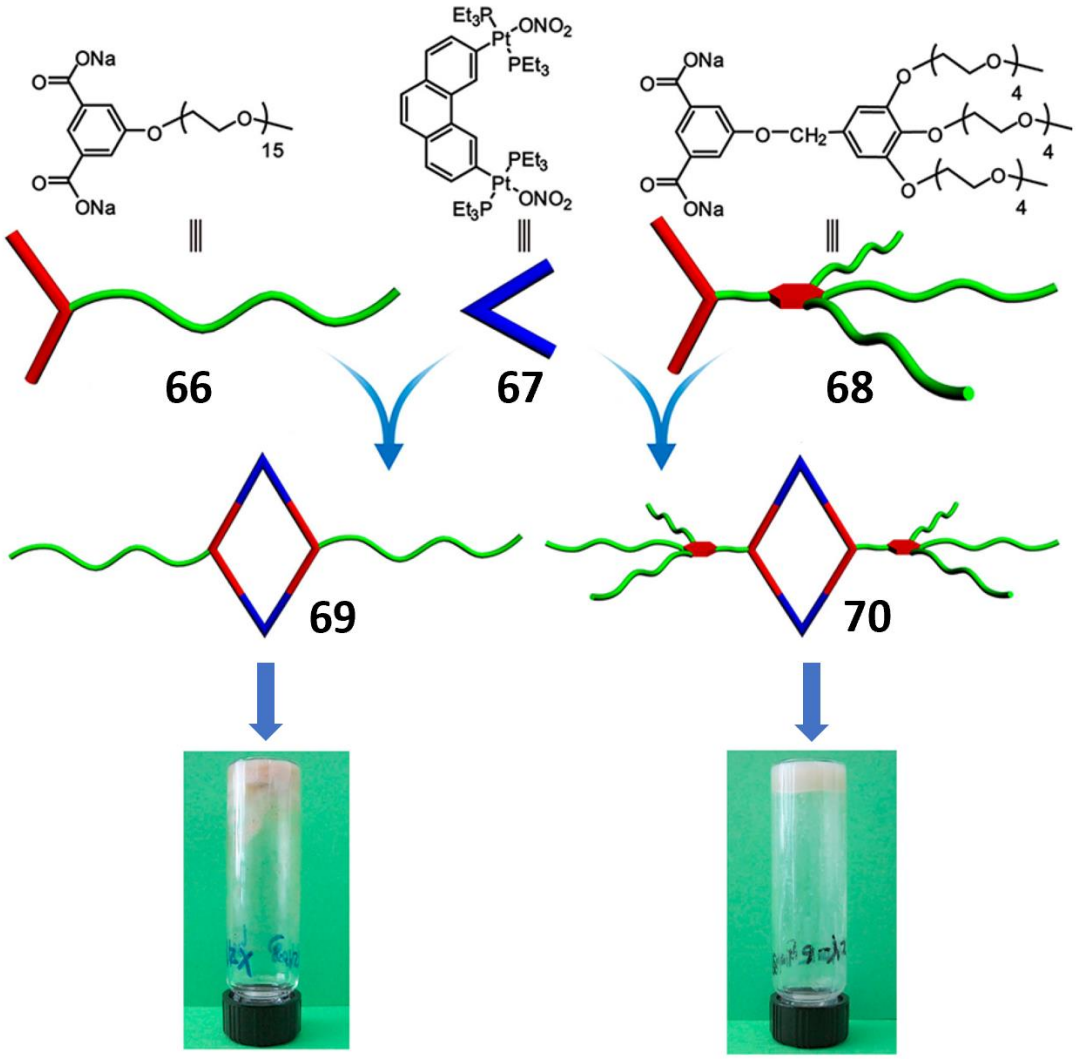

Figure 1.8: Stang and coworkers utilized a coordination-driven self-assembly to form discrete Pt (II) macrocycles **69** & **70**, which further aggregate to form hydrogels.[39] Reprinted with permission from the American Chemical Society.

Chen, Yang and coworkers designed building blocks **70-72**, which all have 120° bite angles to enable formation of hexagonal metallocycles **73/74**.[40] These metallocycles are pre-formed and anchored to poly-N-isopropylacrylamide (PNIPAAM) polymers via post-assembly modification of the ligand (**Figure 1.9a**). Compared with PEG, PNIPAAM chain not only improved water solubility of the metallocycles but also brought LCST (lower critical solution temperature) behavior. The resulting star polymers **75/76** form self-standing hydrogels. Addition of bromides (Br^-) caused disassembly via coordination to Pt(II) core and break apart the macrocycles, which shows promise for trap and release of small molecules. Furthermore, the hydrogel containing **75** exhibits self-healing properties, which is presumably caused by reversible metal-ligand interactions (**Figure 1.9c**).

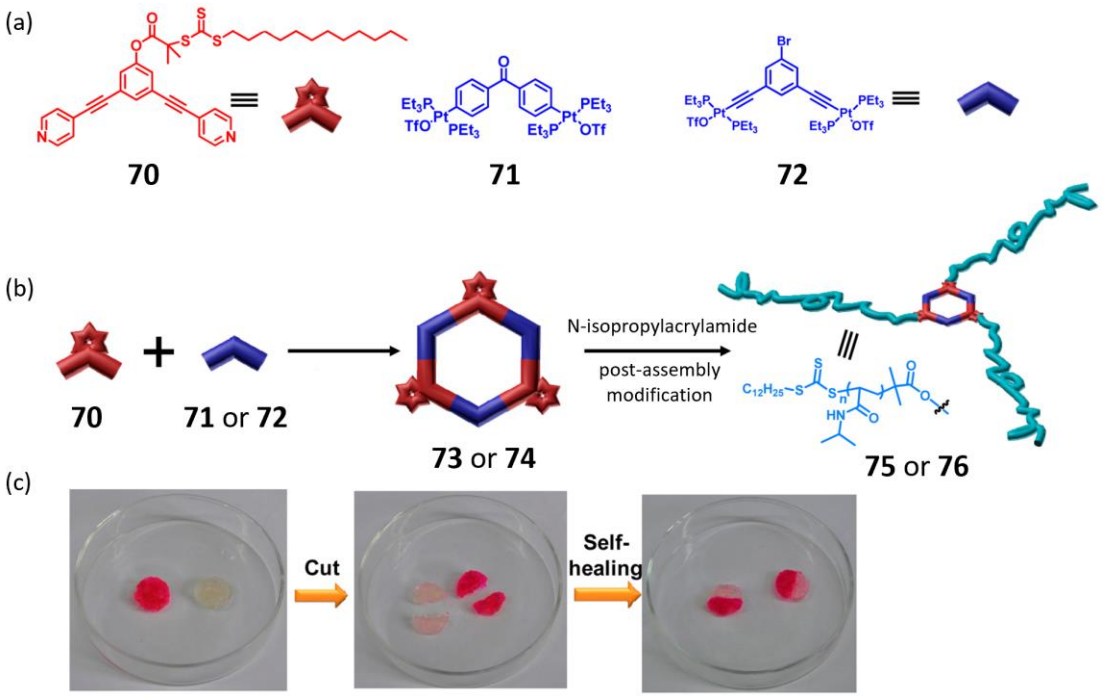

Figure 1.9: Polymeric hydrogel crosslinked by hexagonal metallocycles. (a) Structure of ligands **70-72**. (b) **70** and **71/72** self-assemble into a hexagon, which are subsequently modified with poly-N-isopropylacrylamide to give star polymers. (c)

Two pieces of hydrogels made from **75** (red one is colored with sulforhodamine B) were cut and recombined. After 1 min at room temperature, the two separate halves rejoined.[40] Reprinted with permission from the American Chemical Society.

The authors continued to utilize the same post-translational modification on the hexagon **73** to anchor block copolymers of PNIPAAM and poly-N,N-dimethylaminoethyl methacrylate (PDMAEMA), the latter of which can bring CO_2 responsiveness.[41] They discovered that CO_2 bubbling into an aqueous solution of hexagon-polymer conjugates followed by heating to 34°C gave a self-standing hydrogel, while the block copolymers alone failed to trigger gelation. Bubbling N_2 at 34°C removes CO_2 from the system and triggers gel-sol transition. Cooling the gel to room temperature gave a homogeneous solution, demonstrating the LCST behavior of the system. The resulting hydrogel is injectable and has low cytotoxicity, showing promise for biomedical applications.

Besides 2D-macrocycles, 3D metal-organic polyhedral (MOP)[42] can also serve as crosslinks between water soluble polymers. Nitschke's group developed a hydrogel from polymers crosslinked by self-assembled metal-organic cages.[43] 4,4′-diaminobiphenyl **77** forms imines with two PEGylated 2-formylpyridine molecules **78** in water, which self-assemble into a tetrahedral cage **79** in the presence of Fe(II) under basic condition (**Figure 1.10**). Gelation occurred at room temperature within 1 min after simply mixing all subcomponents in water. In contrast to the 2D macrocycles, the inner cavity of the 3D cages allows for guest trapping (benzene, fluorobenzene and furan) via host-guest interactions. The authors also fabricated hydrogel microparticles using a microfluidic device to mix different components. The resulting microgels are

easily disassembled by adding Fe(II) chelator (tris(2-aminoethyl)amine), acid (*p*-toluenesulfonic acid) or 2-formylpyridine. The stimuli responsiveness was utilized for the release of a pre-loaded fluorescent cargo. Overall, the strategy of conjugating functional water-soluble polymers to metallocycles could be potentially generalized to potentially a wide variety of macrocycles and cages known in the literature.

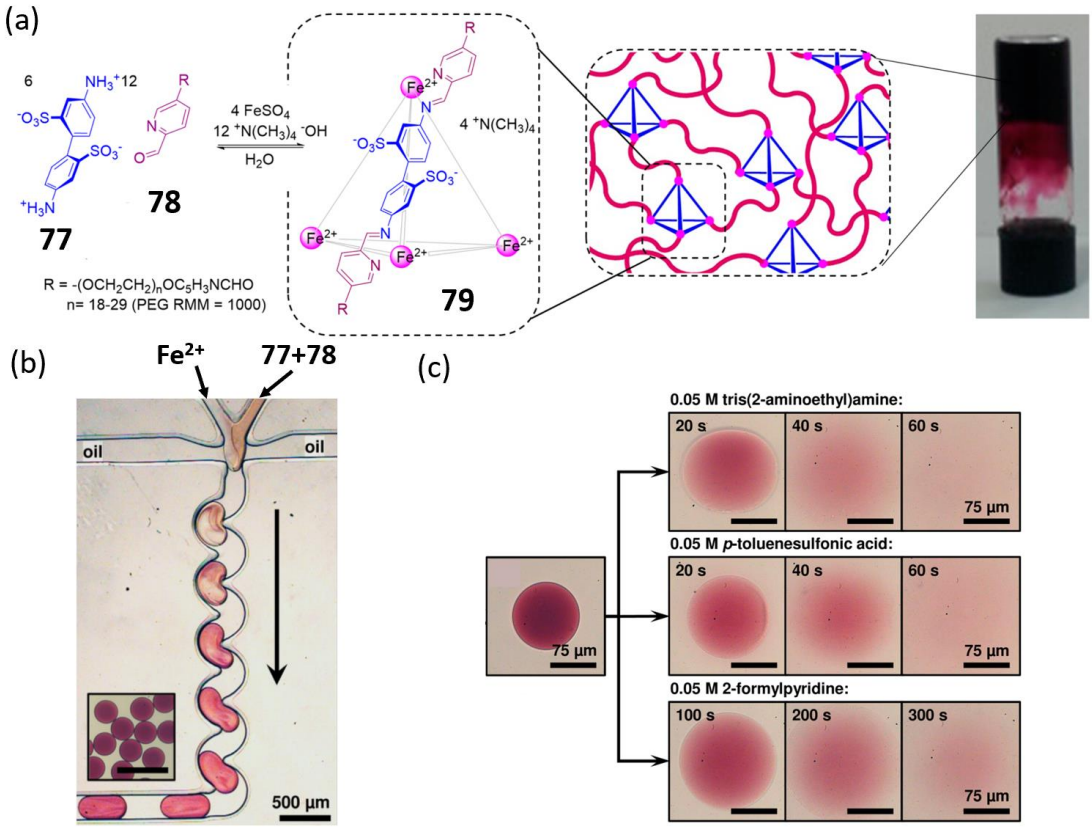

Figure 1.10: (a) Metallocage **79** is formed by simply mixing different subcomponents, which induces gelation. (b) Monodispersed microgels are formed at a 200 µm microfluidic flow-focusing junction. The droplets of mixtures get progressively darker en route to the exit. Inset shows gel particles after exiting microfluidic device. (c) Hydrogel particles are disassembled by tris(2-aminoethyl)amine, *p*-toluenesulfonic acid or 2-formylpyridine.[43] Reprinted with permission from the American Chemical Society.

Purely self-assembled hydrogels (without polymeric backbones) made from MOPs have also been reported. Maji and coworkers synthesized a 3D metal-organic cube **81** from the self-assembly of Ga^{3+} and 4,5-imidazoledicarboxylate **80**.[44] X-ray crystallography shows that the metallocubes are connected by dimethylammonium ions (DMA) via charged-assisted hydrogen bonds (**Figure 1.11**). The ionic nature of the complexes significantly improved the aqueous solubility, which paves the way for hydrogelation. Switching DMA to other amine-based cations such as NH_4^+, N-(2-aminoethyl)-1,3-propanediamine, guanidinium and β-alanine triggered the hydrogelation of the metallocube. Interestingly, the hydrogel made with NH_4^+ can serve as a medium for charge-based separation of dyes.

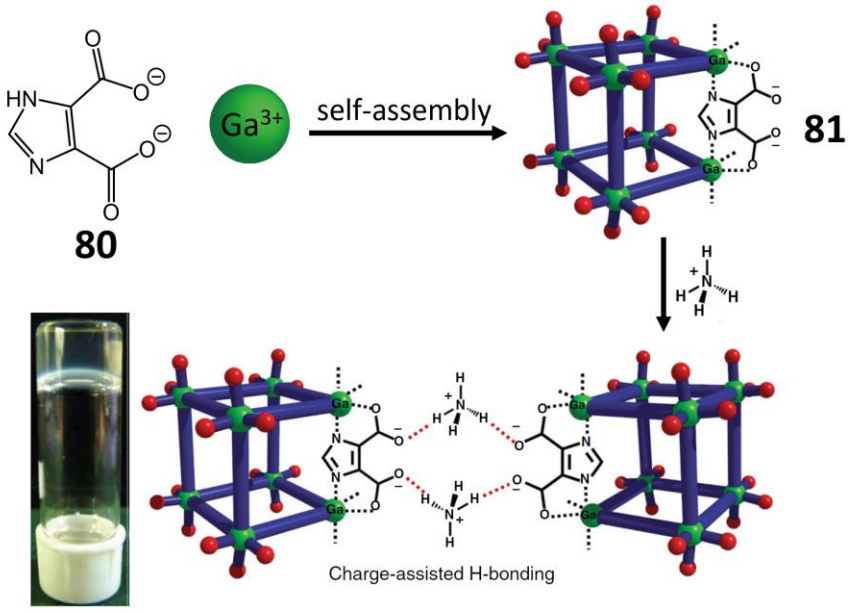

Figure 1.11: Ligand **80** and gallium(III) self-assemble into a metallocube **81**, which are non-covalently connected by ammonium ions to give a transparent hydrogel.[44] Reprinted with permission from Nature Publishing Group.

With more insight into the gelation mechanism, the authors rationally designed a diammonium linker **82**, which contains tetraphenyl ethylene (TPE) for aggregration-induced emission properties (**Figure 1.12**).[44] When incorporated into cube **81** to give a hydrogel, TPE modules in **82** are anchored and aggregated via charge-assisted hydrogen bonds, which causes emission at 474 nm under UV light. This resulting hydrogel has potential for use as a processible coating for UV-lamps. Importantly, the hydrogel formation required no heating or polymeric backbone, demonstrating the power of self-assembly to construct functional materials from mixing simple building blocks at room temperature.

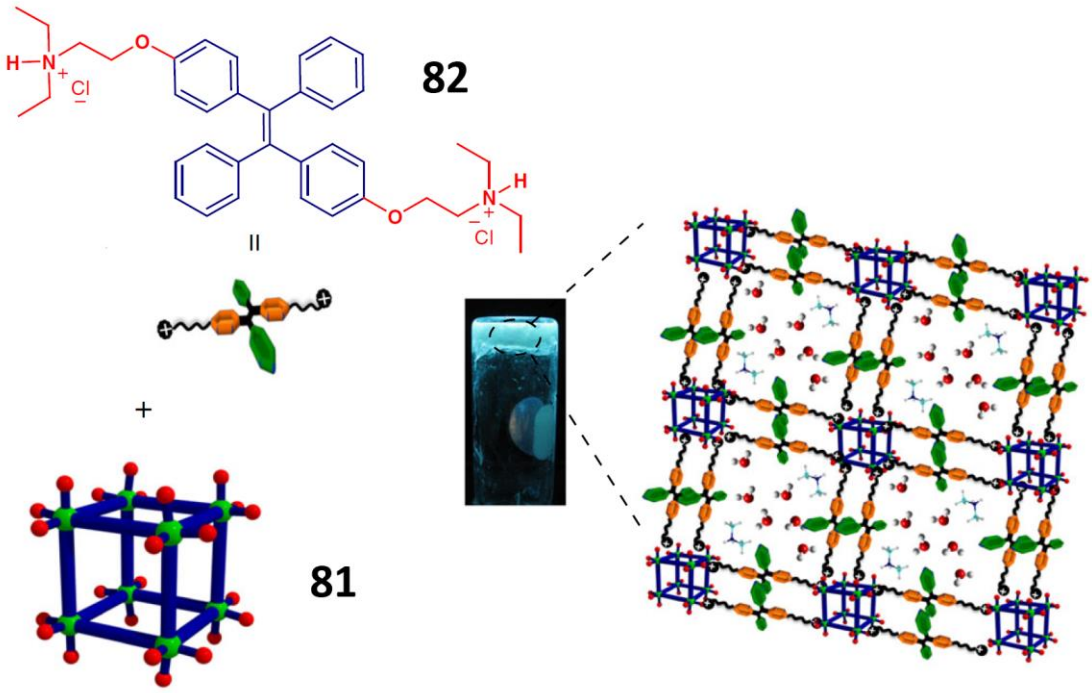

Figure 1.12: Metallocube **81** forms a light-emitting hydrogel under UV-lamp when tetraphenyl ethylene diammonium **82** is incorporated to introduce aggregation-induced emission.[44] Reprinted with permission from Nature Publishing Group.

Zheng and Cao synthesized a copper-based polyhedron **84** from 5-nitroisophthalate **83** and $Cu(OAc)_2$.[45] Simply sonicating the resulting powder in water gave a blue hydrogel (**Figure 1.13**). IR and XPS analysis indicated the existence of water-mediated hydrogen bonding between nitro groups on the MOP, which explains the reason for the gelation. The resulting hydrogel shows good biocompatibility on mice skin, while inhibiting the bacterial growth of *S. aureus* and *E. coli*.

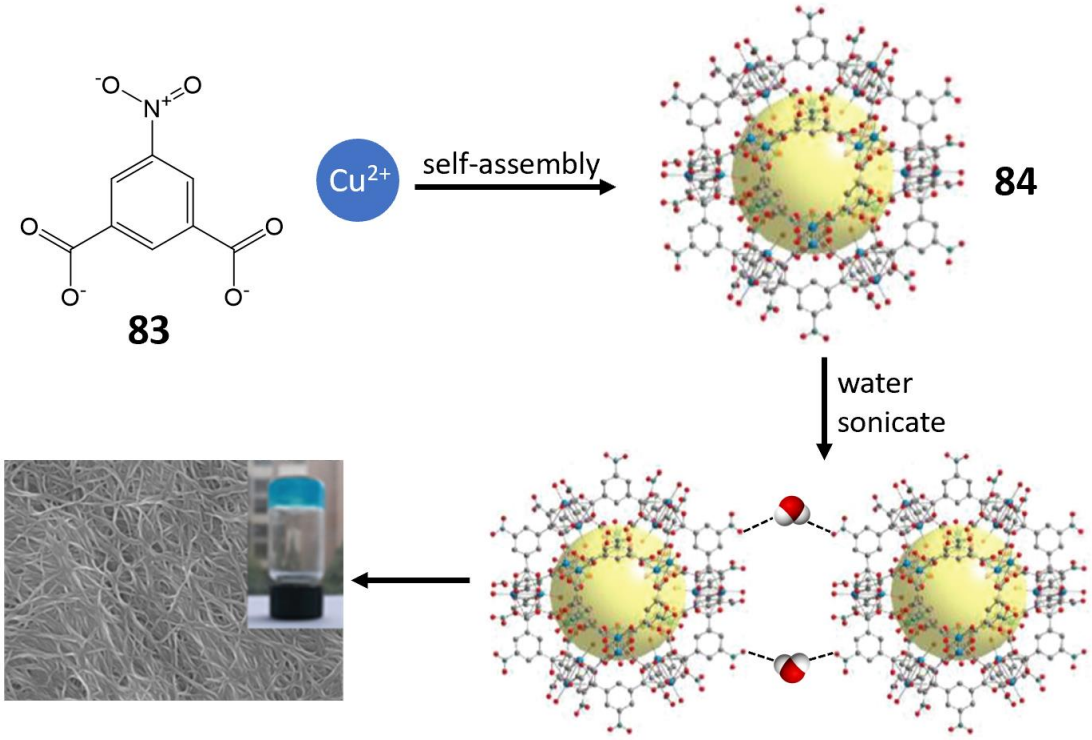

Figure 1.13: 5-nitroisophthalate **83** and Cu(II) self-assemble into polyhedron **84**. Sonication of **84** in water gave a blue and self-standing hydrogel with fibrous network (SEM). Hydrogen bonds between water and nitro groups are responsible for gelation.[45] Reprinted with permission from the Royal Society of Chemistry.

Overall, self-assembled metallocycles and metallocages are preliminarily applied to induce hydrogelation. Hydrophobic assemblies are applicable to aqueous environment due to the functionalization with water soluble polymers. More recently, hydrogels

containing MOPs that crosslinked by hydrogen bonding are starting to emerge. The facile synthesis and the multifunctionality of these materials demonstrate potential for new biomaterial design. Due to the diversity of metallo- cycles and cages known in literature, we foresee more exciting development in the field.

1.7 Hydrogels containing non-covalent hydrogen-bonded macrocycles

Nucleobases and their analogs contain aromatic units with rich recognition chemistry, which are often capable of forming higher order assemblies. With complementary H-bond donors and acceptors, the molecules can associate to form macrocycles. The planarity of the cycles often leads to chiral stacking to form 1D polymers via π-π interactions, which are used to construct supramolecular materials. H-bonded macrocycles commonly found in hydrogels are folate-quartets, isoG-pentamers, TAP_3CA_3-rosettes and G-quartets (**Figure 1.14**). This section summarizes macrocyclic hydrogels containing folate-quartets, isoG-pentamers and TAP_3CA_3-rosettes and in section **1.8** we focus on G-quartet hydrogels, which is the main focus of this thesis.

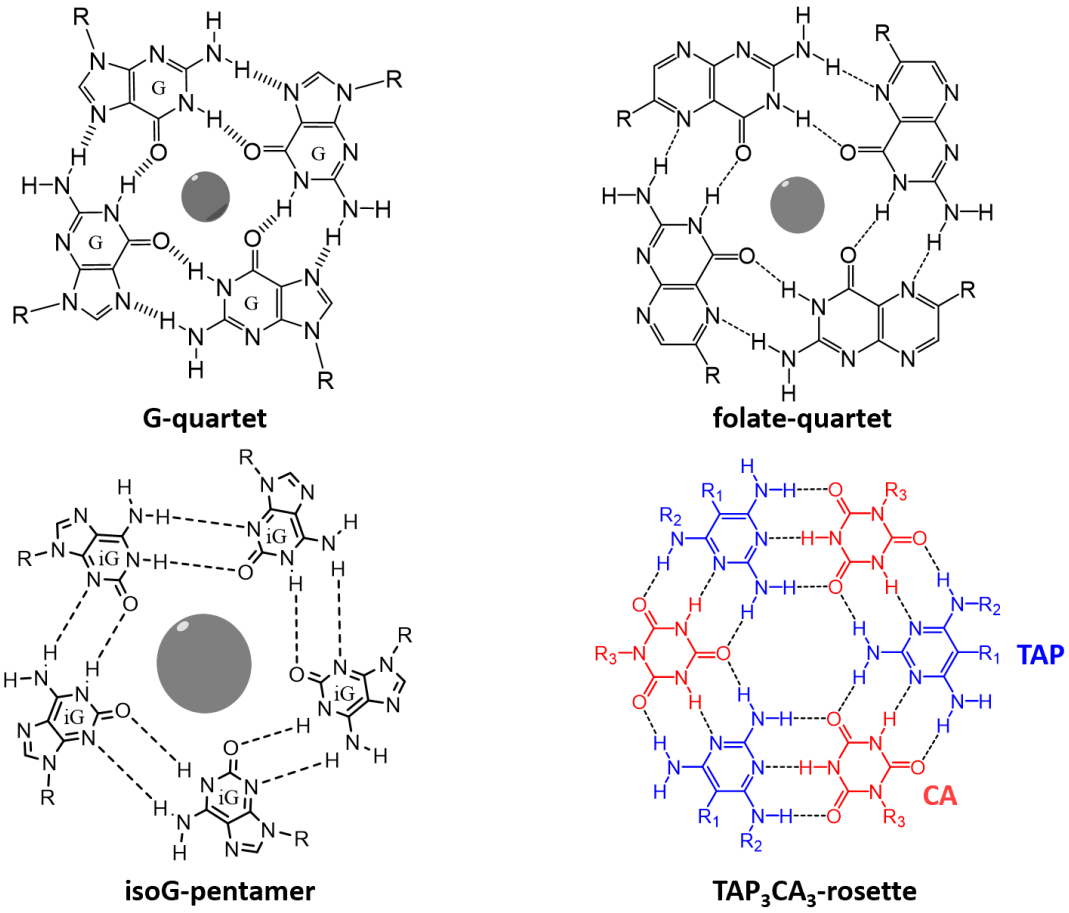

Figure 1.14: Structures of non-covalent macrocycles commonly used in supramolecular hydrogels.

1.7.1 Hydrogels containing folate-quartets

Folic acid **85** (Vitamin B9) and its corresponding salts are known to self-associate in solution to form folate-tetramers (**Figure 1.15**). These tetramers further stack and aggregate to form columnar structures.[46] Limited by its poor water solubility, folic acid (FA **85**) itself can only form organogels in a DMSO/water mixture.[47,48] Yet constructing supramolecular hydrogels from this biocompatible gelator would be beneficial for potential biomedical applications. With two carboxylic acid groups on

the far end, the folic acid **85** molecule is pH switchable. Nandi and coworkers prepared folate-tetramer based hydrogels via the addition of glucono-δ-lactone (GdL) to a solution of FA **85**.[49] GdL is hydrolyzed and lowers the pH of the medium to trigger gelation by **85**, which was then used for controlled release of drug molecules.

Furthermore, the carboxylic acids on **85** can also be non-covalently modified via metal-ligand interactions, or covalently modified via ester or amide bond, both of which do not interfere with the formation of folate tetramers. Modifying **85** with functional molecules that can also improve the solubility of the gelator would be ideal.

Yan and coworkers discovered that mixing potassium folate solution (pH=11) and Zn^{2+} solution gave a clear and self-standing hydrogel within 20 mins at room temperature (**Figure 1.15**).[50] The authors propose that interfiber crosslinks caused by Zn^{2+} coordination between carboxylates is responsible for gelation. The resulting hydrogel has shear-thinning properties, which can be used as injectable gels and bioinks for 3D printing. Besides being highly biocompatible toward cells, this folate-zinc hydrogel can be doped with Gd^{3+} for magnetic resonance imaging (MRI) applications.

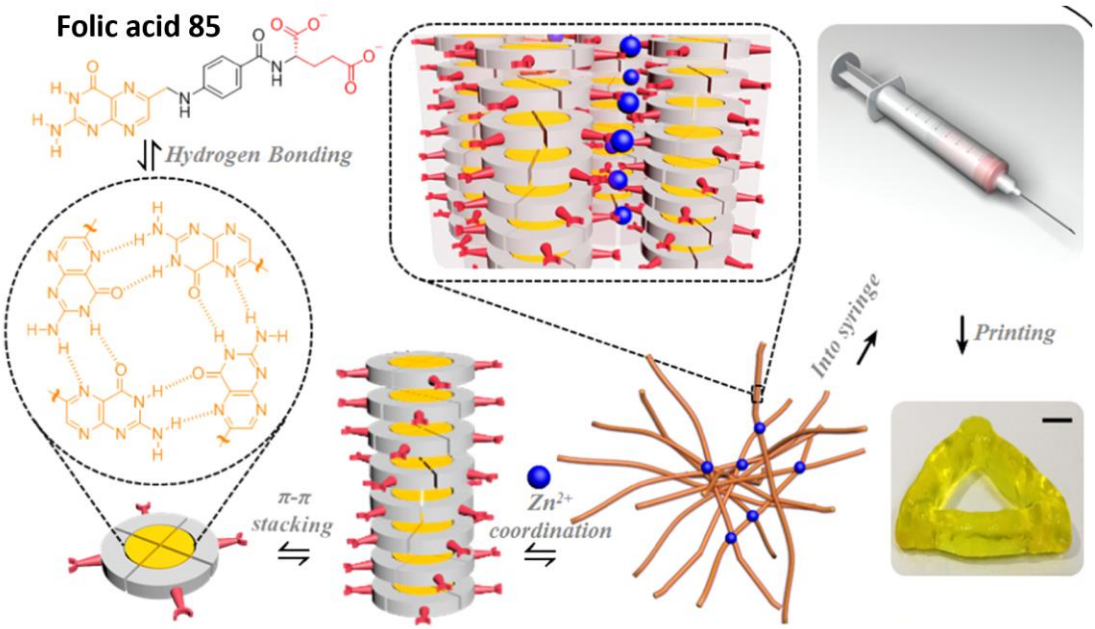

Figure 1.15: Proposed gelation mechanism for FA-Zn^{2+} hydrogels. The resulting hydrogel is shear-thinning, which can be squeezed through a syringe for printing applications.[50] Reprinted with permission from the American Chemical Society.

On the other hand, Yang and coworkers developed a series of hydrogels from covalent conjugates of **85** and drug molecules/peptides.[51–55] In an initial report, the authors synthesized a FA-Taxol conjugate **86** with a phosphorylated and succinated tripeptide linkage (**Figure 1.16**).[55] Taxol is a commonly used anti-cancer drug. While the phosphorylated compound **86** only gave a solution in a phosphate buffer, addition of phosphatase enzyme can hydrolyze the phosphate group and induce gelation within 3 min. Unlike most other systems, hydrogel made from **86** shows a morphology of uniform nanospheres. The hydrogel showed comparable efficacy compared to free Taxol against HepG2 cells, which shows great potential for a novel delivery system of anti-cancer drugs.

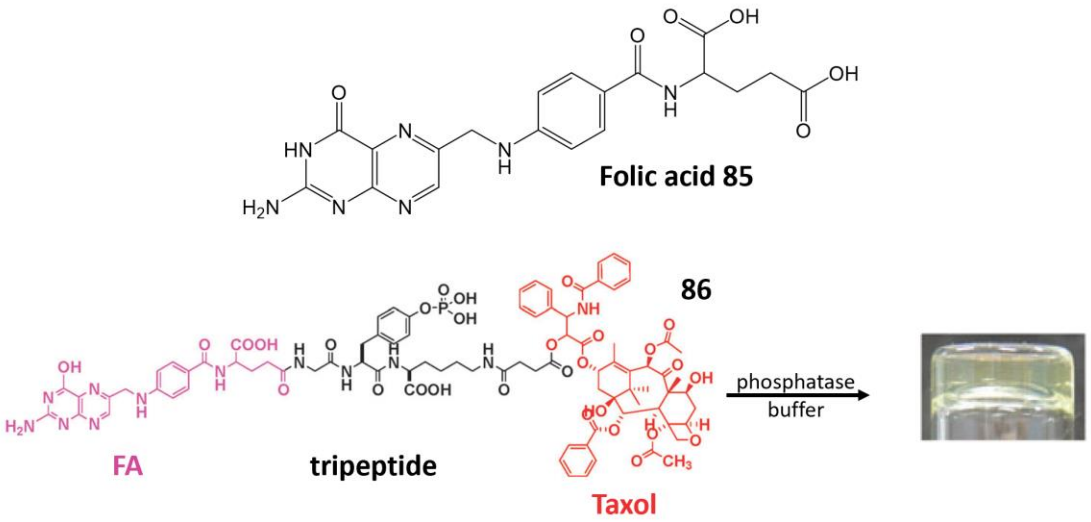

Figure 1.16: A conjugate **86** containing FA **85**, phosphorylated tripeptide and Taxol forms a clear hydrogel upon addition of phosphatase.[55] Reprinted with permission from the Royal Society of Chemistry.

The authors continued to modify **85** with a head group that contains both disulfide bond and ester bonds (**Figure 1.17**).[51] When treated with glutathione **89** (GSH), the disulfide bond in **87**/**88** is reduced and triggers hydrogelation via formation of FA tetramer. On the other hand, the hydrolysable ester bond is used to conjugate triamcinolone acetonide or rapamycin, drugs that are used to treat eye diseases. Hydrogels made from **87** and **88** showed excellent biocompatibility against rabbit eye tissue with controlled release of the corresponding drugs, which could be beneficial for recovery after eye surgeries. The Yang group also designed a similar gelator with GSH **89** responsiveness and conjugated with Taxol.[53] The intratumor injection of GSH-triggered gels showed extended release with over 4 times the potency of intravenous injection of Taxol against breast cancer cells.

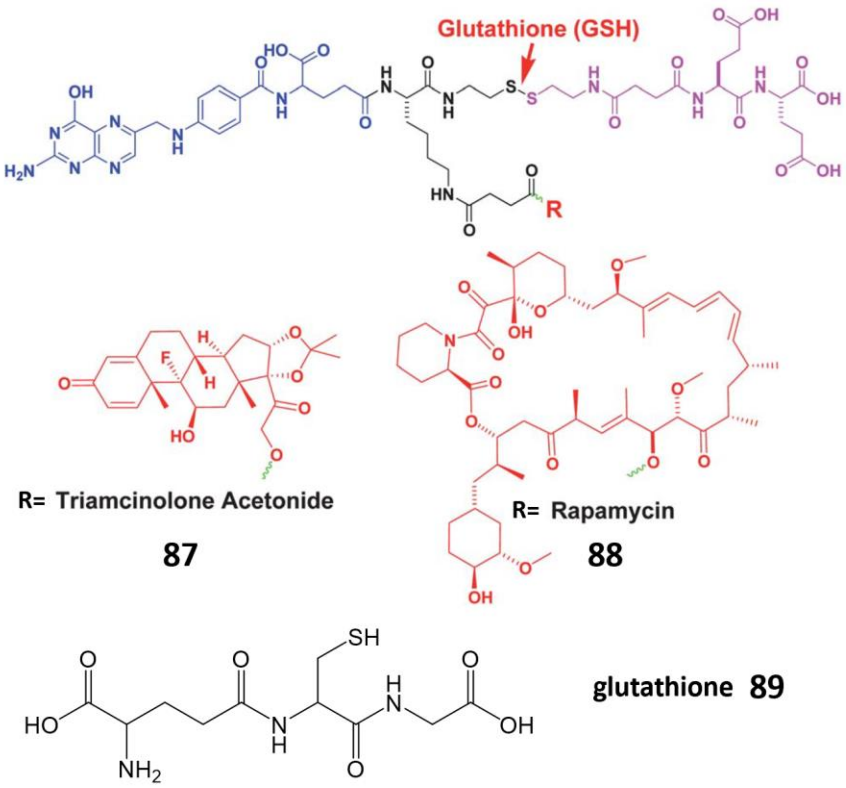

Figure 1.17: Structures of FA-drug conjugates **87**/**88** and glutathione **89**.[51] Reprinted with permission from the Royal Society of Chemistry.

Yang, Ou and Chen designed a FA-peptide conjugate **90** that contains triphenylalanine to promote self-assembly, and disulfide bond to enable the redox-responsive gelation (**Figure 1.18a**).[54] Addition of GSH **89** triggers gelation in PBS buffer and cell culture medium (**Figure 1.18b**). The hydrogels serve as a biocompatible extracellular matrix mimic for induced pluripotent stem (iPS) cells, which are used for myocardial repair. Results showed that with FA-peptide hydrogel encapsulation, the retention and survival of iPS cells after injection was significantly improved in mice after acute myocardial infarction, as compared to control groups with only iPS cells

(**Figure 1.18c**). This injectable hydrogel has great promise for tissue engineering and regenerative medicine.

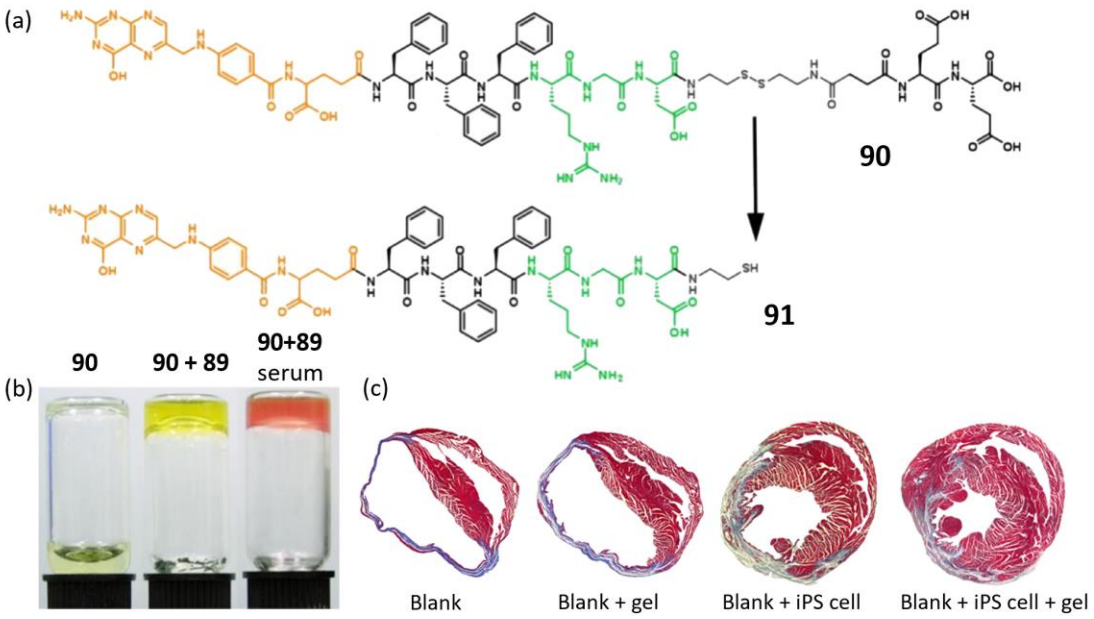

Figure 1.18: (a) Structures of conjugate **90** and gelator **91**. (b) Conjugate **90** does not form hydrogels, but addition of GSH **89** triggers gelation in both a buffer solution and a cell culture medium. (c) Injection of gel-encapsulated iPS cell improves myocardial infarction recovery compared to iPS cell without gel.[54] Reprinted with permission from the American Chemical Society.

1.7.2 Hydrogels containing isoG-pentamer and other isoG-macrocycles

Isoguanosine (isoG **92**) is an isomer of guanosine (G **1**) with transposed carbonyl (C=O) and amino (NH_2) groups on guanine. Isoguanosine is known to form tetramer and pentamers in solution depending on templating cations (**Figure 1.19**).[56–59] The macrocycles can further stack to form a sandwich structure with a cation in between. Previous studies from our group showed that the cavity in isoG **92** pentamer has strong affinity for larger cations such as Cs^+ and Ra^{2+}. This property as an ionophore was used

for remediation of radioactive waste in water.[57,60] The hydrogelation of **92**, however, were not thoroughly explored until recently.[61] Seela and coworkers synthesized isoguanosine and their analogs **92-94** and examined their hydrogelation in the presence of different alkali cations (**Figure 1.20**).[62] Interestingly, **92** formed stable hydrogels with all cations tested (Li^+, Na^+, K^+, Rb^+, Cs^+) while **93** and **94** have different selectivity toward cations despite similar recognition unit on the nucleobase. G **1**, however, fails to form hydrogels with all cations. The resulting hydrogels were used to trap and release methylene blue, which shows that the isoG **92** hydrogels can be used for drug release devices.

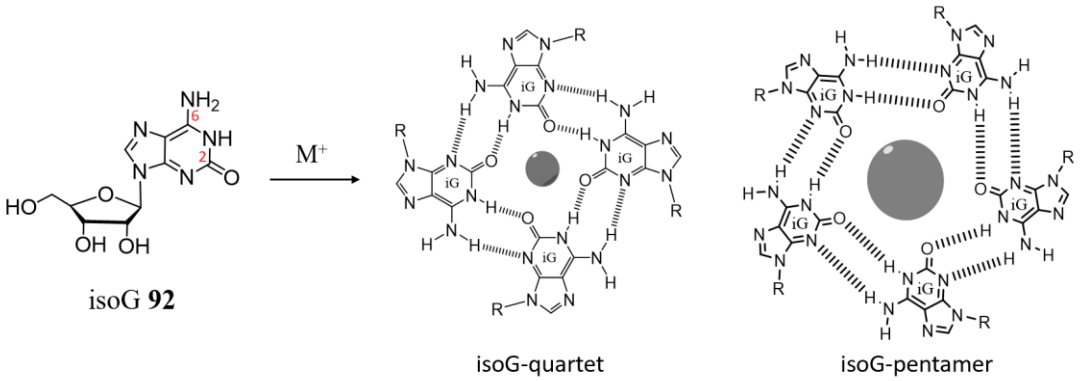

Figure 1.19: IsoG **92**, in the presence of templating cation, can form quartets or pentamers.

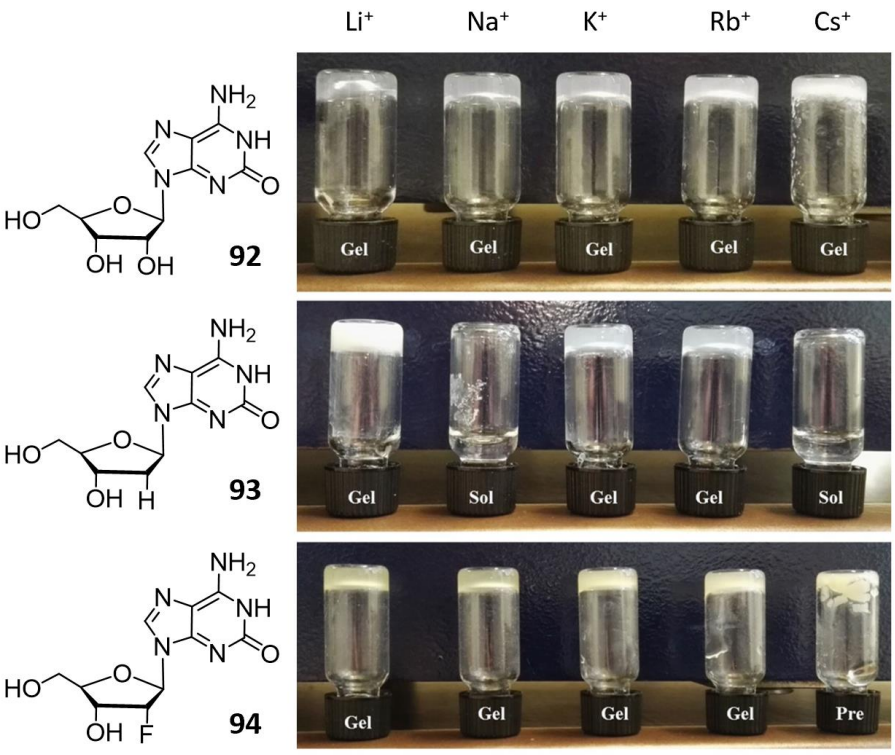

Figure 1.20: Gelation tests on nucleoside analogs **92-94** with different cations.[62] Reprinted with permission from John Wiley & Sons.

Dan and Zhao discovered that a 1:1 binary mixture of G **1** and isoG **92** formed a self-standing hydrogel with K^+ and Rb^+ (**Figure 1.21**).[63] The authors proposed that the gel is made of mixed quartets between **1** and **92**. The resulting gels have a lifetime of 1 day (K^+) and 10 days (Rb^+).

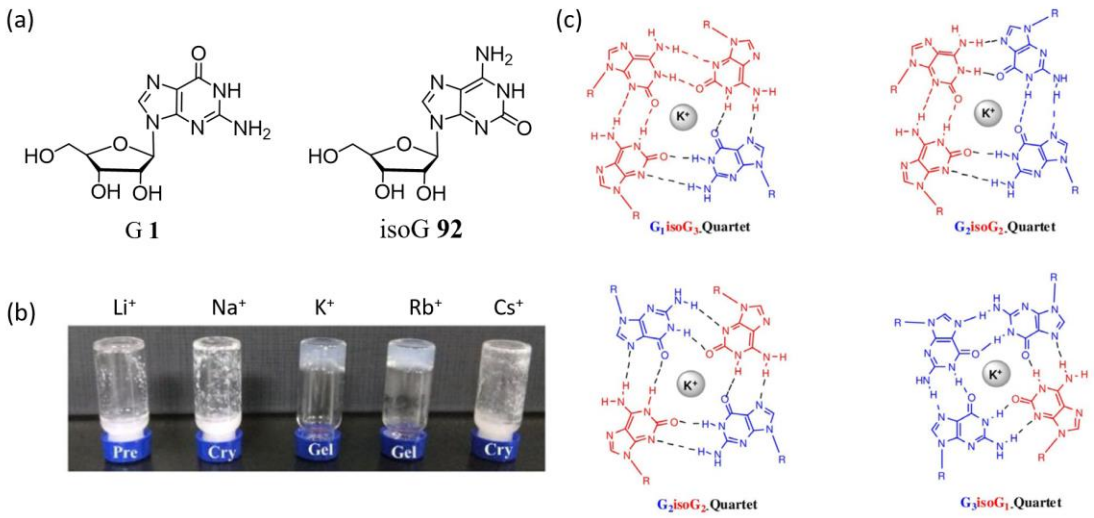

Figure 1.21: (a) Structures of G **1** and isoG **92**. (b) 1:1 binary mixture of G **1** and isoG **92** forms self-standing hydrogels with K^+ and Rb^+. (c) Structures of possible mixed quartets between **1** and **92**.[63] Reprinted with permission from John Wiley & Sons.

Seela and coworkers also synthesized 8-aza analogs of 2′-deoxyguanosine **95** and 2′-deoxyisoguanosine **96**, and found that only a combination of **96** and K^+ gave a self-standing hydrogel (**Figure 1.22**).[64] The resulting gel with **96** is fluorescent under a 360 nm UV lamp, while isoG gel with **92** showed no fluorescence. pH also influences fluorescence intensity of the hydrogels, presumably by alternating the protonation state of the nucleobase analogs.

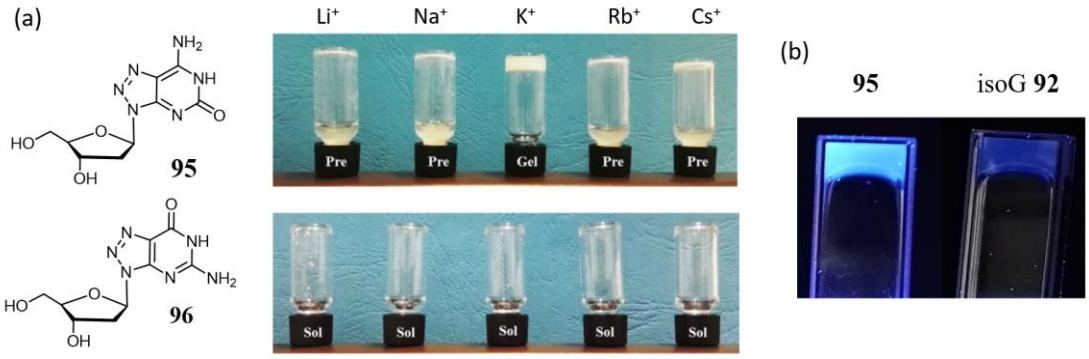

Figure 1.22: (a) 8-aza analog **95** only form hydrogel with K^+ while **96** fails to give hydrogels with any cation. (b) Under a UV-lamp, **95** hydrogel is highly fluorescent

while isoG **92** gives weak responses.[64] Reprinted with permission from John Wiley & Sons.

Overall, while isoG related hydrogels are starting to emerge, the relative inaccessibility of these analogs significantly limited their applications for material design.

1.7.3 Hydrogels containing TAP_3CA_3-rosettes

For the past 30 years, 2,4,6-triaminopyrimidine (TAP), cyanuric acid (CA) and their analogs have been used to construct higher-order structures. The complementary H-bond donor-acceptor pattern with 120° directionality leads to the formation of TAP_3CA_3-rosettes, which can form supramolecular stacks (**Figure 1.23**). Hud and coworkers began a series of investigations into these rosette shaped structures.[29,65–69] They reason that the π-surface (1.6-1.7 nm^2) is large enough to compensate for hydration energy so that these motifs can form very long aggregates; the self-assembly properties of these primitive nitrogenous molecules could shine light on the origin of nucleic acids and homochirality. We herein review the exciting developments on the self-assembled hydrogels containing TAP_3CA_3-rosettes.

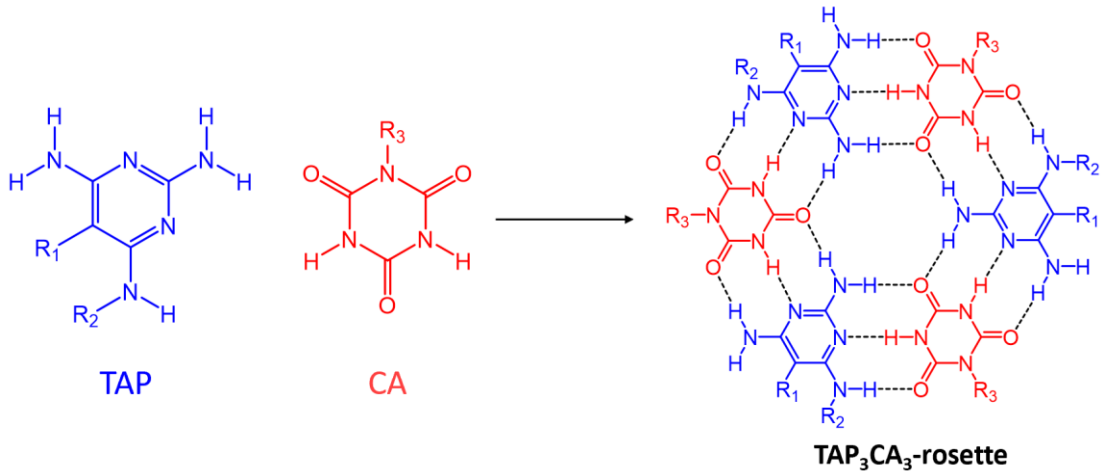

Figure 1.23: TAP and CA can self-assemble into hydrogen bonded macrocycle, TAP_3CA_3-rosettes.

In the seminal work by Hud et al, TAP is modified with succinic acid group to give TAPAS **97**.[29] The modification is expected to improve solubility in water and sterically inhibit ribbon structures. At room temperature, equimolar mixture of **97** and **98** gave a self-standing hydrogel at concentrations higher than 5 mM (**Figure 1.24**). UV-vis spectra of the resulting hydrogel has a new absorption peak at 320 nm, a feature consistent with J-type aggregates. AFM image shows long fibers (over 1 μm) with a width of 1.5-2.2 nm, consistent with predicted width of a single rosette. In ^{1}H NMR spectra, no intermediate structures were observed, indicating the exchange between monomers and assemblies is slow. The length of polymers and the lack of intermediate structures in ^{1}H NMR indicate that the assembly process is highly cooperative, which is presumably caused by the large π-surface and its favorable stacking (The estimated stacking interaction between two rosettes is -27 kcal·mol^{-1}). G-quadruplex polymer formation, however, is less cooperative than the rosette system for two reasons: the smaller π-surface and electrostatic repulsion between cations. Finally, the authors

propose that the inability of canonical base pairs to stack in water indicates that they are a result of evolution from a mixture which can self-organize into linear polymers before being connected by a covalent backbone.

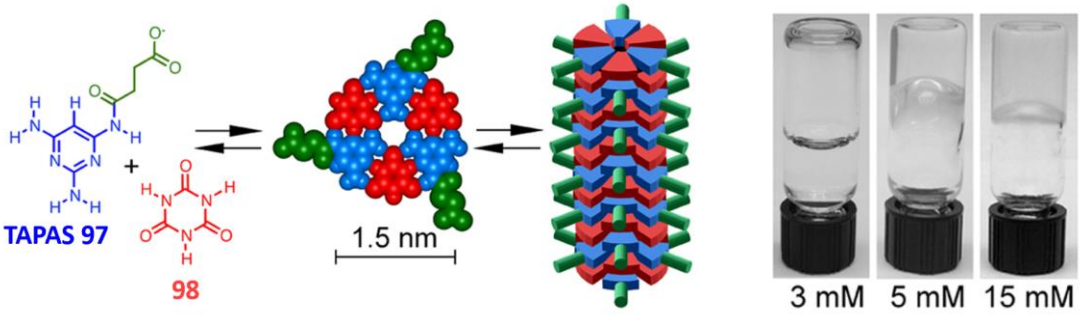

Figure 1.24: TAPAS **97** and **98** self-assembled into macrocycles that stack and form hydrogels.[29] Reprinted with permission from the American Chemical Society.

The Hud group continued to explore the influence of pH on the assembly properties of the gels.[69] A mixture of **99** and **100**-C6 were used as model compounds to create TAP_3CA_3-rosette hydrogels. They discovered that a self-standing gel formed at pH 7, but the same mixture only gave a solution at pH=6 and 8. This result indicates that the system is highly sensitive to pH changes near neutral conditions, which is unprecedented for supramolecular hydrogels. The authors propose that nucleobases of **99** and **100** share a common $pK_a \sim 7$, which is the primary reason for the ultra-high pH sensitivity: above the pK_a, **99** would be neutral while the aromatic ring of **100** would be anionic; below the pK_a, **99** would be cationic while the aromatic ring of **100** remains neutral; the ionization of the nucleobases leads to the disassembly of the hydrogel. The matching pK_a values of H-bond donor and acceptor might lead to stronger H-bonding, which further contribute to the stability of assembly. ^{1}H NMR pH titration indicates that the hydrogels are maximally assembled at physiological pH=7.4 and any minute

deviation leads to disassembly of the hydrogel. The hydrogel stability can be further fine-tuned by using a mixture of **100**-C4 and **100**-C6, which inhibit crystallization and promote gelation. This high pH-sensitivity can be potentially applied to drug delivery in slightly acidic tumor (pH=6.3-7.2) environments.

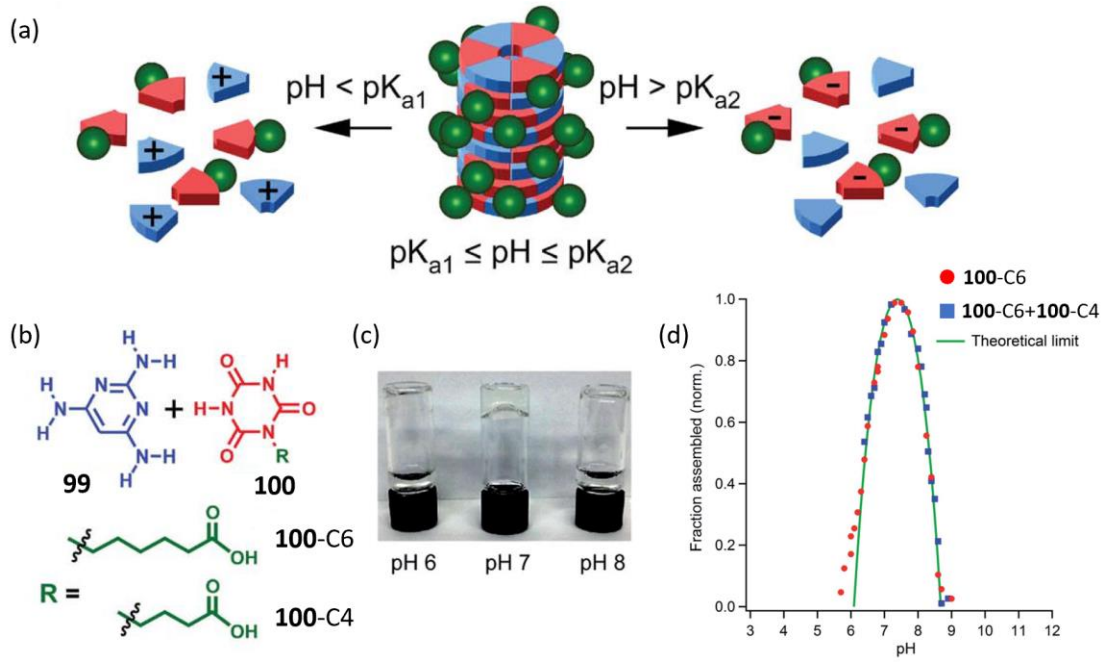

Figure 1.25: (a) Graphical illustration of pH mediated disassembly of rosette hydrogels. (b) Structures of gelators **99**, **100**-C4 and **100**-C6. (c) Hydrogel only forms at pH=7 and disassembly of the gel was observed at pH=6 and 8. (d) At pH=7.4, the hydrogels containing **99** and **100** are most efficiently assembled, as indicated by ^{1}H NMR pH titration. Increasing or lowering the pH causes the disassembly of the gel. Experimental observations are consistent with theoretical limit curve.[69] Reprinted with permission from the Royal Society of Chemistry.

The chiral behavior of the resulting hydrogels at pH=7 were also investigated (**Figure 1.26**).[67] Initial discovery revealed that hydrogels made from achiral **99** and **100**-C6 exhibit spontaneous symmetry breaking and contain homochiral domains with opposite chirality. From CD spectra of 40 independently prepared samples, 19 samples have positive signs while 21 have negative signs at 280 nm. SEM images of the same

sample at different locations contains helical fibers with opposite chirality, confirming observations from CD spectra.

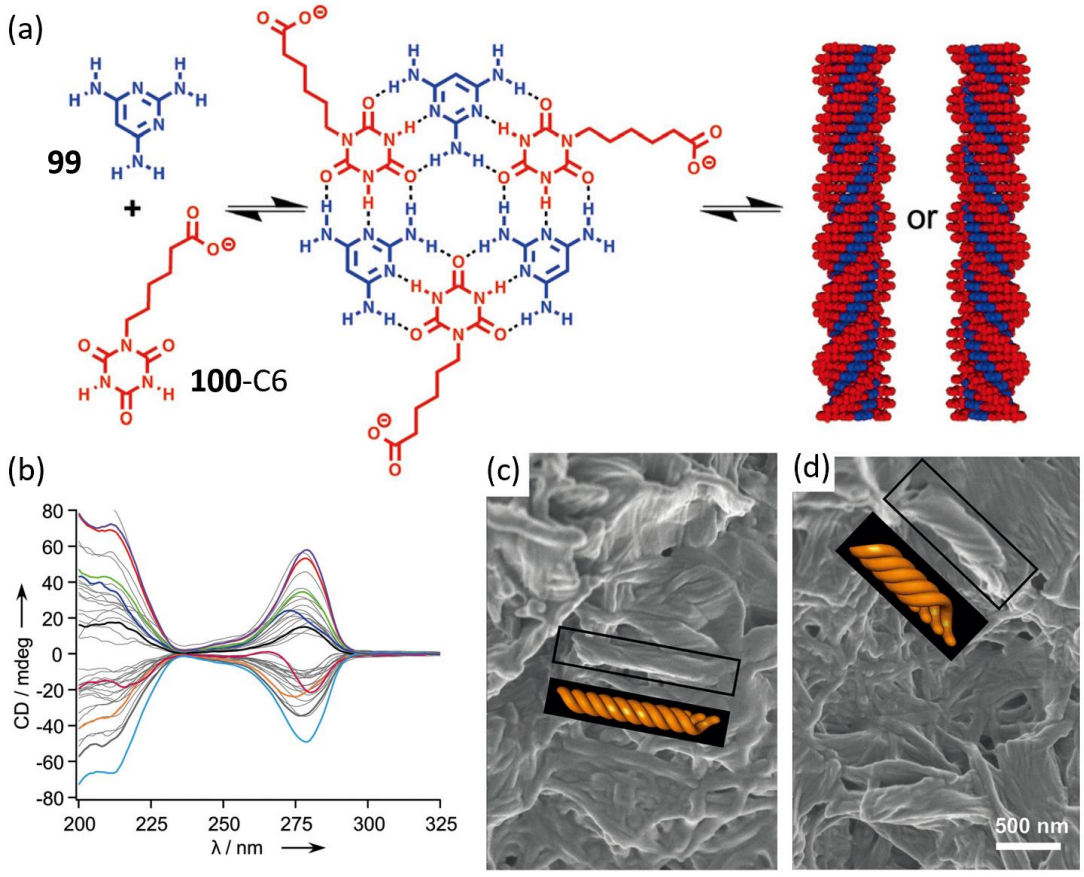

Figure 1.26: (a) The self-assembly of **99** and **100**-C6 gives hydrogel fibers with opposite helicity despite the lack of chirality in the monomers. (b) CD spectra of 40 independently made samples containing **99** and **100**-C6. (c) & (d) SEM images of hydrogel in a single sample at two different imaging locations, which show opposite helicity.[67] Reprinted with permission from John Wiley & Sons.

Two enantiomers **101**-R,S were synthesized to further investigate the influence of chiral monomers on supramolecular chirality (**Figure 1.27**).[67] Hydrogels form upon combining **99** and **101**-R or **101**-S, and the hydrogels exhibit same CD spectral features with opposite signs. Inspired by the "sergeant and soldier" observations by Green et al,[70] where a small amount of chiral molecule (sergeant) is significantly amplified and

alter the helicity of assemblies from achiral molecules (soldiers), the authors added a small amount of **101**-R or **101**-S to a hydrogel containing achiral **99** and **100**-C6. Surprisingly, adding 0.1% of **101**-R or **101**-S relative to **100**-C6 gave hydrogels with single chirality. This corresponds to a chiral amplification of 1000 times (1 sergeant commands 1000 soldiers), which is the highest chiral amplification in polymeric systems known in literature. This result demonstrates that these supramolecular assemblies are capable of converting a small amount of chiral information into a homochiral domain of nucleic acid analogs.

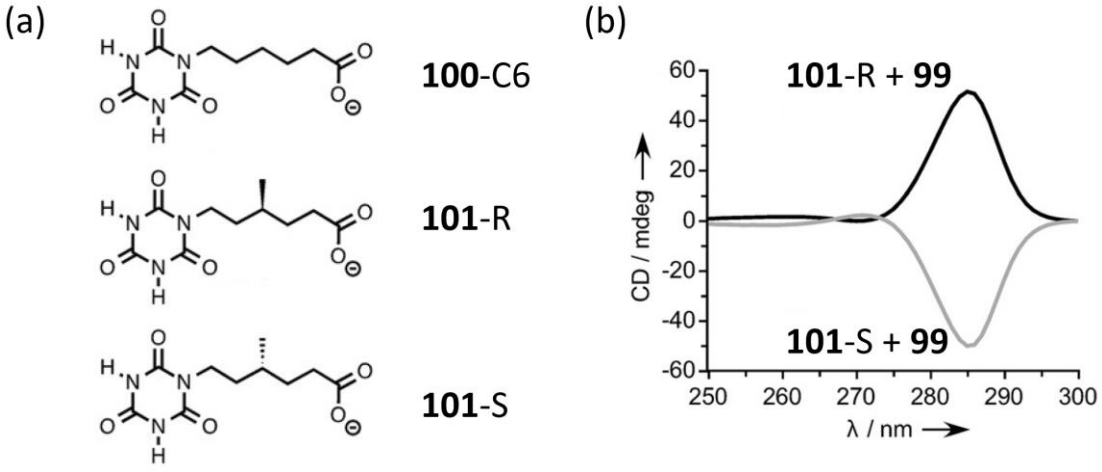

Figure 1.27: (a) Structures of CA analogs with achiral (**100**-C6) and chiral side chains (**101**-R,S) (b) CD spectra of hydrogels made from 1:1 mixtures of **99** and **101**-R or **101**-S.[67] Reprinted with permission from John Wiley & Sons.

While compounds **100** and **101** were prepared and purified using modern techniques, the authors also attempted to synthesize gelators under prebiotic conditions (**Figure 1.28**).[65] Vacuum assisted drying and mild heating (35 °C) of **99** with ribose **102**, both of which are simple and potentially prebiotic compounds, gives ribonucleosides with 60% yield after 10 days. The major form that is isolated is β-ribofuranosyl-C-

nucleoside (**103**, 20% yield), which is consistent with the fact that C5 on TAP **99** is the most nucleophilic. The nucleoside crude after 10 days of drying and heating, when combined with CA in sodium borate buffer, gave a hydrogel. The crude itself only gives a solution without adding CA, indicating coassembly was formed. Simply mixing **99** and ribose for 10 days in water, only gave precipitates when combined with **98**, which indicated the heating and drying is crucial for gelation. This research indicates that under prebiotic conditions, ribonucleoside can be formed from simple alternative nucleobases and ribose, which further self-assemble into informational polymers. Overall, research on TAP_3CA_3-rosette hydrogels not only provides insights on the origin of life and homochirality, but also paves the way for future gelator design of functional materials using self-assembly.

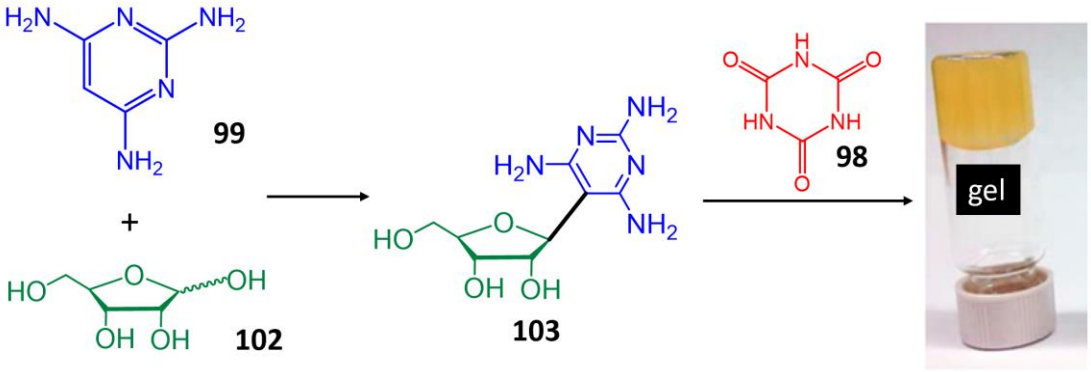

Figure 1.28: Under drying and mild heating, **99** and **102** form C-ribonucleoside **103** as a major product, which self-assembles into a hydrogel with **98** in water.[65] Reprinted with permission from the American Chemical Society.

1.8 Hydrogels containing G-quartets

While hydrogels containing self-assembled macrocycles are starting to emerge, G-quartet based systems are still the most commonly found in literature (**Figure 1.29**).[1,4] As a natural product, the nucleoside G **1** and its analogs has a fairly low price ($0.09

per gram of G **1** at Carbosynth) and hydrogels made from nucleosides generally have good biocompatibility.[1] The synthesis of guanosine hydrogels is also straightforward, which only involves mixing of guanosine analogs in salt solution followed by heating and cooling. All these factors contribute to the recent resurgence of G-quartet hydrogel research.

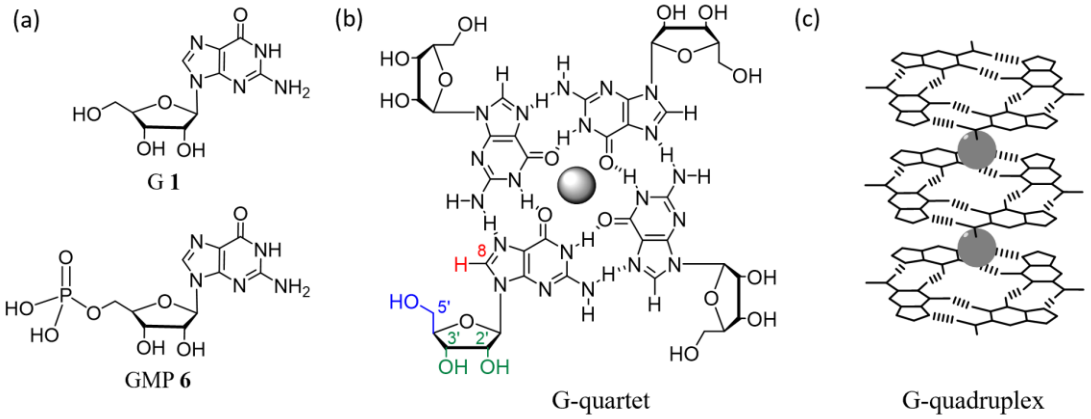

Figure 1.29: (a) Structures of G **1** and GMP **6**. (b) Structure of a G-quartet. Positions available for modification are highlighted in color. (c) Structure of G-quadruplex.

The first report on the gelation of guanylic acid was described by Ivar Bang in 1910.[3] The structural basis for the resulting materials were not elucidated until 1962, when Gellert, Lipsett, and Davies first proposed the structures of hydrogels made from guanosine monophosphates.[71] Based on X-ray diffraction data of the gel fibers, the authors proposed that H-bonded macrocyclic tetramers, namely G-quartet, form helical stacks and form gels in water (**Figure 1.29b & c**). In 1978, Pinnavaia and coworkers highlighted the importance of cation chelation to stabilize these structures and found that K^+ is the best at stabilizing G-quadruplex structures in 5′-GMP **6** assemblies.[72] G_4 DNAs and oligomeric G-quartet stacks have also been extensively characterized in the

past 30 years, which provide rich structural information that guides future design of materials containing this motif.[73–77]

Furthermore, while the H-bond donor and acceptors are crucial for gelation, G **1** has a highly modifiable periphery, which opens up a myriad of possibilities for hydrogel design (**Figure 1.29b**). Reaction of the ribose 2′, 3′-diol with boron species has become a common strategy for G **1** hydrogel synthesis and conjugation of functional molecules;[78] The 5′-position of G **1** contains a primary alcohol, which can be turned into electrophilic alkyl halides and carboxylic ester for further functionalization.[79,80] The C8 position of G **1** can be turned into 8-BrG **29** by adding Br_2 to G **1**, which can be modified to fine-tune nucleoside conformation and alter the electronics of the aromatic ring.[81] Although a series of interesting hydrogels made from naturally occurring G **1**, GMP **6** and their deoxy-counterparts have been reported in literature,[3,71,82–94] this section focuses on using organic chemistry to create functional guanosine hydrogels containing the macrocyclic G-quartet structures. Some strategies and design principles can potentially be generalized to other non-guanosine hydrogel systems. The most recent developments in the past 5 years are highlighted.

1.8.1 Modifying 2′, 3′-diol with boron species

While G **1** is highly polar, its water solubility is fairly low (2 mM) due to the formation of insoluble guanosine ribbons.[5] Heating G **1** in water with excess KCl gave a hydrogel initially, but crystallization occurs within a few hours. In 2014, our group reported that borate anion can stabilize the hydrogel formation from G **1**.[78] Borate anion forms borate esters **104**-**106**, which then self-assemble into stacks of $G_4 \bullet K^+$ quartets

and trap water to form hydrogels. The resulting hydrogel is strong, transparent, and remains stable for over a year. Most importantly, the improvement of hydrogel stability is simply achieved by anion switching. Furthermore, this hydrogel has anionic borate periphery, which was used for charge-based absorption of cationic dye. After soaking a G **1** borate hydrogel in a mixture of cationic methylene blue and anionic rose bengal, the gel edge became more blue over time, indicating its preference for cationic species (**Figure 1.31**).

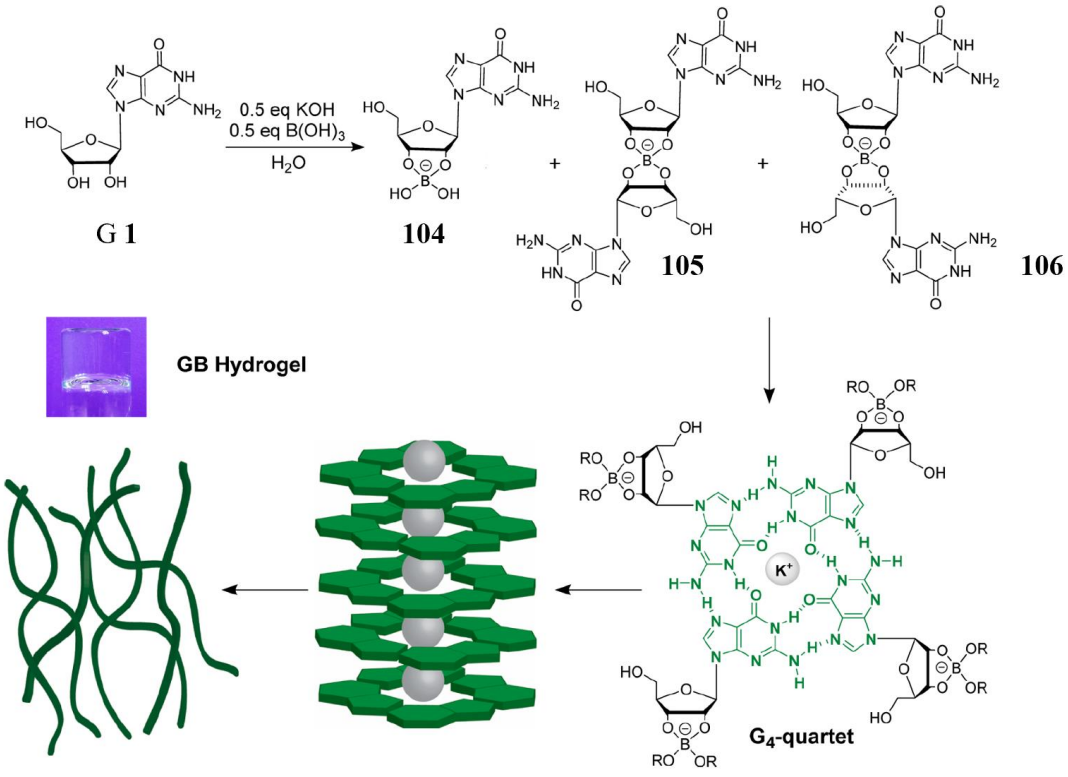

Figure 1.30: G **1**, in the presence of 0.5 eq $KB(OH)_4$, forms borate monoester **104** and diesters **105/106**, which self-assemble into G-quartets that stack to give hydrogels.[78] Reprinted with permission from the American Chemical Society.

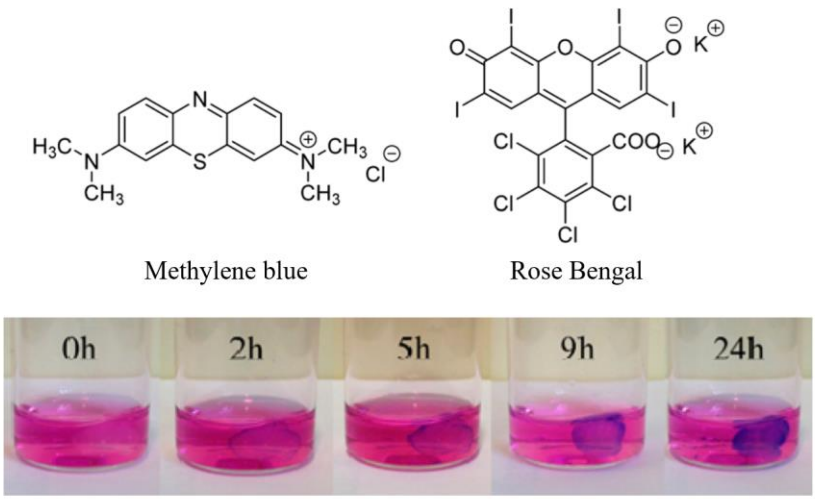

Figure 1.31: A piece of G **1** $KB(OH)_4$ gel preferentially absorbs cationic methylene blue over anionic rose Bengal.[78] Reprinted with permission from the American Chemical Society.

Our group continued to explore the influence of G-quadruplex ligands on G **1** borate hydrogels. Substoichiometric amount of ThT **107** was found to increase the stiffness of borate hydrogels made from Li^+ and promote the self-healing process compared to blank control (**Figure 1.32b**).[95] We proposed that ThT **107** acts as a molecular chaperone and shifts the equilibrium toward G-quadruplex formation (**Figure 1.32a**). Similar results were observed with other planar, aromatic dyes. It was suggested that this Li^+ hydrogel could potentially be used as an inexpensive system for identifying G-quadruplex ligands.

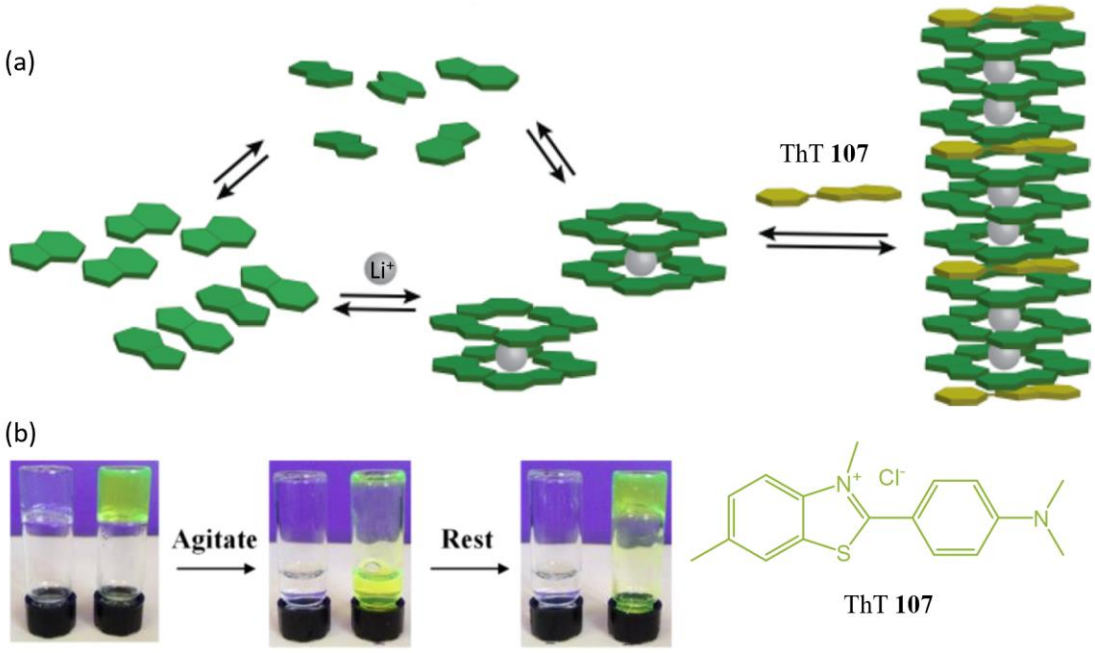

Figure 1.32: (a) Different structures and assemblies exist in equilibrium in a G **1** $LiB(OH)_4$ gel. Adding ThT **107**, a G-quadruplex ligand, shifts the equilibrium toward gelation. (b) Gel containing **107** reforms faster after agitation.[95] Reprinted with permission from the American Chemical Society.

Sadler reported another interesting application of G **1** borate gel.[96] The authors synthesized **108**, a platinum (IV) prodrug containing catechol, which can also form borate ester and become conjugated to G **1** (**Figure 1.33**). The Pt (IV) drug is inert but photoactivable by 465 nm light, and Pt (IV) is reduced to Pt (II) with concomitant release of azidyl radicals, both of which contribute to the cytotoxicity. Incorporation of the drug molecule into a hydrogel can facilitate the slow release of the drug at the active site. It was found that after being conjugated to give a hydrogel containing **109**, the prodrug **108** became more cytotoxic (IC_{50}=3 μM) toward ovarian cancer than **108** without hydrogel (IC_{50}=74 μM) after photoactivation. This research provides the basis for future development of therapeutic agent design.

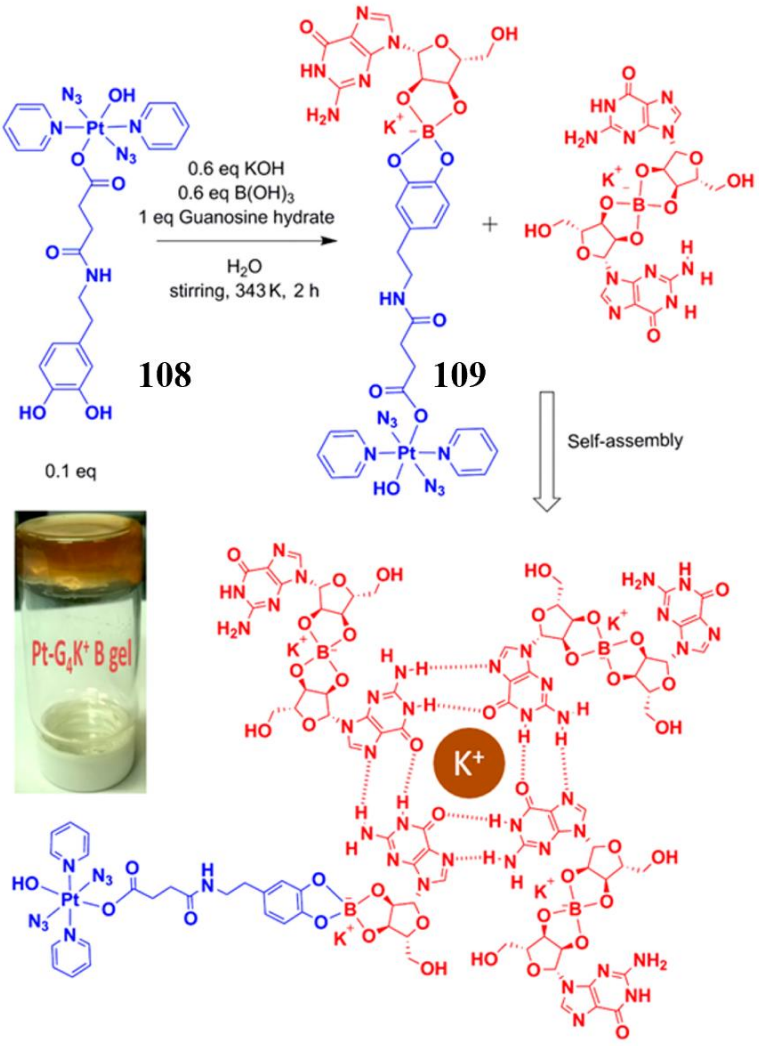

Figure 1.33: Prodrug **108** can be incorporated into guanosine hydrogels via borate ester linkage.[96] Reprinted with permission from the American Chemical Society.

1.8.2 Hydrogels containing 5′-modified guanosine species

In a seminal report, Lehn and coworker synthesized a 5′-modified analog of G **1**, hydrazideG **3** (**Figure 1.34**).[97] The compound forms stable and strong G-quartet hydrogels with a wide variety of cations. The hydrazide functional group can form acylhydrazones at pH=6 and these functionalities are commonly used to construct

dynamic combinatorial libraries (DCL). The authors synthesized a hydrogel containing compounds **3**, **109**, **110** and **111** in 1:1:1:1 ratio, which react to form a library of acylhydrazones **112-115**. Without gelation, the isoenergetic acylhydrazones **112-115** should exist as a 1:1:1:1 mixture. However, the author discovered that hydrogelation with **113** is more efficient than **112**, and **113** is selectively enhanced in the DCL, which is reflexed in the enhancement of **114**. In this case, the cohesive force dictates the outcome of the DCL and selected the fittest within the system.

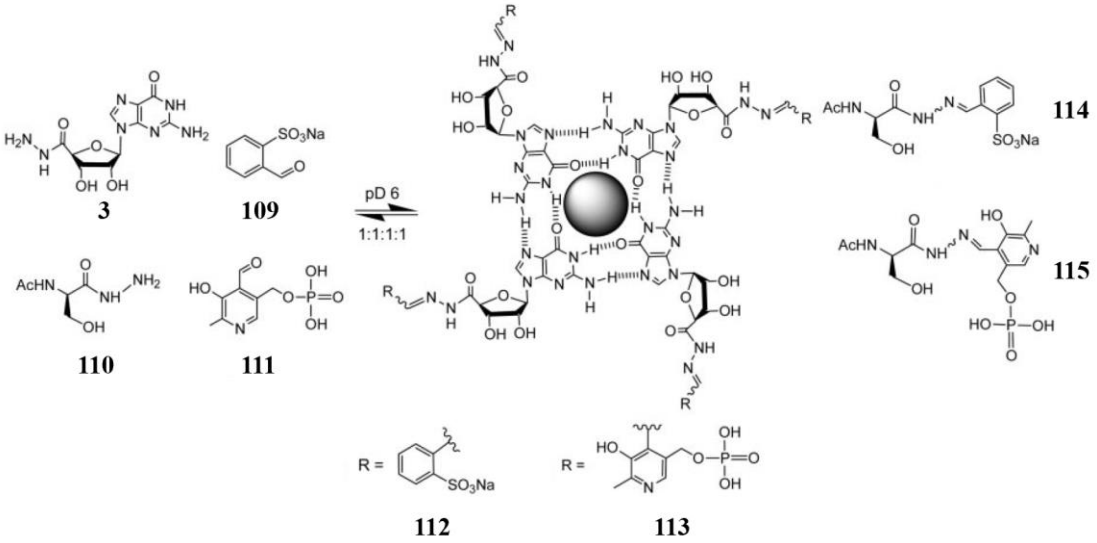

Figure 1.34: HydrazideG **3**, when combined with **109-111** in 1:1:1:1 ratio, generates a dynamic combinatorial library (DCL) containing **112-115**. Hydrogel formation with **113** is more favorable, which enhanced **113** and **114** in the DCL.[97] Reprinted with permission from the United States National Academy of Sciences.

Electrophiles on the 5′-position of guanosine can also influence the hydrogelation properties and functions. Our group reported a borate hydrogel made from 5′-IG **39** (**Figure 1.35a**). Under basic condition, **39** can cyclize intramolecularly in solution and displace the leaving group I^- to form **116**. Cyclized **116** should form weaker G-quartet structures than **39** and lead to disassembly of the hydrogel (**Figure 1.35b&c**). The

disassembly process is also accelerated by extra heating. This temperature self-destruction was indeed observed and utilized for the release of an antiviral drug containing guanine motif, acyclovir **117** (**Figure 1.35d**). After 72 hrs, 85% of acyclovir **117** was released from the gel into the solution at 37°C, while only 15% was released at room temperature. This research shows promise for future design of drug release systems under physiological conditions.

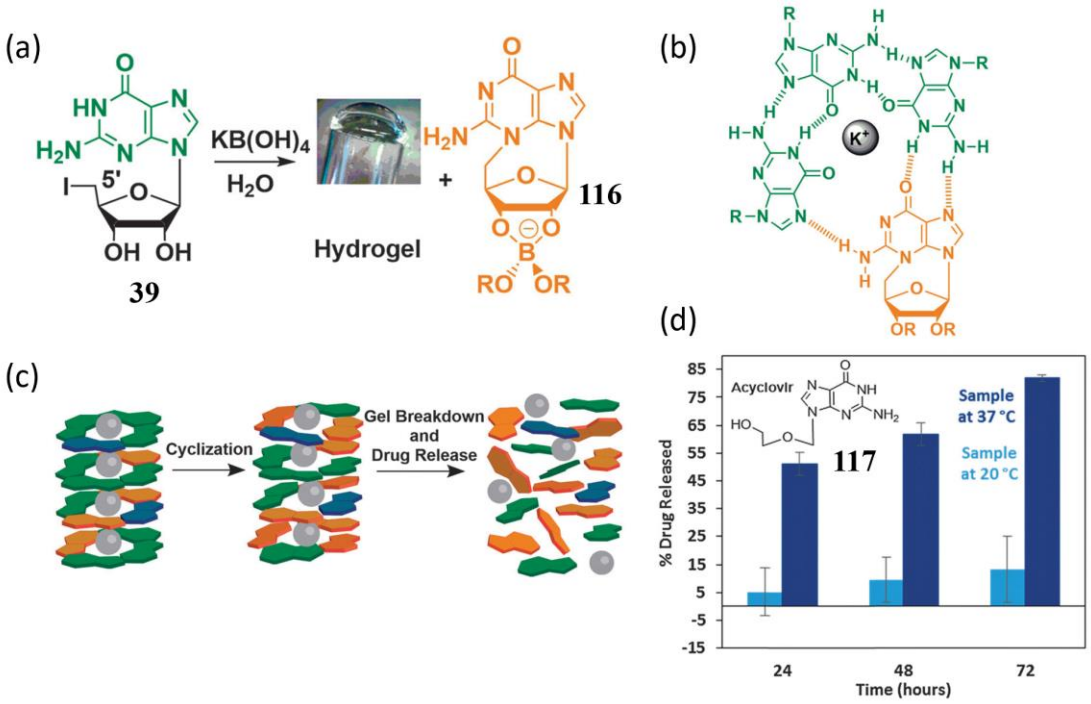

Figure 1.35: (a) IG **39** forms a hydrogel with $KB(OH)_4$ that contains **116**. (b) Compound **116** forms weaker G-quartets than IG **39**. (c) Schematic illustration of gel disassembly caused by the formation of **116** (orange) that leads to drug release (blue). (d) Pre-incorporated acyclovir **117** was released more efficiently at 37°C than 20°C.[98] Reprinted with permission from the Royal Society of Chemistry.

This thesis is also focused on creating hydrogels from 5′-modified guanosine analogs. In **Chapter 2**, we describe the gelation study on guanosine analogs containing 5′-thiol and 5′-disulfide functional groups. Inspired by Lehn's research, we explored

the self-assembly of a 5′-hydrazine guanosine analog in **Chapters 3 & 4**. In **Chapter 5**, a hydrogel made from a 5′-hydroxamic acid guanosine analog was explored.

1.8.3 Hydrogels containing 8-modified guanosine species

Modifying the C8 position on the aromatic ring of guanosine can also potentially bring new functions to the G_4 hydrogels. Our group synthesized hydrogels containing a mixture of 8-aminoG **31** and G **1** (**Figure 1.36**).[99] The modification of amino group on guanine might lead to the protonation of the nucleobase and result in a cationic hydrogel for anion binding; switching from monovalent K^+ to divalent Ba^{2+} can enhance the affinity of the gel toward anionic species. Furthermore, the hydrogel can be formed with either NO_3^- or $B(OH)_4^-$ as counterions, which allows the synthesis of hydrogels with different charge states. Dye absorption experiment shows that binary hydrogels made from KNO_3 preferentially absorb anionic Naphthol Blue Black (NBB) and Rose Bengal (RB) while $KB(OH)_4$ gel favors cationic Safranin O (SO). Interestingly, Ba^{2+} gels have similar charge preference as KCl, but absorb dyes with higher efficiency. This research showed that simply changing the salt identity can drastically influence the properties of guanosine gels.

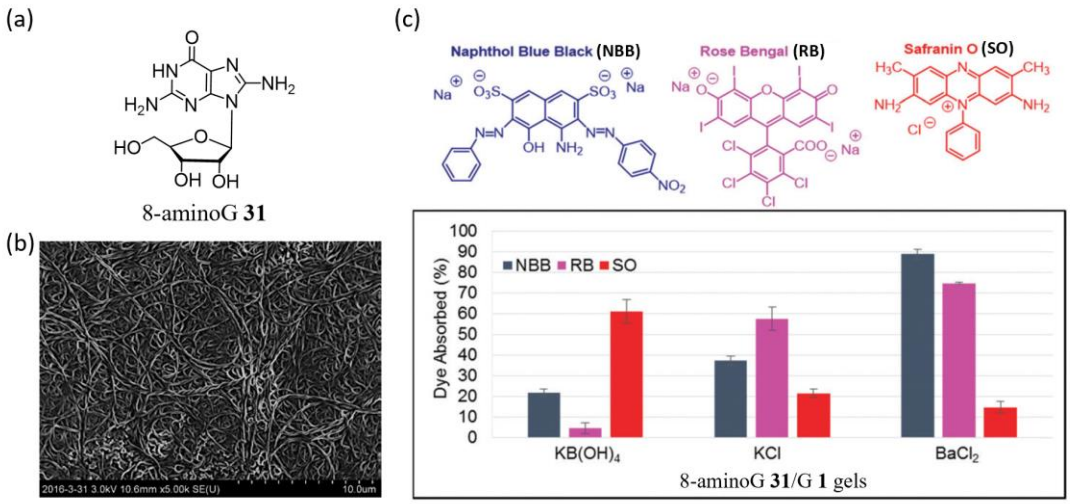

Figure 1.36: (a) Structure of 8-aminoG **31** (b) An SEM image containing 8-aminoG **31**, G **1** and Pb^{2+}. (c) The percentage of the dyes absorbed by different hydrogels.[99] Reprinted with permission from the Royal Society of Chemistry.

Other than altering the electronics of the guanine and its protonation state in water, C8 position modifications can also change the conformation of the nucleoside. For guanosine, introducing bulky groups on C8 position often favors a syn conformer due to sterics. In this way, the ribose moiety could potentially block the sugar face of guanine and expose the Hoogsteen base pairing for G-quartet formation. 8-BrG **29** exist mostly in *syn* conformation and could act as a "catalyst" that triggers the G-quartet formation. Initial test shows that a 1:1 mixture of G **1** and 8-BrG **29** forms a hazy hydrogel at room temperature within 20 seconds of adding 0.5 eq $KB(OH)_4$.[100] The gel gets significantly clearer after 20 min, indicating large aggregates are solubilized and have assembled into hydrogel fibers. This hydrogel formation at room temperature could be potentially applied to trap and release of enzymes and ester-containing drugs, which are highly sensitive to heat.

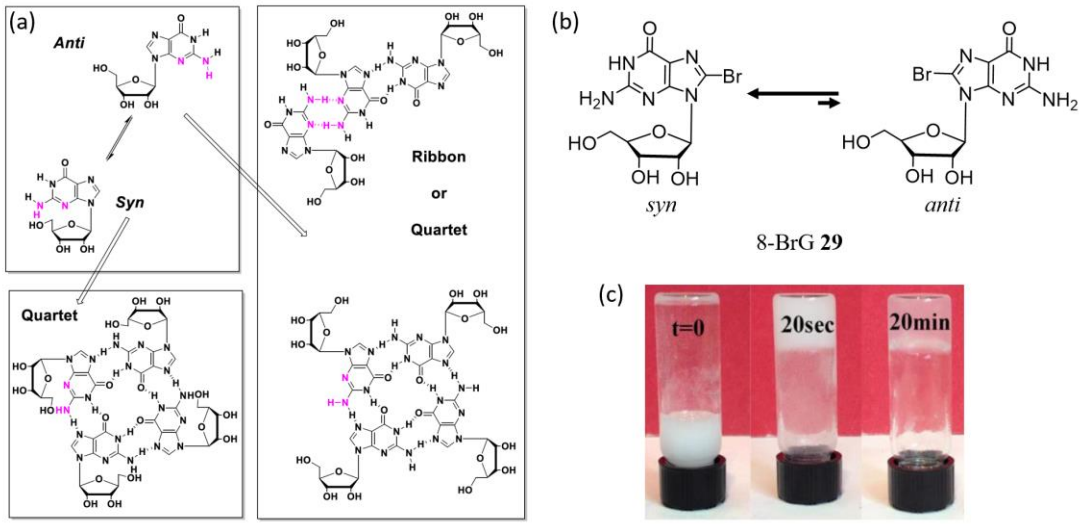

Figure 1.37: (a) *Syn* conformer could potentially favor G-quartet formation. (b) 8-BrG **29** favors *syn* conformation. (c) A binary borate system containing a 1:1 mixture of G **1** and 8-BrG **29** gives a self-standing gel at room temperature.[100] Reprinted with permission from the Digital Repository at the University of Maryland.

In **Chapter 2**, we describe the self-assembly of 8-thione and 8-disulfide containing guanosine analogs and their potential applications. Overall, the C8 position of G **1** can potentially be modified with a wide range of functionalities and still remains to be explored in future research.

1.9 Summary

This chapter has introduced a summary of hydrogels containing non-covalent macrocycles. The non-covalent macrocycles can serve as crosslinkers between polymers, but can also aggregate to give 1D-polymers. Finally, we focus on G-quartet hydrogels, which will be discussed in more detail in **Chapters 2-5**.

Chapter 2: Synthesis and Gelation Properties of Sulfur-containing Guanosine Analogs

2.1 Summary

This chapter focuses on the synthesis and self-assembly properties of different sulfur containing guanosine analogs, namely 5′-thiolG **27**, 8-thioG **37** and the corresponding disulfides **28** and **38** (**Figure 2.1**). We demonstrate that addition of base or borate salts can promote the hydrogelation properties of the poorly soluble **27**. G-quartet hydrogels were also successfully synthesized from **28** and $KB(OH)_4$, and the resulting hydrogels were characterized using NMR and CD spectroscopy.

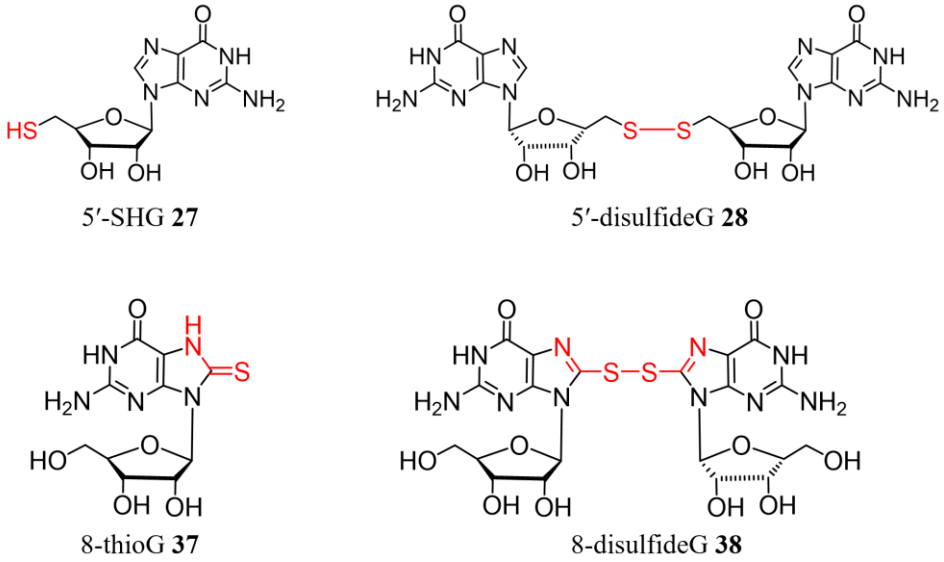

Figure 2.1: Structures of compounds that are discussed in the chapter

We also obtained a crystal structure for 8-thioG **37**. An 8-thione tautomer is observed and the compound adopts a *syn* conformation about the C-N glycosidic bond. Since **37** lacks Hoogsteen base pairing and is less likely to form G-quartets, we proposed

different methods to induce its hydrogelation. Finally, disulfide **38** spontaneously self-assembles into gels in acetone and ethylene glycol. Construction of thiol/disulfide-containing materials has promise for environmental remediation applications and smart material design.

In sections 2.12 and 6.6, we report the synthetic procedures of some guanosine analogs and their NCI-60 screening results.

2.2 Introduction of thiol/disulfide chemistry

Sulfur-containing compounds are ubiquitous, and many have significant biological relevance. They serve as nucleophiles, ligands, crosslinkers and odorants in biological context.[101] While in the same chalcogen group as oxygen, sulfur chemistry is unique from oxygen in many ways. We herein introduce thiol and disulfide chemistry on a basic level.

2.2.1 Thiols are more acidic than alcohols

Thiols are generally more acidic than alcohols (**Figure 2.2**). The phenomenon can be explained by comparing the corresponding conjugate bases. When methanol (pK_a=15.5) and methanethiol (pK_a=10.4) are deprotonated, corresponding methoxide and methanethiolate anions are formed.[102] Since the sulfur atom has a much larger van der Waals radius (1.8 Å), as compared to oxygen (1.5 Å),[103] thiolate can disperse the negative charge better than alkoxide, which in turn makes the corresponding thiol more acidic than the alcohol. The same trend also applies to the relative acidity of phenol (pK_a=10) vs thiophenol (pK_a=6.5).[102]

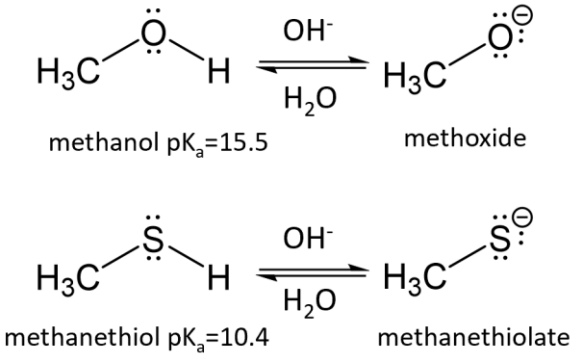

Figure 2.2: Methanethiol is 10^4 times more acidic than methanol

2.2.2 Thiolates are more nucleophilic than alkoxides

Thiolates, the conjugate bases of thiols, are more nucleophilic than alkoxides. The $3sp^3$ lone pairs on anionic sulfur are higher in energy than $2sp^3$ oxygens so that the thiolates are more reactive. The larger size of sulfur vs. oxygen also makes thiolates more polarizable than alkoxides, which contributes further to the increased nucleophilicity. Interestingly, thiols are poorly nucleophilic. The differential nucleophilicity of thiols and thiolates has been used to perform pH-dependent attack on electrophiles such as alkyl halides and Michael acceptors for bioconjugation and construction of functional materials (**Figure 2.3**).[104–106] Thiolates also play an important role as a nucleophile in catalytic triads of enzymes.[107]

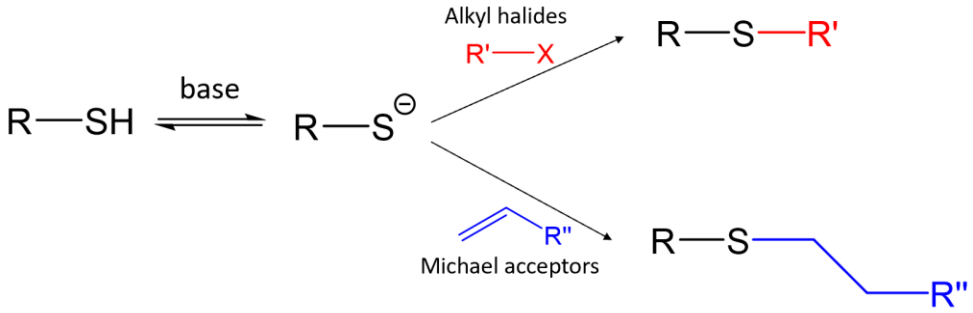

Figure 2.3: Thiols, when deprotonated, give thiolate anions that can be alkylated by alkyl halides or Michael acceptors to form thioethers.

2.2.3 Thiol-disulfide redox chemistry

Thiols and thiolates are susceptible to oxidation and readily form disulfides (**Figure 2.4**). Disulfide linkages are crucial to the tertiary structures of many proteins. The oxidation of thiols to symmetric disulfides is commonly achieved by adding iodine I_2 to a solution of thiol. In the presence of peroxidases, oxidation with O_2 gas can be achieved at a high rate.[108]

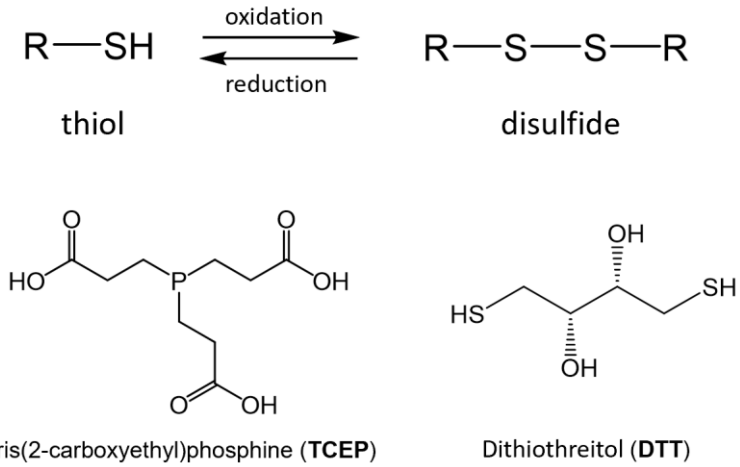

Figure 2.4: (top) Thiol-disulfide redox reaction. (bottom) Structures of two reducing agents that turn disulfides into thiols.

For small molecule disulfides, the reduction to free thiol is best carried out with tris(2-carboxyethyl)phosphine (TCEP) since it is odorless, functions at a wide pH range and the reaction is irreversible (**Figure 2.4**).[109] For disulfide cleavage within proteins, dithiothreitol (DTT) is more efficient than TCEP.[110]

2.2.4 Thiolate-disulfide exchange

Nucleophilic thiolates attack disulfides to form new thiolates and new disulfides in water (**Figure 2.5**). This S_N2 reaction is reversible and happens at room temperature

with moderate rates. The disulfide bond is labile and considered a dynamic covalent bond.[32] Protonation of thiolate stops the reaction completely.[111]

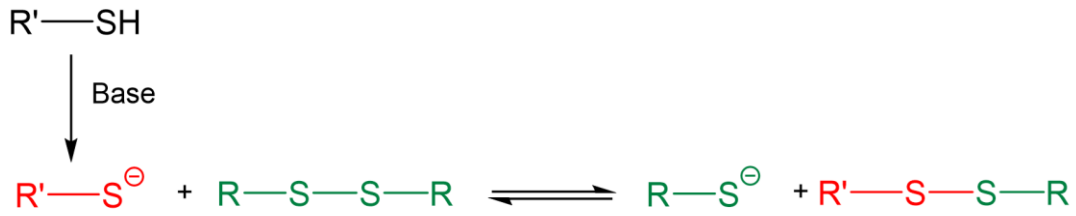

Figure 2.5: Thiolates attacks disulfides to form new thiolates and new disulfides

2.2.5 Disulfide metathesis

The exchange reaction between two different disulfide molecules to form a statistical mixture of symmetric and asymmetric disulfides is called disulfide metathesis (**Figure 2.6**). While the reaction does not happen spontaneously upon mixing two disulfide species, this entropically favorable reaction can be catalyzed or induced by thiolates,[112] bases,[113] phosphines,[114,115] rhodium catalysts,[116] UV light[117] or ultrasonication.[118]

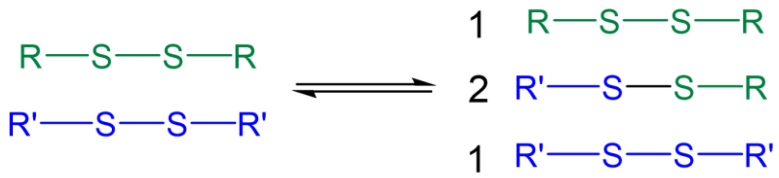

Figure 2.6: Two symmetric disulfides undergo metathesis reactions to form a statistical mixture of symmetric and asymmetric disulfides.

2.2.6 Metal binding

Due to the large size and high polarizability of sulfur atoms, thiols/thiolates/disulfides are generally considered to be soft Lewis bases. They have strong affinities for soft Lewis acids such as Pb^{2+}, Hg^{2+}, Au^{3+}, which make

thiol/disulfide containing compounds ideal candidates for binding toxic metal ions and modifying metal surfaces.[119–122]

2.3 Inspiration and synthesis of 5′-thiol/disulfideG

2.3.1 Drawing inspiration from nature

Of the 20 amino acids that appear in the genetic code, serine and cysteine are an interesting pair in that they are highly structurally similar: serine contains a primary alcohol whereas cysteine contains a primary thiol (**Figure 2.7**). Yet, they are different in many aspects involving the chemistry that occurs inside a protein. The most interesting feature of cysteine is its capability to form disulfide cystine upon oxidation, which is often crucial to the higher-order structure of proteins. Similar to serine, nucleosides also contain a primary alcohol on the 5′-position. However, we performed a literature search on the 5′-thiol counterparts of nucleosides, and found to our surprise that these compounds have not been reported to exist in nature. We were particularly interested in 5′-thiolguanosine (5′-SHG **27**) since it could potentially form hydrogels with thiol functional groups on the periphery via formation of G_4 quartets.[2] Such thiol containing hydrogels could be applied to heavy metal remediation and surface conjugation of bioactive molecules. Addition of peroxidases to the thiol-containing hydrogel could alter the material properties by forming disulfide bonds.[108] Furthermore, the disulfide compound **28** could potentially form hydrogels with more crosslinks than those formed from thiol **27**, and these disulfide crosslinks could be cleaved and disassembled by reducing agents or other thiolates (e.g. glutathione). Such

a hydrogel system made from guanosine analogs would potentially be biocompatible and biodegradable and is ideal for delivery of payloads inside human body.

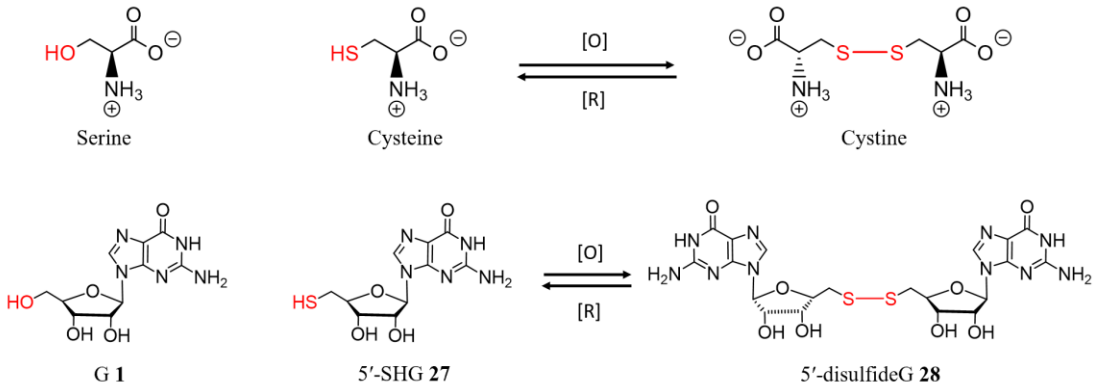

Figure 2.7: 5′-modification of G **1** to give compounds **27** and **28** is parallel with serine/cysteine/cystine series.

Efforts have been devoted to the synthesis of 5′-thiol containing nucleoside analogs.[123–125] Reese and coworkers reported a universal synthesis of these analogs using 5′-chloro nucleoside and 9-(4-methoxyphenyl)xanthen-9-thiol.[124] However, the use of protected G **1** and extra preparation of thiol nucleophile limits the applicability. Hodgson and coworkers improved the procedure by performing the synthesis of 5′-SHG **27** in 2 steps from G **1** with high yields.[123] The resulting product, however, contained a mixture of thiol **27** and disulfide **28**. Piccirilli first isolated pure disulfide **28** in 5 steps, but the procedure required protection and deprotection steps.[126] In the chapter, we successfully isolated pure forms of both **27** and **28** in 3 simple steps from G **1** based on Hodgson's procedure and thoroughly characterize the two compounds with 1D/2D NMR spectroscopy and mass spectrometry. Furthermore, with pure compounds isolated, we describe the gelation properties of the two guanosine analogs, which have not been reported before in literature.

2.3.2 Synthesis and characterization of analogs 27 and 28

We successfully prepared the mixture containing both **27** and **28** based on literature (**Figure 2.8** middle spectrum). Addition of excess NaI/I_2 solution to the solid mixture of **27/28** followed by extensive sonication oxidized all the remaining thiol **27** and produced pure disulfide **28** as a light yellow solid (**Figure 2.8** bottom spectrum). Excess TCEP, on the other hand, efficiently cleaved all disulfides in the mixture and gave thiol **27** as a fine white powder (**Figure 2.8** top spectrum). Close examination of 2-3 ppm region of the NMR spectra (**Figure 2.8** blowup) of the mixture led us to find two peaks that can be assigned as 5′-CH2 of **28**, two peaks that can be assigned as 5′-CH2 of **27**, and a triplet that is assigned as 5′-SH proton of **27**. The spectra for pure **27** and **28** only give 1 set of peaks each that matched our assignment.

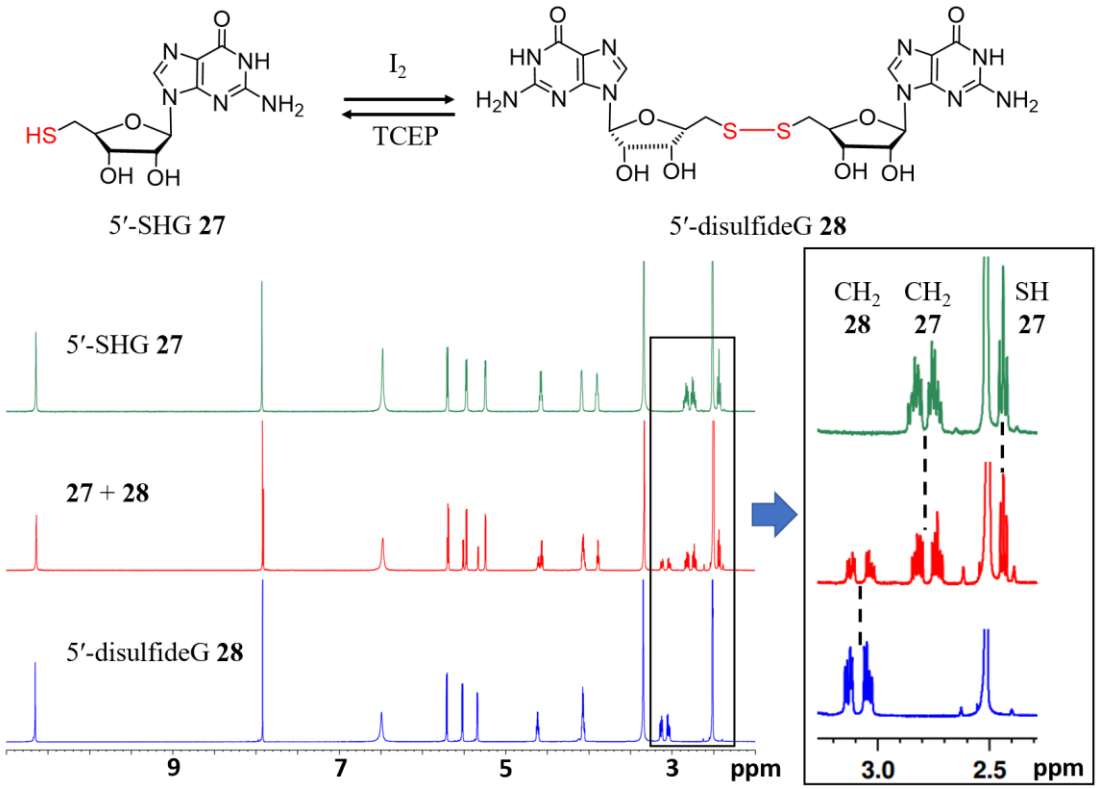

Figure 2.8: ^{1}H NMR shows formation of 5′-SHG **27** and 5′-disulfideG **28** by performing redox reaction on a **27** + **28** mixture in DMSO-d_6. Blow-up of 5′-region of the spectra unambiguously shows characteristic peaks for both analogs in the mixture, whereas only one set of peaks are found in the spectra of pure analogs.

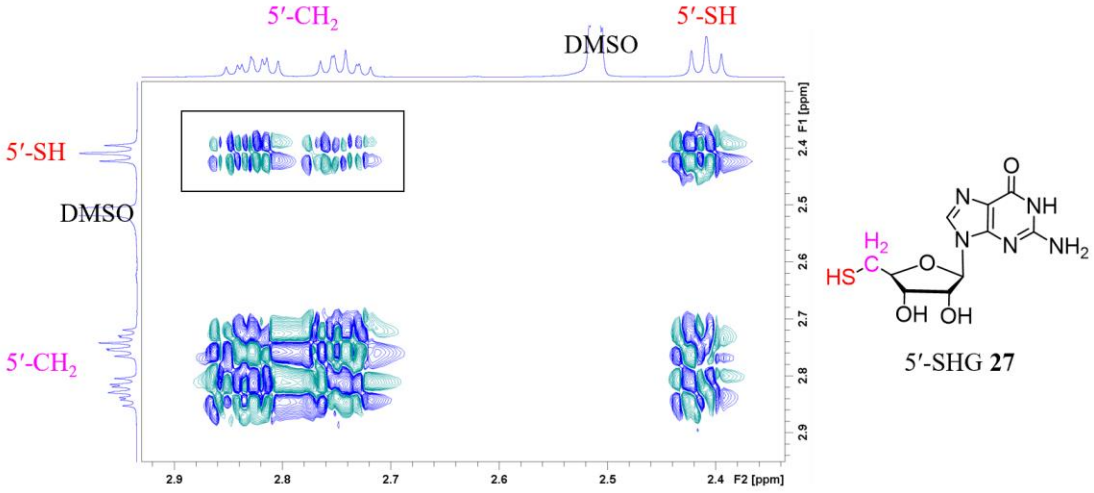

Figure 2.9: ^{1}H-^{1}H COSY shows a crosspeak between 5′-SH and 5′-CH_2, thus confirming the CH_2SH spin system in DMSO-d_6.

The 5′-thiol proton shows around δ= 2.4 ppm as a well-defined triplet due to the coupling with 5′-CH2 of **27** and the peak assignment was confirmed by ^{1}H-^{1}H COSY. The correlation peak between 5′-SH and 5′-CH_2 confirms the CH_2SH spin system in 5′-SHG **27** (**Figure 2.9**).

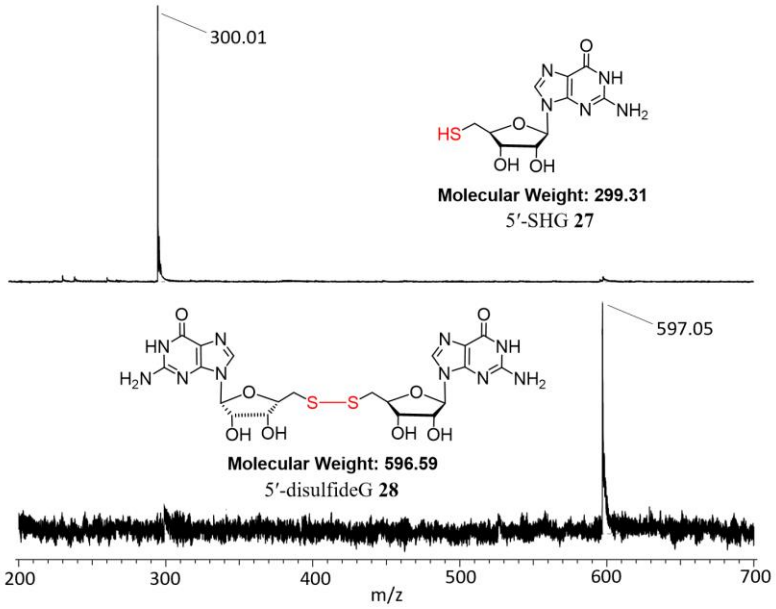

Figure 2.10: Electrospray ionization mass spectrometry confirms the identity of both **27** and **28**.

Finally, mass spectrometry shows a single peak at m/z = 300 for thiol **27** and m/z = 597 for disulfide **28**, which unambiguously confirms the identity of both compounds (**Figure 2.10**). In simple ways using water as the solvent and TCEP/I_2 as reducing/oxidizing reagents, we were able to prepare pure forms of **27** and **28**.

2.4 Gelation test of 5′-SHG 27

2.4.1 Summary of methods to construct a G_4 hydrogel from 5′-SHG 27

We previously demonstrated that medium solubility is required for gelation of 5′-modified guanosine analogs with KCl.[5] Compounds containing divalent sulfurs (thiol/disulfide) are usually poorly soluble in water, as compared to their oxygen counterparts. This is caused by the lack of hydrogen bonding of sulfur atoms with water, which reduces the degree of solvation. Thus, the modification of G **1** into SHG **27** should reduce the aqueous solubility of the nucleoside, which suggest that SHG **27** would be a fairly poor hydrogelator. Preliminary gelation test of a mixture containing **27** (2 wt%, 64 mM) and 0.5 eq KCl only gave a precipitate (**Figure 2.11**). We propose four approaches to construct hydrogels from SHG **27**: 1) adding strong base to produce thiolates with better solubility; 2) adding borate salts to form water soluble borate esters;[127] 3) adding G **1** to create a binary gel and prevent crystallization,[99] and 4) a combination of the three approaches.

2.4.2 Higher pH favors gelation by thiolate of 27

First, we added 0.5 eq KOH instead of KCl into an aqueous suspension of compound **27** (2 wt%, 64 mM) inside a glass vial. The mixture was flushed with N_2 gas before heating with a hotgun. After cooling at room temperature, a white gel formed, suggesting that higher pH improves hydrogelation of **27** (**Figure 2.11**). A gel containing thiolates could be applied to remediation of alkylating toxins such as acrolein and acrylonitrile.[128]

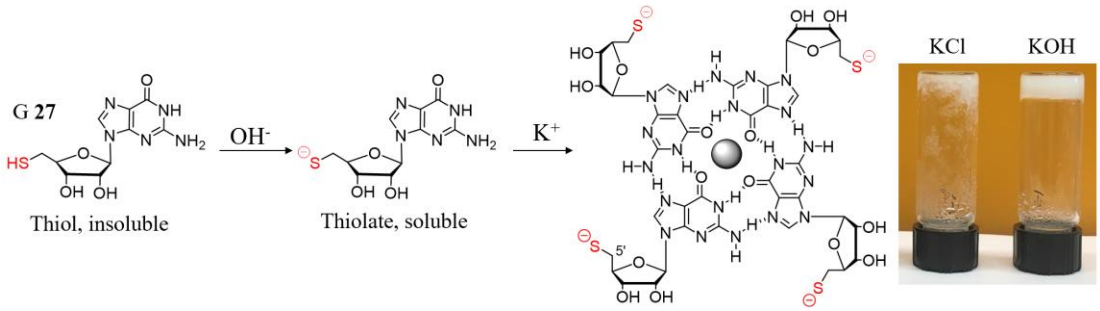

Figure 2.11: Addition of hydroxide improves the hydrogelation of **27**.

2.4.3 Addition of 5′-aminoG 4 to thiolG 27 promotes gelation

We also tried creating a 1:1 mixture of 5′-aminoG **4** and 5′-thiolG **27** in order to create a bianry mixture of guanosine analogs by utilizing the basic amine group of **4** to form thiolates (**Figure 2.12**). Gelation test shows that the binary mixture (2 wt%, 64 mM) again formed a white hydrogel with KCl (0.5 eq). As a control, a mixture of non-basic G **1** and 5′-thiolG **27** only gave a precipitate, which shows the importance of high basicity to induce hydrogelation. The electrostatic interactions between the resulting ammonium and thiolates could also contribute to the stability of the gel.

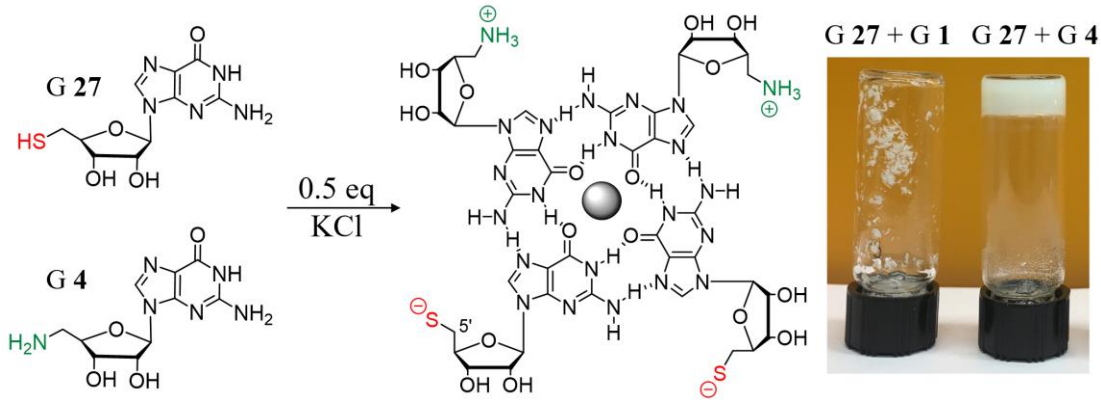

Figure 2.12: A 1:1 binary mixture of 5′-aminoG **4** and 5′-thiolG **27** forms a hydrogel.

2.4.4 Potassium borate hydrogels of 27

Previously, our group reported that addition of $KB(OH)_4$ to G **1** gave a strong and transparent hydrogel.[78] The optimal stoichiometry of borate salt was found to be 0.5 eq. We also started by adding 0.5 eq of $KB(OH)_4$ (made from two separate stock solutions of $B(OH)_3$ and KOH) to **27** and found that a self-standing but translucent hydrogel (1 wt%, 32 mM) formed (**Figure 2.13**).

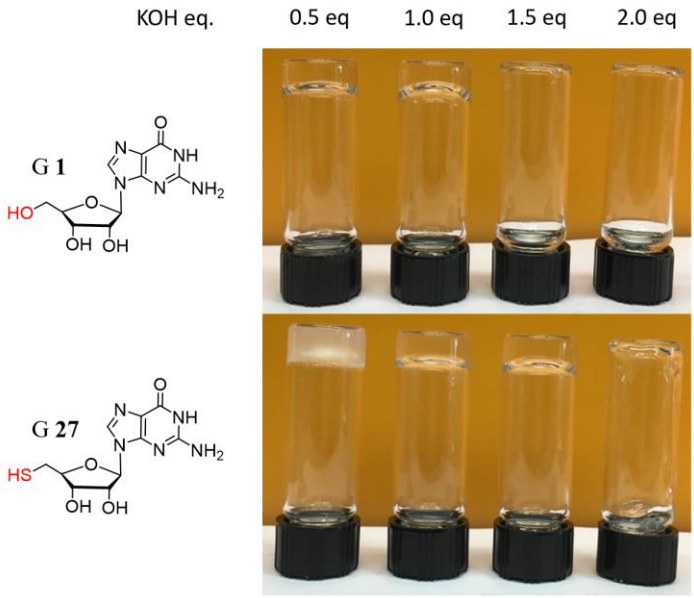

Figure 2.13: Addition of 0.5 eq KOH and 0.5 eq $B(OH)_3$ to SHG **27** (1 wt%, 32 mM) gives a translucent hydrogel while further increasing KOH amount to 1.0 and 1.5 eq gave hydrogels with better clarity.

To improve hydrogelation we proposed that addition of more than 0.5 eq KOH, while maintaining the same amount of $B(OH)_3$, would solubilize undissolved **27** (1 wt%, 32 mM) and form a more uniform hydrogel (**Figure 2.13**). KOH titration test showed that transparent hydrogels were formed with addition of 1.0 & 1.5 eq KOH. As a comparison, G **1** hydrogels are best with 0.5 eq KOH while further addition of KOH weakens or disassembles the resulting gel. This result is again in accordance with the

previous result that higher pH is required for thiol **27** to form a better hydrogel by favoring the formation of thiolate anions. Addition of 2.0 eq KOH only gave a viscous solution.

2.4.5 Potassium borate hydrogels made from a 1:1 binary mixture of 27 and 1

Finally, we decided to combine two aforementioned approaches, namely using a binary mixture and adding borate salts (**Figure 2.14**). The combination of these methods was previously used in our lab to create an 8-aminoG **31**/G **1** hydrogel for remediation of cationic dyes.[99] Satisfyingly, a mixture of **27** and **1** (2 wt%, 64 mM) together with 0.5 eq of $KB(OH)_4$, after purging with nitrogen gas and a regular heating-cooling cycle, resulted in a self-standing and transparent hydrogel. Future work involves more detailed structural characterization of the hydrogel.

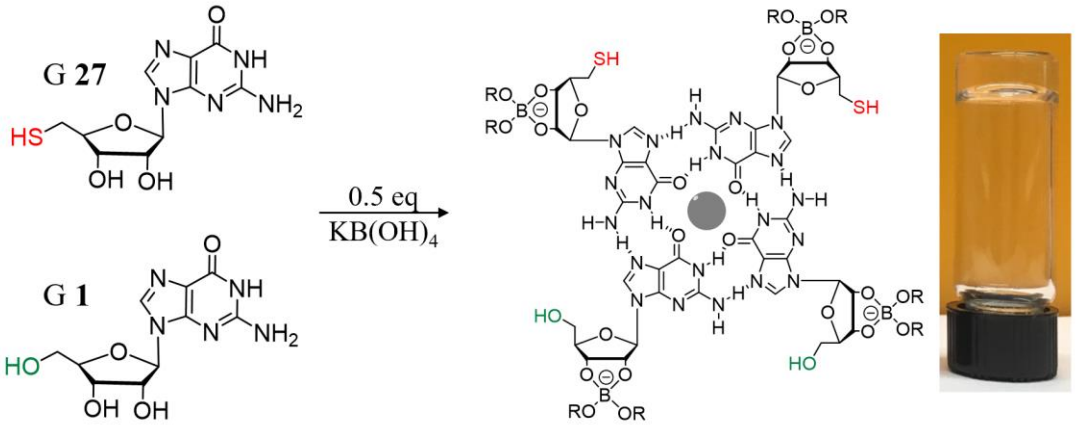

Figure 2.14: A 1:1 binary mixture (2 wt%, 64 mM) of **27** and **1** forms clear and self-standing hydrogel.

2.4.6 Future work on the hydrogelation of 27

Having explored different conditions to induce the hydrogelation of **27**, future work involves more detailed characterization of the resulting hydrogels using NMR, CD, rheology, etc. Then the potential application of the thiol-containing hydrogels for water remediation of toxic metal and alkylating agents will be explored. Finally, we are interested to see if peroxidase enzymes can crosslink the resulting hydrogels by forming a disulfide bond and how it would influence the structure and the behavior of the hydrogels. This research could provide insights into the design of thiol-containing biomaterials.

2.5 Hydrogelation of 5′-disulfideG 28 and preliminary characterization

2.5.1 5′-disulfideG 28 is poorly soluble but can be dispersed in a water/DMSO mixture

Guanosine and its analogs are notoriously insoluble in water despite the seemingly high polarity of the compound. The formation of insoluble ribbon structures is the primary reason (**Figure 2.15**).[129] For **28**, the layers of ribbons are potentially crosslinked by disulfide bonds, which would likely further reduce the aqueous solubility of this nucleoside.

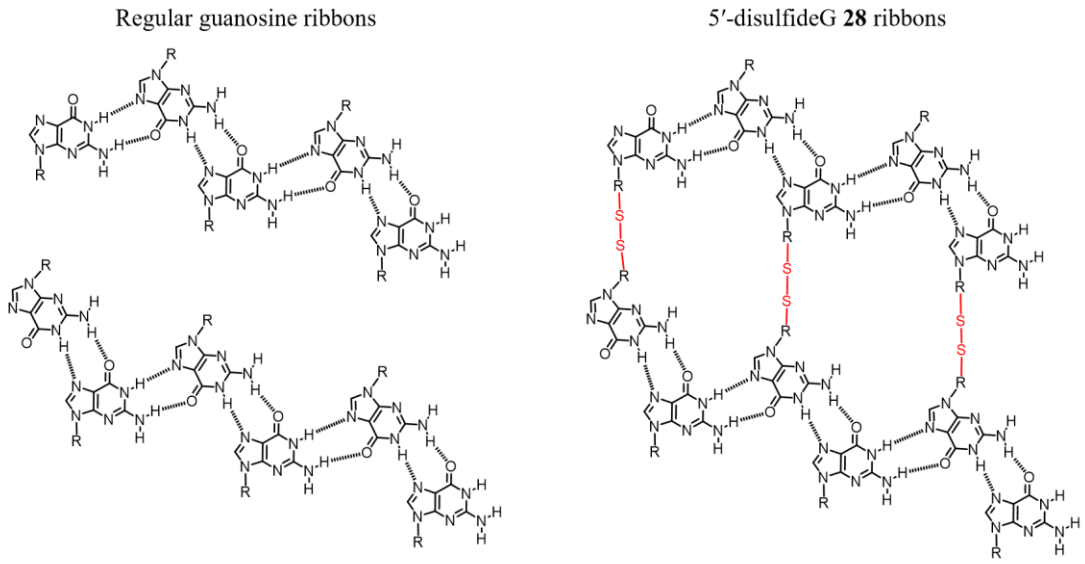

Figure 2.15: Proposed disulfide crosslinking in the solid phase of **28** to cause its poor aqueous solubility.

Initial attempts to create hydrogels using disulfide **28** failed due to its poor solubility; the fine powder obtained after grinding cannot be further broken down in water by sonication. Heating the aqueous suspension of **28** (2 wt%, 32 mM) to boiling, with or without borate salt, also failed to solubilize most of the compound.

Figure 2.16: Addition of finely ground **28** into water gave rapid precipitation, while dissolving **28** in DMSO followed by adding water gave a well-dispersed suspension (0.25 wt%, 4 mM).

While synthesizing the compound, we found that DMSO can dissolve **28** at a high concentration (over 50 g/L). We transferred a small amount of DMSO stock solution of **28** to a glass vial, which was then diluted with water to give a well-dispersed suspension (0.25 wt% **28**, 95% water, 5% DMSO, 4 mM). Addition of borate salts to such a suspension followed by heating can efficiently solubilize all the solid. Without dissolving in DMSO first, the solids of **28** precipitated within a minute in water and cannot be easily dissolved (**Figure 2.16**). Using 5% DMSO, we efficiently broke down crystalline solids of **28** into a fine aqueous suspension, which is beneficial for compound solubilization and gel preparation.

2.5.2 Gelation test of disulfide 28 with borate salts shows better gelation with $KB(OH)_4$

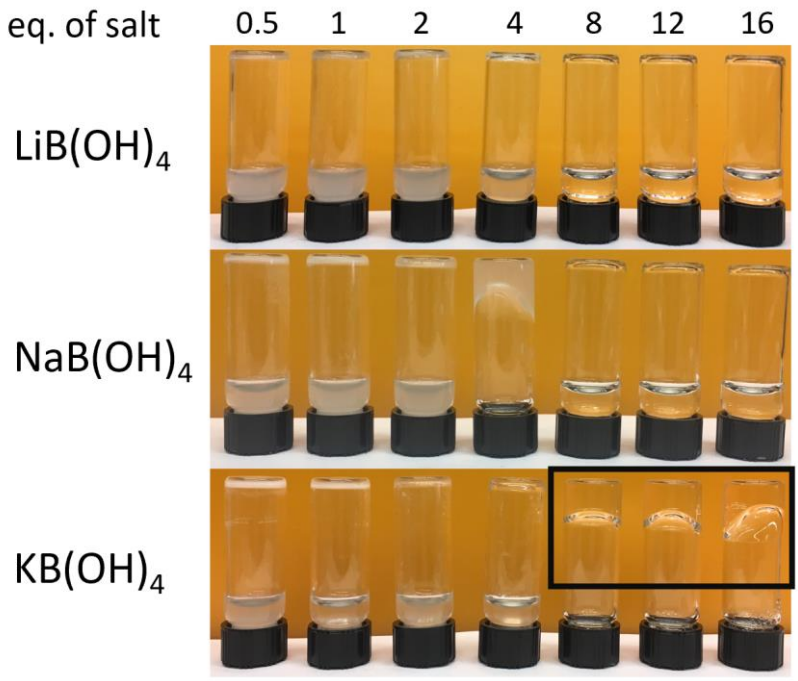

Figure 2.17: Gelation tests with disulfideG **28** (0.25 wt%, 4 mM) and different borate salts in 95% water and 5% DMSO. Sample containing 8 eq $KB(OH)_4$ gave a clear and self-standing hydrogel.

We first performed gelation tests in the 95:5 DMSO:water mixture on disulfideG **28** with borate salts. Both salt concentration and cation identity could potentially influence gelation behavior.[127] Of all the alkali metal cations tested, K^+ formed the best hydrogels with **28**, which reflects K^+ cation's preference at stabilizing G-quartets. Titration experiments indicated that 8 eq of $KB(OH)_4$ (34 mM) gave a self-standing hydrogel (0.25 wt%, 4 mM, 95% water and 5% DMSO). With less than 8 eq. borate gave a suspension, while over 8 eq gave weaker gels as judged by the curvature of inverted hydrogel/air interface (**Figure 2.17**). Switching K^+ into Li^+ and Na^+ mostly gave solutions instead of gels.

2.5.3 CD spectra of K/Na hydrogels show G-quadruplex features

We first studied the resulting hydrogels using circular dichroism spectroscopy (CD) which is a powerful technique to probe the chiral orientations of G-quartet layers (**Figure 2.18**).[2,130] K^+/Na^+ samples of **28** gave strong signals at 200-300 nm that are characteristic of chiral stacks of G-quartets. Li^+ samples fail to show any significant assembly, showing its poor ability to template G-quartet gel formation. The CD spectra support our hypothesis that the hydrogel with K^+ is G-quartet based.

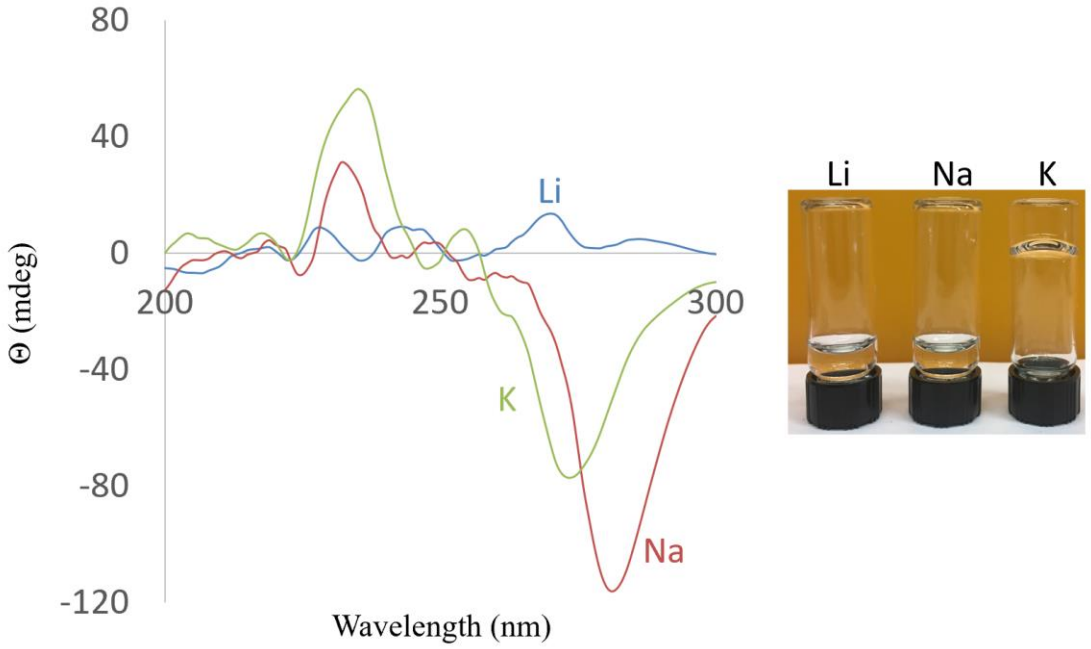

Figure 2.18: CD spectra of different borate samples of **28** (0.25 wt%, 4 mM, 95% H_2O and 5% DMSO, 8 eq $MB(OH)_4$). The path length of the quartz cuvette is 1 mm.

2.5.4 ^{11}B NMR of the resulting gels only show monoester

We then used ^{11}B NMR to probe to composition of different boron containing species in solution. Our group previously reported that with G **1** and 0.5 eq $KB(OH)_4$,

both borate monoester (δ ~ 6 ppm) and diesters (δ ~ 11 ppm) were observed in ^{11}B NMR.[131] In this case, however, since 4 eq of $KB(OH)_4$ were used relative to all riboses (8 eq relative to **28** since each **28** molecule contains 2 ribose units), we propose only monoesters exist due to the large excess relative to **28**.

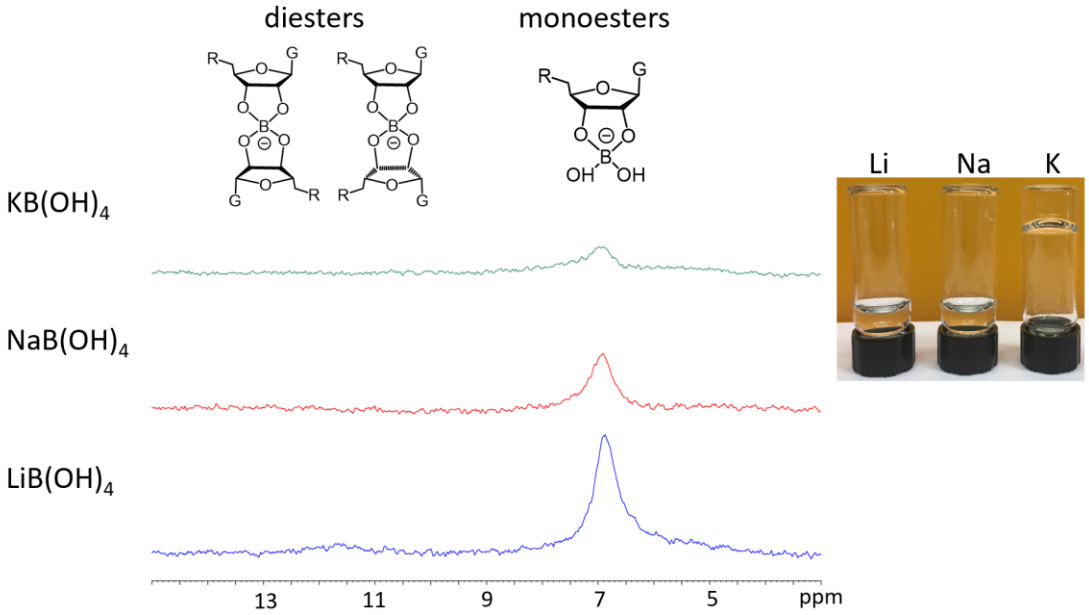

Figure 2.19: ^{11}B NMR spectra of different borate gels from **28** (0.25 wt%, 4 mM, 95% D_2O and 5% DMSO, 8 eq $MB(OH)_4$) show only peaks for monoester.

First, hydrogels containing **28** (0.25 wt%, 4 mM, 95% D_2O and 5% DMSO, 8 eq $MB(OH)_4$) were prepared and transferred into a hot NMR tube. The samples were allowed to cool down and ^{11}B NMR experiments were performed (**Figure 2.19**). Results show that only monoester peaks (δ ~ 6.5 ppm) exist in solution phase due to the large excess of borate salts for Li^+, Na^+ and K^+ borates. No peaks for diesters are found in all three spectra, consistent with our hypothesis. Also significantly stronger peak was seen in the Li^+ sample than K^+, indicating more borate ester species are in the

solid phase for K^+ sample than Li^+ sample. This result is consistent with the stronger capability of K^+ to template G-quartet and induce gelation.

2.5.5 ^{1}H NMR of disulfideG 28 hydrogels

Solution state ^{1}H NMR experiments were performed on samples containing **28** (0.25 wt%, 4 mM, 95% D_2O and 5% DMSO, 8 eq $MB(OH)_4$). Results show that multiple sets of peaks exist in each spectrum, presumably due to borate ester formation (**Figure 2.20**). Li^+ hydrogel shows the most guanosine species in the solution by NMR integration relative to DMSO internal standard while K^+ shows the least. Since all samples contain the same amount of **28** and ^{1}H NMR can only show signals for the solution phase, this result implies more of **28** exists in the solid phase of K^+ sample than Li^+/Na^+ sample. This is consistent with K^+ giving a much stronger hydrogel due to more efficient assembly into hydrogel fibers. Addition of conc. HCl (50 μL) regenerated monomers of **28** (**Figure 2.20** top spectrum), which indicates that all borate esters are hydrolyzed and no side reactions occurred during the process.

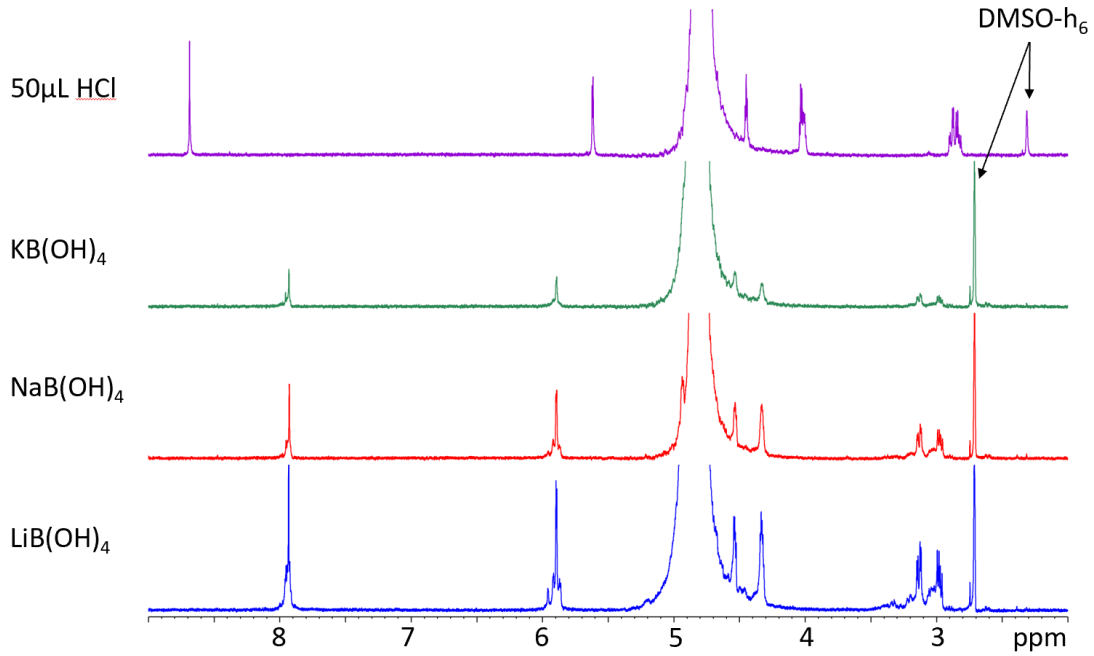

Figure 2.20: ^{1}H NMR full spectra of borate samples with different cations from **28** each show multiple peaks due to borate ester formation. Addition 50 µL conc. HCl regenerated **28** (top spectrum). DMSO-h_6 peak is marked and serves as an internal standard for integration.

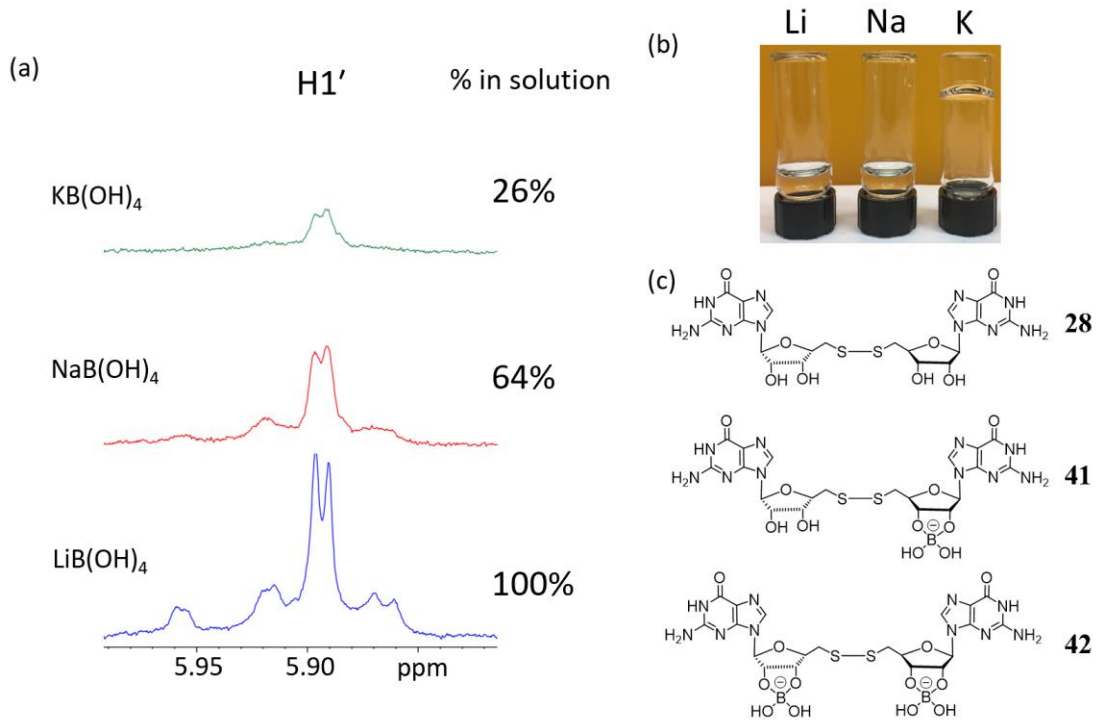

Figure 2.21: (a) ^{1}H NMR H1′ region shows that only 26% of all species are in solution phase for K^+ hydrogel, indicating K^+ is better than Li^+ at templating G-quartet formation. (b) A picture of **28** hydrogels containing different cations. (c) Possible species that exist in the systems.

Since ^{11}B NMR show only borate monoester peaks (**Figure 2.19**), three possible structures exist in the system: **28**, single borate monoester **41** and double borate monoester **42** (**Figure 2.21c**). While **28** and **42** are symmetric compounds and should each have 1 ^{1}H NMR signal, **41** is an asymmetric compound and should have two sets of signals. Close examination of H1′ region of the spectra of Li^+ sample showed 4 peaks overall, which is consistent with our analysis (**Figure 2.21a**).

NMR integration of the H1′ region shows that all the species (100%) in the Li^+ sample are in the solution phase. Switching from Li^+ to Na^+ and K^+ gave progressively weaker intensity for the H1′ signal. Compared to Li^+ sample, only 64% (Na^+) and 26%

(K^+) of all the disulfideG species remain in the solution. This result indicates that K^+ likely shifts the equilibrium toward G-quartet formation to give a self-supporting hydrogel while Li^+/Na^+ complexes remain in the solution (**Figure 2.21b**).

2.5.6 Proposed gelation mechanism

Based on CD spectra, ^{1}H NMR and ^{11}B NMR data, we propose the gelation mechanism for disulfideG **28** $KB(OH)_4$ hydrogel (**Figure 2.22**): in the presence of 8 eq $KB(OH)_4$, **28** react to form borate monoesters **41** and **42**, which self-assemble in the presence of K^+ to give G-quartets. The G-quartets further stack into 1D G-quadruplex fibrils and traps water to give hydrogels. Compared to G **1** borate gels, **28** forms at lower concentration, potentially due to the extra crosslinks from the 5′-disulfide bonds. Based on the mechanism, the hydrogel fibers from **28** should give thicker fibers, which could be probed using SANS and microscopy.[131]

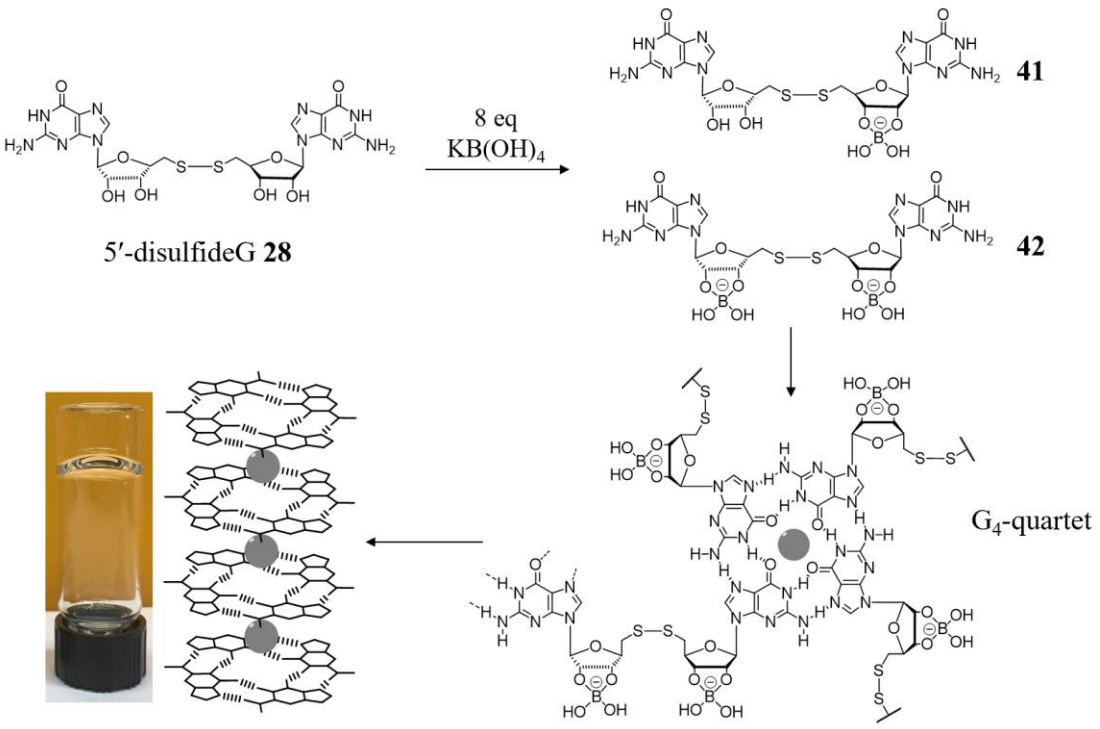

Figure 2.22: Proposed gelation mechanism of disulfideG **28**: addition of 8 eq potassium borate gave borate monoesters **41** and **42**, which self-assemble into $G_4 \bullet K^+$ quartets that stack on top of each other to give hydrogels (5% DMSO and 95% water).

2.5.7 Future work on disulfideG 28 hydrogels

We have successfully formed stable and self-standing hydrogels from disulfide **28** and studied its gelation mechanism. Upcoming work involves using the gel for environmental remediation of Pb^{2+}, a toxic metal ion of environmental concern. Also it would be interesting to see the gelation behavior of a binary gel containing both thiol **27** and disulfide **28**, where the thiolate-disulfide exchange reactions could impart self-healing properties to the resulting hydrogels.

2.6 Biological relevance, synthesis and characterization of 8-thioG 37 and 8-disulfideG 38

2.6.1 8-thioG 37 and 8-oxoG 48 tautomerism

Guanine is known to have the lowest ionization potential and most easily targeted by oxidizing species among all canonical nucleobases.[132] 8-oxoG **44** and 8-thioG **37** are both molecules generated in human body in response to oxidative stress and the structural permutations could significantly change their molecular recognition and self-assembly behaviors (**Figure 2.23**). In literature and in practice, the terms 8-oxoguanosine **44** and 8-thioguanosine **37** are used interchangeably with their corresponding tautomers 8-hydroxyguanosine (**45**) and 8-mercaptoguanosine (**43**). Cho and coworkers utilized ^{15}N NMR to study the tautomerism of 8-modified guanosine analogs in solution (DMSO-d_6).[133] The large coupling constants (^{15}N-^{1}H) for N7 peaks in compounds **44** (-98.5 Hz) and **37** (-99.6 Hz) is consistent with 1-bond distance between N7 and H atoms confirming the structures as keto/thio tautomeric form. They also demonstrated that 8-thio/oxo modications on the imidazole ring of G **1** does not alter the tautomerism in the 6-member ring. In section 2.7, we present X-ray single crystal data of 8-thioG **37** • $2H_2O$, which unambiguously confirm this evidence from solution phase NMR.

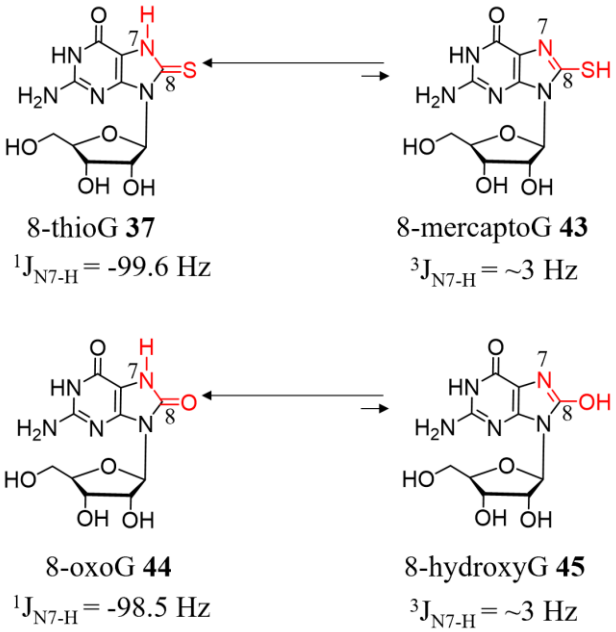

Figure 2.23: Tautomerism of 8-thioG **37** and 8-oxoG **44**. Large ^{15}N-^{1}H coupling constants (-99.6 and -98.5 Hz) in ^{15}N NMR confirmed **37** and **44** are the only form in DMSO solution.[133]

Probing the structures and understanding the self-assembly behaviors of **44** and **37** could provide insight into their interaction with ligands and enzymes. While G **1** self-associates and forms flat ribbon structures on its own, lipophilic analogs of 8-oxoG **44** form supramolecular helices.[134] To our knowledge, the self-assembly behavior of more reactive and redox sensitive 8-thioG **37** has not been explored before.

2.6.2 Biological relevance of 8-thioG 37 analogs

8-thioG **37** and its analogs are compounds of significant biological relevance. **37** is known to reduce *Leishmania amazonensis* infection,[135] and serves as an adjuvant for immune responses.[136–138] Akaike and coworkers identified several unique redox signaling pathways involving 8-thio/thioether guanosine: cGMP **46** can be oxidized into electrophilic 8-nitro-cGMP **47** with reactive oxygen species and nitric oxide,

which is then attacked by nucleophilic hydrogen sulfide or persulfide to form 8-thio-cGMP **48** (**Figure 2.24**).[139,140] Protein cysteine thiolates and glutathione in cells can also react with electrophilic **47** to form **49** and **50**, a process call "S-guanylation".[141] The reaction has been explored to conjugate fluorescent labels onto proteins.[142] Hwu, Tsay and coworkers discovered that conjugates of 6,8-dithioguanosine and coumarins show inhibition against Chikungunya virus.[143]

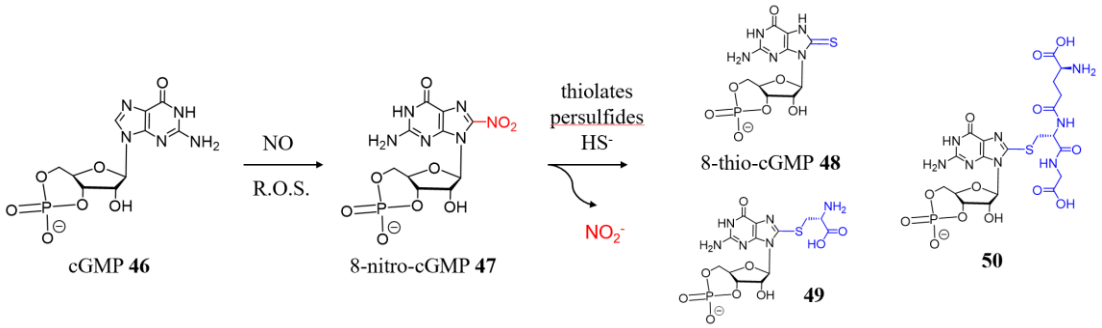

Figure 2.24: cGMP **46** forms 8-nitro-cGMP **47** in the presence of nitric oxide (NO) and reactive oxygen species (R.O.S.). Nucleophilic substitution of **47** by different thiolate/sulfide/persulfide species gives 8-thio-cGMP **48** and thioethers **49**/**50**.

2.6.3 Synthesis of 8-thioG 37

Holmes and Robins first described the synthesis of 8-thioG **37** by nucleophilic aromatic substitution of 8-BrG **29** with thiourea (**Figure 2.25**).[81] We initially set out to synthesize 8-methylthioguanosine (8-SMeG **51**) with **29** and aq. sodium thiomethoxide. After acidifying the resulting solution with conc. HCl, a white and crystalline solid precipitated from the solution. Single crystal X-ray crystallography showed a unit cell for 8-thioG **37** • $2H_2O$ (see section 2.7). ^{1}H NMR analysis of the crystalline material was also consistent with literature NMR data for **37**.[144] For gelation experiments and synthesis of 8-disulfideG **38**, we use the standard thiourea procedure

from the literature to avoid unwanted interference by Na^+ in promoting G-quartet formation.

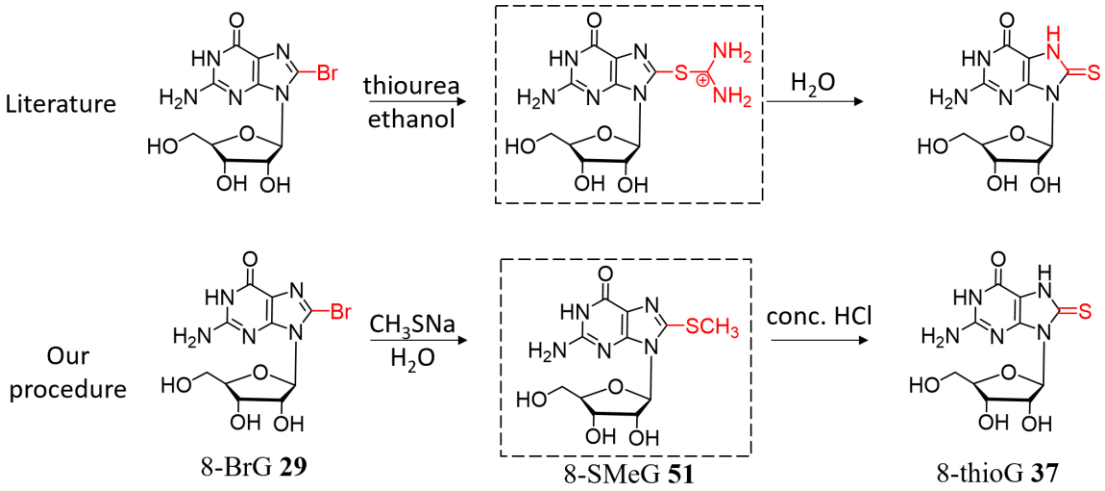

Figure 2.25: 8-thioG **37** synthesis from literature procedures[81] and our procedure.

2.6.4 Synthesis of 8-disulfideG 38

We first attempted the oxidation of **37** into disulfide **38**, a new guanosine analog that was not reported to our best knowledge. Excess I_2 was added to drive the reaction to completion and we obtained a dark brown solid with significant peak changes in its ^1H NMR spectrum. The N1H peak of **37** and **38** on the aromatic ring remains the same, while importantly N7H peak for **38** disappeared (**Figure 2.26**).[145] Also, H1′ shifted from 6.24 ppm for **37** to 5.93 ppm for **38**. Interestingly, addition of excess TCEP to **38** fully regenerated the signature peaks for **37**, indicating that the putative disulfide **38** can be reduced by TCEP. ^{13}C NMR also shows significant shifts of C8 from δ 165.7 ppm for **37**,[145] to δ 139.4 ppm for **38**, which is consistent with literature values for methimazole disulfide (**Figure 2.27**).[146] All this information leads us to believe that pure disulfide **38** was obtained upon treating **37** with I_2. The UV-vis spectrum has been

reported in literature,[147] and the UV-vis spectrum of disulfide **38** in water has significantly different features from **37** (**Figure 2.28**). **37** has absorption peaks at 234, 283 and 301 nm, which is consistent with literature results,[147] while **38** has peaks at 225 nm, 263 nm and a broad peak centered 355 nm. The broad peak extends to ~410 nm, which contributes to the brown color of the disulfide **38**. Future work involves more detailed characterization of **38** using UV-vis/Raman spectroscopy, mass spectrometry and diffusion-order NMR (DOSY).

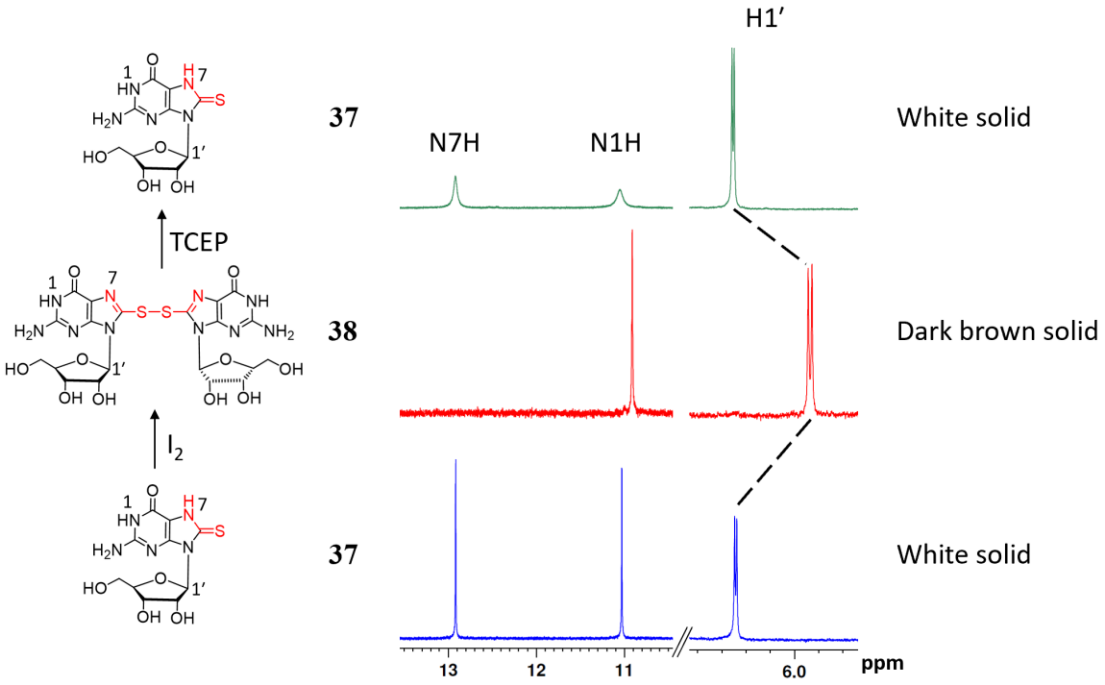

Figure 2.26: Oxidation of **37** with I_2 gives disulfide **38**. ^{1}H NMR in DMSO-d_6 shows that addition of TCEP to **38** regenerates the signature peaks for thio **37**.

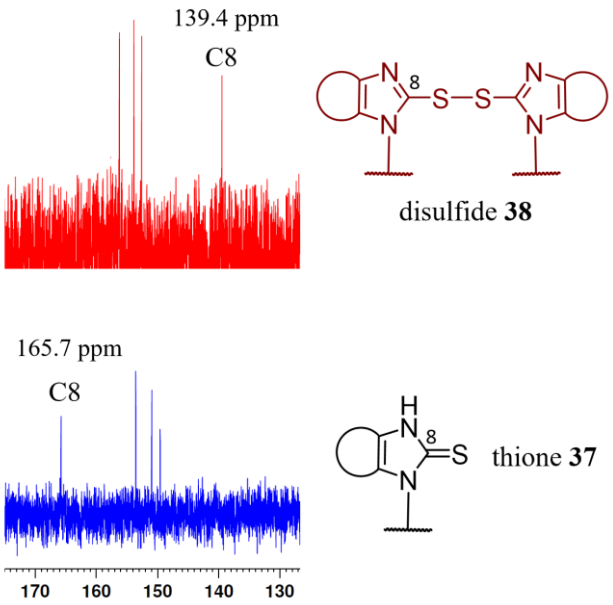

Figure 2.27: After iodine oxidation, ^{13}C NMR peak for C8 showed a 26 ppm shift from 165.7 ppm (**37**) to 139.4 ppm (**38**).

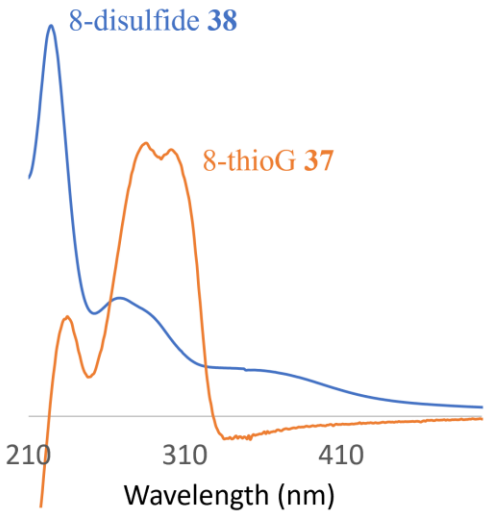

Figure 2.28: UV-vis spectra of **37** and **38** in water.

2.7 Crystal structure of 8-thioG 37 dihydrate

As mentioned in section 2.6.3, we obtained a highly crystalline solid after treatment of 8BrG **29** with thiomethoxide solution followed by hydrolysis (**Figure 2.29a**). X-ray

crystallographic analysis shows a structure 8-thioG **37** dihydrate (**Figure 2.29b**). The data unambiguously confirms the C=S double bond on position 8 of guanine. This means that 8-thioguanosine instead of 8-mercaptoguanosine should be used as the name for **37**.[133] The C=S bond length (1.69 Å) is identical to the C=S bond in ergothioneine **53** dihydrate (**Figure 2.29c**),[148] but much shorter than C=S bond in thiourea (1.746 Å).[149] This could be caused by the weaker ability of the nitrogen atoms to donate electrons via resonance in the aromatic ring system. The glycosidic bond length for **37** is 1.45 Å, which is identical to G **1**, but shorter than 8-BrG **29** (1.47 Å).[150,151] This is consistent with the stability of **37** in acidic solutions during synthesis.

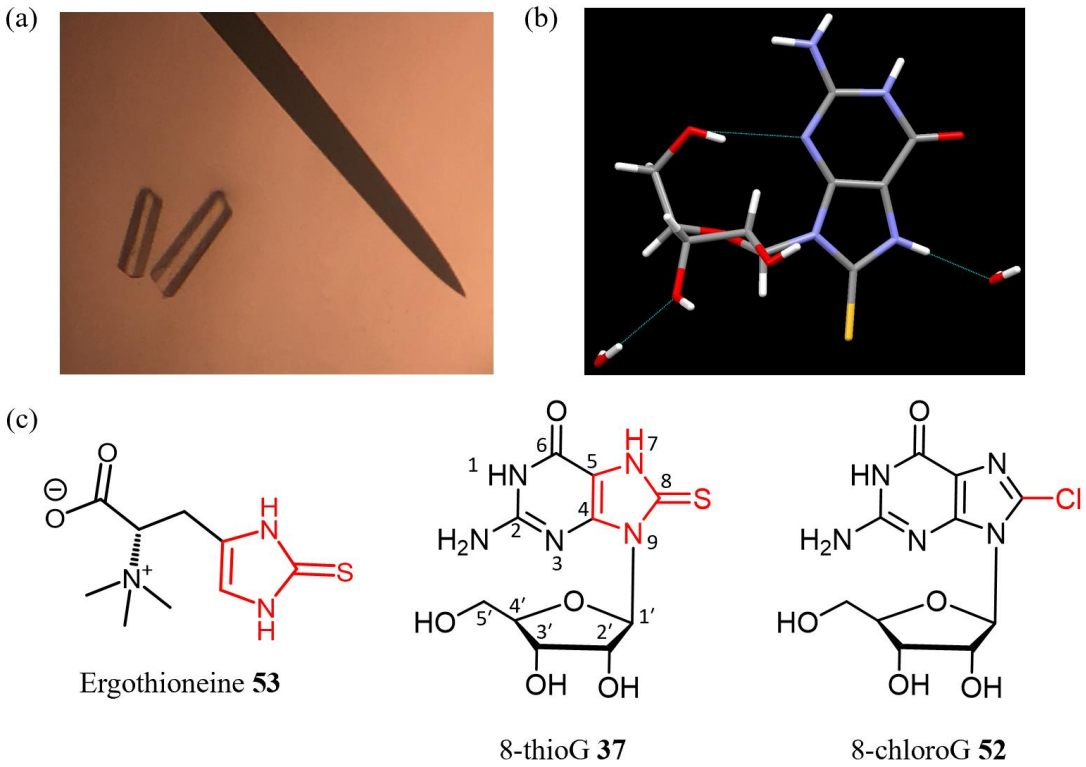

Figure 2.29: (a) A picture of crystals containing **37** dihydrate under microscope. (b) Stereoscopic view of **37** dihydrate. (c) structures of ergothioneine **53** and 8-chloroG **52**.

The ribose adopts a C2′ endo sugar puckering, which is also similar to the crystal structures of **29** and **52** (**Figure 2.29b**).[151,152] The molecule has a *syn* conformation about the C-N glycosidic bondwith a torsion angle of 64.0° due to the large size of sulfur atoms. In the ^{1}H NMR spectrum of **37** (DMSO-d_6), H2′ has a chemical shift of δ 4.95 ppm that corresponds to a ~96% *syn* conformation.[153] Hence, the solution phase data for 8-thioG **37** is in good agreement with its solid state conformation.

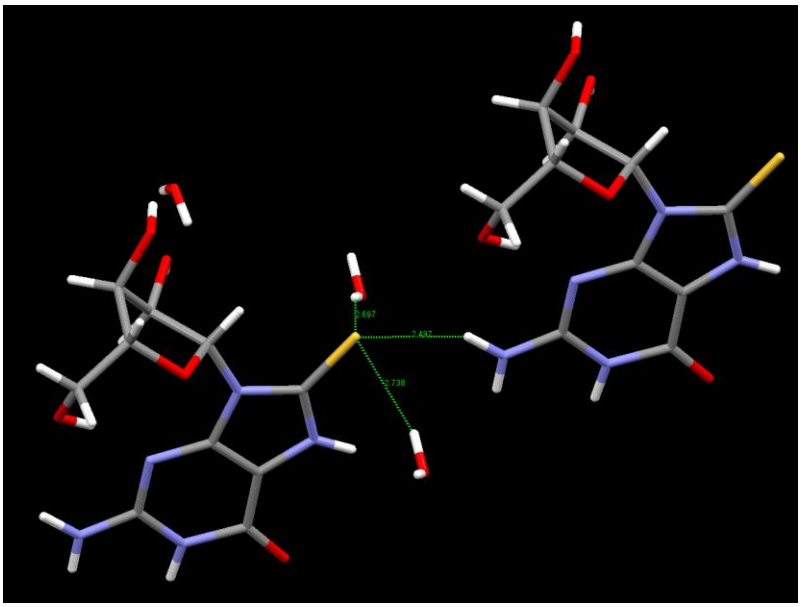

Figure 2.30: 8-sulfur atom of **37** in the crystal structure hydrogen bonds with two water molecules and exocyclic amine of another guanine.

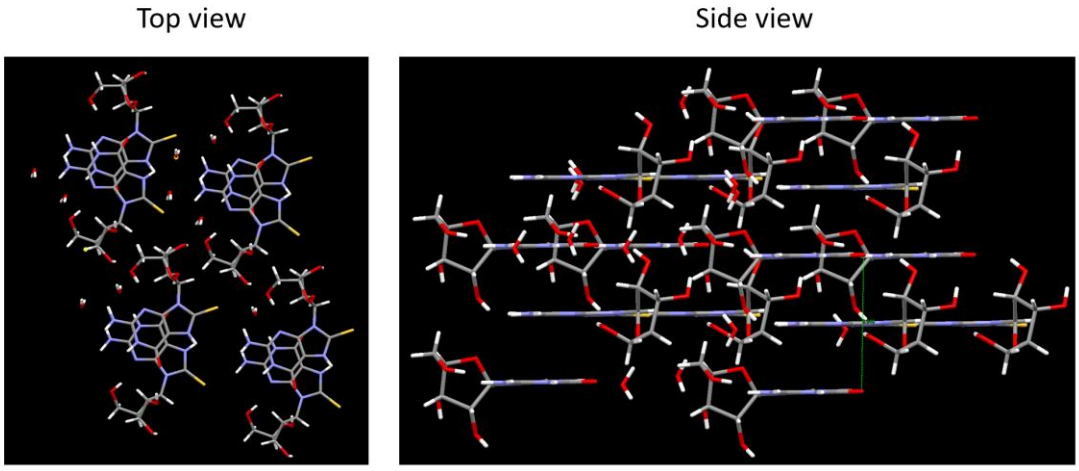

Figure 2.31: Top and side view of crystal packing in **37** dihydrate.

In a unit cell, 8-thioG **37** forms hydrogen bonds with two water molecules on 3′-OH and N7H positions. An intramolecular hydrogen bond is formed between 5′-OH and N3, which was similar to the crystal structures of 8-BrG **29** dihydrate and 8-chloroG dihydrate **52** (**Figure 2.29b**).[151,152] The sulfur atom forms three hydrogen bonds: two with water molecules and one with exocyclic N2H (**Figure 2.30**). π-π interactions are found between different layers of nucleobases with stacking distance of 3.17 Å (**Figure 2.31**).

2.8 Possible methods to regenerate Hoogsteen base pairing in 8-thioG 37 for G-quartet hydrogel synthesis

2.8.1 8-thioG 37 is less likely to be incorporated into G-quartets

Guanine has the most diverse recognition patterns among naturally occurring nucleobases. The Hoogsteen face is important for G-quartet formation to construct functional assemblies (**Figure 2.32a-b**). 8-thioG **37** and 8-oxoG **44**, however, are less

likely to form G-quartets due to the hydrogen atom on N7 that breaks complementarity of hydrogen bonding (**Figure 2.32c**). Plavec and coworkers demonstrated incorporation of 8-oxo-deoxyguanosine into human telomeric oligonucleotide sequence can maintain G-quadruplex structure but with weaker stability.[154] We now propose ways of regenerating N7 lone pair and triggering gelation from **37**.

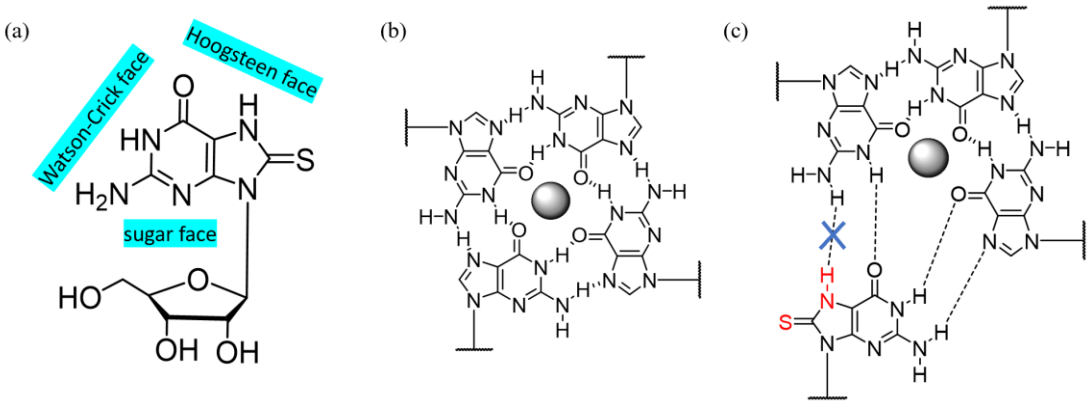

Figure 2.32: (a) Different recognition faces on guanine nucleobase of **37**. (b) Regular G-quartet. (c) 8-thioG **37** potentially forms weaker G-quartets due to alteration on N7 position.

2.8.2 Oxidation of 37 into disulfides

Disulfide **38** formation using oxidants could potentially trigger the gelation (**Figure 2.33**). In fact during synthetic attempts, we observed organogel formation upon adding I_2 to a suspension of **37** in acetonitrile. Asymmetric disulfides can potentially be obtained by oxidizing **37** in the presence of other thiol-containing molecules (cysteine, glutathione etc.)

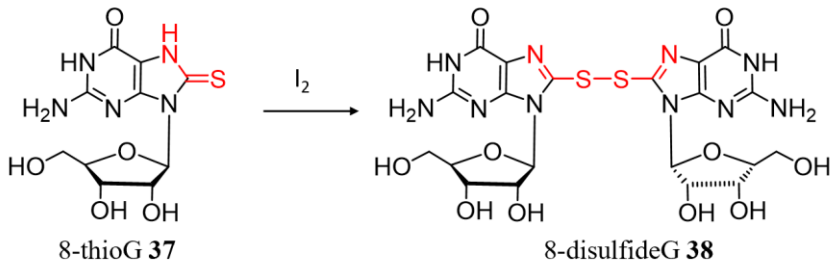

Figure 2.33: Oxidation into disulfide regenerate Hoogsteen base pairing on N7.

2.8.3 Alkylation of 8-thioG 37 to form thioethers

The N7H in **37** is expected to be highly acidic since significant deshielding is observed in its ^{1}H NMR (N7H 12.9 ppm). Addition of KOH is expected to easily deprotonate N7H and generate thiolates. In the presence of alkylating reagents (Michael acceptors, alkylhalides), stable thioethers can form and regenerate N7 lone pair, which will further assemble into a hydrogel in water (**Figure 2.34**). This is can be applied to covalent trapping and sensing of toxic electrophiles.

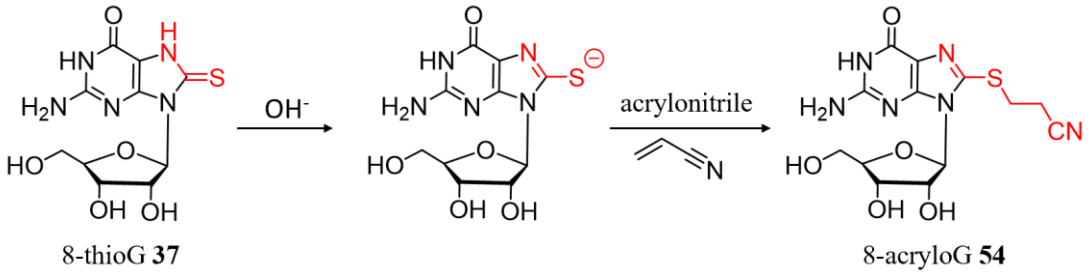

Figure 2.34: Formation of thioether by alkylating thiolate regenerates Hoogsteen base pairing on N7

2.8.4 Heavy metal ion binding

Other than covalent binding of toxic organics, non-covalent binding of toxic heavy metal ions could also reform the regular Hoogsteen face (**Figure 2.35**). Since sulfur

atoms are soft bases, they interact strongly with soft metal ions such as Pb, Cu, Hg, Au. Previously studied on the interaction between **37** and Hg/Pd/Rh shows that **37** serves as a good ligand with high affinities for such metal ions or complexes.[144,145,155,156] We envision that upon metal binding in waste water, the resulting metal complexes self-assemble (in the presence of K^+) into hydrogels that trap toxic metals *in situ*.

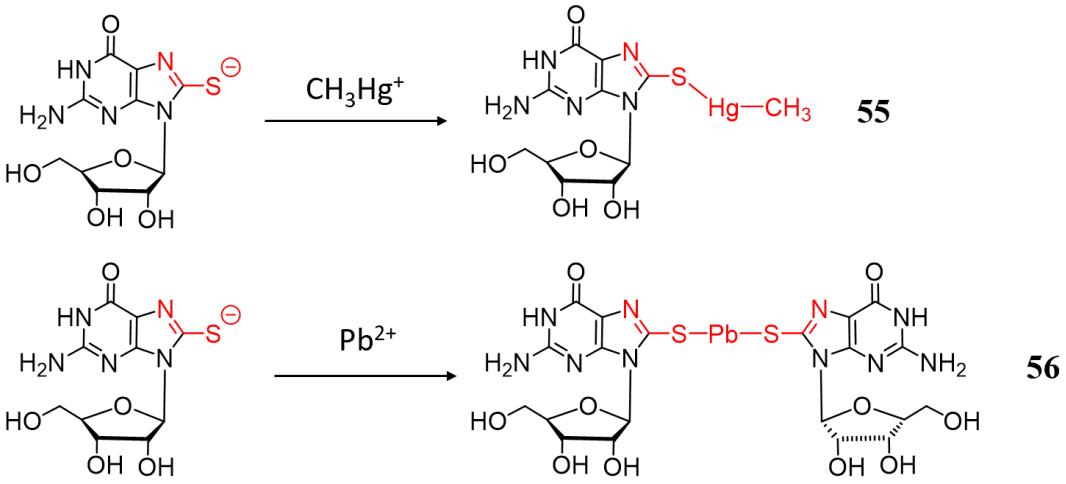

55

56

Figure 2.35: Binding of thiolates with soft metal ions regenerates Hoogsteen base pairing on N7

2.9 Preliminary gelation test of 8-thioG 37 and 8-disulfideG 38 and future work

2.9.1 8-thioG 37/G 1 form a binary hydrogel with 0.5 eq $KB(OH)_4$

We first performed a preliminary gelation test on 8-thioG **37** (**Figure 2.36**). As expected, no gelation occurred with 0.5 eq KCl or 0.5 eq $KB(OH)_4$, which confirms our hypothesis that **37** cannot form G-quartets. We next added 0.5 eq G **1** to create a binary hydrogel, which can potentially prevent precipitation. While thioG **37**/G **1** binary system cannot form hydrogels with 0.5 eq KCl, addition of 0.5 eq $KB(OH)_4$ gave a translucent hydrogel, which could be caused by G **1**-quartet assemblies while

thioG **37** is covalently attached on the periphery of the G-quartet via borate ester linkage (**Figure 2.36**). This result demonstrates the potential to incorporate thione functional group into hydrogels for environmental applications.

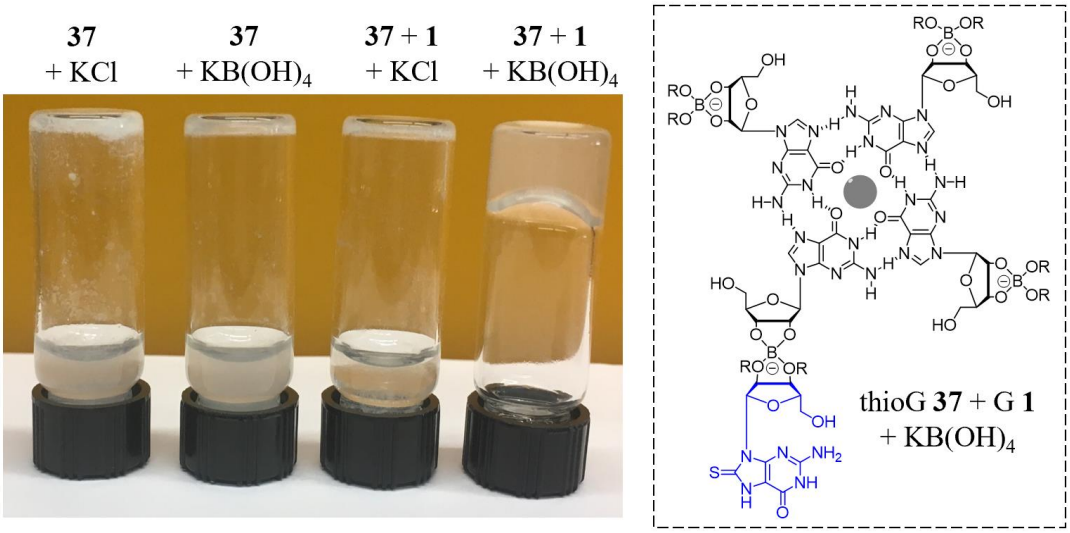

Figure 2.36: Preliminary hydrogelation test of 8-thioG **37** under different conditions. Binary mixture of **37** and G **1** forms a hazy hydrogel with 0.5 eq $KB(OH)_4$, possibly due to the G-quartet self-assembly of G **1**.

2.9.2 8-disulfideG 38 forms organogels at room temperature

Due to the poor aqueous solubility of 8-disulfideG **38**, no hydrogels (1 wt%, 0.5 eq KCl or 0.5 eq $KB(OH)_4$) formed in all conditions we attempted (**Figure 2.37**). However, during the synthesis, we serendipitously discovered that **38** spontaneously formed gels by simple mixing and sonication in acetone without added salt. We screened some common solvents and discovered that organogels were formed in acetone and ethylene glycol (1 wt%, 16 mM), while others solvents simply gave precipitates ($CHCl_3$, CH_2Cl_2, ether, ethyl acetate and ethanol) or solutions (DMSO, DMF) (**Figure 2.38a**). These organogels are unique in that the gels form without any heat and most other guanosine

organogels require lipophilic groups to increase solubility.[1] The gelation without salt indicates that the structural basis could be guanosine ribbons,[157] or empty G-quartets due to the large *syn* conformation of **38** (>99% syn).[153] Sessler and coworkers have previously shown the crystal structure of a salt-free G-quartet.[158]

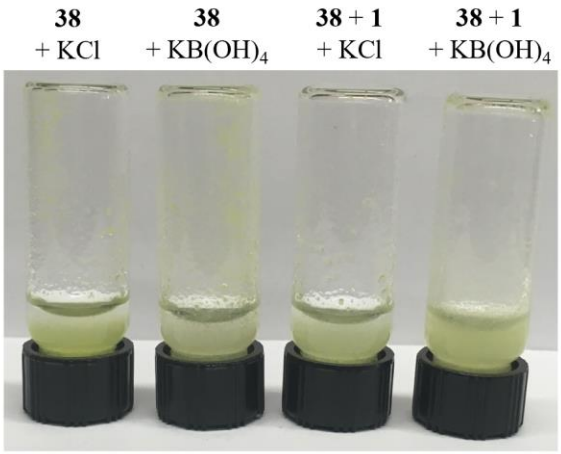

Figure 2.37: Preliminary hydrogelation test of 8-disulfideG **38** under different conditions

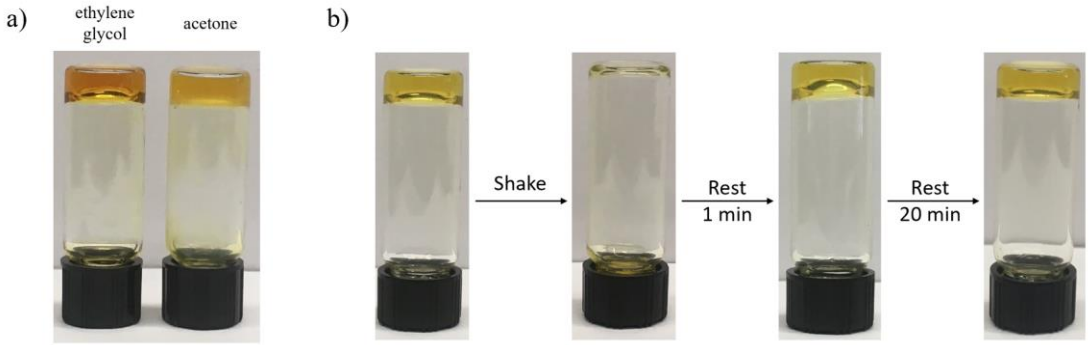

Figure 2.38: a) **38** form organogels in ethylene glycol and acetone. b) **38** acetone gel exhibits self-healing behaviors

Most interestingly, while in ethylene glycol the gel is robust and stiff, **38** acetone gel exhibits self-healing properties (**Figure 2.38b**). Agitation of the organogel (0.5 wt%, 8 mM) originally gave a solution. Resting for 1 min reform a weaker gel and original strength was restored after 20 mins. While the weak hydrogen bonding between

guanine bases could lead to the self-healing properties, the labile aromatic disulfide in **38** could also contribute to the phenomenon. Future work involves more detailed characterization of the resulting organogels using different spectroscopy methods with focus on the self-healing properties.

2.10 Conclusions

In this chapter, we have demonstrated the detailed synthesis and characterization of four interesting sulfur-containing guanosine analogs. While these compounds are highly insoluble, our preliminary attempts demonstrate that these analogs can self-assemble into gels under certain circumstances (binary systems, adding borates, adding base, adding organic solvents). Results show that 5′-disulfideG **28** self-assembles into a G-quartet hydrogel with excess $KB(OH)_4$. The reduced form of **28**, thiol **27**, form hydrogels under basic conditions, presumably due to deprotonation of 5′-thiol to give more soluble thiolates.

For the first time, we obtained a single crystal for 8-thioG **37**. X-ray crystallographic analysis unambiguously showed an 8-thione tautomer and the compound favors *syn* conformation about the glycosidic bond, which is consistent with previous reports in literature. While a binary mixture of **37** and G **1** forms a hydrogel with 0.5 eq $KB(OH)_4$, we only observed precipitation in other attempts, which supports our hypothesis that 8-thioG **37** is less likely to form G-quartets. Finally, we synthesized and studied a new guanosine analog, 8-disulfideG **38**, and found that it self-assembled into a self-healing organogel in acetone without any added salt. This gel formed spontaneously at room temperature and shows promise for future design of smart materials. The versatile

chemistry of thiol/disulfide, in combination with supramolecular gels from natural product guanosine, is an exciting field of research for us to explore in the future.

2.11 Future work

2.11.1 8-thioG 37 as potential anti-thyroid drugs

Thiamazole, together with other aromatic thiourea analogs, are commonly used as anti-thyroid drugs (**Figure 2.39a**). While the mechanism of action is unclear, it is proposed that formation of halogen bonding adducts between these thiourea compounds and I_2 can competitively inhibit thyroid peroxidase (**Figure 2.39b**).[159,160] Laurence and coworkers called thiamazole a "diiodine sponge" and determined the 1:1 adduct formation constant in CH_2Cl_2 to be 92400 L/mol.[161] Since thioG **37** is a guanosine analog with a thiourea motif, we propose it can also interact with I_2 and serve as a potential drug candidate for hyperthyroidism.

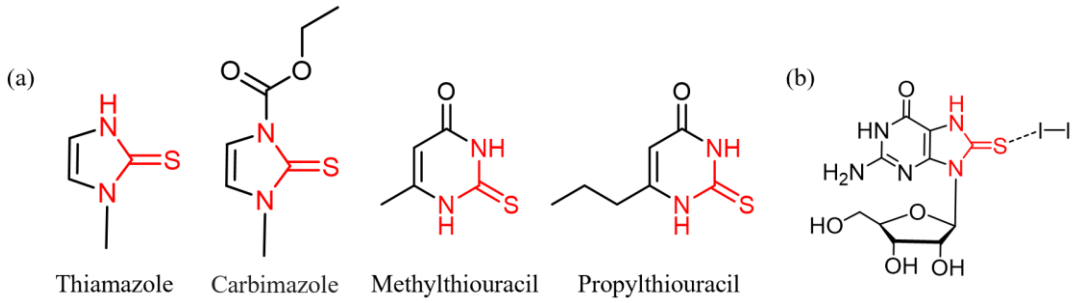

Figure 2.39: (a) Structures of anti-thyroid drugs. (b) Possible interaction between 8-thioG **37** and I_2.

2.11.2 8-selenoguanosine and 8-diselenideguanosine self-assembly

Diselenide bonds are dynamic covalent bonds with lower bond energy (41 kcal/mol) than disulfide bond (57 kcal/mol), so the exchange process can be induced by visible

light without any catalysts.[162] The diselenide exchange chemistry has been extensively applied to the construction of stimuli-responsive materials.[163,164] Incorporation of such motifs into guanosine hydrogels enables us to design supramolecular polymers with interesting light responsiveness. 8-selenoguanosine (8-selenoG **57**) has been described in literature (**Figures 2.40**) and the corresponding cyclic 3′,5′-phosphate has anti-cancer activities.[165] Since we examined the self-assembly behavior of 8-thioG **37** and 8-disulfideG **38**, 8-selenoG **57** and 8-diselenideG **58** can also serve as an interesting comparison.

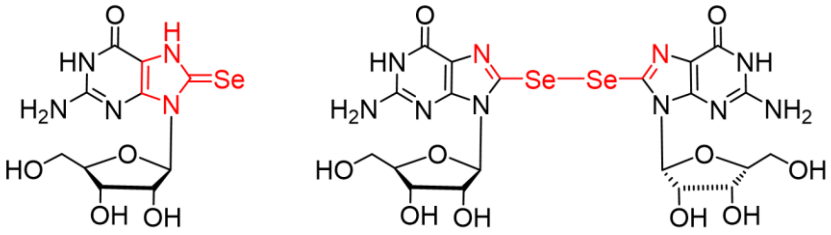

Figure 2.40: Structures of 8-selenoG **57** and 8-diselenideG **58**.

2.12 Synthesis of guanosine analogs and NCI60 screening data

2.12.1 Modifiable positions on a G-quartet

In order to form a G-quartet hydrogel, the Hoogsteen base pairing needs to be preserved, which leaves guanine C8H and ribose 2′, 3′ and 5′-OH positions available for modification (**Figures 2.41**). Starting from naturally occurring G **1**, important electrophilic intermediates **20**, **29** and **39** can be conveniently synthesized, which opens a myriad of possibilities for modifications (**Figures 2.42**). In Chapters 3&4, we construct a 5′-hydrazinoguanosine (HG **2**) hydrogel which has applications in water

purifications. In Chapter 5, we discuss the hydrogelation of guanosine 5′-hydroxamic acid (HAG **15**) and utilize the hydrogel for surface patterning with $FeCl_3$.

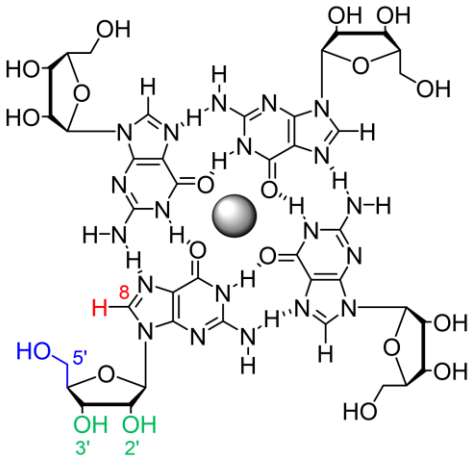

Figure 2.41: Positions available for modifications on a guanosine quartet.

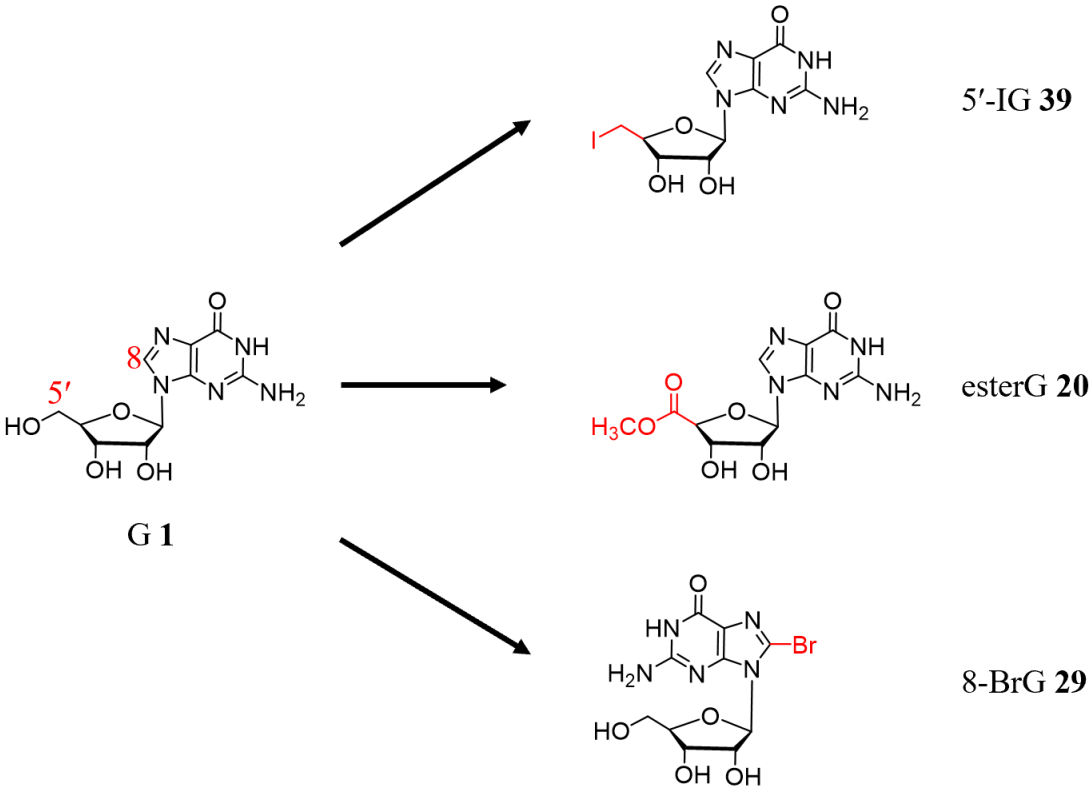

Figure 2.42: G **1** can be modified intro electrophilic intermediates.

2.12.2 Synthetic guanosine analogs and NCI-60 screening

Nucleobase, nucleoside and nucleotide analogs are excellent candidates for anti-cancer and antiviral drugs.[166,167] We synthesized or purchased different guanosine and inosine analogs (**Figures 2.43-2.46**), 25 of which were submitted to National Cancer Institute for anti-cancer activity screening (NCI-60).[168] In chapter 6.6 we report the synthesis and characterization of these analogs and in chapter 6.7 we report preliminary screening results from NCI-60.

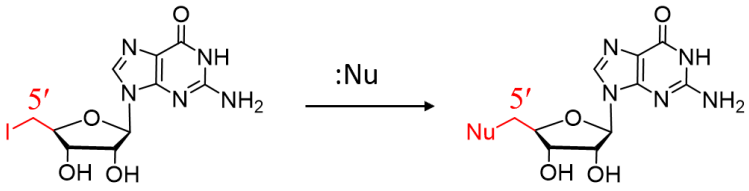

5′-IG **39**

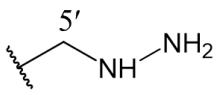

HG **2**

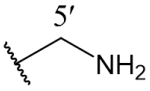

5′-aminoG **4**

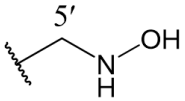

5′-NHOHG **5**

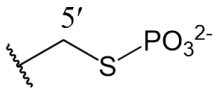

5′-thiophosG **26**

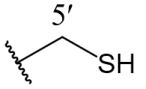

5′-SHG **27**

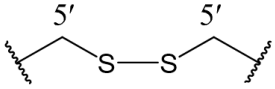

5′-disulfideG **28**

Figure 2.43: Synthesis of guanosine analogs from 5′-IG **39**.

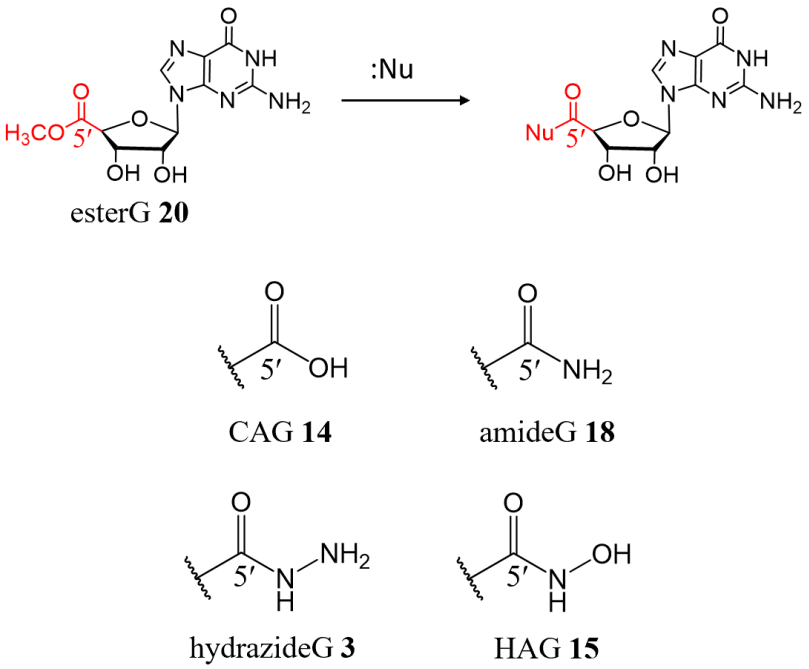

Figure 2.44: Synthesis of guanosine analogs from 5′-esterG **20**.

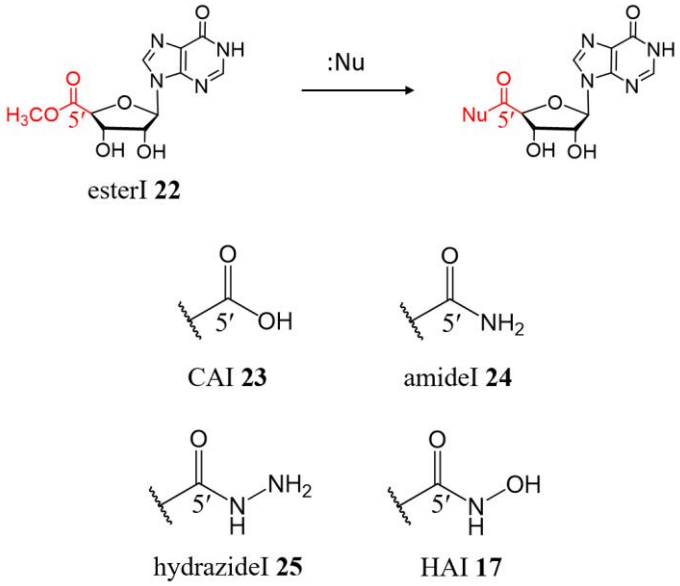

Figure 2.45: Synthesis of inosine analogs from 5′-esterI **22**.

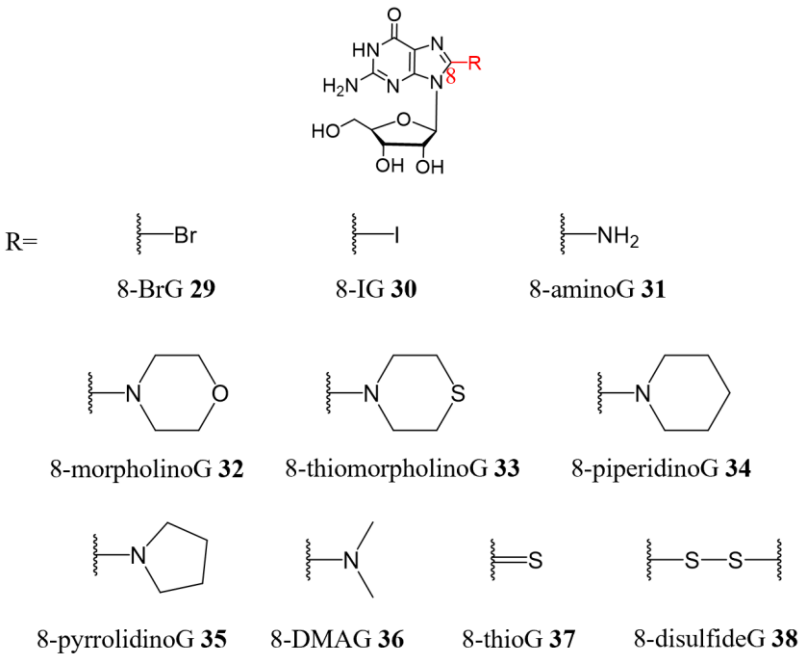

Figure 2.46: Structures of 8-modified guanosine analogs.

Chapter 3: Hydrogels from 5′-hydrazinoguanosine for the purification of water

The majority of this chapter has been published in reference [5]*:*

Xiao, S.; Davis, J. T. G_4-Quartet Hydrogels from 5′-Hydrazino-Guanosine for the Non-Covalent and Covalent Remediation of Contaminants from Water. *Faraday Discuss.* **2018**, *209*, 97–112.

3.1 Summary

This chapter focuses on the self-assembly of a synthetic guanosine analog, 5′-deoxy-5′-hydrazinoguanosine (HG **2**) and the applications of these assemblies for binding of dyes and absorption of toxic electrophiles in water. We find that HG **2** self-assembles into a self-standing hydrogel in the presence of stoichiometric amounts (0.25 equiv) of KCl. The higher water solubility of HG **2** (14.5 mM), as compared to the parent compound G **1** (2.1 mM), likely contributes to its enhanced gelation. The structural basis for this HG **2**•KCl hydrogel, confirmed by PXRD, IR and CD, is the G_4•K^+ quartet, which form extended 1D ion-channels that entangle to give a stable and long-lived hydrogel. We also find that adding KCl to a saturated solution of HG **2** triggers generation of colloidal G_4•K^+ assemblies *in situ* that selectively and efficiently bind the anionic dye naphthol blue black (NBB) over a cationic dye. In addition to this non-covalent electrostatic binding of anions, the nucleophilic 5′-hydrazino group in the HG **2**•KCl hydrogel HG **2** enables efficient absorption of propionaldeyde from both the gas phase and from water solution, via formation of covalent hydrazone linkages with the gel matrix.

3.2 Introduction

Supramolecular hydrogels, which consist mostly of water but are actually soft solids made by the molecular self-assembly of low molecular weight gelators (LMWG), have many applications in areas such as drug delivery, sensing, catalysis, materials science and environmental remediation.[169–171] The power of self-assembly can be used to create these supramolecular hydrogels from a rich variety of LMWGs, including synthetic compounds as well as natural products such as peptides, sugars, lipids and nucleosides/nucleotides.[13,172] Our group is especially interested in using supramolecular assemblies,[57,60,173] including hydrogels,[99] for separation of environmental contaminants in water. The significant surface area of hydrogel fibers can be useful for absorption and/or reaction with toxic compounds, enabling removal of pollutants from water via either non-covalent and/or covalent interactions.[171]

In this chapter, we describe the preparation, characterization and applications of a supramolecular hydrogel/colloid made from a synthetic analog of guanosine (G **1**), namely the LMWG 5′-deoxy-5′-hydrazinoguanosine (HG **2**)[123] (**Figure 3.1**). This simple modification of the nucleoside's 5′-sidechain, from 5′-OH (G **1**) to 5′-$NHNH_2$ (HG **2**), provides a LMWG that self-assembles in the presence of KCl to form a transparent and stable supramolecular hydrogel. We then developed a method to generate *in situ* a colloidal suspension of this HG **2**•KCl assembly that enables the selective and rapid precipitation of an anionic dye from water (*vide infra*) (**Figure 3.2A**) We also show that the HG **2**•KCl hydrogel, with its high density of nucleophilic

5′-hydrazino groups, can efficiently remove aldehydes from water by forming covalent bonds (**Figure 3.2B**).

Guanosine derivatives have long been known to form supramolecular hydrogels and other nanostructures.[3,61,71] In the past decade there has been a resurgence in the study of guanosine-based hydrogels, due in large part to their biocompatibility and myriad of useful functions.[1,87,174–177] The structural basis for most of these hydrogels is the cation-templated G_4-quartet, wherein 4 guanine bases self-assemble into a hydrogen-bonded macrocycle with simultaneous coordination to an alkali(ne earth) metal cation.[2,71] These individual $G_4 \bullet M^+$ quartets further stack to form extended 1D G_4-wires that can be hundreds of microns in length. These G_4-wires then entangle to give the 3D mesh that the hydrogel uses to entrap water (**Figure 3.1**).

We reasoned that the central cation channel within these G_4-wires would make $G_4 \bullet M^+$ hydrogels promising candidates for non-covalent, electrostatic binding of anionic species (**Figure 3.2A**).[178–180] The poorly-soluble guanosine (G **1**) is itself, however, not a good gelator. In the presence of KCl G **1** forms transient hydrogels that then crystallize (in minutes or hours), precluding the use of soft materials that are made only from G **1**. So, effort has been devoted to enhance the ability of G **1** and analogs to form longer-lived and functional hydrogels.[1,174]

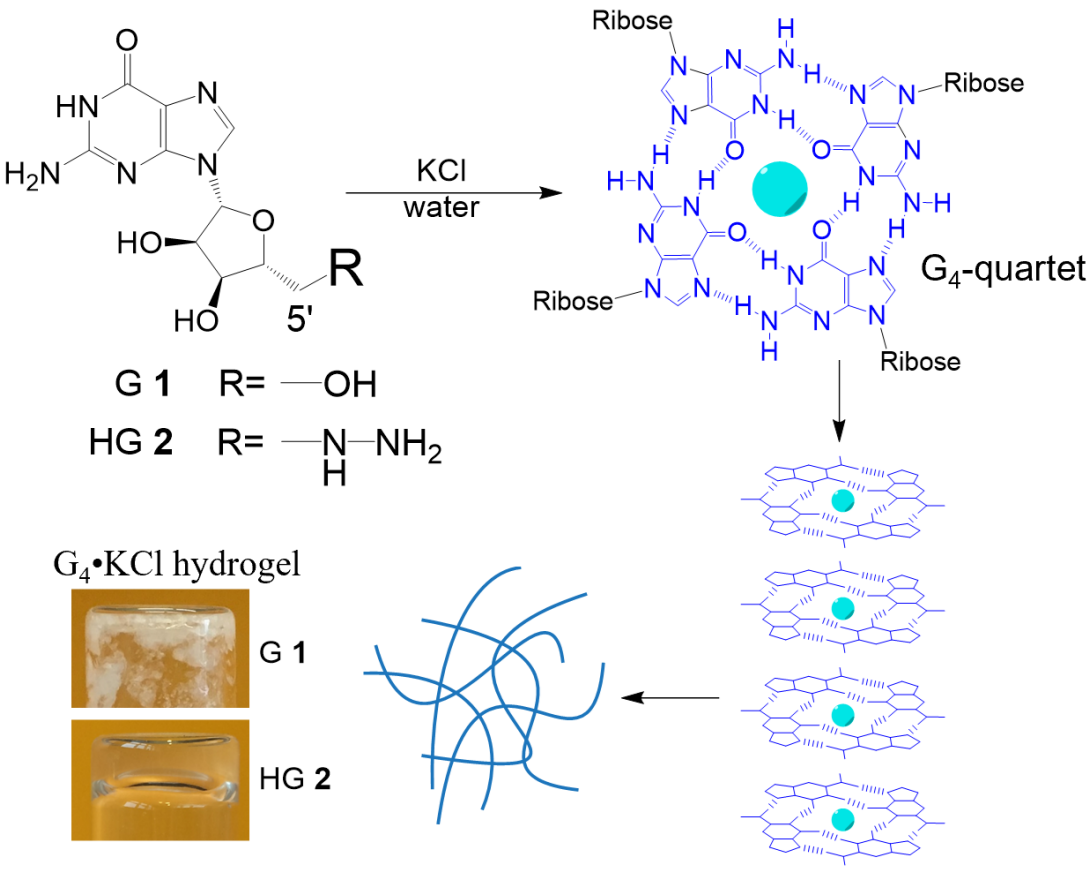

Figure 3.1: Hierarchical self-assembly leads to formation of G_4-quartet based hydrogels. Hydrogen-bonded G_4-quartets, templated by K^+ cations, stack to give 1D G-quadruplexes, which then entangle to form a hydrogel. A transparent and long-lived hydrogel is formed with HG **2** (2 wt %, 68 mM) and 0.5 eq of KCl. In contrast, the parent nucleoside G **1** precipitates from solution in the presence of KCl.

One effective strategy for making stable G_4-quartet hydrogels, introduced by the McGown and Rowan groups,[85,94] is to use a binary mixture of different G analogs, which presumably adds enough disorder to the system so as to disfavor crystallization and maintain the hydrogel phase as the thermodynamically favored phase. We recently used this approach to prepare G_4-quartet hydrogels from KCl and a 1:1 mixture of 8-aminoguanosine (8-aminoG **31**) and G **1**.[99] These 8-aminoG **31**: G **1** hydrogels, kinetically stable when suspended in KCl solution, absorb anionic dyes from water into

the gel matrix, effecting a "water-in-water" type of purification of these dye contaminants. However, one key drawback with the 8-aminoG **31**: G **1** gel was that this absorption of anionic dyes took a relatively long time (days) because of slow diffusion into the bulk hydrogel. Formation of colloidal G_4-quartet assemblies that aggregate in water to form functional phases, such as micelles and microgels, has recently been demonstrated by the Rivera group.[181,182] These G_4-quartet colloidal assemblies have been used to reversibly encapsulate drugs. We decided to take a similar approach by screening for conditions that might give rise to colloidal suspensions of G_4-quartet nanoparticles, rather than the dense 3D matrix of a hydrogel.[181,182] In this present study, we find that generation of a colloidal suspension of G_4-quartets in water at ambient temperature, done simply by mixing HG **2** and KCl, greatly increases the efficiency of the binding and separation of an anionic dye from water. We reason that the surface area of these colloidal G_4-quartet assemblies is larger than that of the bulk HG **2**•KCl hydrogel, so that non-covalent absorption of the anionic dye is no longer limited by slow diffusion.

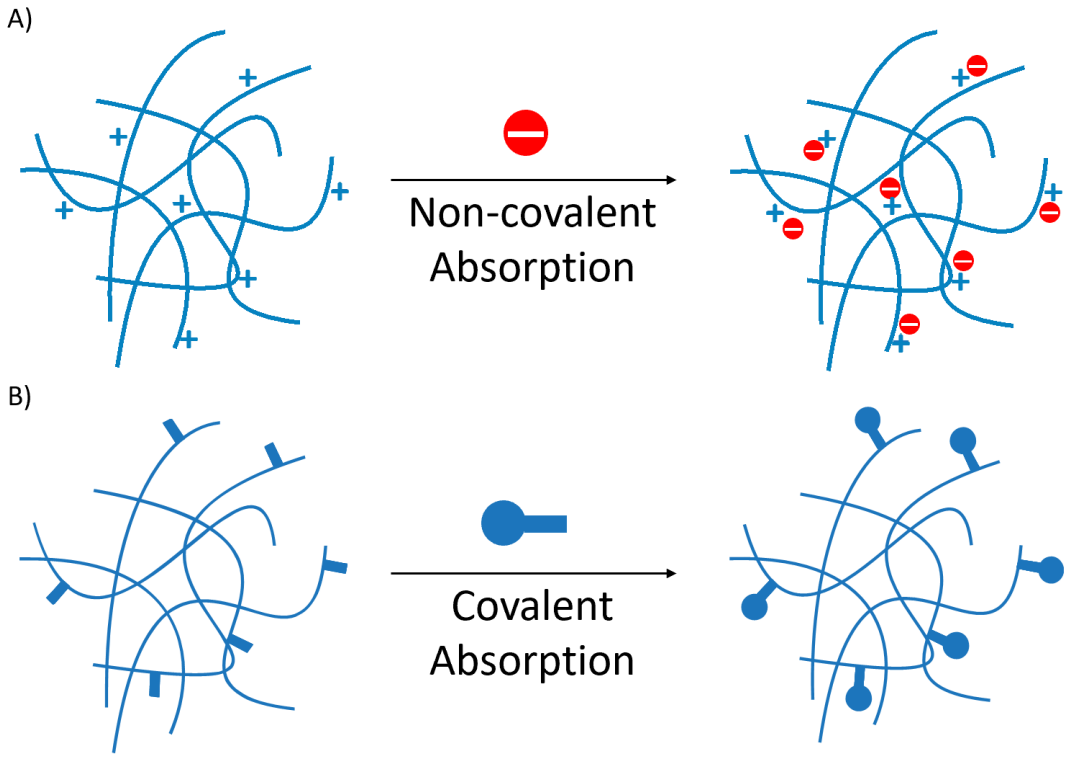

Figure 3.2: The cationic HG **2**•KCl hydrogel can A) absorb anionic species via non-covalent interactions and B) trap aldehydes by forming covalent hydrazone bonds.

Another approach toward improving the hydrogelation properties of G **1** involves chemical modification of the nucleoside's sugar to enhance its water solubility. Whereas the unique hydrogen-bonding pattern of the G nucleobase is crucial for self-assembly to give a G_4•M^+ quartet structure, the ribose can be readily modified to change the properties of the LMWG and its corresponding hydrogel. For example, we have used borate ester chemistry to produce stable G_4-quartet hydrogels.[78,127] Borate esters, which form by reaction of cis-1,2-diols with borate, are anionic and this helps solubilize the intractable G **1**. These guanosine-borate hydrogels have recently been shown to have many interesting uses, including environmental remediation of cationic dyes,[95] as

drug delivery vehicles,[183,184] as media for cell culture,[185] and as catalysts and sensors.[186,187]

Modification of the 5′-position of G **1** can also provide new guanosine analogs with enhanced solubility and better hydrogelation properties. The primary 5′-position of G **1** is relatively straightforward to chemically modify and typically such modifications do not impact formation of the key G_4-quartets since the 5′-position is remote from the hydrogen-bonding nucleobase. For example, Lehn and Sreenivasachary discovered a stimuli-responsive G_4-quartet hydrogel made from 5′-hydrazidoguanosine (hydrazideG **3**).[97] Importantly, the gel's 5′-hydrazide sidechain could form covalent acylhydrazone linkages with aromatic aldehydes. The Lehn group used this system, in a series of studies, to develop dynamic G_4-quartet hydrogels that enabled component selection in a dynamic combinatorial library.[80,97,188] Inspired by the utility of a compound such as hydrazideG **3**, and also motivated by our ongoing program in environmental remediation using G_4-quartet assemblies, we undertook a survey (and comparison with hydrazideG **3**) of the gelation properties of some other 5′-modified guanosines. At the outset, 3 major factors guided our choices in the 5′-modification of G **1**: 1) we wanted to find a LMWG that would give a self-standing hydrogel with low (ideally stoichiometric) equivalents of KCl template; 2) the functional group should be basic enough to be significantly protonated at neutral pH so that, in combination with its cationic $G_4 \bullet K^+$ core, the gel would favor non-covalent binding and extraction of anionic dyes;[189] and 3) we wanted the 5′-group to be a good nucleophile, such as a hydrazino or hydroxylamino group with their potent α-effect,[190,191] so that the gel could be used to form covalent bonds with electrophiles such as aldehydes.[192,193] In short, we aimed

to incorporate a basic and nucleophilic group into the 5′-position and have it function as a useful gelator for a range of environmental separations. Herein, we describe our initial studies on a G_4•KCl hydrogel made from 5′-hydrazino HG **2**. This G_4-quartet based system can be used to both non-covalently extract an anionic dye and also covalently absorb an aliphatic aldehyde from water.

3.3 5′-Substituent influences the water solubility of guanosine derivative and its ability to form hydrogels in the presence of added KCl.

As described below, during our ongoing studies on guanosine-based hydrogels we discovered that the known 5′-hydrazino HG **2** has some useful properties: 1) it forms transparent and self-standing G_4-quartet hydrogels upon addition of stoichiometric amounts of KCl; 2) these HG **2**•KCl hydrogels selectively bind anionic dyes (vs. cationic dyes); and 3) the HG **2**•KCl hydrogels, adorned with nucleophilic 5′-hydrazine sidechains, efficiently absorb propionaldehyde from both the gas phase and solution phase.

One property of HG **2** that we recognized was key for hydrogel formation was its enhanced water solubility, relative to poorly soluble G **1**. Smith and colleagues have shown that the water solubility of a LMWG can be crucial for hydrogelation.[194] As shown in **Figure 3.3** we compared the hydrogelation properties and water solubility of 6 different G analogs that differed in their 5′-sidechain. These compounds included: the parent nucleoside, guanosine G **1**; this study's featured gelator, 5′-hydrazino HG **2**;[123] the 5′-hydrazideG **3**;[97] the 5′-amino derivative, 5′-aminoG **4**;[79] the 5′-hydroxylamino analog, 5′-NHOHG **5**;[123] and the free acid of guanosine 5′-monophosphate, GMP **6**. We

purchased compounds **1** and **6** and we synthesized compounds **2-5** using known methods.

We first compared the ability of these different 5′-modified guanosines to gel water in the presence of 0.5 molar eq of KCl. We chose KCl as the salt to trigger self-assembly of G analogs **1-6** because of the well-established propensity of K^+ to template formation of G_4-quartets.[1,174] Thus, 2 wt % (ca. 68 mM) of each analog was added to water and heated until we obtained a clear solution. Then 0.5 eq of KCl (per monomer of **1-6**) was added and the solution was allowed to cool to rt. As shown in the inverted vials in **Figure 3.3B**, only the 5′-hydrazino HG **2** and hydrazideG **3** formed self-standing hydrogels under these conditions. The 5′-aminoG **4** and 5′-NHOHG **5** analogs precipitated while cooling. The parent G **1**, although it initially formed a hydrogel, turned into a precipitate within just 30 min. As expected, the highly soluble GMP **6** remained in solution, without any sign of hydrogelation or crystallization.

A)

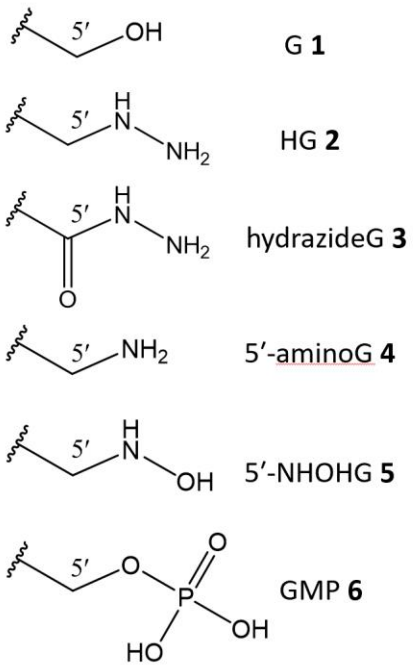

B)

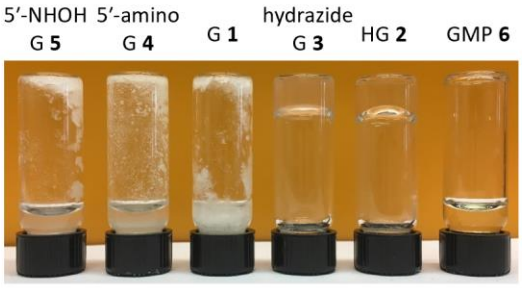

C)

	solubility (mM)	Gelation?
5′-NHOHG **5**	0.84 ± 0.13	precipitate
5′-aminoG **4**	1.26 ± 0.15	precipitate
G **1**	2.08 ± 0.3	precipitate
hydrazideG **3**	4.17 ± 0.27	gel
HG **2**	14.53 ± 0.76	gel
GMP **6**	197.18 ± 19.08	solution

Figure 3.3: A) Guanosine derivatives **1-6**, each with a different 5′-substituent. B) Vial-inversion test (after 1 day at rt) shows that only HG **2** and hydrazideG **3** form self-standing hydrogels. Each sample contains 2 wt % (ca 68 mM) nucleoside and 0.5 molar eq of KCl in H_2O. C) Molar solubilities of **1-6** at 22 ^oC in increasing order, as determined by UV measurements at = 254 nm. The green shading for hydrazideG **3** and for 5′-hydrazino G (HG **2**) highlight that these 2 derivatives, with "moderate" water solubility, form transparent and self-standing hydrogels.

We next determined the water solubility of G analogs **1-5** at 22 ^oC by adding 10 mg of each compound to 1 mL of deionized water. The suspensions were sonicated for 30 seconds and then stirred at 22 ^oC for 1 h before ultracentrifugation was performed to remove insoluble material. The supernatant was diluted and guanine's UV absorbance at λ= 254 nm was measured to calculate the solubility at 22 ^oC for **1-6** in water (see **Figure 6.3**). **Figure 3.3C** shows that the poorly soluble compounds (< 2 mM), namely G **1**, 5′-aminoG **4** and 5′-NHOHG **5** do not form hydrogels with added KCl, but give copious precipitation. The 2 compounds that form hydrogels in the presence of KCl,

HG **2** (14.53 mM) and hydrazideG **3** (4.17 mM), both have moderate solubility in water, when compared to analogs **1**, **4** and **5**. Most notably, substitution of 5′-OH in G **1** to the 5′-hydrazino group in HG **2** enhanced the nucleoside's aqueous solubility by 7-fold and resulted in efficient K^+ templated gelation of water instead of leading to precipitation.

These results, although based on a limited sample size, indicate a connection between a guanosine analog's solubility and its ability to form hydrogels in the presence of KCl; moderate solubility of the G monomer is needed for formation of G_4•K^+ hydrogels. This is not surprising since a proper balance of a hydrophobicity and hydrophilicity for the LMWG is often required to give a stable hydrogel.[194] If a monomer (like G **1**) is too insoluble in water, then the resulting G_4•K^+ structures are not well stabilized by hydration and the material crystallizes or precipitates. On the other hand, if the monomer is too soluble (such as GMP **6**) then the equilibrium favors high concentrations of soluble aggregates and the self-assembled fibers needed for gelation simply don't form in ample amount. While other factors (e.g. disorder, conformation, charge) surely play a role in controlling gelation vs. precipitation/crystallization vs. dissolution, consideration of the relative solubility of G derivatives is probably a good start when designing, or screening, for new G_4-quartet hydrogels.

3.4 The HG 2•KCl hydrogel is made up of G_4-quartets.

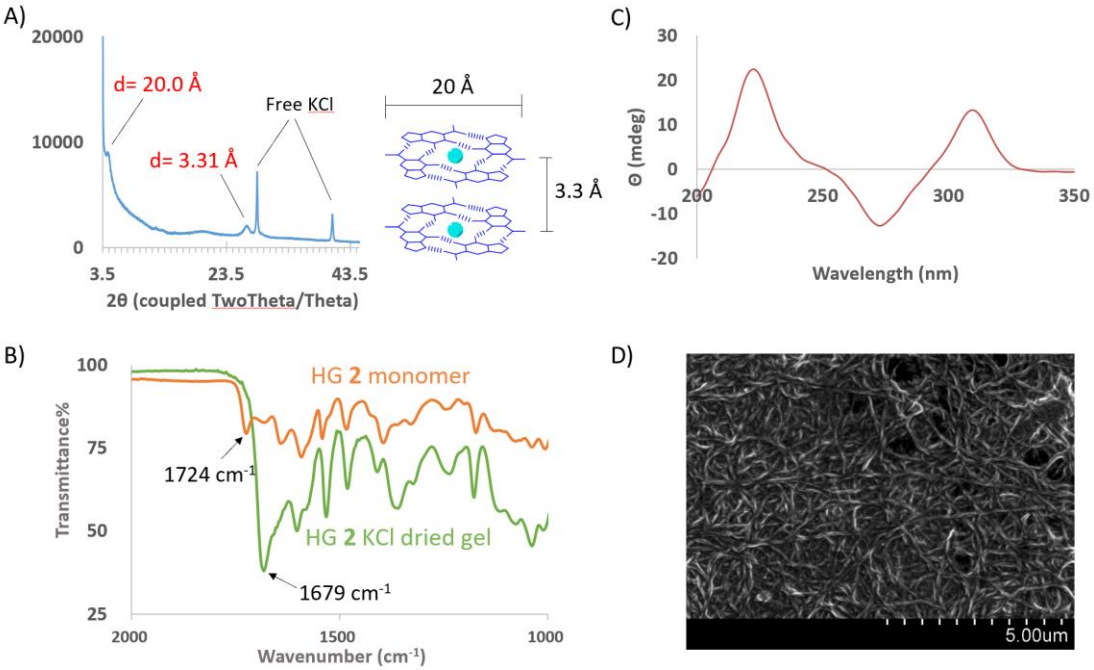

Figure 3.4: Characterization of G_4-quartet based HG **2**•KCl hydrogel. A) Powder X-ray diffraction pattern of a dried hydrogel shows evidence for G-quadruplex formation. B) Infrared spectrum of HG **2** monomer and the freeze-dried HG **2**•KCl gel. The stretching frequency of the guanine carbonyl showed a 45 cm^{-1} red shift. C) CD spectrum of the HG **2**•KCl hydrogel indicates a chiral G-quadruplex structure. D) An ESEM image of HG **2**•KCl hydrogel (2 wt%, 68 mM, 0.5 eq KCl) shows a fibrous and entangled network.

That addition of 0.5 equiv of KCl to a 2 wt % solution of HG **2** gave a transparent and self-standing hydrogel indicated that K^+ was likely responsible for templation of a G_4-quartet assembly. To confirm G_4-quartets on the molecular level we used data from powder X-ray diffraction (PXRD), infrared (IR) spectroscopy and circular dichroism (CD) analyses. The PXRD pattern of a lyophilized HG **2**•KCl gel showed characteristic diffraction peaks indicative of G-quadruplex formation: namely, the π-π stacking distance between individual G_4•K^+ quartets (d= 3.31 Å, 2θ= 26.9°) and the diameter of an individual G_4•K^+ quartet (d= 20.0 Å, 2θ= 4.4°) (**Figure 3.4A**).[76] IR spectroscopy

also indicated that the HG **2**•KCl gel was composed of G_4-quartets. As shown in **Figure 3.4B**, the IR spectrum of a freeze-dried HG **2**•KCl hydrogel, when compared to that for "monomeric" HG **2**, showed a significant red shift of 45 cm^{-1} for the guanine's carbonyl stretching frequency after addition of KCl. This shift from 1724 cm^{-1} for the HG **2** monomer to 1679 cm^{-1} for the HG **2**•KCl gel is consistent with the carbonyl of a G_4-quartet being involved in strong intermolecular H-bonding and coordination to a central K^+ cation, as shown by Setnička, Lehn and colleagues in their IR study of hydrogels formed by hydrazide LG **3**.[195] Finally, CD spectroscopy also supported G_4-quartet formation by HG **2**. The CD signals in the 250-320 nm region arise due to stacking of G_4-quartets in a helical arrangement.[196] **Figure 3.4C** shows that the CD spectrum for a 2 wt % HG **2**•KCl hydrogel (68 mM **2**, 1.0 eq KCl) has a strong negative band near 270 nm and a strong positive band near 310 nm, which is diagnostic of the chiral stacking of individual G_4-quartets.[78,127,197] These pieces of information together, namely the PXRD, IR and CD data, support the proposal that the molecular structure of the HG **2**•KCl gel is based on stacks of G_4-quartets that form 1D nanowires containing a central K^+ ion channel.

To gain a firmer understanding about the morphology of the HG **2**•KCl hydrogel we used environmental scanning electron microscopy (ESEM) to image the material. The ESEM technique, increasingly being used to directly image supramolecular hydrogels,[198] enables one to observe the gel's porous network under wet conditions. **Figure 3.4D** shows an ESEM photo obtained from a 2 wt % HG **2**•KCl hydrogel (68 mM, 0.5 eq KCl) that had been immersed in an ionic liquid. The ESEM shows that this HG **2**•KCl hydrogel is a highly porous material with significant exposed surface area

due to its mesh of entangled fibers. These fibers, which are 1-2 microns in diameter and hundreds of microns long, appear to be composed of bundles of strands (presumably G_4-nanowires) that wrap around one another to give a helical macrostructure.

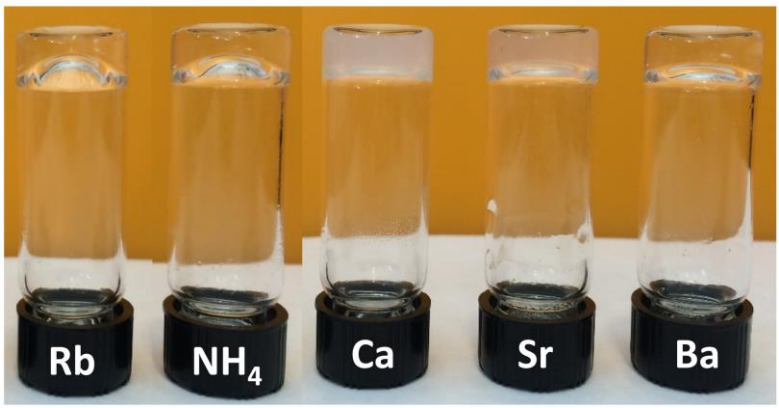

Figure 3.5: HG **2** forms hydrogels with various chloride salts (2 wt%, 0.5 eq salt).

In addition to hydrogelation with K^+, HG **2** also forms self-standing hydrogels with 0.5 eq of other monovalent and divalent chloride salts, including Rb^+, NH_4^+, Sr^{2+}, Ba^{2+}, and most notably Ca^{2+} (**Figure 3.5**). The ionic radii of Ca^{2+} (1.12 Å) is much smaller compared to K^+ (1.51 Å),[103] and K^+ is more similar in size to the G-quadruplex central cavity and promotes hydrogelation more efficiently.[2] This hydrogelation with the less favorable Ca^{2+} might again result from the moderate solubility of HG **2**, which enhances hydrogel stability. To the best of our knowledge, this is the first guanosine-Ca^{2+} hydrogel reported.

3.5 The mechanical properties of the HG 2•KCl hydrogel can be modulated by K^+ concentration.

Crystal structures of DNA G-quadruplexes and lipophilic G-quadruplexes typically show K^+ ions sandwiched between every G_4-quartet.[74,199] Such an organization indicates that 0.25 eq of K^+ relative to G monomer is required to form the G-quadruplex ion channel (**Figure 3.1**). But, because of the poor water solubility of many G derivatives one typically needs excess KCl to form a G_4-quartet hydrogel. And, often, that G_4-quartet gel is only a kinetic product, as it crystallizes or precipitates over time. Because of the enhanced water solubility of HG **2**, we were hopeful that stoichiometric KCl (0.25 eq) might trigger the gelation of water by templating the formation of a G_4-quadruplex assembly. This was, indeed, the case. **Figure 3.6A** shows a series of inverted vials containing day-old hydrogels, each made with 2 wt% (68 mM) of HG **2** but with different amounts of KCl. The gel on the left, with 0.25 eq of KCl, is transparent, indicating complete dissolution of the gelator HG **2**. The curvature at the gel-air interface indicates that HG **2**•KCl gel made with 0.25 eq of KCl is more pliable than samples containing additional KCl (0.5-2.0 eq). Indeed, as more KCl was added, the HG **2**•KCl hydrogels became noticeably stiffer and hazier, perhaps due to formation of larger, insoluble HG **2**•K^+ assemblies.

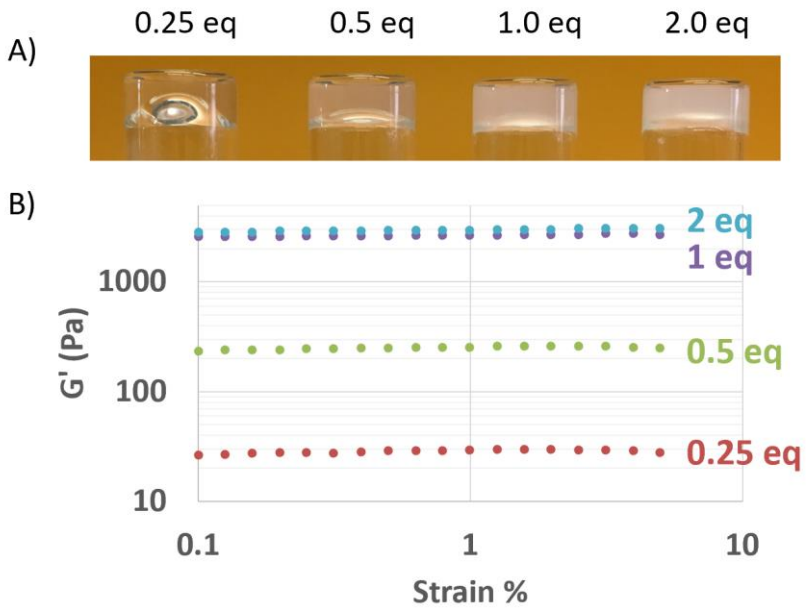

Figure 3.6: Changing KCl concentration influences HG **2** hydrogel properties. (A) Photos of HG **2**•KCl hydrogels (2 wt %, 68 mM) made with different amount of KCl 1 day after gel preparation. (B) Storage modulus (G′) of HG **2**•KCl hydrogels increases with KCl concentration. Strain sweeps of HG **2** hydrogels were taken at a constant angular frequency of 10 rad/s 1 day after gel preparation.

In addition to these qualitative observations from the vial inversion tests we also used rheology to quantify the influence of KCl concentration on the macroscopic properties of the HG **2**•KCl hydrogel. **Figure 3.6B** shows rheology measurements on a series of HG **2**•KCl hydrogels, each 68 mM (2 wt %) in nucleoside but differing in their KCl concentration. After 1 day, the value of the storage (elastic) modulus (G′), which indicates a material's stiffness,[198] varied from ~30 Pa for a sample with 0.25 eq of KCl, to ~3000 Pa for a hydrogel that contained 2.0 eq of KCl. This spectrum of hydrogels with different mechanical properties (G′ storage moduli that vary by over 2 orders of magnitude) indicates that changing KCl salt concentration is an easy and useful method to tune the properties of this G_4-quartet hydrogel. If one desires a flexible

gel, perhaps to facilitate diffusion of compounds in and out of the matrix, simply use stoichiometric KCl. If one needs a tougher material to serve a specific purpose then one can add more KCl salt. In particular, gelation of water by guanosine analogs such as HG **2** using stoichiometric concentrations of KCl would likely be beneficial for biological applications.

3.6 Self-assembly of the cationic HG 2•KCl colloidal suspensions in situ is crucial for anionic dye removal.

Previously, we have demonstrated the use of appropriately modified G_4-quartet hydrogels to remediate either anionic or cationic dyes via non-covalent, electrostatic interactions.[95,99] The slow diffusion of dye molecules into the bulk hydrogel limited, however, the efficiency and kinetics of dye uptake. In this section, we show that insoluble G_4•K^+ assemblies,[181,182] which are colloidal suspensions and "gel-like" in their physical appearance, can be formed *in situ* by adding KCl to a saturated aqueous solution of HG **2**. This new phase for HG **2**, templated by the added KCl, can be used to bind and selectively precipitate anionic dyes (in the presence of cationic dyes). This technique, which relies on formation of a colloidal suspension of G_4•K^+ assemblies from HG **2**, represents a promising method for the easy and rapid remediation of water contaminated with anionic dyes. [200–202] To test the ability of soluble HG **2** to form self-assembled aggregates in the presence of K^+, we first prepared a saturated solution of HG **2** (14.5 mM) at rt, after which aliquots of a KCl stock solution were added and the resulting solution was then well mixed. Instead of forming a continuous and self-standing hydrogel, a suspension of milky-white particles appeared immediately after

addition of the KCl (**Figure 6.5**). As a control, a saturated solution of poorly soluble G **1** (2.1 mM) showed no sign of any new phase after addition of the same concentration of KCl (**Figure 6.5**). Subsequent ultracentrifugation enabled separation of this new insoluble material formed by addition of KCl to the saturated solution of HG **2**. IR spectra of this freeze-dried material showed the characteristic carbonyl shift (1680 cm^{-1}) for a G_4-quartet structure (**Figure 6.6**), identical to that previously observed for the HG **2**•KCl hydrogel. This IR analysis confirms that this new phase arose from G_4-quartet self-assembly,[31] triggered by addition of KCl to the saturated solution of HG **2**.

Importantly, we also found that the concentration of added KCl could be used to control the amount of the new G_4-quartet colloidal suspension formed *in situ*. As shown in **Figure 6.7**, increasing concentrations of KCl were added to vials containing saturated solutions of HG **2** (14.5 mM), incubated for 1 h at rt and then subjected to ultracentrifugation to separate out the insoluble G_4•K^+ assemblies. **Figure 6.7A** shows that whiter, "gel-like" material accumulates at the bottom of the vials with increasing amounts of added KCl. The concentration of HG **2** remaining in the supernatant 1 hour after addition of KCl was quantified by UV spectroscopy, again by monitoring the guanine absorption at λ=254 nm. The data in **Figure 6.7B** confirm that increasing concentrations of KCl lead to a significant decrease in the amount of HG **2** remaining in solution, as more insoluble G_4•K^+ assemblies are formed by self-assembly of HG **2** and the higher concentrations of KCl. This rapid and facile generation of insoluble G_4•K^+ assemblies at ambient temperature allows one to create a new phase that is easily separated from the aqueous phase. The central role of KCl in this self-assembly process is critical since it triggers the shift of equilibrium from the "monomeric" HG **2** form

toward larger G_4•KCl assemblies, creating a new phase that can then be used as a separation media.

As a first step toward using this *in situ* formation of insoluble G_4•K^+ material for environmental remediation, we confirmed the electrostatic nature of dye binding by the HG **2**•K^+ hydrogel itself. Thus, we found that this cationic hydrogel, with its central K^+ channel and its partially protonated 5′-hydrazino groups (pK_a of R-$^+NH_2NH_2$ is 7.9)[189], could maintain strong affinity for an anionic dye, as opposed to a cationic dye. We prepared 2 different solid cubes of the HG **2**•K^+ hydrogel (68 mM, 2 wt %, 2 eq KCl), with one sample containing the cationic dye crystal violet (CV), and the other sample of HG **2**•K^+ containing the anionic dye, naphthol blue black (NBB), a major pollutant generated by the textile industry (**Figure 3.7A**).[203] The two hydrogel samples were then added to a 5 mL solution of 155 mM KCl solution. As shown in **Figure 6.8**, the 2 gels had much different properties in terms of their ability to retain the 2 different dyes. Thus, the cationic CV dye diffused out of the HG **2**•K^+ hydrogel immediately to give a dark purple solution. In marked contrast, the anionic NBB dye remained bound within the HG **2**•K^+ hydrogel, showing no visible leakage under these same conditions, even after days. This experiment, which highlights the ability of the cationic HG **2**•K^+ hydrogel to selectively bind anionic vs. cationic dyes using non-covalent electrostatic interactions, bodes well for our aim to develop a method to selectively extract anionic dyes from solution using K^+-templated self-assembly of HG **2**.

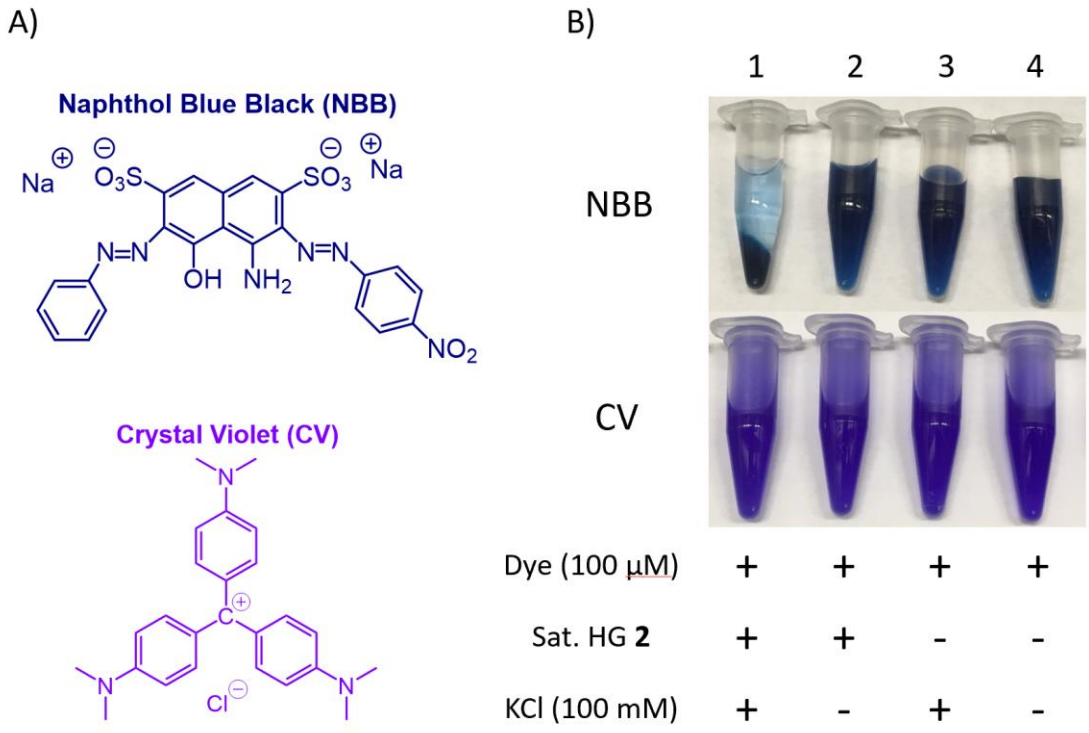

Figure 3.7: A) The structures of two dyes used. B) Self-assembly is crucial for anionic dye remediation: Addition of both saturated HG **2** and KCl followed by ultracentrifugation promotes self-assemblies of G_4 KCl that preferentially binds anionic NBB not cationic CV (all vials contain 1 mL solution with 100 μM dye).

We next studied the charge preference of the aforementioned G_4-quartet assemblies, made by adding KCl to a saturated solution of HG **2**, to selectively remediate anionic dyes from water. Each of the vials shown in **Figure 3.7B** contained equal concentrations of NBB or CV dyes (100 μM). Vial 1 contained both of the components needed for self-assembly of G_4-quartets, namely saturated HG **2** (14.5 mM) and KCl (100 mM). Vial 2 contained saturated HG **2** but no templating KCl. Vial 3 (dye and 100 mM KCl) and vial 4 (dye only) served as blank controls. After sufficient mixing and allowing to stand at rt for 1 hour, the samples were spun down by ultracentrifugation. While the solutions in vials 2, 3 and 4 remained blue (**Figure 3.7B**

top picture), and showed no visible precipitate (indicating no electrostatic binding of NBB), vial 1 showed a dark-blue solid phase at the bottom of the vial and the supernatant was much more lightly colored than the other 3 samples. These experiments clearly indicate that the combination of gelator HG **2** and added KCl are able to form a new G_4-quartet-based phase *in situ* that can bind and co-precipitate the anionic contaminant NBB from solution. As a control, to demonstrate the system's electrostatic binding selectivity, we carried out similar experiments with the cationic dye CV (100 μM). In this case, the solutions in all 4 vials remained the same in color after mixing and ultracentrifugation, indicating the preference of the G_4-quartet assemblies to bind anionic dyes (**Figure 3.7B** middle picture).

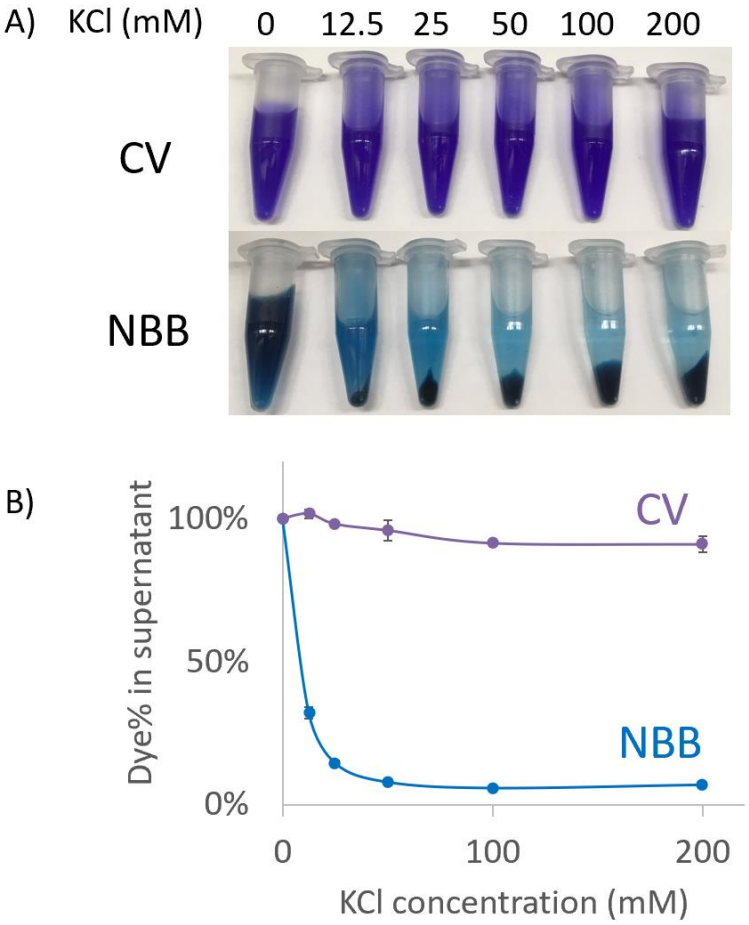

Figure 3.8: Increasing concentration of KCl, when added to saturated solutions of HG **2** (14.5 mM), increase the efficiency of precipitation of anionic dye NBB from solution. A) Qualitatively, addition of more KCl produces more blue colloids seen at the bottom of the vials for the anionic dye NBB, while no obvious change is observed for the cationic CV. All vials contain 1 mL solution with 100 μM dye. B) UV quantification of the amount of cationic CV and anionic NBB dyes remaining in solution as a function of added KCl concentration.

We also studied the influence of KCl concentration on the efficiency of dye removal by self-assembly of HG **2**. We found that increasing the concentration of KCl, presumably by shifting the equilibrium toward formation of $G_4 \bullet K^+$ assemblies, increased the amount of visible precipitate and the efficiency of the anionic NBB absorption. After incubation and ultracentrifugation we used UV-vis spectroscopy to

measure the amount of dyes, either anionic NBB or cationic CV that remained in solution. Interestingly, with only 12.5 mM of KCl added, almost 70% of NBB was removed from solution (**Figure 3.8**). With more KCl added, the amount of NBB in the supernatant decreases exponentially. By contrast, less than 10% of the cationic CV was removed into the solid phase, even with the addition of 200 mM KCl. These experiments in **Figure 3.8** once again demonstrate the selectivity of the HG **2**•KCl assemblies for binding anionic vs. cationic dyes. This strategy for anionic NBB removal utilizes the power of self-assembly, with KCl serving as a trigger, to promote formation of a cationic G_4-quartet based material from HG **2**. The system can potentially be expanded to the remediation of other water-soluble and toxic anions such as fluoroacetate, a potent inhibitor of the citrus acid cycle.[204]

3.7 The nucleophilicity of the HG 2•KCl hydrogel enables remediation of propionaldehyde from both the gas phase and from solution.

Being able to readily generate a stable HG **2**•KCl hydrogel, whose surface is covered with nucleophilic 5′-hydrazino groups, should allow one to use this material to covalently trap aldehydes via hydrazone formation.[80,188–193,205] As a proof of concept we carried out initial uptake experiments with propionaldehyde, a volatile compound used extensively in the manufacture of polyvinyl and other plastics, in the synthesis of rubber chemicals, and as a preservative. Propionaldehyde was one of the 18 organic chemicals detected most frequently in the drinking water of 10 surveyed US cities and its remediation serves as an example of how supramolecular hydrogels like HG **2**•KCl might be used to purify aldehyde-contaminated water.[206]

Based on the well-known chemistry of alkylhydrazines,[192,193] we expected that the HG **2**•KCl hydrogel would react with propionaldehyde to form stable hydrazone adducts (**Figure 3.9**). As described below, we examined the covalent trapping of propionaldehyde by HG **2**•KCl hydrogel in both the gas phase and in aqueous solution. One could imagine formulating this HG **2**•KCl hydrogel into thin films that would filter volatile aldehydes from the air that we breathe. Also, since the self-assembled HG **2**•KCl hydrogels are kinetically stable in solutions containing KCl (since the K^+ helps maintain the integrity of the gel fibers composed of G_4-quartet assemblies) we reasoned that one could covalently capture water-soluble aldehydes by soaking the HG **2**•KCl hydrogel in a salt solution containing these electrophiles.

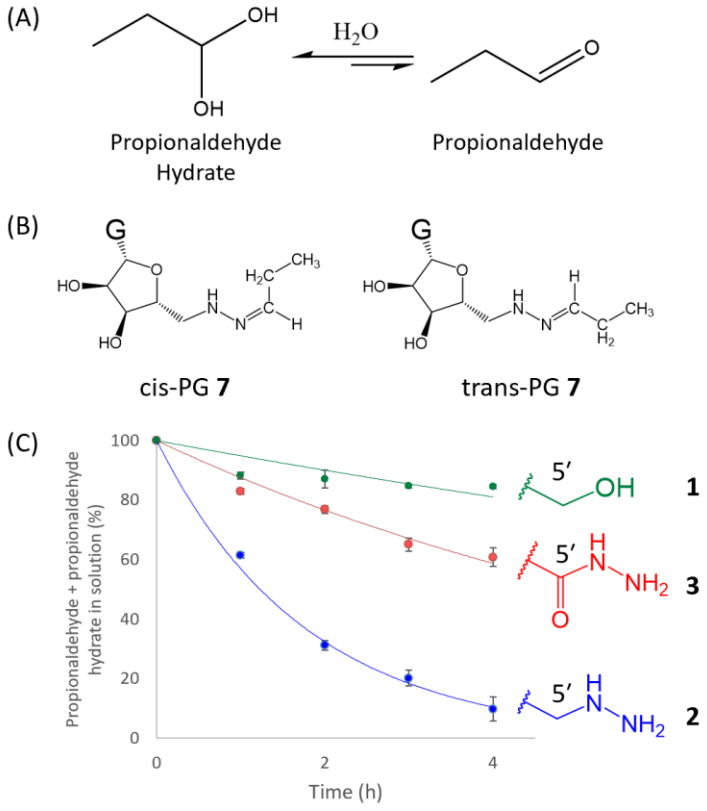

Figure 3.9: The HG **2**•KCl hydrogel can extract propionaldehyde from water (A) When dissolved in water propionaldehyde is in equilibrium with its hydrate. (B) The 5′-

hydrazino HG **2** reacts with propionaldehyde to form a 1:3.55 mixture of hydrazones, cis-PG **7** and trans-PG **7**. (C) The time-course for absorption of propionaldehyde (3.37 mM) from 155 mM KCl using different G_4•K^+ hydrogels (2 wt%, 68 mM). The amount of propionaldehyde and its hydrate in solution decreases after addition of hydrogels, as determined from ^{1}H NMR integration relative to an internal standard.

We first examined the gas phase absorption of propionaldehyde. Thus, we placed an uncapped vial containing a 0.5 mL portion of a 2 wt % HG **2**•KCl hydrogel (68 mM, 0.5 eq KCl) inside a larger vial. Then 1.0 eq of neat propionaldehyde was added to the large vial, after which we capped and tightly sealed the setup (**Figure 6.9**). After allowing the system to incubate for 1 day at rt we lyophilized the sample and analyzed the freeze-dried powder using both ^{1}H and ^{13}C NMR spectroscopy. NMR analysis of the freeze-dried powder dissolved in DMSO-d_6 indicated that 2 new hydrazone compounds had been formed in > 95% yield from reaction of propionaldehyde and the HG **2**•KCl hydrogel. Both ^{1}H-^{1}H COSY and ^{1}H-^{13}C HSQC NMR analysis of the reaction products showed 2 separate sets of peaks, consistent with formation of the cis- and trans-hydrazones, cis-PG **7** and trans-PG **7** (see **Figure 3.9B** & **Figures 6.10 & 6.11**). The hydrazone diastereomers were assigned unambiguously from 1D NOE data (**Figure 6.12**) and the cis:trans ratio was determined to be 1:3.55, indicating a preference for the more stable trans isomer, trans-PG **7**. Electrospray ionization mass spectrometry of the lyophilized powder showed a single intense peak with m/z=338.12, again consistent with hydrazone formation from HG **2** and propionaldehyde to give cis/trans-PG **7** (**Figure 6.13**). These experiments demonstrate that a HG **2**•KCl hydrogel can be used to efficiently react with propionaldehyde in the gas phase so as to remove that volatile compound from the air. We are currently probing the use of thin

films of the HG **2**•KCl hydrogel to react with a range of volatile aldehydes for their environmental remediation.

Having established that reaction occurs at rt between HG **2** and propionaldehyde in the gas phase, we next tested the ability of the HG **2**•KCl hydrogel (2 wt %, 68 mM, 2 equiv KCl) to absorb this same aldehyde from aqueous solution. We also prepared the G_4-quartet hydrogel made from G **1** and $KB(OH)_4$ (2 wt %, 0.5 eq $KB(OH)_4$)[78] and the hydrazideG **3**•KCl hydrogel (2 wt %, 2 eq KCl) made from the hydrazideG **3**[97] so that we could compare their uptake of propionaldehyde with that of the HG **2**•KCl hydrogel (**Figure 3.9C**). The various hydrogels (2 wt %, 68 mM, 1 equiv K^+) were each prepared using D_2O, allowed to cool in the mold for 1 h at rt and were placed into a 155 mM KCl solution of D_2O containing propionaldehyde (3.37 mM). The kinetics of propionaldehyde uptake from solution by the G_4-quartet based hydrogels was monitored over time by removing aliquots of the supernatant and analyzing them by ^{1}H NMR spectroscopy (**Figure 3.9C**). At rt, propionaldehyde exists as a equilibrium mixture of the aldehyde and its hydrate. Signals for both the -CH_2- group of the aldehyde (2.57 ppm) and the -CH_2- group of the hydrate (1.60 ppm) decreased significantly when the solution of propionaldehyde was soaked in the presence of the HG **2**•KCl hydrogel. As shown in **Figure 3.9C**, the HG **2**•KCl hydrogel was the best of the 3 G_4-quartet based gels at reacting with propionaldehyde. Thus, after 4 h, the G **1**•$KB(OH)_4$ hydrogel showed minimal absorption (< 10%) of propionaldehyde whereas the hydrazideG **3**•KCl hydrogel containing the 5′-hydrazide (which Lehn and colleagues have shown reacts with a range of aldehydes)[80,97,188,205] demonstrated moderate uptake (~ 40%) of this aldehyde from solution after 4 h. The HG 2•KCl

hydrogel, with its 5′-hydrazine, was the most effective in reaction with propionaldehyde, as ^{1}H NMR integration after 4 h showed that > 90 % of the compound had been removed from the supernatant that bathed the HG **2**•KCl hydrogel.

3.8 Conclusions

We have determined that by simply substituting the 5′-OH in G **1** for a 5′-$NHNH_2$ group gives a LMWG, HG **2**, whose water solubility is enhanced 7-fold and that gives a self-standing and stable G_4•KCl hydrogel even with stoichiometric concentrations of KCl (0.25 eq). The role of KCl to promote G_4•KCl self-assembly is further highlighted in dye remediation experiments, where the addition of KCl to a saturated solution of HG **2** solution creates cationic colloidal assemblies that can electrostatically bind to the anionic dye, NBB, and extract it from water. We have also demonstrated that the HG **2**•KCl hydrogel can be used as a "water-in-water" material to absorb dissolved propionaldehyde from both the gas and solution phases and sequester it in the gel's insoluble matrix. The ability of the supramolecular HG **2**•KCl hydrogel to remediate different classes of aldehydes could well be beneficial for broader environmental applications and purification of aldehyde-contaminated water. As discussed in more detail in the following chapter, we are currently conducting such studies, with an eye toward environmental remediation.

Chapter 4: A G_4•K^+ hydrogel made from 5′-hydrazinoguanosine for remediation of α,β-unsaturated carbonyls

The majority of this chapter has been published in reference [6]*:*

Xiao, S.; Davis, J. T. A G_4•K^+ hydrogel made from 5′-hydrazinoguanosine for remediation of α,β-unsaturated carbonyls. *Chem. Commun.* **2018**, *54* (80), 11300–11303.

4.1 Summary

A G_4•K^+ hydrogel made from 5′-hydrazinoguanosine **2** and KCl reacts with α,β-unsaturated carbonyls of different electrophilicities (acrolein, methyl vinyl ketone and methyl acrylate) in water and the gas phase to form cyclic adducts. This aza-Michael addition/cyclization domino reaction by the 5′-hydrazino G_4•K^+ hydrogel has promise for environmental remediation of toxic α,β-unsaturated carbonyls from water and the atmosphere.

4.2 Introduction

Supramolecular hydrogels are made from low-molecular-weight compounds and held together by non-covalent bonds.[13,207] One application of supramolecular hydrogels is environmental remediation of ions, dyes and pollutants.[171,208,209] Using an "off-the-shelf" or "easy-to-make" compound to prepare self-assembled gels that can remove contaminants has potential for water purification. DNA hydrogels can bind metal ions and dyes, but the cost of DNA synthesis makes such hydrogels prohibitive for large-scale.[210] One solution is to use hydrogels made from nucleosides or nucleotides.[1,211] Such materials retain many of DNA's molecular recognition properties while being

easier and cheaper to make. We have used hydrogels made from guanosine (G **1**) to absorb dyes and aldehydes from water.[5,99]

A century after their discovery,[3] G gels are undergoing a resurgence due to their ease of preparation, biocompatibility and applications.[4,184–186,212,213] The basis for most G gels is the G_4-quartet, a macrocycle templated by K^+.[2] The G_4-quartets stack to form entangled nanowires that give a matrix that immobilizes water. As shown in **Figure 4.1**, we describe a G_4•K^+ hydrogel that contains bisnucleophilic 5′-hydrazines (G **2**) for covalent capture and remediation of α,β-unsaturated carbonyls (α,β-UCs).

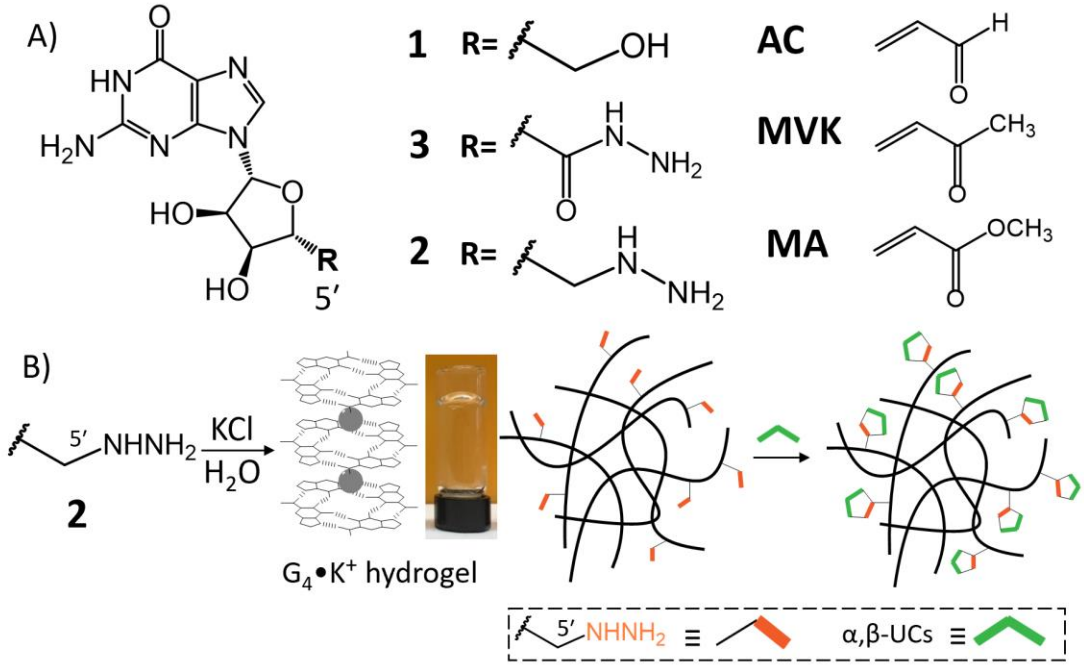

Figure 4.1: A) Nucleosides **1-3** used to make G_4•K^+ hydrogels and α,β-UCs (acrolein-**AC**, methyl vinyl ketone-**MVK** and methyl acrylate-**MA**) targeted for remediation. B) A G_4•K^+ hydrogel made from hydrazine **2** reacts with α,β-UCs to give cyclic adducts, enabling removal of these toxins from water and atmosphere.

Electrophilic α,β-UCs, pervasive due to both natural and industrial processes, pose a threat to our health and environment. Acrolein (AC), methyl vinyl ketone (MVK) and

methyl acrylate (MA), all important commodity chemicals, are also cytotoxic. These α,β-UCs with two reactive ends, a Michael acceptor and carbonyl, are potent electrophiles that trap nucleophiles in proteins and nucleic acids, thus damaging living organisms.[206] Although resins containing alkylhydrazines have been used for solid-phase synthesis of hydrazones and scavenging of aromatic aldehydes,[214–216] and resins with the less nucleophilic sulfonylhydrazides have been developed for scavenging AC,[217] there have not been, to our knowledge, reports of soft materials that can react with and absorb α,β-UCs from solution or the atmosphere. One could imagine formulating a gel into thin films that would filter volatile α,β-UCs from the air that we breath or make flexible membranes to remove α,β-UCs from the water that we drink.

Our initial design involved synthesizing a G_4•K^+ hydrogel from a G analog **2** with a bisnucleophilic hydrazine at its 5′-position. The hydrazine group, known for effective conjugation of aldehydes and ketones near neutral pH,[193,218] should "cap" both ends of α,β-UCs inside the gel matrix to give cycloadducts (**Figure 4.1 and 4.2**),[219] resulting in extraction of these volatile α,β-UCs from water or air. While alkylhydrazine polymers are known, they are typically used to couple with aldehyde-containing polymers to generate hydrogels with hydrazone cross-links.[220–222] To our knowledge, there have been no reported hydrogels, either supramolecular or polymeric, that contain nucleophilic alkylhydrazines. This is also the first report of a hydrogel designed to target α,β-UCs. We chose a supramolecular G_4-quartet hydrogel for covalent capture of α,β-UCs because: 1) we have experience with G_4-quartet gels;[1,5,99]2) synthesis of gelator **2** from G **1** is easy;[123] 3) the gel is stimuli-responsive, and its stability and mechanical properties can be modulated by K^+ concentration, temperature and pH;[5] 4)

the gel can be disassembled after covalent modification by α,β-UCs, enabling characterization of products **8-10** and 5) G_4-quartet gels are often biocompatible,[1] which may enable use of this hydrazine gel for remediation of α,β-UCs in damaged tissue.[223–226] While we chose the G_4-quartet gel to showcase remediation of α,β-UCs, alkylhydrazines can be made from 1° alcohols, so this approach should be useful with other gels, be they supramolecular, polymeric or double-network materials.

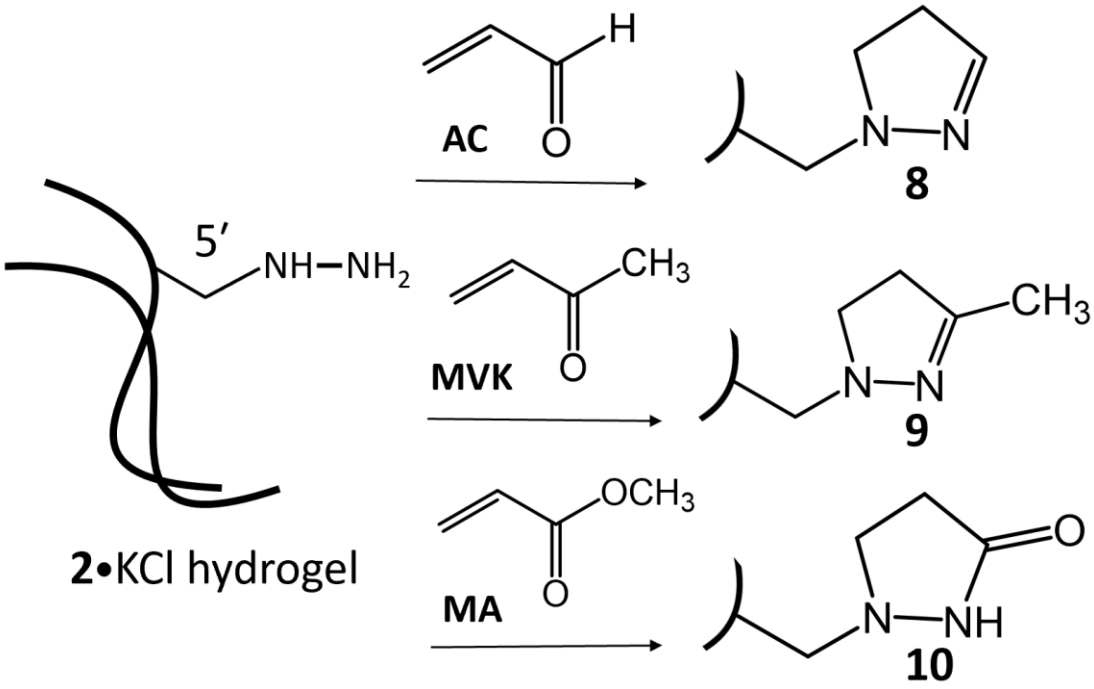

Figure 4.2: Bisnucleophilic hydrazine **2**, in the G_4•K^+ hydrogel, traps α,β-UCs of varying electrophilicity to form cyclic adducts **8**-**10**.

Sreenivasachary and Lehn published seminal studies on the gelator 5′-hydrazidoguanosine (**3**), which forms G_4•K^+ hydrogels that react with aromatic aldehydes to give acylhydrazones.[97,205] Intrigued by the potential to use such hydrogels containing nucleophilic sidechains to scavenge toxic aldehydes we developed a related

G_4•KCl hydrogel with a more basic and nucleophilic sidechain than the hydrazide in **3**. As described in the previous chapter, we recently used G_4•K^+ hydrogels containing 5′-deoxy-5′-hydrazinoguanosine **2**[123] to react with and remove propionaldehyde from water.[5] Since both nitrogen atoms in the $–NHNH_2$ hydrazine are nucleophilic, we reasoned that a hydrogel made from **2** would be ideal for remediation of α,β-UCs, since tandem aza-Michael addition and cyclization with AC/MVK should form pyrazolines (**Figure 4.2**).[219] We also expected that tandem aza-Michael addition/transacylation between a gel containing hydrazine **2** and the α,β-unsaturated ester MA would work, since tandem aza-Michael addition/cyclization proceeds in reaction of methyl hydrazine and ethyl acrylate.[227,228] We show that the G_4•KCl hydrogel made from hydrazine **2** covalently traps AC, MVK, and the less reactive MA, removing all 3 α,β-UCs from the gas phase and from water solution.

4.3 Remediation of toxic acrolein (AC) from the gas and aqueous phase using hydrazine 2•KCl hydrogel

4.3.1 Experimental setup for gas phase absorption of acrolein and analysis of the product

We have shown that hydrazine **2** and KCl form robust G_4•K^+ hydrogels that are stable when suspended in KCl solution.[5] We expected that this G_4•KCl hydrogel made from hydrazine **2** would covalently trap AC, a toxin found in wood smoke, tobacco smoke, generated during cooking, and released into the environment during chemical manufacturing.[206,224,229] AC, which forms mutagenic DNA adducts and cross-links proteins,[230,231] has been implicated in cancer, atherosclerosis, Alzheimer's and

alcoholic liver disease.[224,229,232,233] We first tested the ability of the **2**•KCl hydrogel to absorb the volatile AC from the gas phase. We placed an uncapped vial, containing the hydrogel (made from 0.5 mL of water and containing 68 mM of **2** and 34 mM of KCl) inside a larger vial, added 1.0 eq of AC per monomer of **2** to the outer vial and sealed the set-up (**Figure 6.14**). After 2 days at RT we lyophilized the gel, dissolved the resulting powder in DMSO-d_6 and analyzed it by NMR and electrospray ionization mass spectrometry (ESI-MS).

4.3.2 1D ^{1}H and ^{13}C NMR and mass spectrometry show the formation of 5′-pyrazolineguanosine 8

The ^{1}H NMR spectrum of the xerogel indicated formation of pyrazoline **8 (Figure 4.3)**. NMR signals corresponding to hydrazine **2** were gone. The triplet at δ= 6.81 (red dot) is characteristic of a hydrazone CH coupled to adjacent CH_2 protons (inset).[234] The ^{13}C NMR spectrum had 13 peaks, as expected for **8** (**Figure 4.4**).

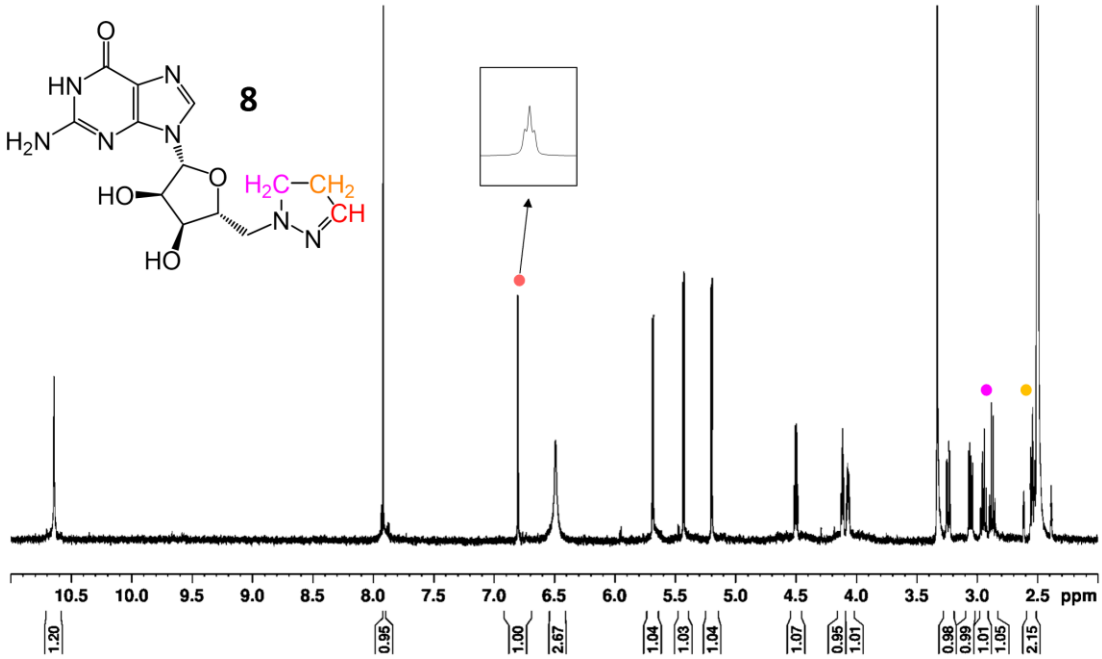

Figure 4.3: ^{1}H NMR spectrum of pyrazoline **8** formed from **2**•KCl hydrogel and 1.0 eq of acrolein in gas phase set-up.

ESI-MS of the reaction product showed a major peak for **8**•H^{+} at m/z=335.98 (**Figure 4.5**).

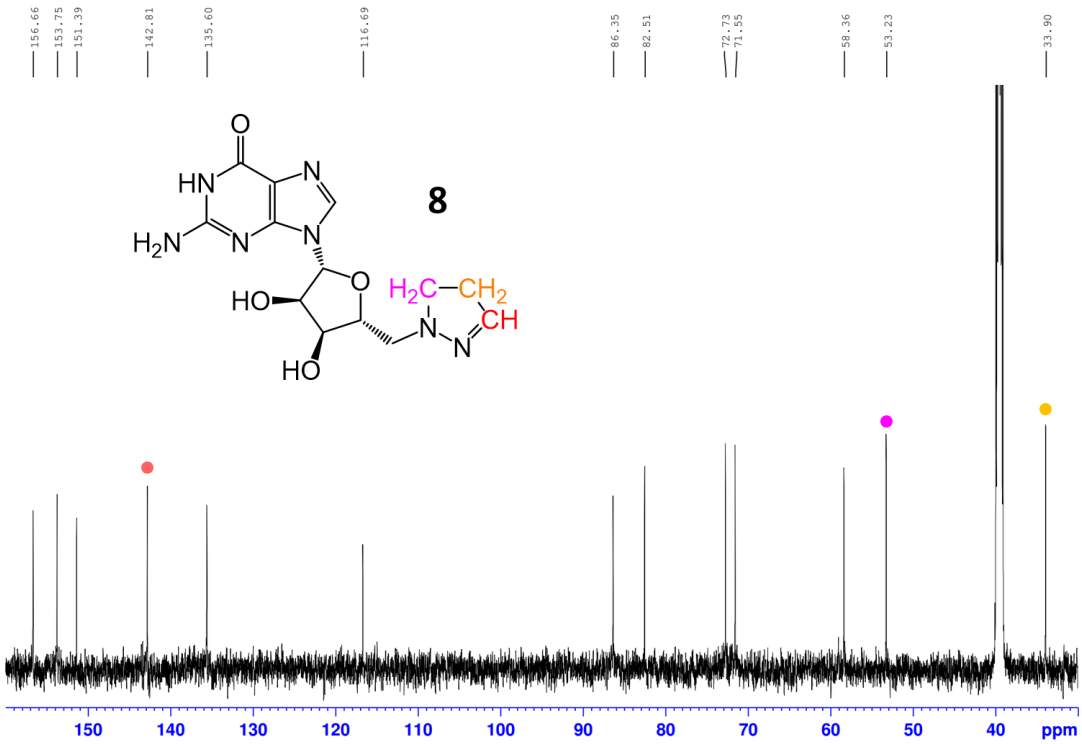

Figure 4.4: The ^{13}C NMR spectrum for pyrazoline **8** shows 13 peaks, consistent with the formation of an adduct between 5′-hydrazinoguanosine **2** and acrolein.

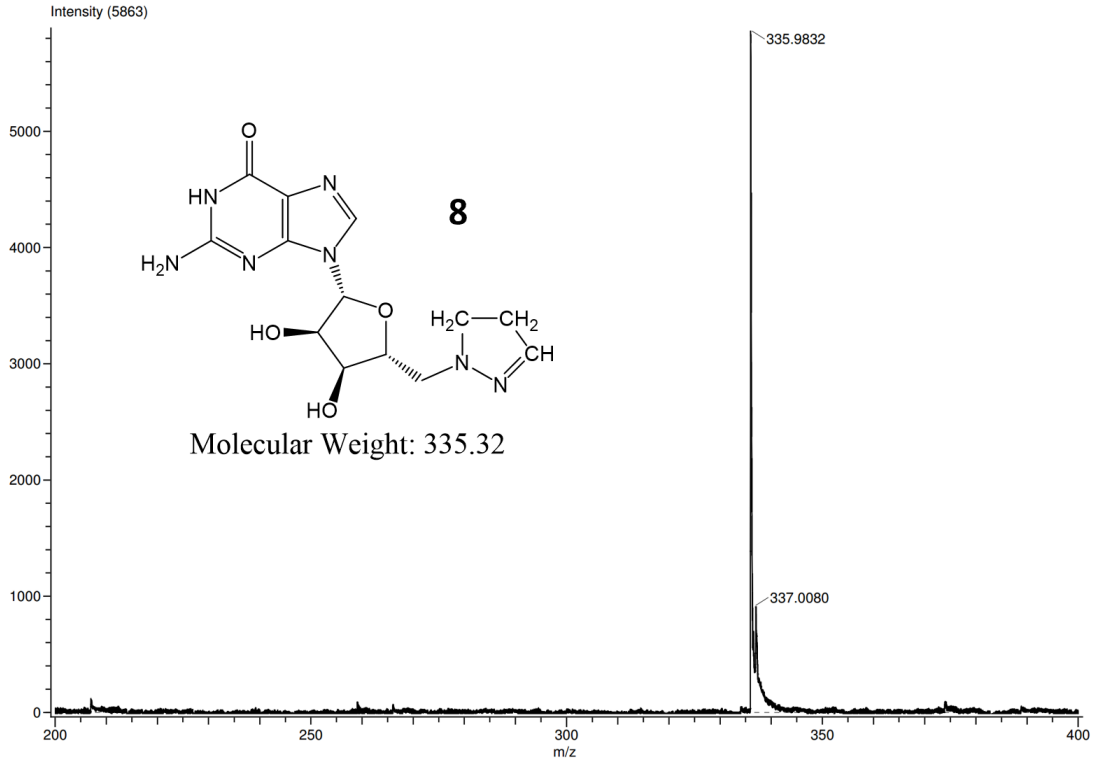

Figure 4.5: ESI-MS of pyrazoline **8**. No peak corresponding to the precursor hydrazine **2** (mw =297.28) was detected.

4.3.3 2D NMR confirms the peak assignment of 5′-pyrazolineguanosine 8

A ^{1}H-^{13}C HSQC spectrum showed 3 CH_2 groups, one for G 5′-CH_2 and the other 2 signals (δ= 2.51 and δ= 2.90) arising from the pyrazoline (**Figure 4.6**).

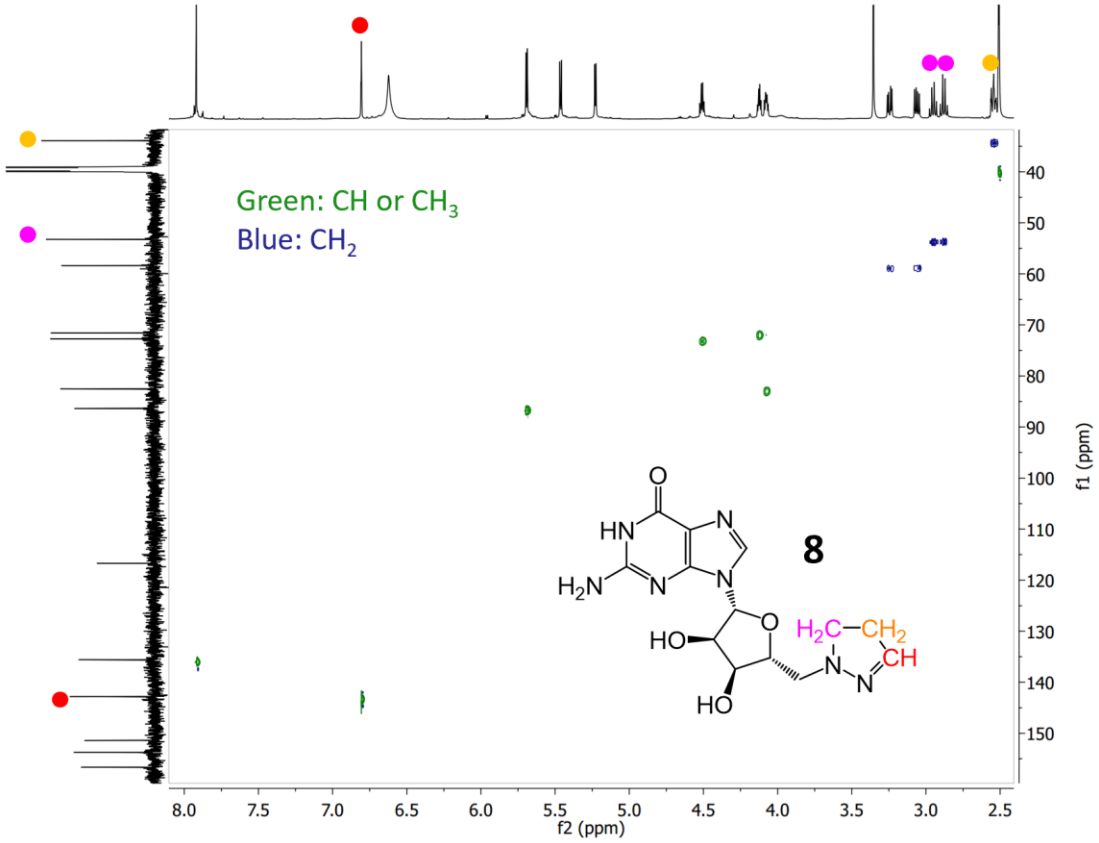

Figure 4.6: ^{1}H-^{13}C HSQC spectrum of **8**. NMR signals for the CH_2 and CH groups in the 5′-pyrazoline ring are indicated by colored dots (pink, orange and red).

In the ^{1}H-^{1}H COSY spectrum, the CH_2 signals at δ= 2.51 correlated with the triplet at δ= 6.81 (red) and multiplet at δ= 2.90 (pink), confirming CH_2-CH_2-CH connectivity in **8** (**Figure 4.7**). Combining this data with the HSQC spectrum in **Figure 4.6**, a CH_2-CH_2-CH linkage can be identified in pyrazoline **8**.

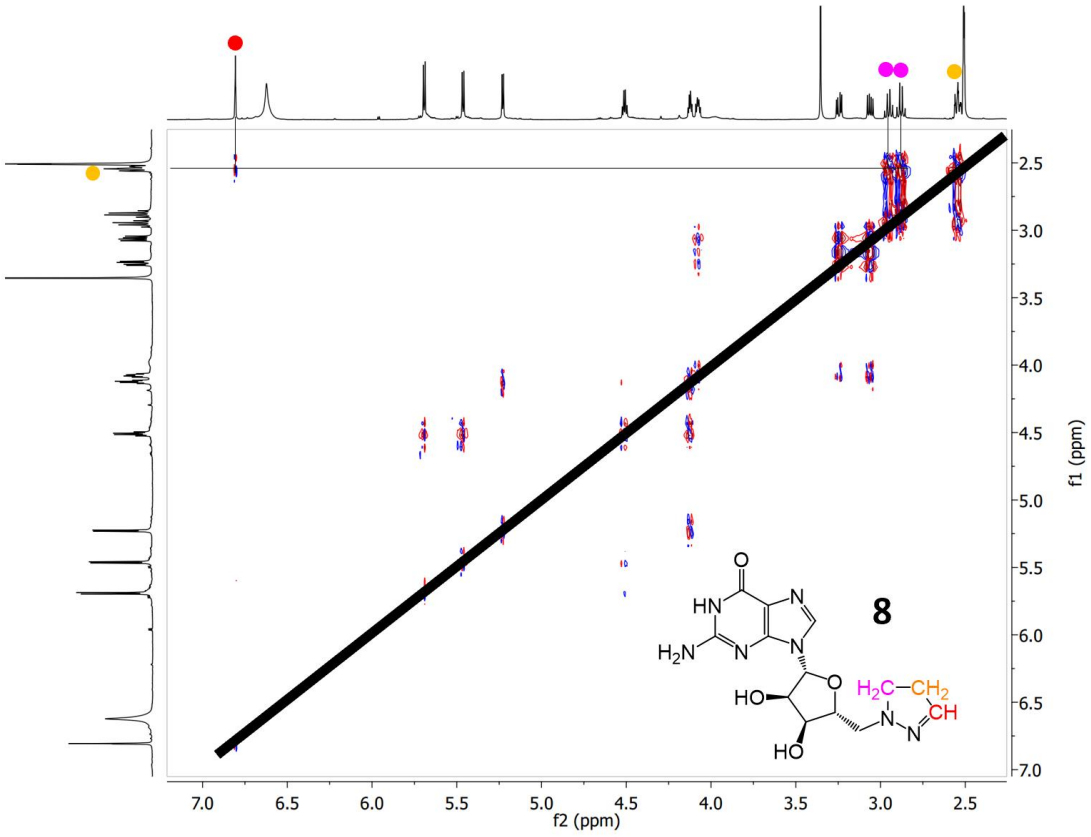

Figure 4.7: ^{1}H-^{1}H COSY spectrum of **8**. The signal for the CH_2 group at δ 2.51 ppm (orange dot) has correlation peaks with both the triplet at δ 6.81 ppm (red dot) and the multiplet CH_2 at δ 2.90 ppm (pink dot).

We found no evidence that the nucleobase of **2** reacted with AC,[128] indicating that the 5′-hydrazine is a better nucleophile than guanine. This data shows that AC is taken up from the air into the hydrogel via formation of covalent adduct **8**, with an absorption capacity of 1.0 eq of AC per eq of hydrazine **2**. For the G_4•KCl hydrogel made with the less nucleophilic hydrazide **3**, we performed similar gas phase uptake of AC. NMR and ESI-MS showed formation of acyclic acylhydrazones **12** (as *cis*/*trans* isomers) and a trace of cyclic adduct **13** (**Figure 6.15-6.18**).

4.3.4 ^{1}H NMR quantification shows fastest absorption of acrolein with hydrazinoguanosine 2 hydrogel

Having characterized the reaction between the 5′-hydrazinoguanosine **2** hydrogel and AC absorbed from the gas phase, we next confirmed that this G_4•K^+ hydrogel could also remove AC from aqueous solution. For comparison, G_4-quartet hydrogels made from the parent G **1** and $KB(OH)_4$,[78] and from hydrazide G **3** and KCl,[97,205] were also evaluated for their relative ability to scavenge AC from solution. The hydrogels (2 wt %, 68 mM, 2 eq KCl in 0.5 mL of D_2O) were made with D_2O and then placed into 5 mL of a 155 mM KCl solution (pD 6.3) in D_2O containing AC (3.37 mM). Absorption of AC by the hydrogels over time was quantified by ^{1}H NMR analysis (**Figure 4.8**). After 4 h, the G_4-quartet gel made from hydrazide **3** showed moderate absorption of AC (53 %). Importantly, the G_4•K^+ hydrogel made from 5′-hydrazine **2** showed complete absorption (> 99%) of AC after 4 h.

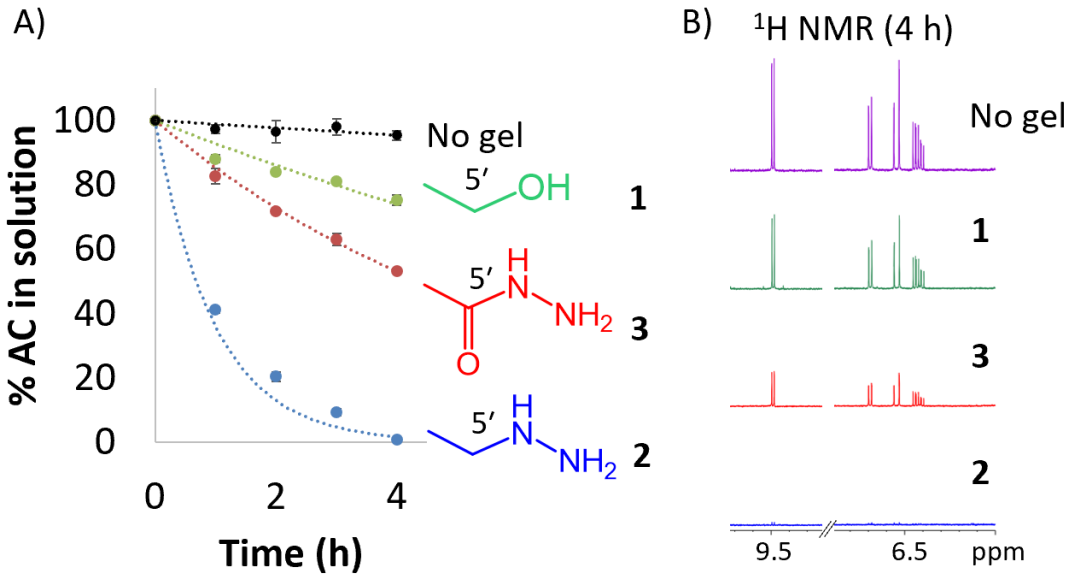

Figure 4.8: A) % **AC** (3.37 mM) remaining in a 5 mL solution of 155 mM KCl in D_2O, pD 6.3 after addition of hydrogels (0.5 mL, 2 wt % gelator and 136 mM KCl) made from **1-3**. B) ^{1}H NMR of the acrolein region shows the most acrolein absorption with HG **2** KCl hydrogel at 4 h.

4.3.5 ^{1}H NMR of lyophilized hydrogel after absorption shows that acrolein in the solution is taken up into the hydrazine 2•KCl hydrogel

^{1}H NMR of the lyophilized **2**•KCl hydrogel after 4 h of reaction with AC showed separate sets of signals for hydrazine **2** and pyrazoline **8** (in an approximate 1:1 ratio), indicating covalent attachment of AC to hydrazine sidechains in this reactive G_4•K^+ hydrogel (**Figure 4.9**).

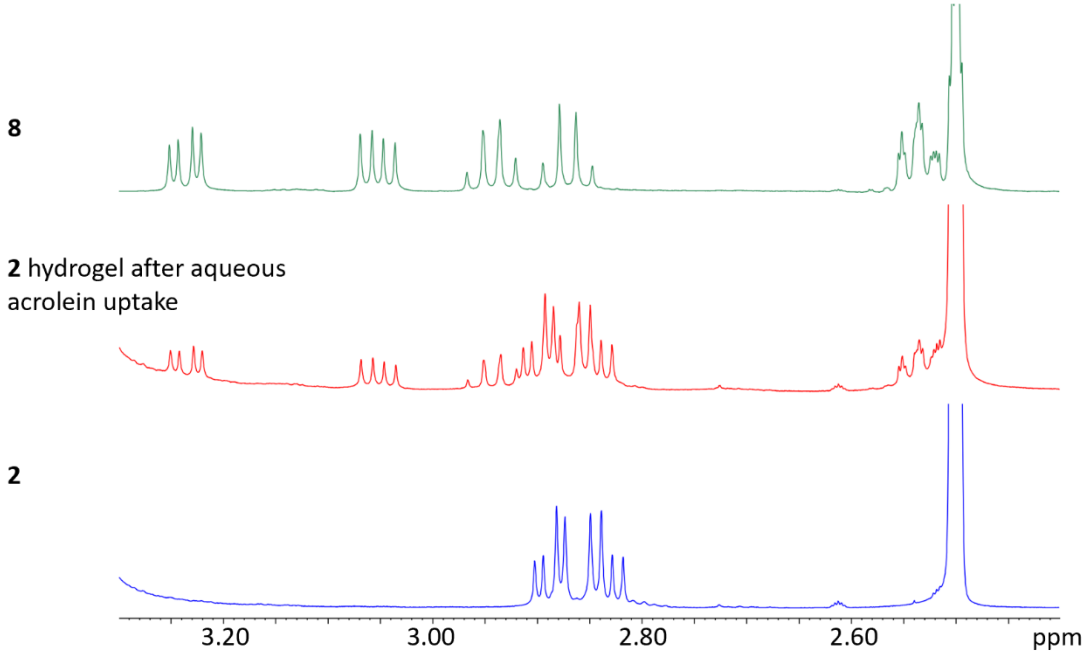

Figure 4.9: Acrolein reacts with the G_4•K^+ hydrogel containing hydrazine **2** (2 wt%, 68 mM, 2 eq KCl) in aqueous solution by forming the cyclic pyrazoline **8**. ^{1}H NMR of the lyophilized gel (middle) shows peaks for both pyrazoline **8** (top) and unreacted hydrazine **2** (bottom). This experiment shows that AC is taken up from the solution into the hydrogels.

4.3.6 Utilizing hydrazine 2 KCl self-assembly for potential cleanup of acrolein in water

Figure 4.10 illustrates how K^+ templated gelation by **2** might be used to effect cleanup of water contaminated by AC. In this experiment, we added hydrazine **2** (68 mM) to a 2 mM solution of AC in 0.5 mL of D_2O to obtain a suspension that was then heated to 75 ^oC to give a clear solution. We then added 2 eq of KCl (136 mM) and let the solution cool to RT. Within 5 min the solution turned into a self-standing hydrogel. Importantly, ^1H NMR of this gel showed that all the signals for AC had disappeared, indicating that this α,β-UC had reacted with the 5′-hydrazinoguanosine **2** in the gel matrix. Overall, the data show that G_4•K^+ hydrogels made from hydrazide **3** and, particularly hydrazine **2**, are excellent scavengers for removing the α,β-unsaturated aldehyde AC from water.

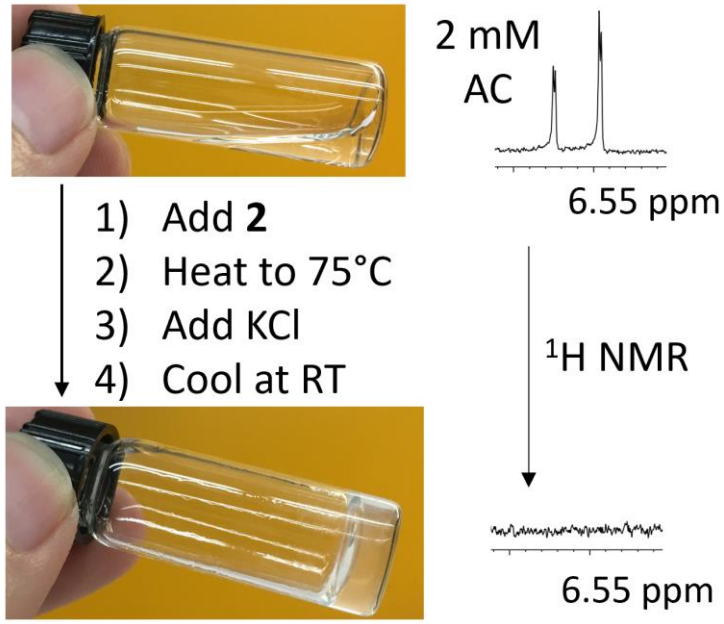

Figure 4.10: Gelation of a 2 mM solution of **AC** in D_2O by adding hydrazine **2** (68 mM) and KCl (136 mM). NMR shows **AC**'s olefinic region before and after hydrogelation.

4.4 Toxic methyl vinyl ketone (MVK) remediation from the gas and aqueous phase using hydrazine 2•KCl hydrogel

4.4.1 MVK remediation via 5-member ring adduct formation utilizing hydrazine 2 hydrogel

We next determined whether $G_4•K^+$ hydrogels made from hydrazide **3** and hydrazine **3** could scavenge MVK, an α,β-UC enone less electrophilic than aldehyde AC.[235] MVK, a valuable commodity chemical, is also a potent DNA alkylating agent, powerful lachrymator and neurotoxin.[229] The cyclization reaction between hydrazine **2** and MVK is shown in **Figure 4.11**.

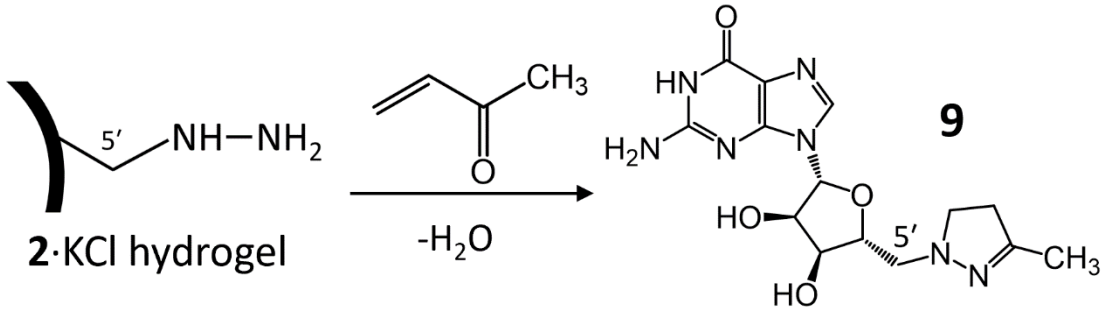

Figure 4.11: Methylpyrazoline **9** from Michael addition/cyclization of **MVK** with hydrazine **2** $G_4•K^+$ hydrogel.

4.4.2 1D ^{1}H and ^{13}C NMR and mass spectrometry show the formation of 5′-methylpyrazolineguanosine 9

The ^{1}H NMR spectrum of the xerogel indicated formation of methylpyrazoline **9** **(Figure 4.12)**. NMR signals corresponding to hydrazine **2** were gone. The singlet at δ= 1.86 ppm (green dot) is characteristic of methylpyrazoline **9** methyl protons.

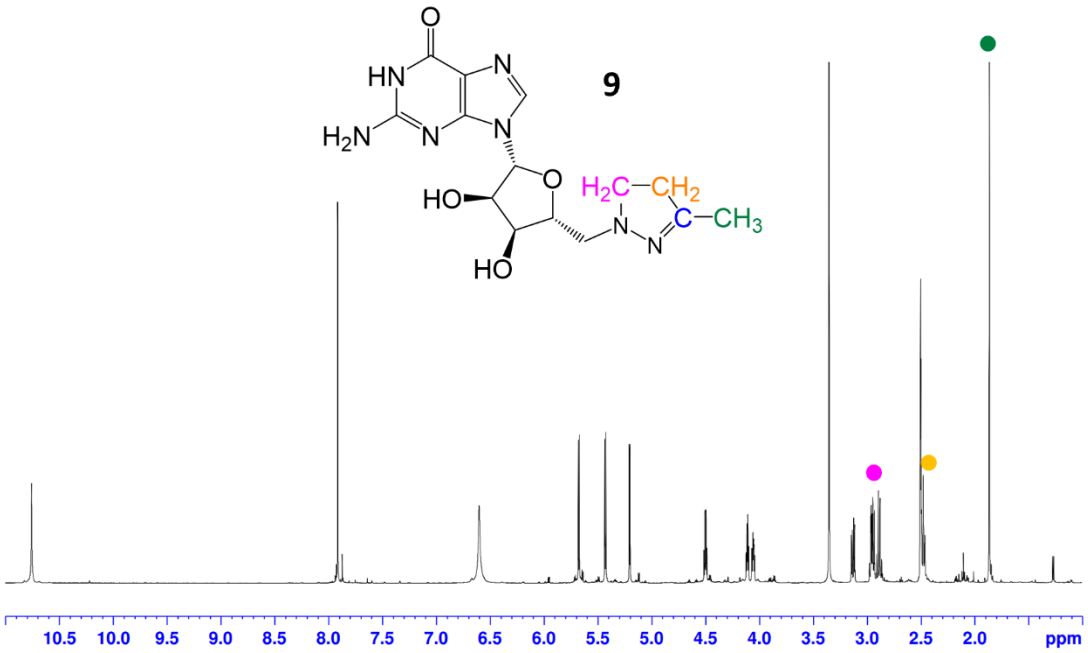

Figure 4.12: ^{1}H NMR spectrum of methylpyrazoline **9**.

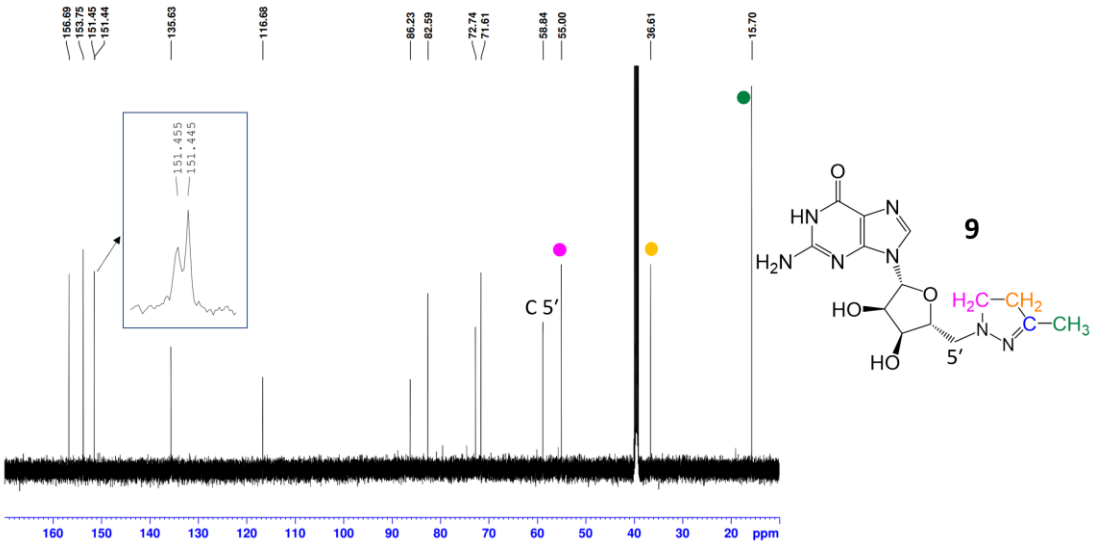

Figure 4.13: ^{13}C NMR spectrum of methylpyrazoline **9.**

The ^{13}C NMR spectrum for methylpyrazoline **9** shows 14 peaks, consistent with the formation of an adduct between 5′-hydrazinoguanosine **2** and MVK (**Figure 4.13**). Inset shows two overlapping peaks at δ 151.45.

2D NMR spectra also confirms the peak assignments (**Figure 6.19-6.20**).

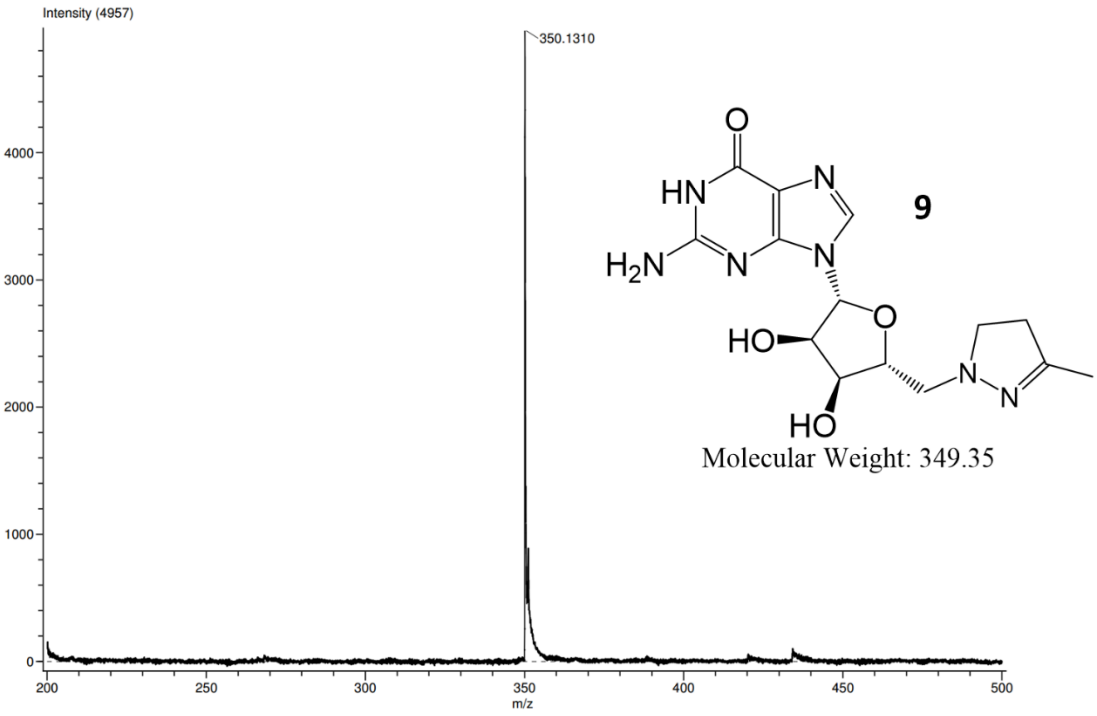

Figure 4.14: ESI-MS spectrum of methylpyrazoline **9**.

ESI-MS analysis of the xerogel after reaction showed 1:1 adduct formation between **2** and MVK to give methylpyrazoline **9** in quantitative yield and no peak corresponding to hydrazine **2** (MW=297.28) was detected (**Figure 4.14**). These spectroscopic data confirm the formation of **9** in the gas phase absorption.

4.4.3 ^{1}H NMR quantification shows fastest absorption of MVK with hydrazinoguanosine 2 hydrogel

Absorption experiments from aqueous solution (155 mM KCl) showed that reaction of MVK was significantly faster with the hydrogel made from hydrazine **2** as compared to the gel containing hydrazide **3** (**Figure 4.15**). Absorption of MVK from water by gels made from hydrazine **2** and hydrazide **3** was confirmed by ESI-MS analysis (**Figure 6.21-6.22**). The comparative data in **Figure 4.15** shows that the G_4-quartet hydrogel made from hydrazine **2** (2 wt %, 68 mM) and KCl (136 mM) is an excellent material for remediation of the neurotoxic MVK, scavenging over 90 % of a 3.37 mM solution in 4 h at RT.

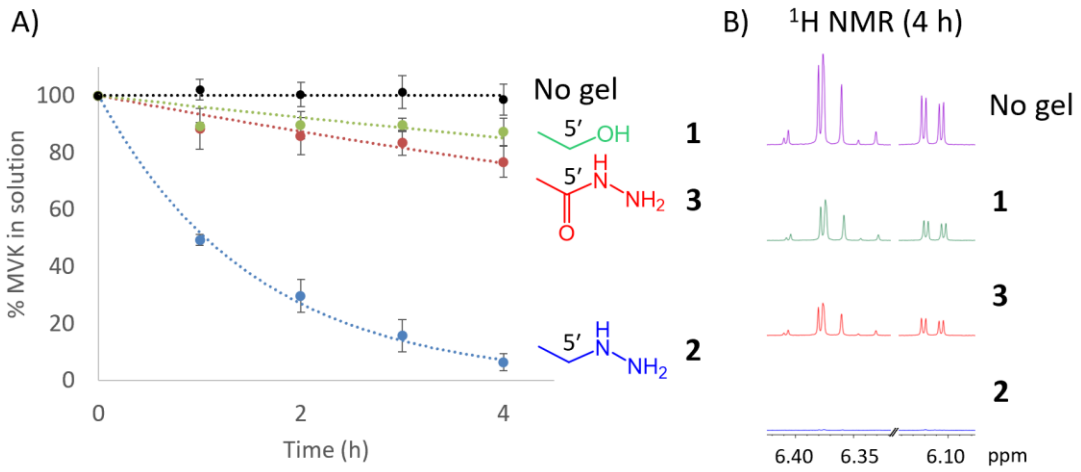

Figure 4.15: A) % **MVK** (3.37 mM) remaining in a 5 mL solution of 155 mM KCl in D_2O, pD 6.3 after addition of hydrogels (0.5 mL, 2 wt % gelator and 136 mM KCl) made from **1-3**. B) B) ^{1}H NMR of the MVK olefinic region shows the most MVK absorption with HG **2** KCl hydrogel at 4 h.

4.5 Toxic methyl acrylate (MA) remediation from the gas and aqueous phase using hydrazine 2•KCl hydrogel

4.5.1 Possible reactions between alkylhydrazine and MA

Methyl acrylate (MA), a feedstock for the polymer industry, is cytotoxic and can contribute to health problems.[236,237] This α,β-UC contains a Michael acceptor and an ester carbonyl, groups that can be also "capped" by the bisnucleophilic hydrazine **2**. Thus, aza-Michael addition followed by intramolecular transacylation should give pyrazolidin-3-one **10** (**Figure 4.16**).[227,228] The electron-donating oxygen makes MA at least 100-fold less electrophilic than MVK,[235] which makes scavenging MA more challenging than for AC and MVK. As described below, G_4•KCl hydrogels containing bisnucleophilic hydrazine **2** can absorb MA from the atmosphere and solution.

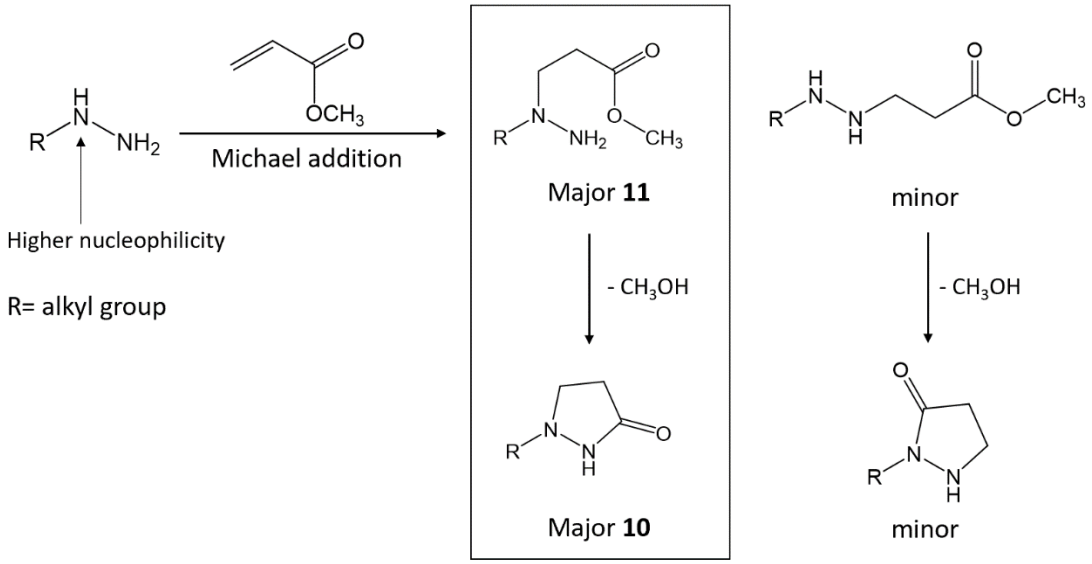

Figure 4.16: Proposed product distribution of 1:1 adduct between hydrazine **2** and MA. Due to the higher nucleophilicity of the alkylated nitrogen of hydrazine,[238] the 1,1-dialkyl hydrazine product (in the box) is favored during absorption, which influences the regioselectivity of linear and cyclic products.

4.5.2 HydrazideG 3 KCl hydrogel does not absorb MA from the gas phase

We began by analyzing for any new adducts formed from gas phase uptake of MA (1 equiv) by G4•KCl hydrogels containing hydrazide **3** or hydrazine **2** (68 mM and 34 mM KCl). Hydrazide **3** gel did not react with MA under these gas phase conditions, as NMR and ESI-MS of the lyophilized gel showed no new products after 2 days at RT (**Figure 4.17 & 4.18**).

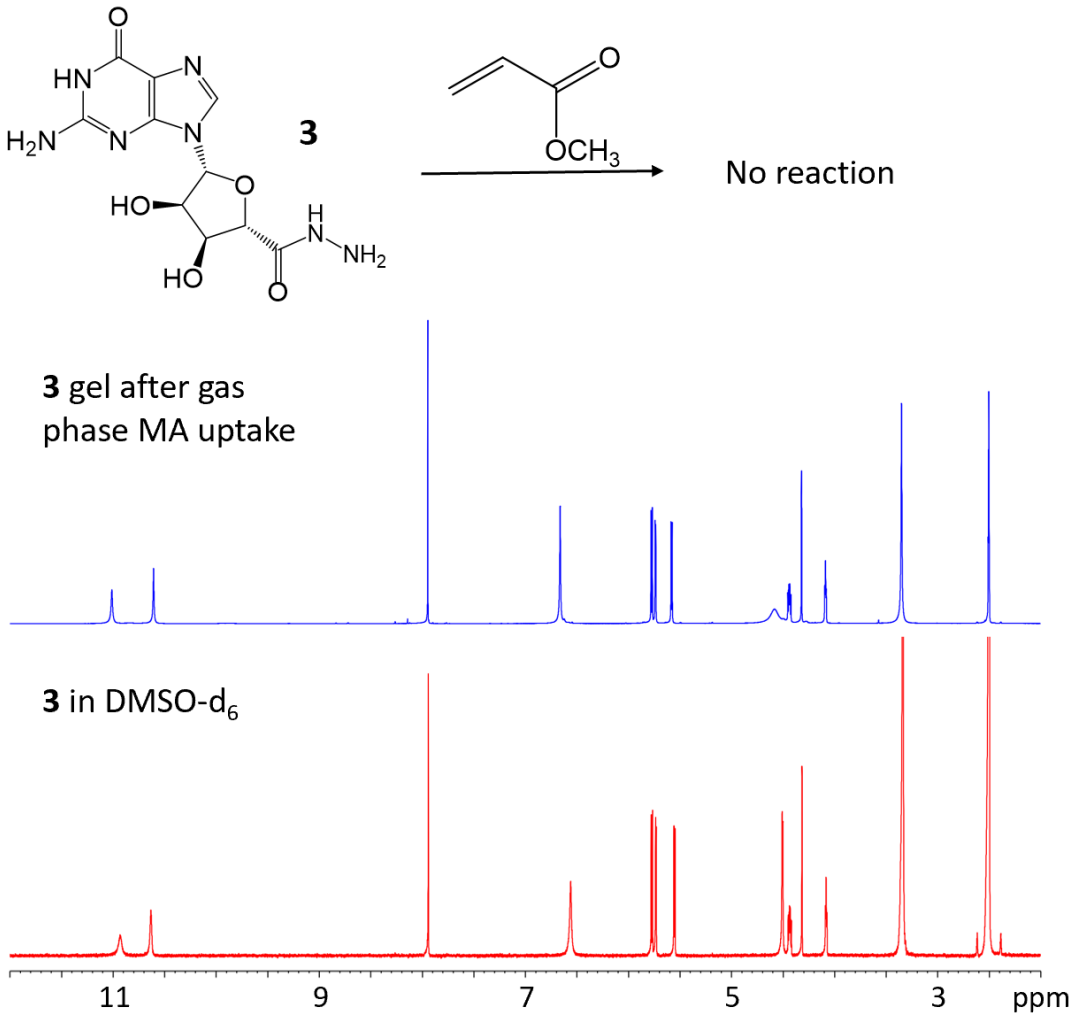

Figure 4.17: ^{1}H NMR shows no reaction of MA with hydrazide **3** gel (2 wt%, 0.5 eq KCl) after 2 days at RT. The gel was lyophilized and dissolved in DMSO-d_6. This result shows that hydrazide **3** hydrogel is far less reactive toward MA than it is toward AC or MVK.

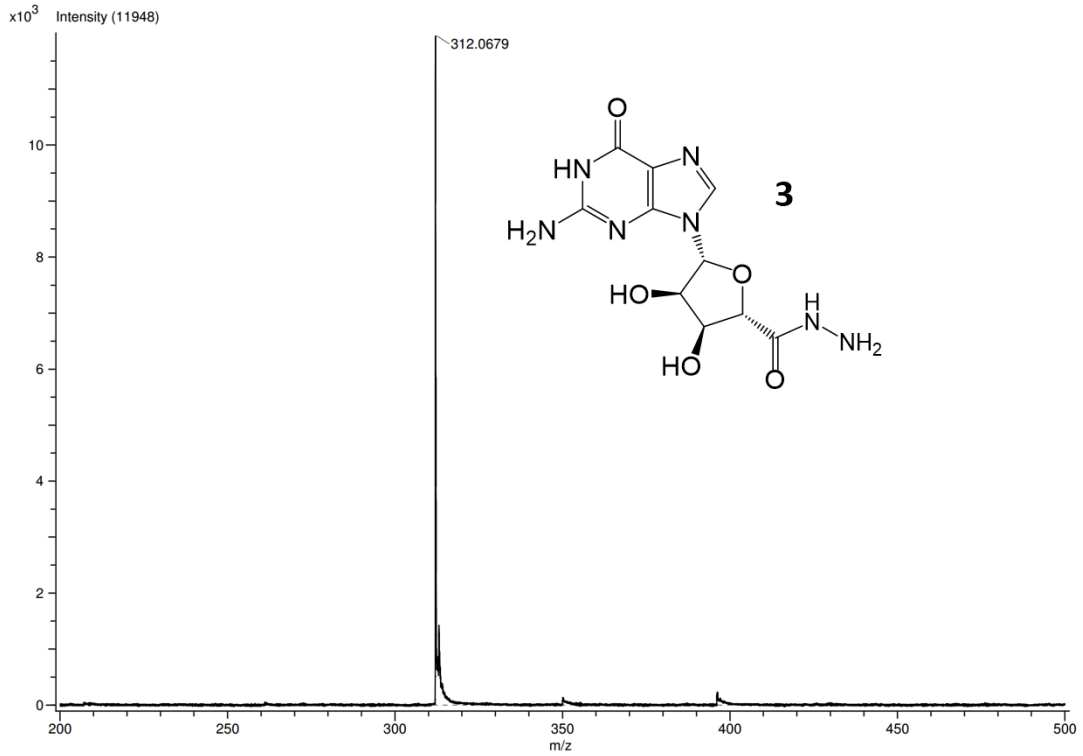

Figure 4.18: ESI-MS shows no covalent adduct formation between hydrazide **3** hydrogel (2 wt%, 0.5 eq KCl) and MA in gas phase uptake experiments after 2 days at RT.

4.5.3 Hydrazine 2 KCl hydrogel absorbs MA from the gas phase

In contrast, the gel made from hydrazine **2** readily absorbed MA from the atmosphere. The ^{1}H NMR of the lyophilized gel after 2 days showed no olefin protons near δ= 6.2 ppm, indicating that all the Michael acceptor in MA had reacted (**Figure 4.19**). ^{1}H-^{13}C HSQC spectrum of reaction products formed by gas phase uptake of 1.0 eq of MA by the G_4•K^+ hydrogel made from 5′-hydrazinoguanosine **2** confirmed that the Michael acceptor end of MA has all reacted to form **10** or **11**. In the light pink region (from δ 3.7-7.5 ppm) where alkene protons are expected, no CH_2 crosspeaks for

unreacted terminal alkene (-CH=CH_2) are found. Meanwhile, multiple CH_2 crosspeaks are identified in the blue region (from δ 2.0-3.7 ppm), indicating different sp^3 CH_2 groups in the resulting adducts. Also, the -OMe peaks around δ 3.6 ppm shows that cyclization must be a slower step than Michael addition. This result demonstrate that the Michael acceptor of MA is more electrophilic than the ester end (inset) toward hydrazine **2**.

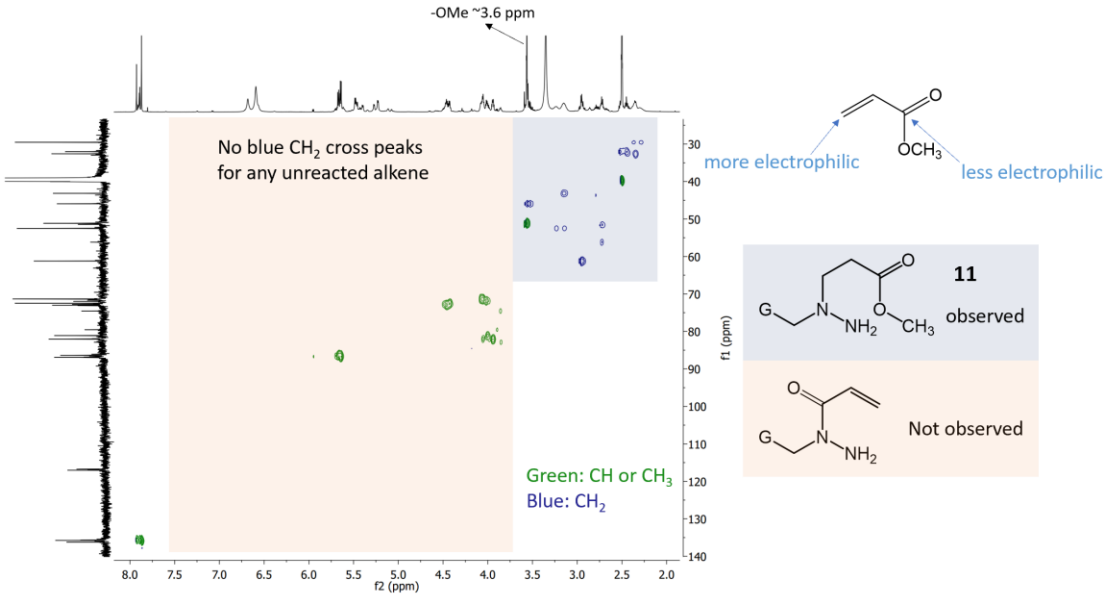

Figure 4.19: ^1H-^{13}C HSQC spectrum of reaction products formed by gas phase uptake of 1.0 eq of MA by the G_4•K^+ hydrogel made from 5′-hydrazinoguanosine **2.**

4.5.4 ESI-MS confirms intramolecular cyclization of 11 to form cyclic adduct 10 over time

As summarized in **Figure 4.20**, ESI-MS of the lyophilized sample showed that hydrazine **2** had been converted into two major products, pyrazolidin-3-one **10** (m/z=352.00) formed by tandem Michael addition/cyclization and the acyclic precursor to **11** arising from aza-Michael addition of **2** to the β-carbon of MA (m/z=384.01).

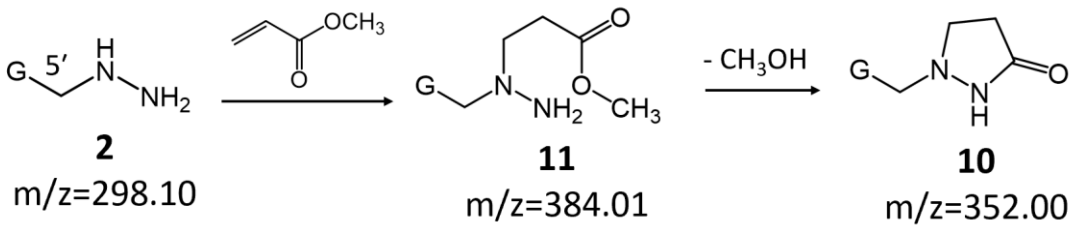

Figure 4.20: ESI-MS showed the main path for remediation of **MA** by hydrazine **3** hydrogel was formation of aza-Michael adduct **11** (m/z=384.01) followed by transacylation to pyrazolidin-3-one **10** (m/z=352.00).

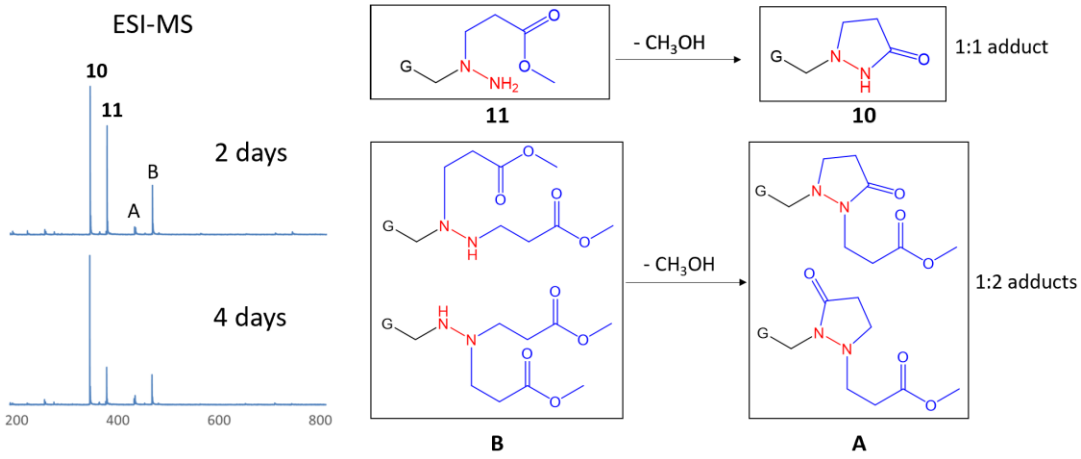

Figure 4.21: (left) ESI-MS spectra of hydrazine **2** hydrogel (2 wt%, 0.5 eq KCl) after 2 and 4 days of MA uptake (1.0 eq) from the gas phase at room temperature. (right) Structures of adducts formed in this reaction. MS shows that 1:1 acyclic adduct **11** (m/z=384.01) is slowly converted into cyclic adducts **10** (m/z=352.00), by losing a molecule of methanol (mw=32). Small amounts of 1:2 adducts, labeled **A** and **B**, were also observed (**A**: m/z=438.02; **B**: m/z=470.06).

In addition to these two major products, there were minor ESI-MS signals for 1:2 adducts wherein both nitrogen atoms in **2** underwent Michael addition with MA (peak B at m/z=470.06 and peak A at m/z= 438.02). Further ESI-MS experiments confirmed that the initial Michael adduct **11** cyclized over time, with loss of CH_3OH, to form the major product **10** (**Figure 4.21**). Two important findings came out of these gas-phase uptake experiments: 1) hydrazine **2** is superior to hydrazide **3** for absorption of MA and

2) hydrazine **2** reacts with MA via the Michael addition/cyclization pathway to give pyrazolidin-3-one **10** as the ultimate reaction product.

4.5.5 Hydrazine 2 KCl hydrogel absorbs MA from the aqueous phase

MA uptake experiments in aqueous solution (155 mM KCl, pD 6.3) confirmed that the G_4•K^+ hydrogel made using 5′-hydrazine **2** was superior to the hydrazide **3** gel for MA remediation. **Figure 4.22A** shows that after 24 h much more MA had disappeared from solution when incubated with the 5′-hydrazine **2** gel as compared to incubating with the G_4•K^+ hydrogel made with hydrazide **3**. Importantly, incubation of MA with the hydrogel made from **2** revealed significant formation of an NMR signal at δ 3.36 for MeOH (**Figure 4.22B**), indicating that the aza-Michael/cyclization tandem reaction had occurred to give the cyclic product **10**. The G_4•K^+ hydrogel containing 5′-hydrazine **2** is an effective scavenger of the less electrophilic α,β-unsaturated ester MA from solution.

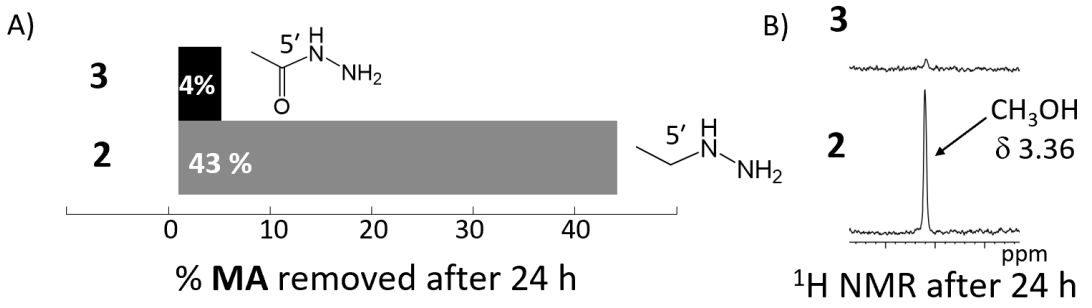

Figure 4.22: A) % **MA** (3.37 mM) removed after 24 h at RT in a 5 mL solution of 155 mM KCl, pD 6.3 after addition of hydrogels (0.5 mL, 68 mM, 136 mM KCl) made from hydrazide **3** or hydrazine **2**. B) ^{1}H NMR after 24 h shows CH_3OH released by reaction of **MA** with G_4•K^+ hydrogel made from hydrazine **2**.

4.6 Conclusions

We have shown that a supramolecular $G_4 \bullet K^+$ hydrogel made from 5′-hydrazine **2** can remove the cytotoxic α,β-UCs AC and MVK, and even the less reactive MA, from both the atmosphere and from aqueous solution via formation of cyclic covalent adducts. The enhanced nucleophilicity of the 5′-hydrazino group in **2** (as compared to hydrazide **3**) contributes to the efficiency of aqueous phase remediation of these α,β-UCs. We plan to 1) study whether this $G_4 \bullet K^+$ hydrogel with its 5′-modified sidechain can be used for remediation of other toxic electrophiles of both natural and man-made origin and 2) determine if this and other hydrazine-containing hydrogels can be used for biomedical applications where trapping α,β-UCs would be advantageous for therapeutic benefits.[226]

Chapter 5: Drawing with Iron on a Gel Containing a Supramolecular Siderophore

The majority of this chapter has been published in reference[7]*:*

Xiao, S.; Paukstelis, P. J.; Ash, R. D.; Zavalij, P. Y.; Davis, J. T. Drawing with Iron on a Gel Containing a Supramolecular Siderophore. *Angew. Chemie - Int. Ed.* **2019**, *58* (51), 18434–18437.

5.1 Summary

We synthesized a guanosine derivative (HAG **15**), containing a 5′-hydroxamic acid (HA) sidechain, which forms G-quartet hydrogels when mixed with equimolar guanosine (G **1**) in KCl solution. The 5′-HA unit (pK_a=8.4) is pH-responsive and also chelates Fe^{3+}. Under basic conditions 5′-HA groups are deprotonated and the anionic hydrogel binds cationic dyes, including thiazole orange (TO). Electrostatic binding of TO by HAG **15**/G **1** gel is signaled by enhanced fluorescence and patterns drawn on the gel surface are visible under UV light. Also, HAG **15** immobilized in the G-quartet polymer functions as a supramolecular siderophore forming red complexes with Fe^{3+}. We patterned the hydrogel's surface by applying a solution of $FeCl_3$, either by hand or by using a 3D-printer. The red patterns, which form instantly and are visible by eye, can be erased by treating the gel with a solution of vitamin C, which reduces Fe^{3+} to Fe^{2+}. This rewritable hydrogel, which combines motifs found in Nature (G_4•K^+ quartet and siderophore-Fe^{3+} complex), is strong, transparent, moldable and stable whether on the bench or submerged in salt water.

5.2 Introduction and compound synthesis

5.2.1 Guanosine supramolecular hydrogels

Supramolecular hydrogels, made from low molecular weight gelators, are soft and wet materials with applications in tissue engineering, drug delivery, environmental remediation and more.[207,239] One challenge in the field is shaping and patterning supramolecular gels,[240] since they are usually not as tough as polymer hydrogels. While photopatterning, via bond isomerization or by generation of acids,[241–243] has been quite successful, other chemical patterning strategies are starting to be developed.[244,245] We are exploring whether supramolecular interactions can be used to generate patterns on these soft materials, which are themselves held together by non-covalent forces. In this chapter, we describe patterning the surface of a supramolecular gel containing hydroxamate (HA) groups by using 1) electrostatics to anchor a fluorescent dye and 2) Fe coordination/redox chemistry to write and erase visible images.

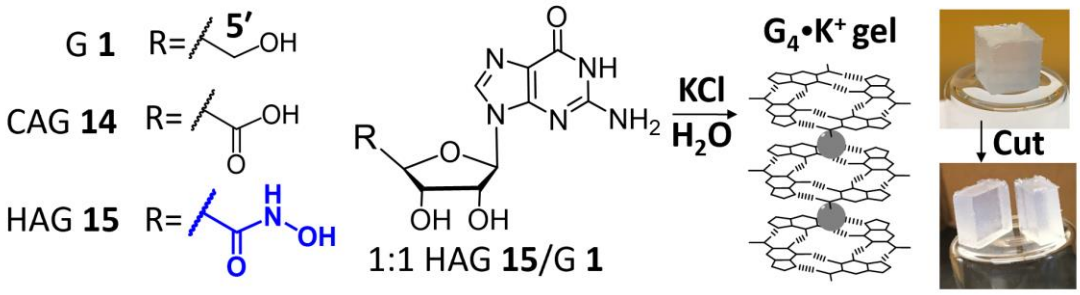

Figure 5.1: A 1:1 mix of 5′-hydroxamic acid guanosine (HAG **15**) and guanosine (G **1**) in KCl solution forms a $G_4 \bullet K^+$ hydrogel that is moldable and retains its shape when cut.

Guanosine (G **1**) and analogs can form robust supramolecular hydrogels, some of which are reliably extruded and molded.[1,4] The structural basis for these hydrogels is

typically the G_4•K^+ quartet (**Figure 5.1**), a H-bonded macrocycle templated by K^+ that then stacks to give entangled nanofibers that trap water. Guanosine hydrogels, first described a century ago,[3] are finding new and diverse applications, including templates for nanomaterials, catalysts, electrochemical sensing, 3D-printing, cell culture, and as anti-cancer agents.[96,185–187,212,246] Since it is not directly involved in G-quartet formation the nucleoside sugar can be chemically modified to give supramolecular gels with unique properties. Reaction of the ribose 2′, 3′-diol with boron species has provided functional guanosine-borate hydrogels.[78,96,127,185–187,212] The 5′-OH sidechain provides another site for chemical modification. Lehn and colleagues used a G_4-hydrogel made from a 5′-hydrazide **3** to form a dynamic covalent library of responsive gels by reaction with aromatic aldehydes,[97] and in chapters 3 & 4 we described a 5′-hydrazine **2** analog that forms G_4-gels useful for covalent trapping of α,β-unsaturated aldehydes and electrostatic binding of anionic dyes.[5,6]

5.2.2 pH-switchable hydrogels from CAG 14

To create a pH-switchable hydrogel for "water-in-water" separation of cationic dyes and metal ions, we first evaluated guanosine-5′-carboxylic acid (CAG **14**) as a possible gelator (**Figure 5.2**). Carboxylic acids are classic pH-responsive groups in supramolecular gels.[247,248] We reasoned that below pH 4, the 5′-carboxylic acid in CAG **14** would be protonated and the K^+-loaded G-quadruplex should favor a "cationic" gel for binding anions. At higher pH, 5′-carboxylates would predominate to give an anionic gel for absorption of cations.

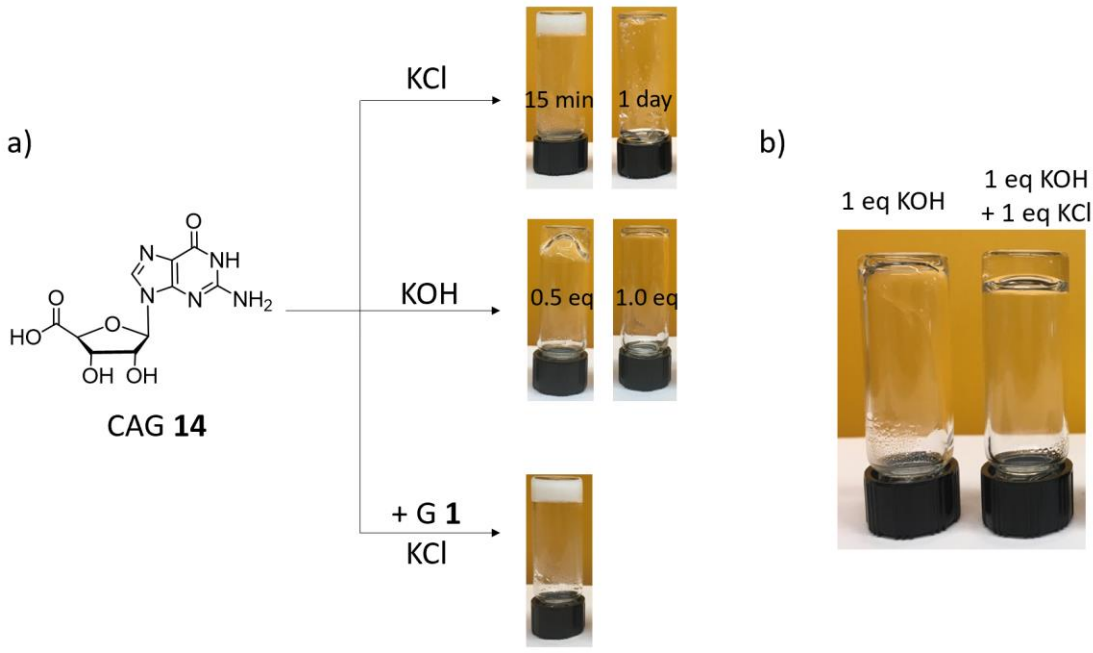

Figure 5.2: (a) CAG **14** forms poor hydrogels (2 wt%) with 0.5 eq KCl (crystallization), 0.5 or 1.0 eq KOH (crystallization or free flowing solution, respectively), or when mixed with G **1** and KCl (white gel containing crystals). (b) CAG **14** (2 wt%) gives a clear hydrogel in a mixture of 1 eq KCl and 1 eq KOH.

However, when we evaluated CAG **14**, whether on its own or when mixed with G **1**, we found it to be a poorly behaved gelator, giving transient gels (2 wt%) that crystallized in hours (**Figure 5.2a**). Addition of 1.0 eq of KOH gave a viscous solution, and addition of 1 eq KCl does make a clear and self-standing hydrogel (**Figure 5.2b**). The resulting gel, however, was difficult to mold and disassembled within a few hours in 155 mM KCl solution.

5.2.3 CAG 14 monohydrate crystal structure

From CAG **14** hydrogels, we found shiny solids that are high quality crystals for X-ray single crystal analysis (**Figure 5.3b**). In a unit cell, CAG **14** forms a hydrogen bond with a water molecule on N3H position (**Figure 5.3a**). Unlike 8-thioG **37**, the ribose in

14 adopts a C3′ endo sugar puckering and the molecule has an *anti* conformation with a torsion angle of 160.5° (**Figure 5.3c**). In ^{1}H NMR of **14** (DMSO-d_6), H2′ has a chemical shift of 4.40 ppm that corresponds to a ~56% *anti* conformation.[153] Hence, the solution phase data is in good agreement with the solid state conformation. The glycosidic bond length for **14** is 1.47 Å, which is elongated compared to G **1** (1.45 Å), but the same as 8-BrG **29**.[150,151]

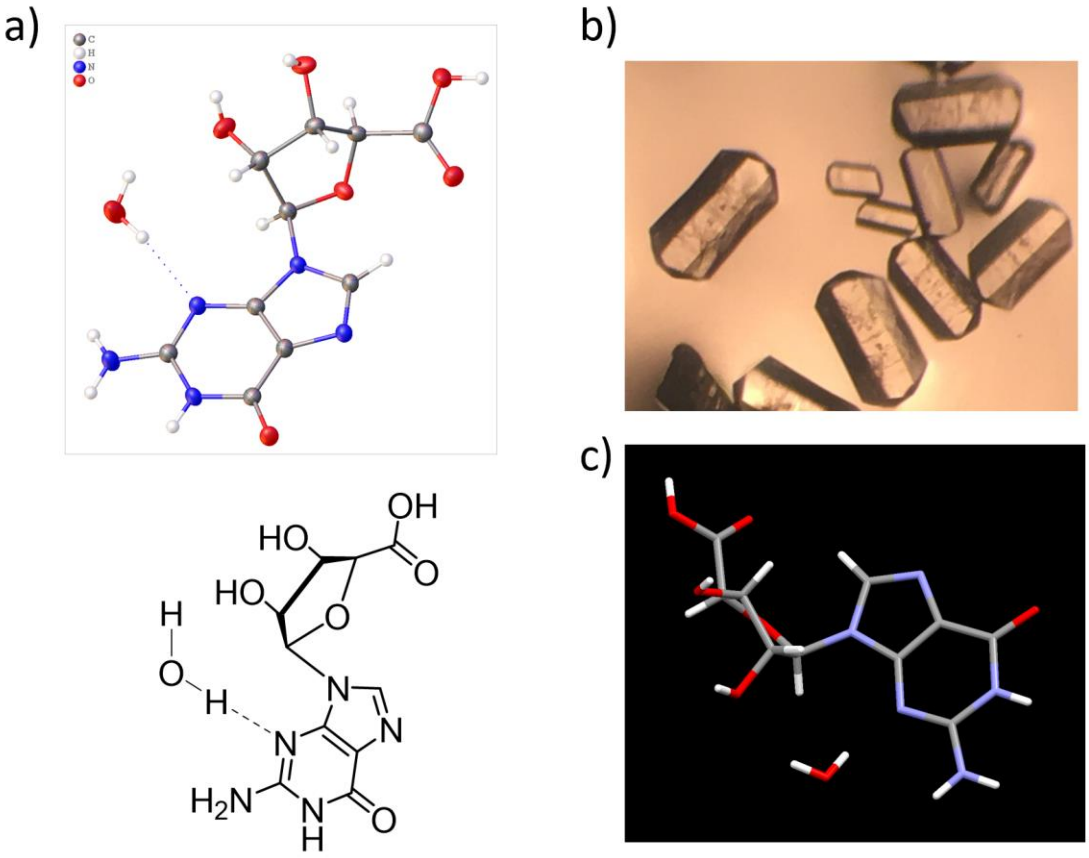

Figure 5.3: (a) Molecular model depiction of X-ray crystal structure and ChemDraw representation of CAG **14** monohydrate (CCDC-1946227). (b) A picture of single crystals of CAG **14** that form over time from CAG **14**•KCl hydrogels. (c) Crystal structure shows C3′-endo sugar puckering and *anti* conformation of the glycosidic bond.

5.2.4 Hydroxamic acid chemistry and siderophores

We next sought a carboxylic acid substitute with better gelation properties than CAG **14**. We identified HAG **15**, a hydroxamic acid (HA) analog of G **1**, as a possible surrogate for 3 main reasons (**Figure 5.4**): 1) HAs are weak organic acids (pK_a of OH is 7.5-9 in water),[249,250] making the group pH-responsive; 2) HAG **15** contains a 5′-amide, which could crosslink neighboring G-quartets via interlayer H-bonds; and 3) hydroxamate anions chelate metal ions strongly.[251] Hydroxamates and Fe^{3+} form complexes that are so stable (e.g. $\beta_3=10^{28}$ for tris(acetohydroxamate)Fe^{3+})[252] that some bacteria secrete HA-containing siderophores to scavenge essential Fe^{3+} from their surroundings.[253,254] While hydroxamates bind Fe^{3+} strongly and with fast kinetics, they have far weaker affinity for Fe^{2+} ($\beta_3=10^{8.6}$ for tris(acetohydroxamate)Fe^{2+})[252]. Indeed, enzymatic release of bound iron from bacterial siderophores is enabled by reducing Fe^{3+} to Fe^{2+}.[255,256] Importantly, there is also a significant color change upon reduction; while the hydroxamate-Fe^{3+} complexes are a deep red color, the weaker hydroxamate-Fe^{2+} complexes are colorless.[252]

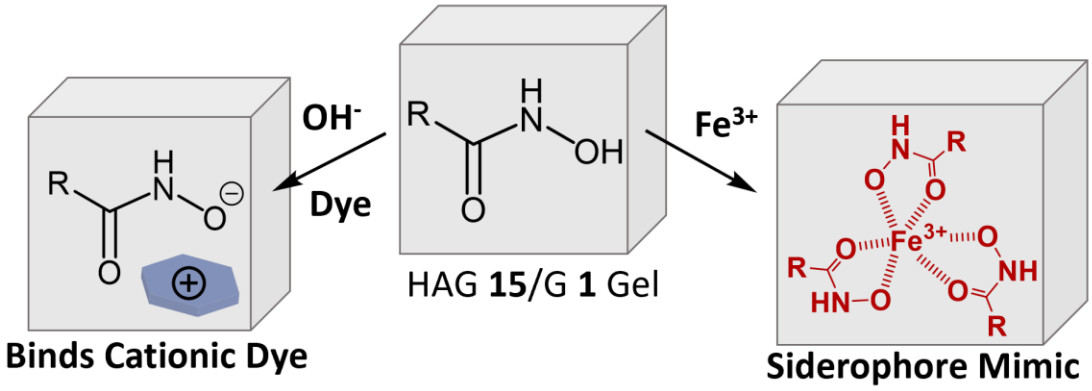

Figure 5.4: 5′-Hydroxamate sidechains in HAG **15**/G **1** gel bind cationic dyes and form supramolecular siderophores that chelate Fe^{3+}.

5.2.5 Hydroxamic acid hydrogels for writing

We reasoned that one should be able to use a solution of $FeCl_3$ to "write" in red on any G_4-gels containing HAG **15**. The resulting pattern should be easy to erase by reducing chelated Fe^{3+} to Fe^{2+}. Although iron complexes of gallic acid are venerable inks,[257] and other phenolic-Fe^{3+} complexes are being developed for writing,[258] our strategy is unique in that the HA chelator is already imbedded in the "paper" and color is generated by applying water-soluble $FeCl_3$. While polymeric gels containing HAs are known, primarily for iron chelation therapy,[259–261] we have not found any examples of supramolecular hydrogels with HA groups. As described, the HA group can indeed endow a supramolecular gel with new and useful properties. Thus, G-quartet hydrogels made with HAG **15** are 1) pH-responsive materials that bind cationic dyes and 2) useful for creating/erasing images using iron coordination and redox chemistry.

5.2.6 Synthesis of guanosine-5′-hydroxamic acid 15

Guanosine-5′-hydroxamic acid (HAG **15**) was prepared in two steps (**Figure 5.5**): ipG **19** was deprotected and esterified to give esterG **20**,[80,262] which was thoroughly rinsed to remove NaCl and prevent gelation during synthesis. Nucleophilic substitution with hydroxylamine at room temperature was then performed. Acidifying the resulting suspension to pH~3 gave HAG **15** as a white powder. Inosine-5′-hydroxamic acid (HAI **17**) was also synthesized for control experiments (**Figure 5.6**). In principle, the synthetic procedures for **15** and **17** might be further simplified using nucleoside oxidase

to directly oxidize nucleoside 5′ position and to avoid protecting groups and toxic reagents.[263]

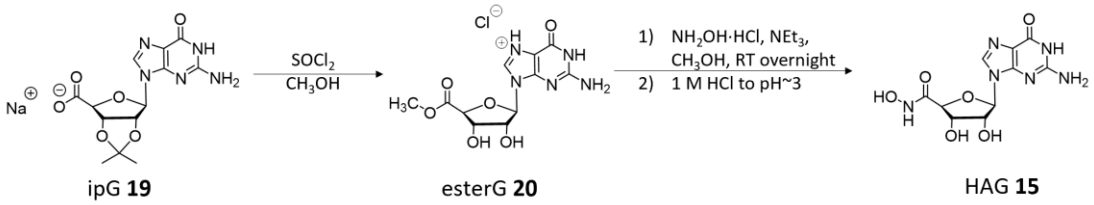

Figure 5.5: Synthetic procedure to prepare HAG **15**.

5.3 Gelation test and hydrogel characterization

5.3.1 Binary HAG 15/G 1 mixture and KCl are required for gelation

We started by exploring the conditions under which hydrogels form from HAG **15**. Neither G **1** nor HAG **15**, when combined with KCl, gave hydrogels on their own, but a 1:1 mixture of the nucleosides and KCl formed a robust gel (**Figure 5.6**). Thus, HAG **15** (32 mM) and G **1** (32 mM) and 2 eq of KCl (128 mM) in water gave a transparent and self-standing hydrogel after a heating-cooling cycle. This binary gel is stable, showing no apparent change after a year on the bench. The disorder caused by combining two different guanosine analogs likely inhibits crystallization and favors formation of the binary gel.[1] A 1:1 mixture of inosine **16** and HAI **17** (64 mM), nucleosides that cannot form G-quartets, remained in solution in the presence of KCl (128 mM), confirming that the G nucleobase is key for gelation (**Figure 5.6**).

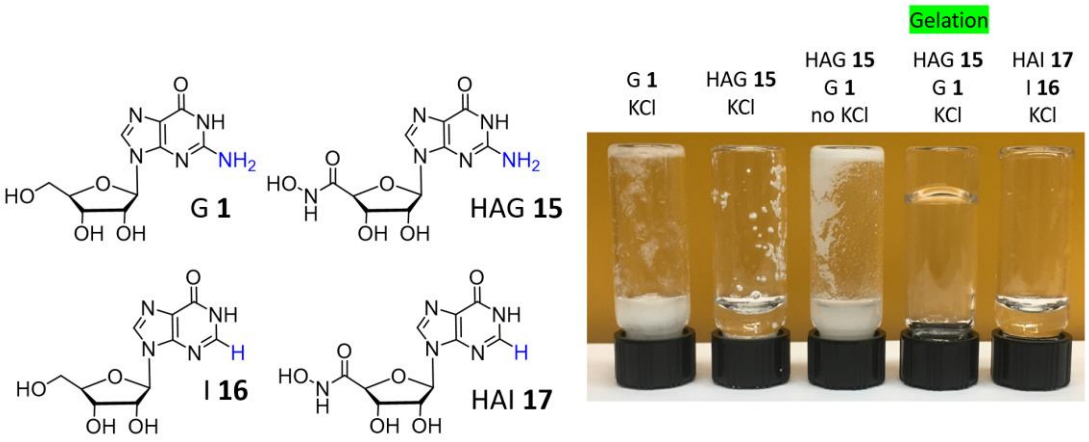

Figure 5.6: Structures of nucleosides **1** & **15-17** are shown on left. Photo on the right shows samples of these nucleosides, with and without added KCl, after allowing hot solutions to cool to rt. Neither G **1** nor HAG **15**, when combined with KCl, gave hydrogels. Only the 1:1 mixture of HAG **15** and G **1** (2 wt %, 64 mM total nucleosides) in the presence of KCl (128 mM) gave a self-standing hydrogel (4th vial from left). A binary 1:1 mixture of HAI **17** and I **16**, nucleosides that lack exocyclic amines and cannot form G-quartets, gave a free-flowing solution (vial on far right). This last experiment indicates that the G nucleobase is required for gelation.

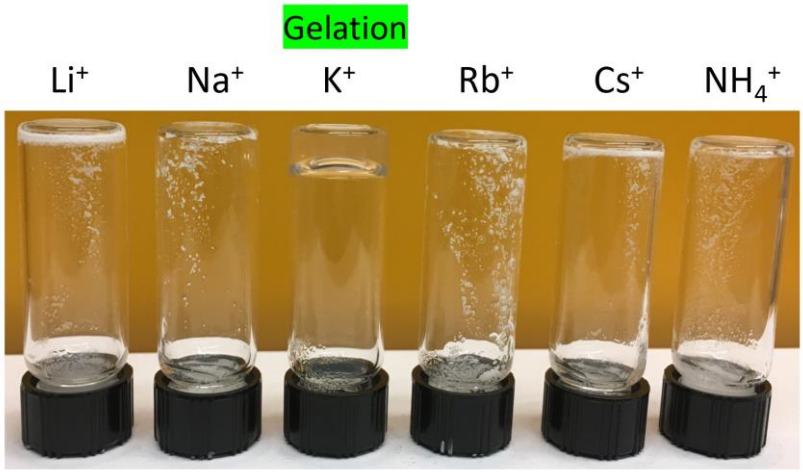

Figure 5.7: A 1:1 mixture of HAG **15** and G **1** forms self-standing hydrogel only with added KCl (3rd vial) amongst all the alkali metals tested (2 wt %, 64 mM, 32 mM MCl), consistent with K^+ being the best cation at stabilizing G-quartets.

Addition of alkali metal salts other than KCl (namely LiCl, NaCl, RbCl and CsCl) to a HAG **15**/G **1** mixture gave precipitates instead of a hydrogel upon cooling (**Figure**

5.7). These results are consistent with K^+ being the best alkali cation for stabilizing G-quartets.[1,4]

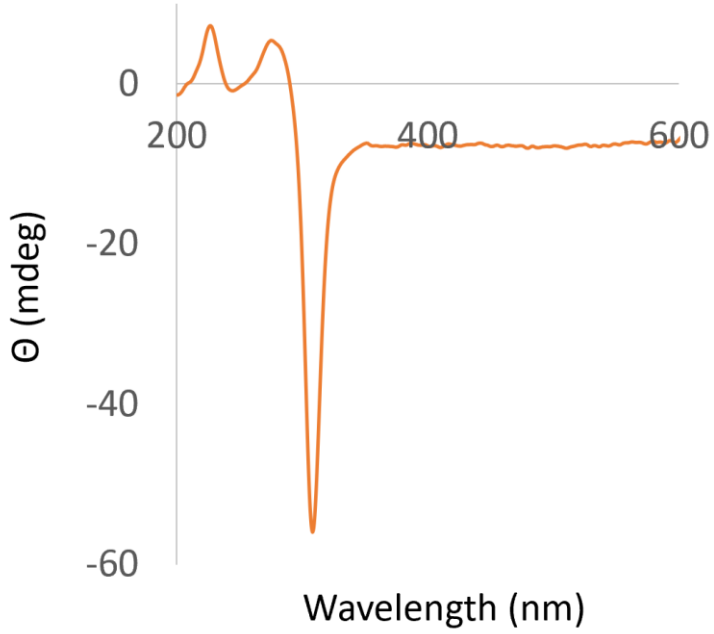

Figure 5.8: CD spectrum of 1:1 HAG **15**/G **1** hydrogel (2 wt %, 64 mM, 128 mM KCl) shows characteristic signals for chiral G-quadruplex between 250-350 nm.

CD spectrum of the HAG **15**/G **1** hydrogel showed characteristic bands between 250-350 nm for a chiral G-quadruplex (**Figure 5.8**).[195] All the information combined shows that the structural basis for HAG **15**/G **1** KCl hydrogel is the G_4•K^+ quartet.

5.3.2 Binary KCl gels of HAG 15 and other guanosine analogs

HAG **15** also forms stable binary gels with amideG **18**, hydrazideG **3** and esterG **20**, while with CAG **14** forms a white gel containing precipitates (**Figure 5.9**). By assembling two or more different modified guanosine molecules into one hydrogel, one can integrate complex functions in the same system. For example, if one can form a hydrogel containing a base, an acid and a nucleophile, the resulting gel could

potentially become a mimic of catalytic triad. In this chapter we focus on 1:1 binary hydrogels of HAG **15** and G **1** since G **1** is commercially available and inexpensive.

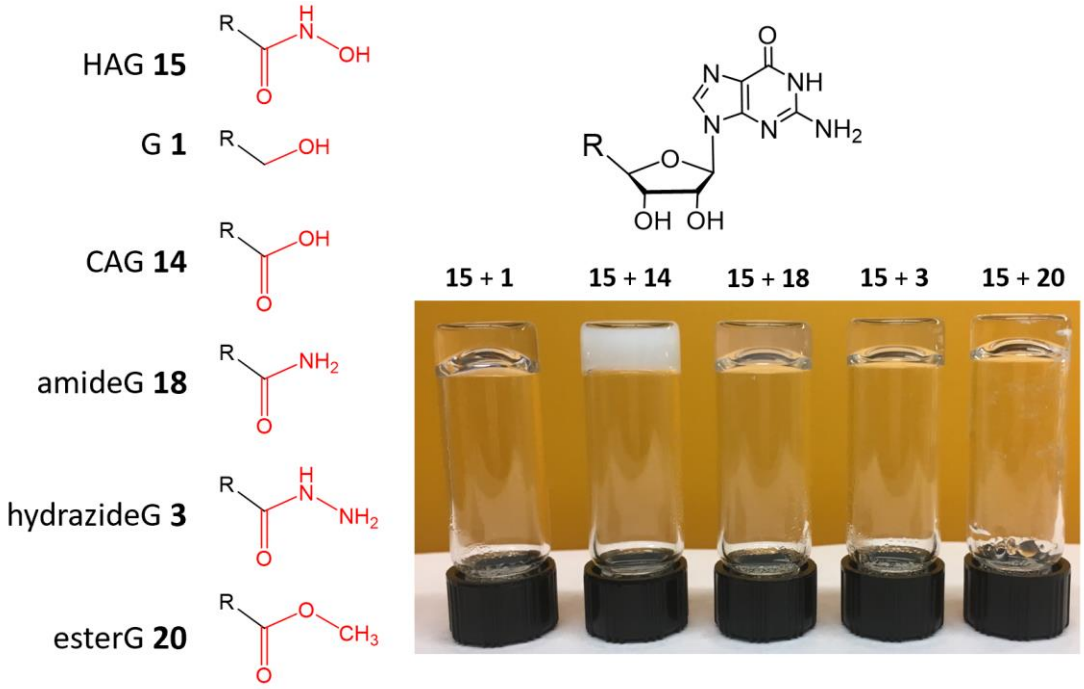

Figure 5.9: Pictures of binary hydrogels between HAG **15** and other 5′-modified guanosine analogs (1 wt% nucleoside, 0.5 eq KCl).

5.3.3 HAG 15 is the major gelator in 1:1 HAG 15/G 1 gel

Solution state ^{1}H-NMR shows that HAG **15** is the major gelation species: the solution phase of a HAG **15**/G **1** gel (2 wt%, 2 eq KCl) has more G **1** (13%) than HAG **15** (2%), indicating HAG **15** is preferentially incorporated into the solid phase of G_4-network (**Figure 5.10b-c**). Two reasons could contribute to this phenomenon: G **1** (2.1 mM) has higher aqueous solubility than HAG **15** (0.6 mM) (**Figure 5.11**);[5,205] gel formation with HAG **15** is likely to be more favorable due to amide hydrogen bonding (**Figure 5.10a**).[264] The amide stabilization can also explain why HAG **15** forms a better

hydrogel than CAG **14** despite the same solubility of CAG **14** and HAG **15** (**Figure 5.11**).

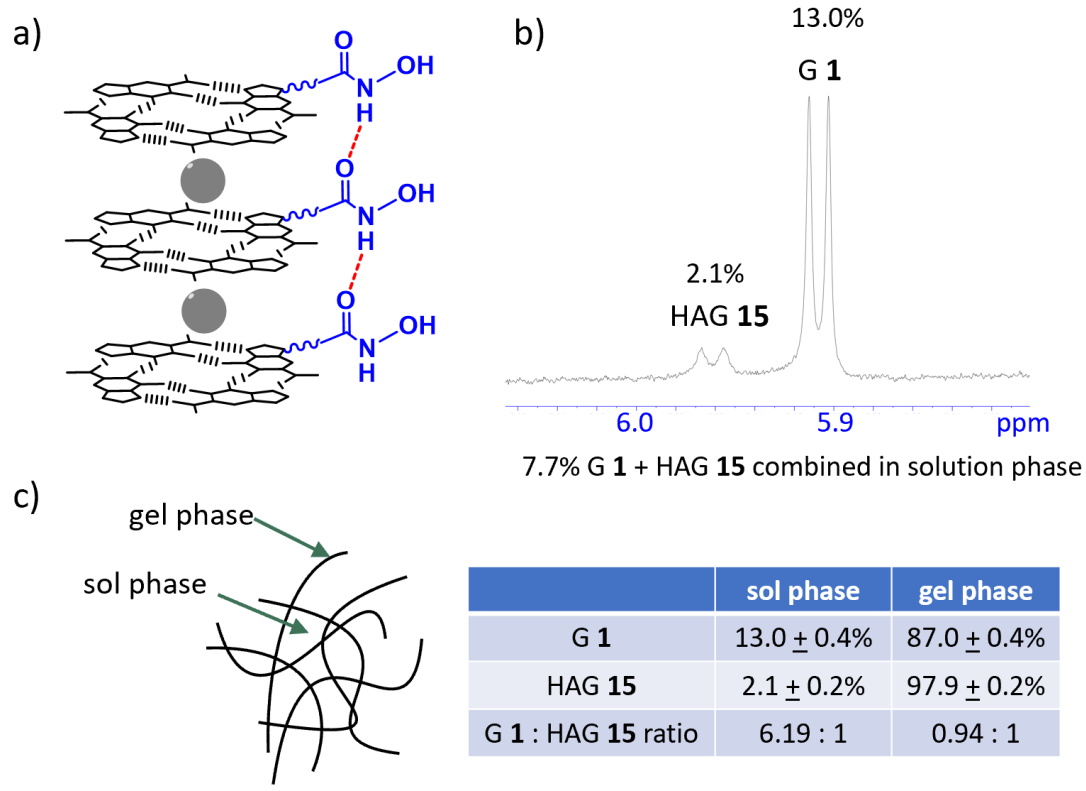

	sol phase	gel phase
G **1**	13.0 ± 0.4%	87.0 ± 0.4%
HAG **15**	2.1 ± 0.2%	97.9 ± 0.2%
G **1** : HAG **15** ratio	6.19 : 1	0.94 : 1

Figure 5.10: (a) Possible interlayer H-bonding interactions between HA groups. (b) Solution phase ^{1}H NMR shows that HAG **15** is the main gelator in a 2 wt % HAG **15**/G **1** binary gel (64 mM, 2 eq KCl) in D_2O. By integration, 2.1 % of HAG **15** is in the solution phase and 97.9 % is in the gel phase, whereas 13 % of G **1** is in solution and 87 % is in the gel. A small amount of DMSO-h_6 was used as an internal standard. H1′ region is shown in the figure. (c) (left) depiction of sol and gel phase in a hydrogel system and (right) relative ratios of G **1** and HAG **15** show that HAG **15** has a modest preference over G **1** (1:0.94) for the gel phase..

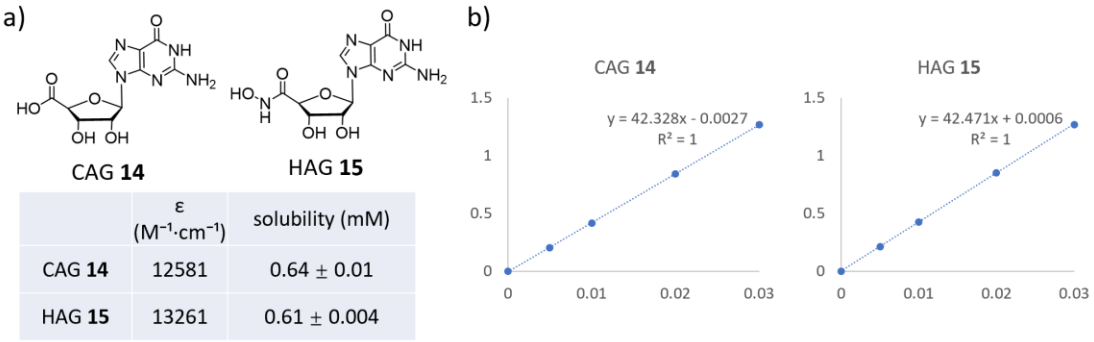

	ε ($M^{-1}·cm^{-1}$)	solubility (mM)
CAG **14**	12581	0.64 ± 0.01
HAG **15**	13261	0.61 ± 0.004

Figure 5.11: (a) Aqueous solubility of CAG **14** and HAG **15** determined by UV-vis spectroscopy (b) UV-vis working curve for determining the solubility of CAG **14** and HAG **15**.

The stabilizing effect is also reflected in the low critical gelation concentration of 8 mM for HAG **15**/G **1** binary hydrogel (2 eq KCl) (**Figure 5.12**). Gelation from natural products with a low concentration could be desirable for cell culture purposes.[185]

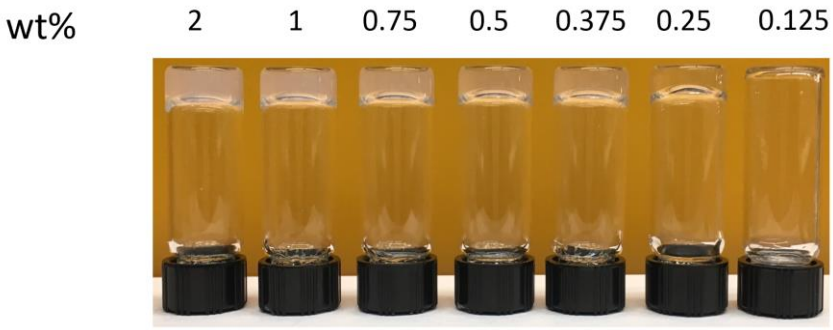

Figure 5.12: Vial inversion tests show that the binary hydrogel made from a 1:1 mixture of HAG **15**/G **1** with 2 eq KCl has a critical gel concentration of at least 0.25 wt % (8 mM).

5.3.4 Material behavior and stability of hydrogel in salt solution

Hydrogels formed from an equimolar mixture of G **1** and HAG **15** with as little as 0.25 eq KCl per nucleoside, exactly the stoichiometry of K^+ needed to form a G-quadruplex polymer (**Figure 5.13**). We could form materials with varying strength

simply by changing the KCl concentration. Thus, rheology revealed that G′ values (a measure of a material's stiffness) ranged from ~30 Pa for gels made with 0.25 eq of KCl to ~14000 Pa with 2 eq of KCl (**Figure 5.13**). The stiffer HAG **15**/G **1** gels are moldable and hold their shape over time, unusual for supramolecular hydrogels.[240] For example, a cube of HAG **15**/G **1** gel (64 mM, 2 eq KCl) was cut in two without the objects losing their form (**Figure 5.1**). SEM image shows nanofibers (~100 nm thick) mixed with micron-scale layered structures (~5 μm thick) (**Figure 5.14**).

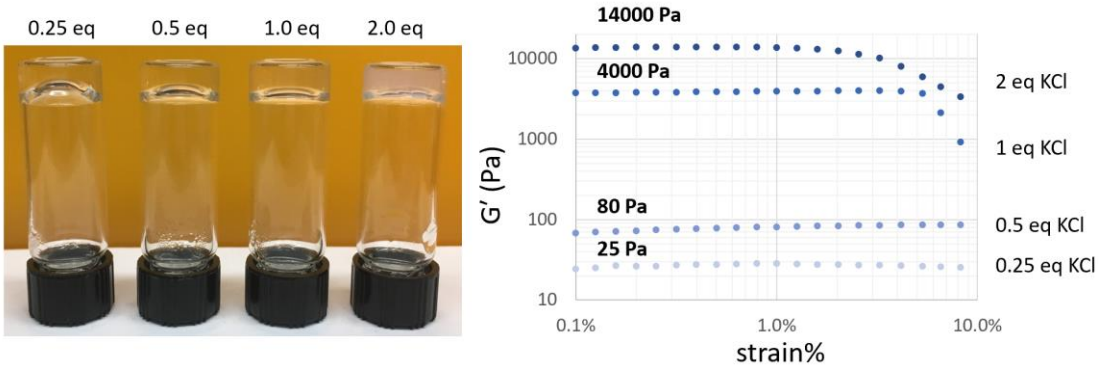

Figure 5.13: A binary hydrogel made from 1:1 mixture of HAG **15**/G **1** (64 mM, 2 wt %) forms hydrogels of different stiffness and strength depending on the concentration of KCl. (left) A picture of hydrogels containing different eq of KCl. (right) Strain sweep data indicates that hydrogels with a wide range of G′ values can be accessed by simply varying the concentration of added KCl. The storage modulus (G′) of HAG **15**/G **1** hydrogels increases with increasing KCl concentration.

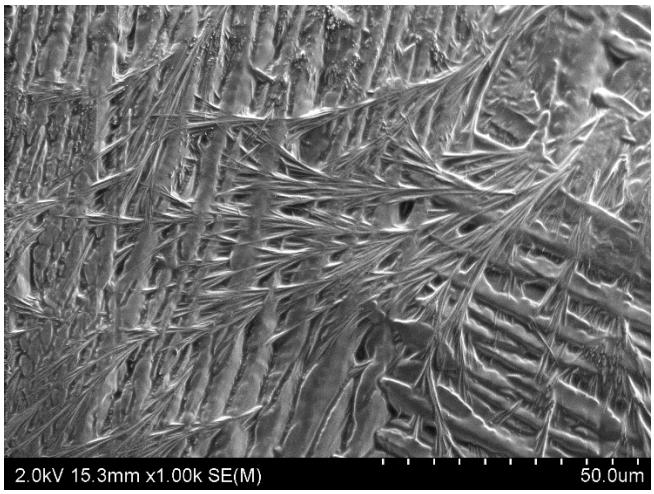

Figure 5.14: SEM image of a 1:1 HAG **15**/G **1** hydrogel (64 mM, 2 wt %, 2 eq KCl) shows a dense network of fibers and layered structures.

As a first step toward establishing whether these solid materials could be used for "water-in-water" applications, we tested their stability in a 155 mM KCl solution. When submerged, a piece of HAG **15**/G **1** hydrogel (64 mM, 2 wt %, 2 eq KCl) stayed intact for over 6 months without noticeable deterioration (**Figure 5.15**).

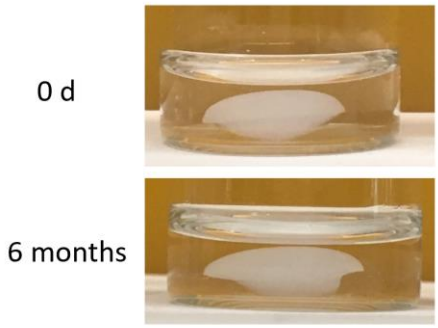

Figure 5.15: A chunk of HAG **15**/G **1** hydrogel (64 mM, 2 wt %, 2 eq KCl) remained unchanged when submerged in a solution of 155 mM KCl for 6 months, indicating its potential utility for "water-in-water" absorption of pollutants.

5.4 Hydroxamic acid as a pH-switchable functional group in HAG 15/G 1 hydrogel

5.4.1 pKa of 5′-hydroxamic acid

We tested our hypothesis that the pH-responsive 5′-hydroxamic acid/hydroxamate would enable the HAG **15**/G **1** gel to switch its protonation state depending on pH. First, we determined the pK_a of the 5′-HA group. HAI **17**, rather than HAG **15**, was chosen for 3 reasons (**Figure 5.16b**): 1) HAI **17** is significantly more soluble than HAG **15** in water; 2) it is structurally similar to HAG **15** and 3) the 5′-hydroxamic acid sidechain is well separated from the nucleobase unit so that its pK_a is probably not significantly influenced by a small modification in the nucleobase structure.

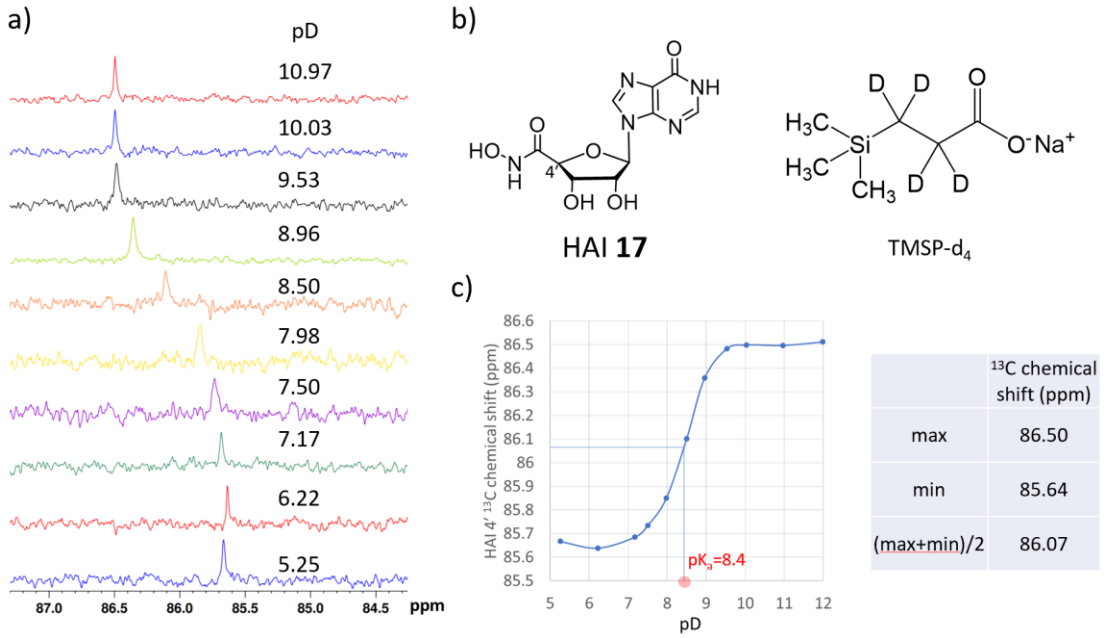

Figure 5.16: Determination of the pKa of the 5′-hydroxamic acid in HAI **17** pKa using ^{13}C NMR. a) Stack plot of C4′ region of ^{13}C NMR spectra at different pD values. b) Structures of HAI **17** and internal standard TMSP-d_4. c) S-shape curve from pD titration. The pK_a of 8.4 for the 5′-hydroxamic acid unit was determined using the middle point on the curve.

We chose to monitor the C4′ chemical shift of HAI **17** (**Figure 5.16a-b**) because 1) C4′ is in close proximity to 5′-HA and its chemical shift would be sensitive to the protonation state of HA; 2) it is a methine carbon with relatively good sensitivity by ^{13}C NMR and 3) it is well separated in the spectra from other NMR peaks. The average value of the C4′ chemical shifts was plotted against pD values of the corresponding sample to generate a S-shape curve. The average of the maximum and minimum values was used to find the pK_a value on the curve. The results from ^{13}C NMR gave a pK_a of 8.4 for the 5′-HA group (**Figure 5.16c**), a value consistent with other hydroxamic acids.[249,250]

5.4.2 HAG 15/G 1 binary gels form at higher pH

Next, we verified that gels could be prepared at pH values where most of the 5′-HA groups were neutral (acidic conditions) or anionic (basic conditions). The standard 1:1 HAG **15**/G **1** (64 mM total) gel made with 2 eq of KCl had a pH of 4.7. Under these conditions the 5′-hydroxamic acids would be neutral and the HAG **15**/G **1** hydrogel should be cationic because of the spine of K^+ ions in the G-quadruplex channel. We also prepared an anionic hydrogel under basic conditions. Addition of 0.5 eq of KOH and 1.5 eq of KCl to a 1:1 mixture of HAG **15**/G **1** gave a moderately stiff gel (G′~3000 Pa) with a pH = 9.5 (**Figure 5.17**) and this hydrogel shows characteristic CD spectra of a G-quadruplex(**Figure 5.18a**). SEM image shows dense and rigid fibers with a thickness of ~0.1 micron (**Figure 5.18b**). We expected that this anionic gel, where most 5′-HA sidechains should be deprotonated, would bind cations.

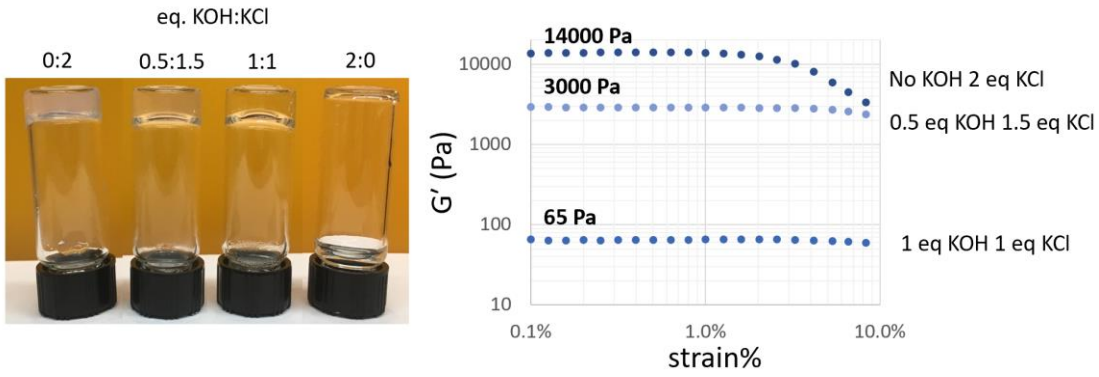

Figure 5.17: HAG **15**/G **1** binary mixture (2 wt %, 2 eq K^+) form hydrogels with KOH/KCl mixture. The pH of the gel made using 2 eq of KCl was 4.7 and the pH of the gel made with 1.5 eq KCl and 0.5 eq of KOH was 9.5. Dynamic strain sweep shows that hydrogel stiffness can be controlled by the concentration of added KOH.

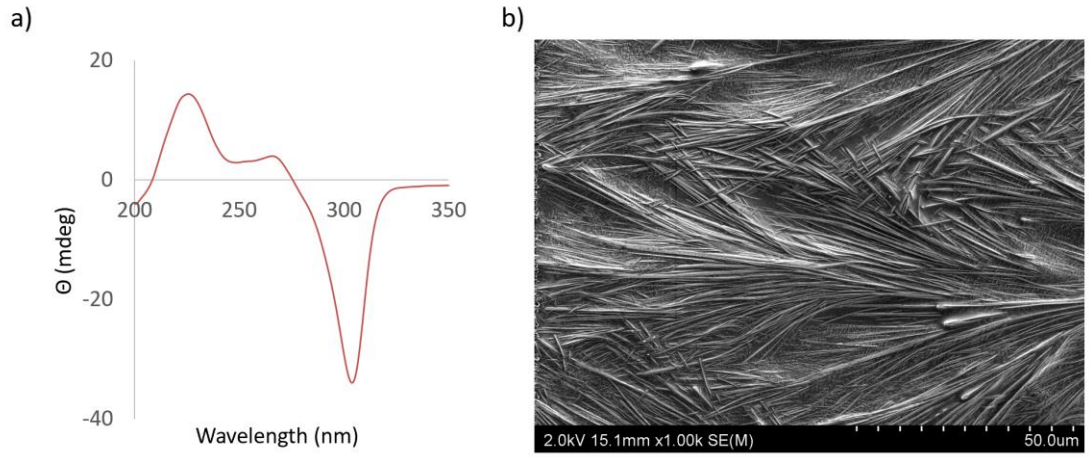

Figure 5.18: a) HAG **15**/G **1** hydrogel with 0.5 eq KOH (2 wt %, 64 mM, 1.5 eq KCl, 0.5 eq KOH, pH 9.5) also shows characteristic features of the helical G-quadruplex CD. b) SEM image of a 1:1 HAG **15**/G **1** hydrogel (64 mM, 2 wt %, 1.5 eq KCl, 0.5 eq KOH) shows a dense network of fibers with a thickness of ~100 nm.

5.4.3 TO binding assay confirms HA group is pH switchable

We chose thiazole orange (TO) as a light-up probe to report on binding of a cationic dye by the G_4-hydrogels made from HAG **15**/G **1** (**Figure 5.19a**). TO has been widely used to detect higher-ordered nucleic acid structures and it is particularly selective for binding G-quadruplexes, be they in DNA polymers or in supramolecular assemblies formed by "small molecule" guanines.[95,265–267] TO is weakly fluorescent in solution

because of rapid rotation about the C-C σ bond that connects its 2 aromatic rings. When TO binds to a receptor (here the G_4-hydrogel) this bond rotation becomes restricted as the dye favors a conformation where the aromatic rings are co-planar. The result is an increase in fluorescence upon TO dye binding to G_4-assemblies. We reasoned that due to electrostatic attraction the cationic TO should have a relatively higher affinity for the anionic pH 9.5 hydrogel but would bind less well to the cationic HAG **15**/G **1** gel with pH 4.7.

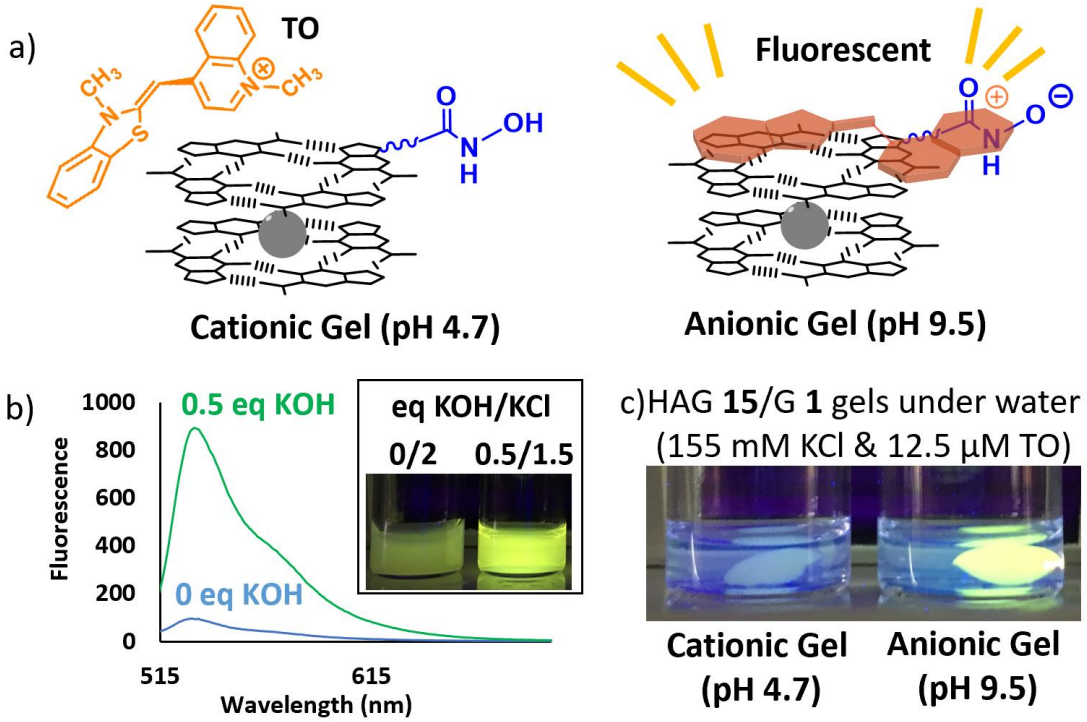

Figure 5.19: a) Deprotonation of 5′-HA sidechains give an anionic HAG **15**/G **1** gel that binds thiazole orange (TO), resulting in enhanced fluorescence. b) Fluorescence increased in HAG **15**/G **1** gel (12.8 mM) containing 0.5 eq KOH and 5 µM TO, relative to a gel without KOH. Inset: A HAG **15**/G **1** gel (64 mM, pH 9.5) made with 1.5 eq of KCl and 0.5 eq of KOH and containing 0.1 mM TO was more fluorescent than a gel made with 2.0 eq of KCl (pH 4.7). c) An anionic HAG **15**/G **1** gel (64 mM, pH 9.5) became fluorescent after sitting in an aqueous solution of TO (12.5 µM, 155 mM KCl), whereas a cationic HAG **15**/G **1** hydrogel (64 mM, pH 4.7) did not fluoresce in presence of TO. Photo was taken, under a UV lamp, after gels had soaked for 24 h in a solution containing TO.

Data in **Figure 5.19** is consistent with our hypothesis. As the photos show (**Figure 5.19b inset**) the HAG **15**/G **1** hydrogel (64 mM, 2 eq KCl, pH 4.7) containing 0.1 mM TO was weakly fluorescent when observed under 365 nm light. In contrast, HAG **15**/G **1** gel (pH 9.5) made with 0.5 eq KOH was much brighter, indicating enhanced binding of TO by this anionic gel. Fluorescence spectroscopy carried out directly on HAG **15**/G **1** gels (0.4 wt %, 12.8 mM, 2 eq K^+, 5 μM TO) revealed a 9-fold enhancement in fluorescence intensity for the anionic gel made with 0.5 eq of KOH, as compared to the cationic gel with pH 4.7 (**Figure 5.19b**).

We also performed a pH titration of HAG **15**/G **1** binary gel (0.4 wt%, 2 eq K^+, 5 μM TO) which was studied by fluorescence spectroscopy (**Figure 5.20**). Fluorescence intensity increased significantly at pH=8 (~28% 5′-HA deprotonated) and reached maximum at pH=9.8 (96% 5′-HA deprotonated). Further increasing pH causes fluorescence decrease, presumably caused by disassembly of G-quartet via N1H deprotonation.

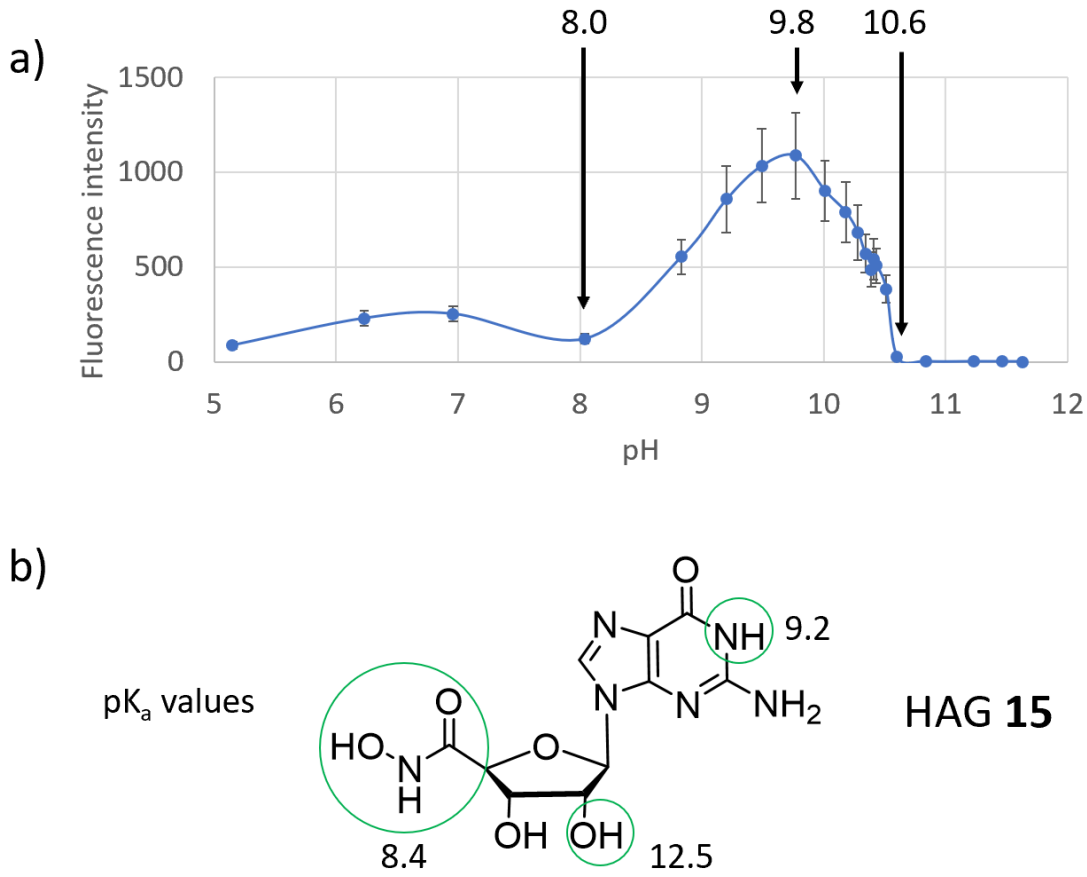

Figure 5.20: a) pH titration experiment of HAG **15**/G **1** hydrogel (12.8 mM, 0.4 wt %, 2 eq K^+, 5 μM TO). Fluorescence intensity increased significantly from pH=8 to pH=9.8, which is close to the pK_a value of the 5′-hydroxamic acid in HAG **15** (8.4). Further addition of KOH caused a decrease in fluorescence intensity, possibly caused by deprotonation of guanine N1H (pK_a 9.2). b) Relevant pK_a values in HAG **15**. We determined the pK_a value for the 5′-hydroxamic acid by ^{13}C NMR and the other values depicted are from the literature.[268]

Lastly, as shown in **Figure 5.19c**, cationic TO (12.5 μM) was selectively extracted from 155 mM KCl solution into the matrix of the anionic hydrogel. The anionic gel was much more fluorescent than the cationic gel after chunks of the 2 G_4-gels were incubated in an aqueous solution of TO (12.5 μM, 155 mM KCl) for 24 h. This experiment confirmed that the affinity of the G_4-hydrogel for TO can be tuned by

changing the protonation state of the 5′-HA sidechains. The HA group is clearly an alternative to the carboxylic acid group when designing pH-responsive hydrogels.[269]

5.4.4 Writing with TO on HAG 15/G 1 gel

Next, we investigated whether the fluorescent response could be used for writing with TO dye as ink on a HAG **15**/G **1** gel. Indeed, under UV-irradiation we observed a "G" pattern, albeit somewhat faint, that we had hand-drawn on the surface of the gel (**Figure 5.21**).

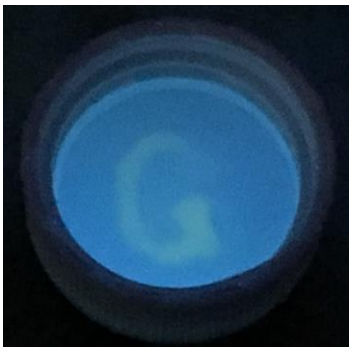

Figure 5.21: A fluorescent "G" pattern shows up on a HAG **15**/G **1** gel (pH=9.5) after writing with a suspension of 1 mM thiazole orange. Gels were placed under 365 nm UV lamp for visualization. Picture was taken 10 min after drawing.

This promising result led us to consider a more water-soluble and environmentally friendly "ink" than TO, and one whose patterns can be seen directly. We identified Fe^{3+} as an ideal stain, especially if the HAG **15**/G **1** gel, loaded with 5′-HA chelating sidechains, were to function as a supramolecular siderophore to give stable and colored hydroxamate-Fe^{3+} complexes.

5.5 Patterning on HAG 15/G 1 binary gel with $FeCl_3$

5.5.1 Hydroxamic acid test

We performed a colorimetric test by mixing colorless solutions of 0.6 mM HAG **15** and 0.2 mM $FeCl_3$. An intense red color appeared instantly (**Figure 5.22**). This solution had a maximum absorbance at 464 nm, characteristic for a (hydroxamate)-Fe^{3+} complex.[270] Addition of 5 mM VC to the HAG **15**-$FeCl_3$ solution instantaneously eliminated the color, demonstrating the potential of VC to erase hydroxamato-Fe^{3+} patterns by reducing Fe^{3+} to Fe^{2+}.

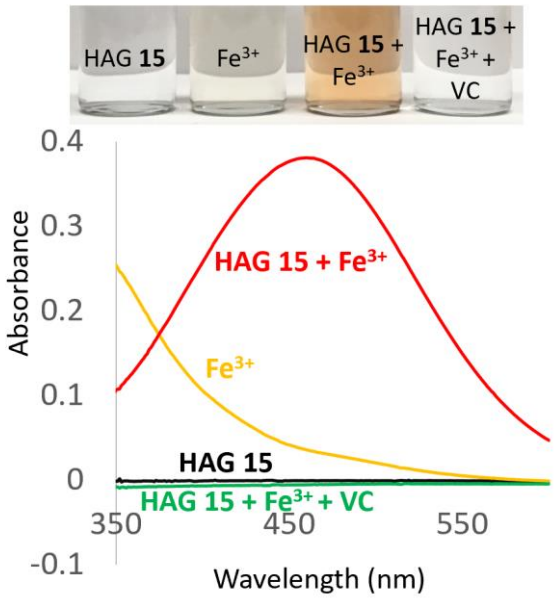

Figure 5.22: (a) A solution of HAG **15** (0.6 mM) passed the "hydroxamic acid test", showing a red color upon mixing with $FeCl_3$ solution (0.2 mM). UV-vis spectroscopy shows a strong absorption around 460 nm for the solution containing HAG **15** and $FeCl_3$.

5.5.2 Formation of HAG 15-Fe^{3+} adducts

Electrospray ionization mass spectrometry confirmed formation of both 2:1 and 3:1 adducts between HAG **15** and Fe^{3+}, with these major signals at m/z = 678.35 and 990.36, respectively (**Figure 5.23**).

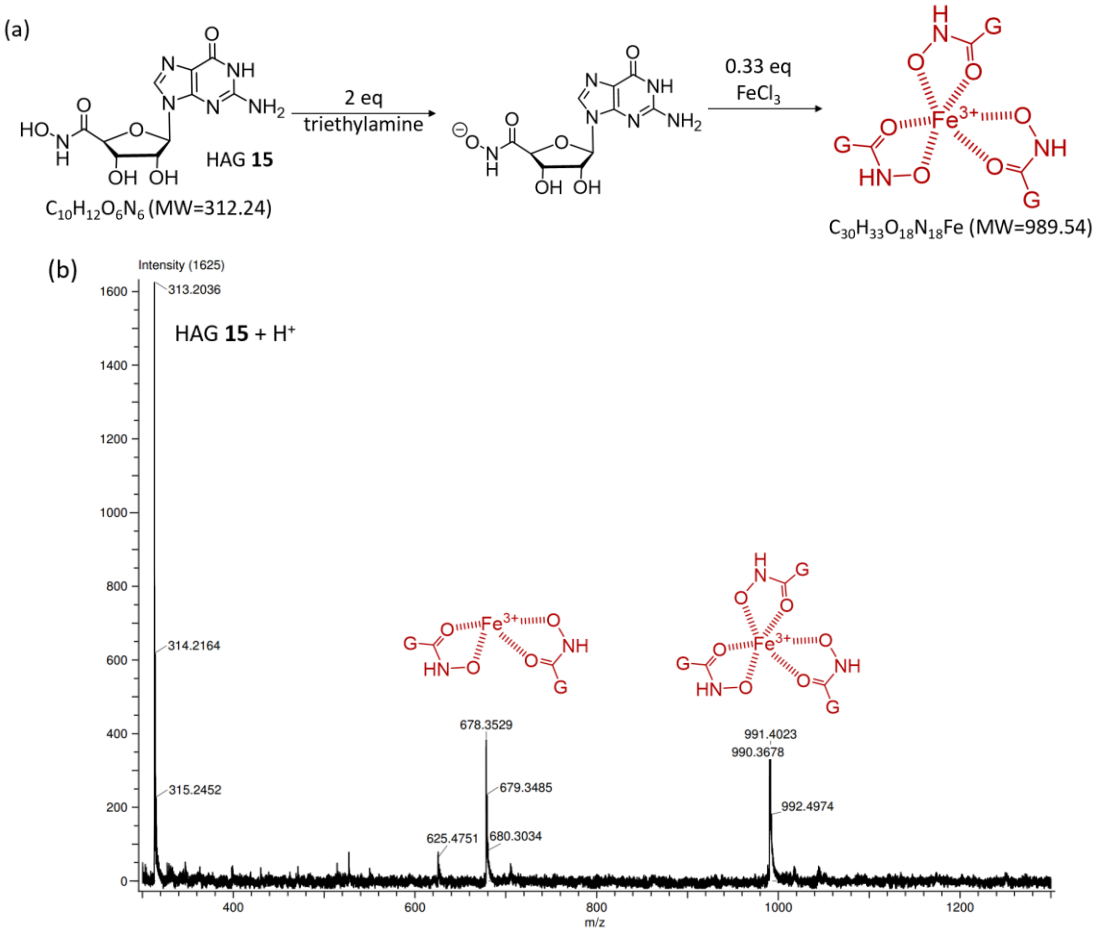

Figure 5.23: (a) Schematic showing formation of HAG **15**-Fe^{3+} complexes. (b) ESI-MS data shows the 2:1 and 3:1 adducts between HAG **15** and Fe^{3+}, with these major signals at m/z = 678.35 and 990.36, respectively.

5.5.3 HAG 15/G 1-$FeCl_3$ hydrogel

A 1:1 mixture of HAG **15**/G **1** (64 mM), in the presence of 2 eq KCl and 0.33 eq $FeCl_3$ (relative to HAG **15**), formed a red hydrogel, indicating the presence of hydroxamate-Fe^{3+} complex embedded within the matrix(**Figure 5.24a**). The hydrogel is self-standing and shows Tyndall effect with a laser pen, indicating the formation of a well-dispersed colloidal system.[271] The Fe(III) binding ability of HAG **15**/G **1** hydrogel could be potentially applied to cell culture to inhibit bacterial growth by competing chelation of Fe(III) with siderophores,[272] and shows promise for biodegradable material to treat iron-overdose/aluminum toxicity.[273]

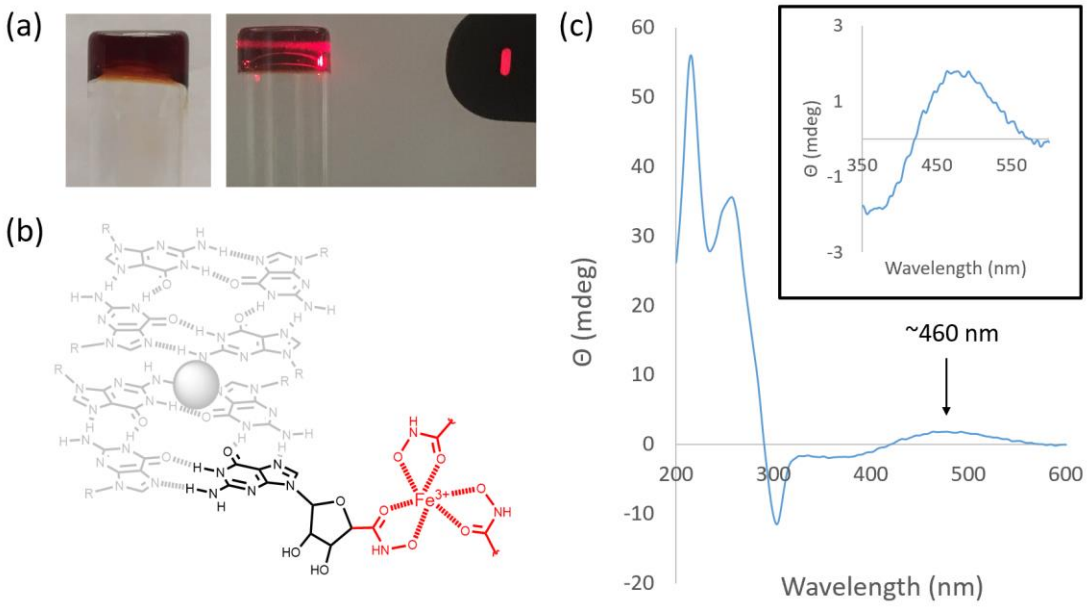

Figure 5.24: (a) In the presence of 2 eq of KCl and 0.33 eq $FeCl_3$ a 1:1 mixture of HAG **15**/G **1** formed a self-standing red hydrogel, indicating formation of the hydroxamato-Fe^{3+} complex in the gel matrix. The red gel showed the Tyndall effect upon shining light from a red laser pen, indicating that the gel is a well-dispersed colloidal system. (b) The ChemDraw image shows a possible coordination complex that is formed by coordination of Fe^{3+} by 5′-HA groups within the hydrogel. (c) CD spectroscopy shows an induced CD signal near 460 nm (inset) for the HAG **15**/G **1** KCl hydrogel (2 wt %, 2 eq KCl) containing 0.33 eq of $FeCl_3$ relative to HAG **15**. This induced CD band is at the same wavelength as the UV absorbance for the hydroxamate-Fe^{3+} complex. This

data indicates that the coordination complex, on the sugar's 5′-sidechain, senses the helical chirality of the core G-quadruplex structure.

Notably, this red gel exhibited an induced CD signal near 460 nm, indicating that the hydroxamate-Fe^{3+} complex, located on the sugar's 5′-sidechain, senses the chirality of the helical G-quadruplex that makes up the core of the hydrogel (**Figure 5.24b-c**).

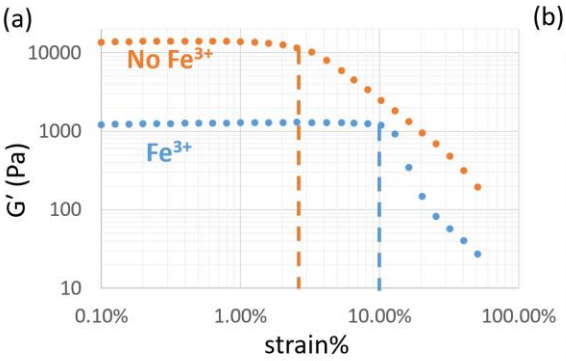

	G′ (Pa)	Critical strain
No Fe(III)	14000	2.5%
With Fe(III)	1300	10%

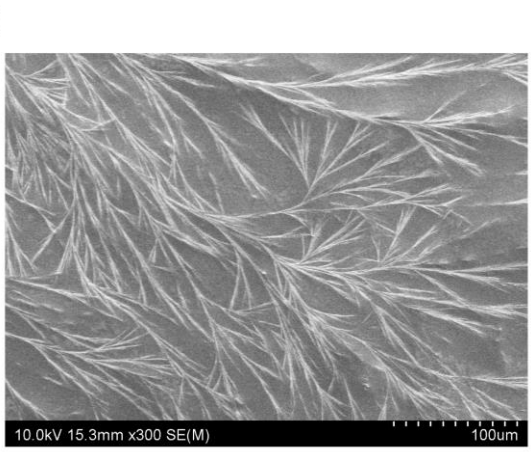

Figure 5.25: (a) Strain sweep rheology data for a 1:1 HAG **15**/G **1** KCl hydrogel (2 wt % nucleoside, 2 eq KCl). The blue plot is for a hydrogel that contains 0.33 eq of $FeCl_3$ relative to HAG **15**. This data shows that incorporation of Fe^{3+} produces a softer (lower G′) and stronger (higher critical strain) hydrogel than the hydrogel that does not contain $FeCl_3$, indicating possible cross-linking of gel fibers produced by formation of hydroxamato-Fe^{3+} complexes (see cartoon in **Figure 5.24**). Comparison of G′ and critical strain data from the strain sweep data is summarized in the table. (b) An SEM image of HAG **15**/G **1** KCl hydrogel (2 wt % nucleoside, 2 eq KCl, 0.33 eq of $FeCl_3$ relative to HAG **15**).

Comparative rheology showed that the Fe^{3+}-containing hydrogel is softer (lower G′ of 1300 Pa vs. 14,000 Pa) but stronger (higher critical strain of 10 % vs. 2.5 %) than the corresponding HAG **15**/G **1** gel without Fe^{3+} (**Figure 5.25a**). The material's increased strength is consistent with additional crosslinks due to hydroxamate-Fe^{3+} coordination from neighboring G_4-nanofibers, as observed for polymer hydrogels

strengthened by catechol-Fe^{3+} cross-links.[274] SEM shows branched and pliable fibers with a thickness of ~30 nm (**Figure 5.25b**).

5.5.4 Guanosine-agarose dual network hydrogels

To make the hydrogel surface more writable, we introduced natural product agarose (Aga) to produce a dual-network hydrogel (**Figure 5.26a**).[275,276] A HAG **15**/G **1**/Aga KCl hydrogel was able to form with higher stiffness than HAG **15**/G **1** KCl hydrogel (**Figure 5.26b-d**).

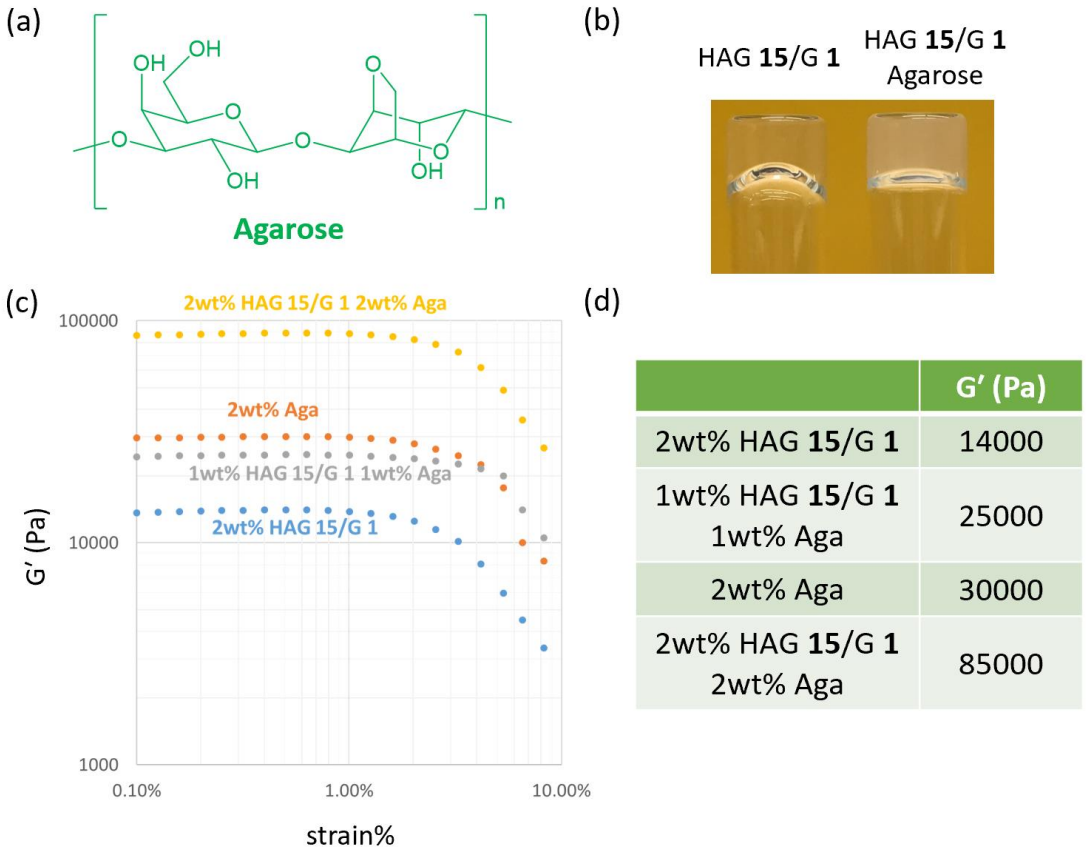

	G′ (Pa)
2wt% HAG **15**/G **1**	14000
1wt% HAG **15**/G **1** 1wt% Aga	25000
2wt% Aga	30000
2wt% HAG **15**/G **1** 2wt% Aga	85000

Figure 5.26: Introduction of agarose (Aga) into the 1:1 binary mixture HAG **15**/G **1** makes dual network hydrogels that are stiffer than the HAG **15**/G **1** hydrogels (a) Structure of agarose. (b) Vial inversion test shows that dual network hydrogel (right: 0.5 wt % HAG **15**/G **1**, 0.5 eq KCl, 0.5 wt % Aga) is stiffer than HAG **15**/G **1** hydrogel (left: 1 wt % HAG **15**/G **1**, 0.5 eq KCl) as judged by the lack of curve at the interface

of the dual network gel. (c) & (d) Rheological strain sweep data shows that addition of Aga significantly increases the stiffness of the G_4-hydrogels (all gels were made using 2 eq of KCl).

5.5.5 Drawing on hydrogel surface by hand

The dual network hydrogel (2wt% Aga, 2wt% HAG **15**/G **1**, 2eq KCl) was easily writable with a 100 mM $FeCl_3$ solution that gives a red "+" pattern (**Figure 5.27**). Control experiments with Aga, Aga+KCl, 5′-amideG **18**/G **1**/Aga and 5′-hydrazideG **3**/G **1**/Aga hydrogels gave no visible patterns, ruling out a guanine nucleobase-Fe^{3+} interaction as being responsible for the red color.

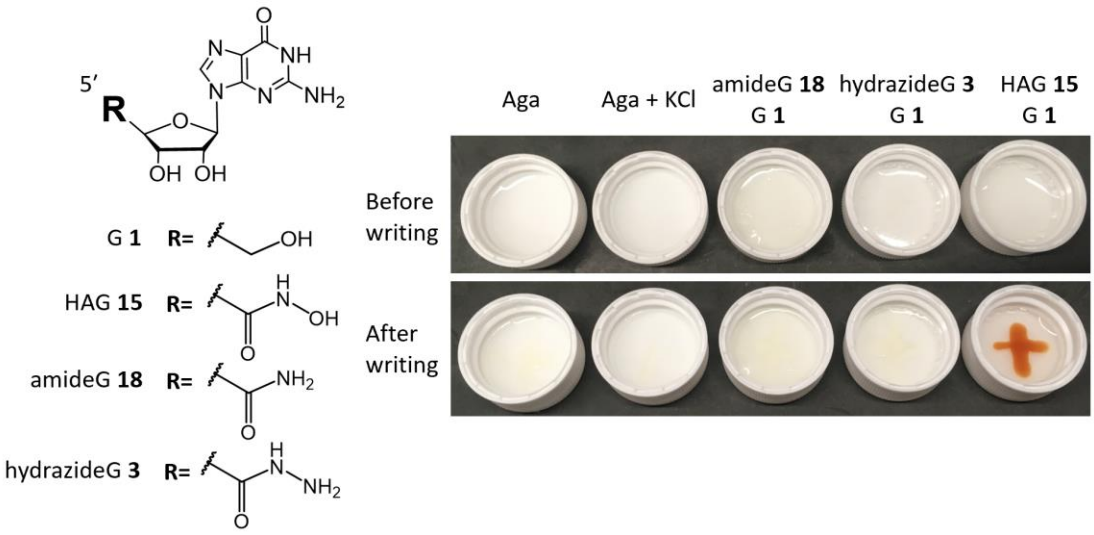

Figure 5.27: On the left are the structures of compounds that were used to make a series of binary G_4-hydrogels. On the right are vial caps containing different hydrogels made from Aga and binary guanosine systems (2 wt % Aga, 2 wt % of a 1:1 mixture of G **1** and 5′-analog, 2 eq KCl). The photographs show that the interaction between the 5′-hydroxamate of HAG **15** and Fe^{3+} interaction is crucial for the production of a visible image, as only the HAG **15**/G **1**/Aga hydrogel showed a "+" pattern after applying a solution of 100 mM $FeCl_3$ to the hydrogel surfaces.

As shown in **Figure 5.28a** we drew, by hand, a red "+" pattern on the gel surface with a glass rod dipped in $FeCl_3$ solution (100 mM). Even after a month, this pattern

remained crisp, showing no diffusion of color. To confirm that the G-quadruplex polymer is essential for fixing the pattern, we drew a red "+" with $FeCl_3$ on a 2 wt % agarose hydrogel containing acetohydroxamic acid (AHA, 32 mM). As shown in **Figure 5.28a** the pattern drawn on the Aga/AHA hydrogel blurred relatively quickly, as the mobile AHA hydroxamate-Fe^{3+} complex diffused through the gel matrix. Using the HAG **15**/G **1**/Aga KCl gel as paper and $FeCl_3$ as ink we drew by hand the Chinese characters "鸟苷" for "guanosine" and we also painted a sailboat out on the water (**Figure 5.28b**).

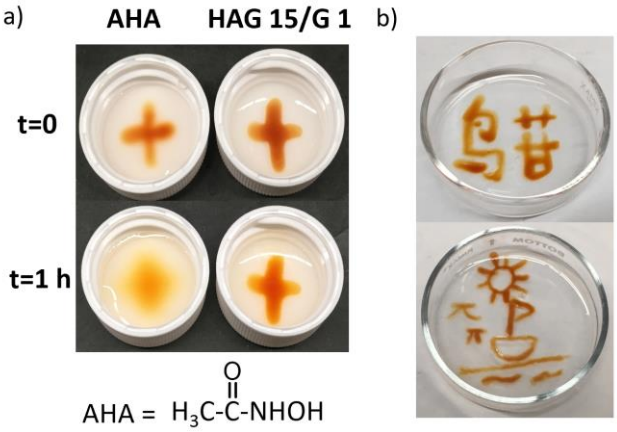

Figure 5.28: A hydrogel made from HAG **15**/G **1** and agarose can be patterned with a solution of $FeCl_3$. a) A "+" pattern made on HAG **15**/G **1**/Aga gel by writing with 100 mM solution of $FeCl_3$ remained fixed over time (right column). A similar image written on an agarose gel containing 32 mM of acetohydroxamic acid (AHA) showed significant diffusion of red color after 1 h (left column). b) Drawings of the Chinese characters "鸟苷" for guanosine and of a sailboat. Patterns on the gel surface were created by hand using a glass rod dipped in a solution of 100 mM $FeCl_3$

5.5.6 Drawing on hydrogel surface using a 3D-printer

While drawing by hand was enjoyable, we could dispense the $FeCl_3$ solution with much finer control by using a syringe pump mounted on a computer-controlled 3D-

printer (**Figure 5.29a-b**). In this way we generated much more intricate patterns, including a G-quartet and the Maryland's mascot *Testudo* (**Figure 5.29c**). Other patterns involve "UMD" with different shades, a Tai-Chi symbol and a guanine. All the patterns in **Figure 5.29c**, created either by hand or with 3D printer, have remained well-resolved for months, whether the gels were allowed to dry in air or kept wet in KCl solution.

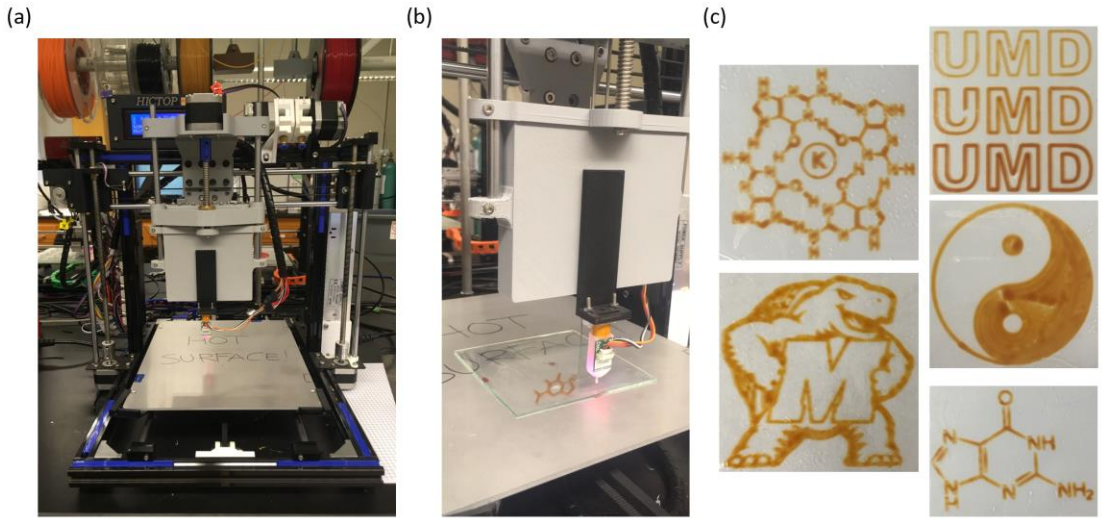

Figure 5.29: a) A picture of the 3D printer used for patterning. b) A close-up picture of the syringe extruding $FeCl_3$ solution onto a flat HAG **15**/G **1**/Aga hydrogel controlled by the 3D printer. c) Images of patterns on the gel surface: a G-quartet and the Maryland's mascot *Testudo*, the letters "UMD" printed with different shades of color, a Tai-Chi symbol, and the molecular structure of guanine.

5.5.7 HAG 15/G 1 can be erased with vitamin C and rewritten with $FeCl_3$

Next, we asked if patterns created by the hydroxamate-Fe^{3+} complex could be erased by treating the gel with a reducing agent, since reduction of Fe^{3+} to Fe^{2+} should greatly decrease the affinity of metal ion for the HA group and also disrupt the LMCT interaction between HA and Fe^{3+} that is responsible for the red color (**Figure 5.30a**). We chose vitamin C (VC) as reductant, as it is well known to reduce Fe^{3+} to Fe^{2+},

especially in the context of supramolecular assemblies and polymer hydrogels.[277,278] We started the write-erase experiment by drawing a "G" pattern on a HAG **15**/G **1**/Aga gel with a 100 mM solution of $FeCl_3$. Bathing the gel in a solution of 155 mM KCl containing VC (100 mM) erased the "G" marking within minutes, consistent with reduction of Fe^{3+} to Fe^{2+} (**Figure 5.30b**). Controls showed that the red pattern remained intact after soaking the gel in 155 mM KCl solution, indicating that the hydroxamate-Fe^{3+} complex stays fixed even when submerged in salt water.

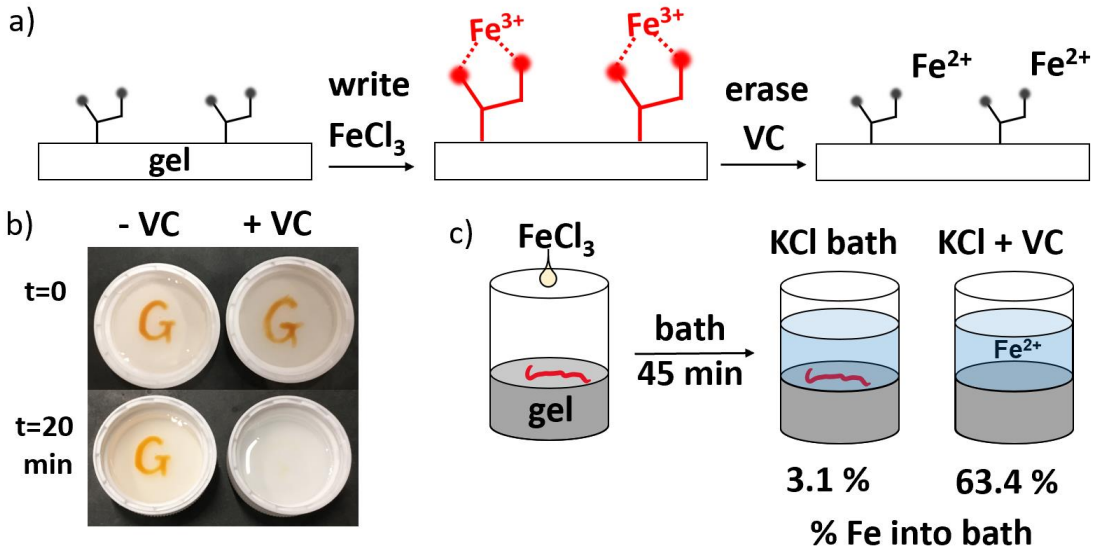

Figure 5.30: a) Illustration of writing/erasing process on HAG **15**/G **1**/Aga hydrogel using Fe coordination & Fe redox chemistry. b) A "G" pattern written on a HAG **15**/G **1**/Aga hydrogel with $FeCl_3$ was erased after bathing with 100 mM VC in 155 mM KCl for 20 min (right). The pattern was stable when bathed in a solution of 155 mM KCl (left). c) A HAG **15**/G **1**/Aga hydrogel (1 mL) patterned with Fe^{3+} was bathed for 45 min with 1 mL of 155 mM KCl solution that did or did not contain 16 mM VC. Quantification of iron in the bath solution and gel, using ICP-MS, showed significantly more iron released into the bath containing VC.

We used ICP-MS to quantify the amount of iron released into the supernatant after the patterned gel had been soaked in 1 mL of 155 mM KCl solution for, with or without

added VC (16 mM). For the gel whose red pattern had been erased by treatment with VC, we found that 63.4 ± 5.5 % of total iron was released into the bathing solution (more iron was undoubtedly released from the gel matrix into its sol phase upon reduction by VC). In contrast, ICP-MS measurements showed that only 3.1 ± 1.7 % of total iron originally loaded onto the gel leached into the supernatant after bathing the gel in a KCl solution that did not contain VC (**Figure 5.30c**).

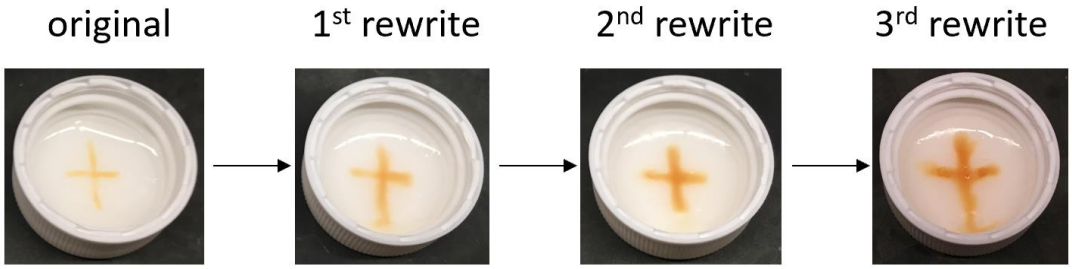

Figure 5.31: The 1:1 HAG **15**/G **1**/Aga (2 wt % nucleoside, 2 wt % Aga, 2 eq KCl) gel is rewritable with $FeCl_3$ (50 mM) for at least 3 cycles.

This write-erase experiment confirms that reduction of Fe^{3+} to Fe^{2+} by VC triggers disassembly of the hydroxamate-iron complex with concomitant release of reduced iron into solution. We also found that the hydrogel could be reused for at least 3 rounds of writing and erasing, demonstrating the reversibility of the Fe^{3+} chelation/reduction process (**Figure 5.31**). Importantly all the components needed for this write-erase system, including the paper (**1** and **15**, agarose and KCl), ink ($FeCl_3$) and eraser (vitamin C) are either naturally occurring or easily derived from natural products, abundant, inexpensive, non-toxic and biocompatible.

5.6 Conclusions

In conclusion, we demonstrated that a HA analog of guanosine, HAG **15**, forms a stable binary hydrogel with G **1** and KCl. The 5′-HA sidechains in the gel (pK_a 8.4) are pH-responsive. Gels containing the anionic hydroxamate bind the cationic dye, TO, resulting in enhanced fluorescence that can be detected under a UV lamp. The ability of the HA sidechains in the HAG **15**/G **1** gel to function together as a supramolecular siderophore to chelate Fe^{3+} provides a patternable/erasable hydrogel made from biocompatible materials. Patterns generated on the surface of this G-quartet hydrogel form instantly, can be seen with the naked eye, remain sharp over time and can be easily erased. From a broader perspective, we believe that the hydroxamic acid group should be quite useful if grafted onto other supramolecular gelators. In just 1 or 2 synthetic steps, common gelators containing carboxylic acid sidechains (such as amino acids, peptides, sugars and fatty acids) should be readily converted into HA analogs, thus altering the self-assembly properties of the gelators and introducing new functions into the resulting supramolecular hydrogels.

Chapter 6: Supporting information

6.1 General experimental

Chemicals and solvents were purchased from Aldrich, Alfa Aesar, Carbosynth, or Oakwood Chemical. NMR spectra were recorded on Bruker DRX-400, Bruker DRX-500, or Bruker AVIII-600 spectrometers. Chemical shifts are reported in ppm relative to the residual solvent peak. Deuterated solvents were purchased from Cambridge Isotope Labs. CD spectroscopy was performed on a Jasco J-810 spectropolarimeter. ESI-MS experiments were done with a JEOL AccuTOF spectrometer. UV-visible spectroscopy measurements were made on a Varian Cary 100 spectrometer. Rheological data was collected with an AR2000 stress-controlled rheometer from TA Instruments. IR spectra were collected on a Thermo Nicolet Nexus 670 FT-IR with ATR module at room temperature. PXRD experiments were performed with a Bruker D8 Advance Bragg-Brentano Diffractometer. SEM images were obtained on a Hitachi SU-70 High Resolution Analytical SEM. X-ray single crystal diffraction was measured on a Bruker Smart Apex2 diffractometer. ICP-MS samples were analyzed using a ThermoFinnigan Element 2 single collector Inductively Coupled Plasma Mass Spectrometer, fitted with aluminum sampler and skimmer cones. Fluorescence spectroscopy measurements were recorded on a Hitachi F-4500 fluorescence spectrophotometer.

6.2 Supporting information for Chapter 2

General Procedure for Preparation of 5′-SHG 27 hydrogels: The desired amount of 5′-SHG **27** together with other guanosine analogs was weighed into a vial and the appropriate amount of deionized water was added. The resulting mixture was sonicated until large aggregates were broken up to give a fine suspension. An appropriate amount of K^+ solution (KCl, KOH or $KB(OH)_4$) was added to the mixture before the vial was flushed with N_2 gas to avoid thiol oxidation by O_2. The suspension was then heated with a heat gun until a clear solution resulted. The vial was removed from the heat and allowed to cool at rt.

Experimental and Summary of Crystal Structure Data for 8-thioG 37•2H₂O. A suitable single crystal of $C_{10}H_{17}N_5O_7S$ (UM3255) was selected and measured on a Bruker APEX 2 SMART diffractometer. The crystal was kept at 120(2) K during data collection. The integral intensity was corrected for absorption using SADABS software[a] via the multi-scan method. Resulting minimum and maximum transmission are 0.862 and 0.990 respectively. The structure was solved with the ShelXT-2014 program,[b] and refined with the ShelXL-2015 program,[c] and least-square minimization using ShelX software.[b] Number of restraints used = 2. The H atoms were located from difference Fourier maps and freely refined. Crystal structure data for the dihydrate 8-thioG **37**•$2H_2O$ have been deposited with Cambridge Crystallographic Data Centre as CCDC-1960382.

[a] Krause, L.; Herbst-Irmer, R.; Sheldrick, G.M.; Stalke, D. Comparison of silver and molybdenum microfocus X-ray sources for single-crystal structure determination. *J. Appl. Cryst.* **2015**, *48*, 3-10.

[b] Sheldrick, G. M. *SHELXT* – Integrated space-group and crystal-structure determination.

Acta Cryst. **2015**, *A71*, 3-8.

[c] Sheldrick, G. M. Crystal Structure Refinement with *SHELXL*. *Acta Cryst.* **2015**, *C71*, 3-8.

Table 6.1 Crystal and Structure Refinement Data for UM3255

Identification code	UM3255
Empirical formula	$C_{10}H_{17}N_5O_7S$
Formula weight	351.34
Temperature/K	120(2)
Crystal system	monoclinic
Space group	C2
a/Å	23.123(2)
b/Å	9.7734(9)
c/Å	6.3397(6)
α/°	90
β/°	91.2914(14)
γ/°	90
Volume/Å^3	1432.3(2)
Z	4
ρ_{calc}g/cm^3	1.629
μ/mm^{-1}	0.275
F(000)	736.0
Crystal size/mm^3	0.31 × 0.09 × 0.035
Radiation	MoKα (λ = 0.71073)
2Θ range for data collection/°	3.524 to 59.968
Index ranges	-32 ≤ h ≤ 32, -13 ≤ k ≤ 13, -8 ≤ l ≤ 8
Reflections collected	8608
Independent reflections	4064 [R_{int} = 0.0213, R_{sigma} = 0.0400]
Data/restraints/parameters	4064/2/242
Goodness-of-fit on F^2	1.186
Final R indexes [I>=2σ (I)]	R_1 = 0.0367, wR_2 = 0.0587
Final R indexes [all data]	R_1 = 0.0452, wR_2 = 0.0596
Largest diff. peak/hole / e Å^{-3}	0.30/-0.30
Flack parameter	-0.05(5)

6.3 Supporting information for Chapter 3

Determination of water solubility of guanosine derivatives 1-6.

Working curve and determination of molar extinction coefficients: For each guanosine analog, dilute aqueous solutions at different concentrations were prepared (0, 0.005, 0.01, 0.02, 0.03 g/L). The absorbance of each sample at λ= 254 nm was measured by UV-Vis spectroscopy at 22 ^{o}C. The experiments were done in triplicate and the absorbance at λ= 254 nm at 22 ^{o}C was plotted against the concentration of G analog (g/L) to give working curves and for determining the water solubility of G analogs **1**-**6** (see Figure 6.1 for molar extinction coefficients).

Solubility determination: To separate vials 10 mg of each G analog **1**-**5** was added to 1 mL of deionized water (for highly soluble GMP **6**, 90 mg was added to 1 mL of water). The mixtures were sonicated and stirred at 22^{o}C for 1 h before ultracentrifugation was done to remove insoluble particles. Then, 10 μL of the supernatant was diluted with 3 mL of DI water (for GMP **6**, 10 μL of supernatant was diluted with 1 mL of water, and 10 μL of that new stock solution was diluted with 3 more mL of water). The absorbance at λ = 254 nm at 22 ^{o}C was then measured by UV spectroscopy for all final diluted solutions of **1**-**6**. All experiments were done in triplicate and the absorbance at λ = 254 nm was used to calculate the concentration of each saturated solution of analogs **1**-**6**.

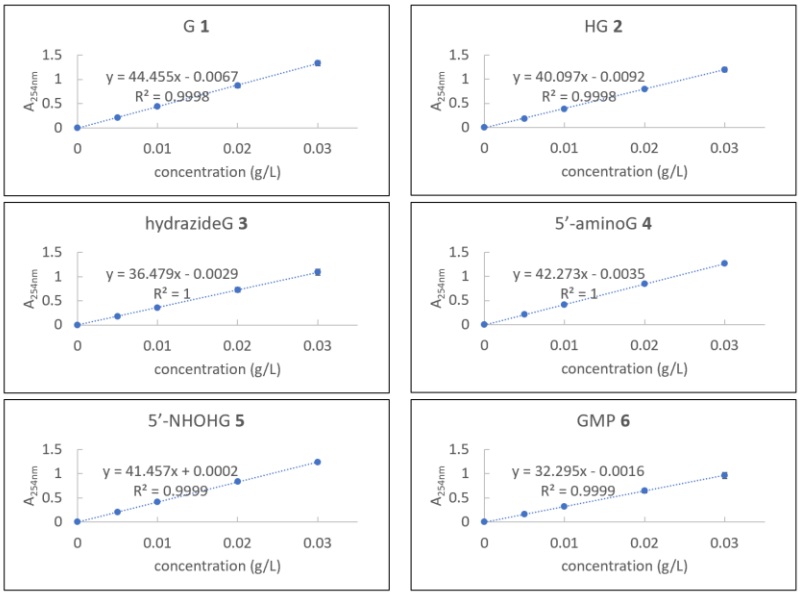

	ε (L·mol⁻¹·cm⁻¹)
5′-NHOHG **5**	12364.96
5′-aminoG **4**	11931.98
G **1**	12591.43
hydrazideG **3**	11354.45
HG **2**	11920.04
GMP **6**	11730.19

Figure 6.1: (left) Plots of A_{254} values vs. concentration for determining water solubility of each G derivative **1-6**. (right) The molar extinction coefficient for G analogs **1-6**.

Procedures for Preparation and Characterization of the HG 2•KCl Hydrogel

General Gel Preparation Procedure: A weighed amount of guanosine derivatives G **1-6** was added to deionized water. The vial was sonicated until any large insoluble particles were broken up. The resulting suspension was then heated with a heat-gun until a clear solution was obtained. The vial was removed from the heat and the appropriate amount of KCl or other salt solution was immediately added. The resulting mixture was then vigorously shaken and heated to a boil again. The mixture was then allowed to cool at room temperature. Experiments, measurements observations on the resulting hydrogels were typically done 1 day after preparation, unless otherwise noted.

While preparing the hydrogels, we found that GMP **6** was easily dissolved, even at rt, whereas extended heating at high temperatures (~ 100 ^{o}C) was required to dissolve G

1, NH_2G **4** and NHOHG **5**. For HG **2** and hydrazideG **3**, milder heating (60-80 ^oC) was needed to obtain a clear solution. As shown below in **Figure 6.2**, the critical gelation concentration for the HG **2**•KCl gel with 0.5 eq KCl is between 0.8 wt % (54 mM) and 0.9 wt % (61 mM).

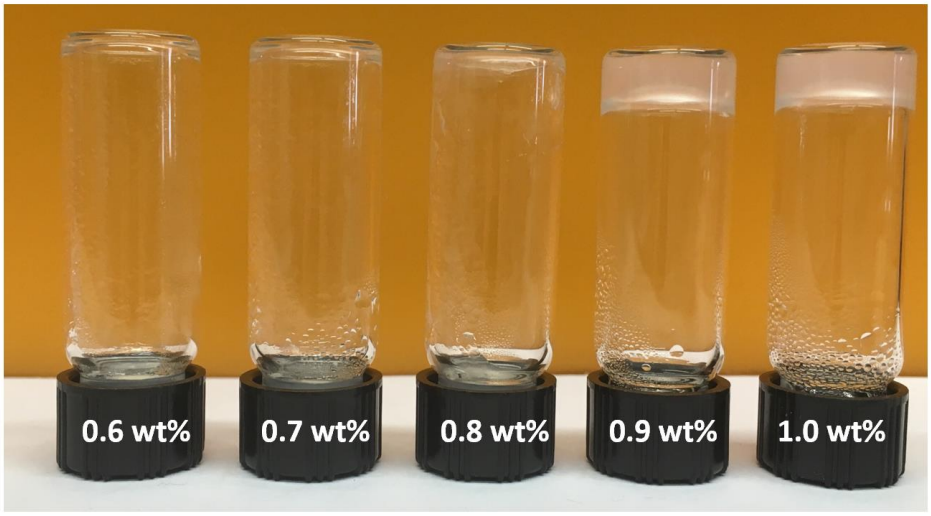

Figure 6.2: The critical gelation concentration for the gel with 0.5 eq KCl is between 0.8 wt % and 0.9 wt %. Picture was taken 1 day after preparation of the hydrogels.

Powder X-ray Diffraction Procedure: A 1 wt % HG **2**•KCl hydrogel (34 mM HG **2**, 17 mM KCl) was prepared using the general gel preparation procedure. After sitting for 1 day at rt the hydrogel sample was lyophilized to give a white powder. X-ray powder diffraction measurements were performed with a Cu radiation source at 20 °C using a Bruker D8 Advance Bragg-Brentano diffractometer equipped with a LynxEye detector.

Infrared Spectroscopy Procedure: A 1 wt % HG **2**•KCl hydrogel (34 mM HG **2**, 17 mM KCl) was prepared using the general gel preparation procedure. After sitting for 1 day at rt the hydrogel sample was lyophilized to give a white powder. Infrared spectroscopy was done using a Thermo Nicolet Nexus 670 FT-IR with ATR module at room temperature. Spectra were recorded for both the lyophilized HG **2**•KCl hydrogel and for "monomeric" HG **2** in the absence of any added KCl.

Circular Dichroism Procedure: A 2 wt % HG **2**•KCl hydrogel (68 mM HG **2**, 1 equiv KCl) was prepared using the general gel preparation procedure. The CD spectra were

recorded at 25 °C with a Hellma 106-QS quartz cell with an optical path length of 0.01mm (scanning speed 200 nm/min; response time 2 seconds). The experiment was repeated at least 3 times, and the curves were smoothed and averaged.

SEM Procedure: A 2 wt % HG **2**•KCl hydrogel (68 mM, 0.5 eq KCl) was prepared using the general gel procedure. A small amount of the hydrogel was loaded onto an AL holder after which 0.3 μL of 3% ionic liquid (HILEM 1000 for Hitachi EM) was pipetted on top of the gel sample. The sample was allowed to equilibrate overnight at room temperature before SEM images were taken.

Rheology Procedure: Gels were made following the general procedure. Experiments were performed on an AR2000 stress-controlled rheometer from TA Instruments at 20 °C with a 20 mm diameter parallel plate geometry. Strain sweeps of 2 wt % HG **2**•KCl hydrogel (68 mM) made with different amounts of KCl were taken at a constant angular frequency of 10 rad/s 1 day after gel preparation.

The *in situ* formation of self-assembled colloidal suspensions by HG 2•KCl and use for separation of anionic dye Naphthol Blue Black.

Procedure for in situ generation **of self-assembled colloidal suspensions by HG 2•KCl*:*** G **1** or HG **2** was added to deionized water to give a suspension containing the nucleoside at a concentration of 10 mg/mL. The mixture was sonicated, stirred for 1 h at rt and ultracentrifuged to remove insoluble particles. The clear supernatant contained a saturated solution of either G **1** (2.17 mM) or HG **2** (14.53 mM). Then, varying amounts of a KCl stock solution was added to the saturated solution of G **1** or HG **2** and the solution was well mixed. Unless otherwise noted, all observations or experiments were performed 1 hour after KCl addition. As shown below in **Figure 6.3** a milky white precipitate formed when 100 mM KCl was added to HG **2**.

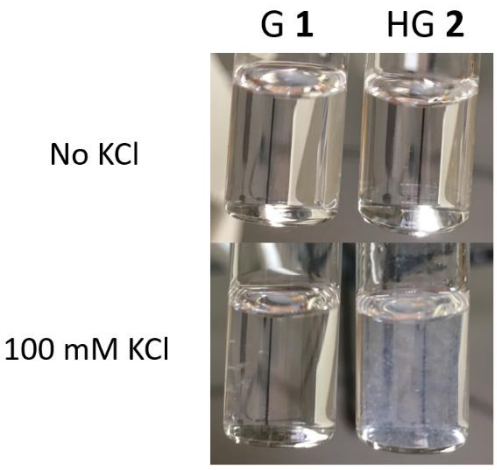

Figure 6.3: Addition of KCl (to give a final KCl concentration of 100 mM) into a saturated solution of HG **2** (14.53 mM) generated milky white aggregates (lower right photo), whereas a saturated solution of G **1** remained clear in the presence of the same concentration of KCl.

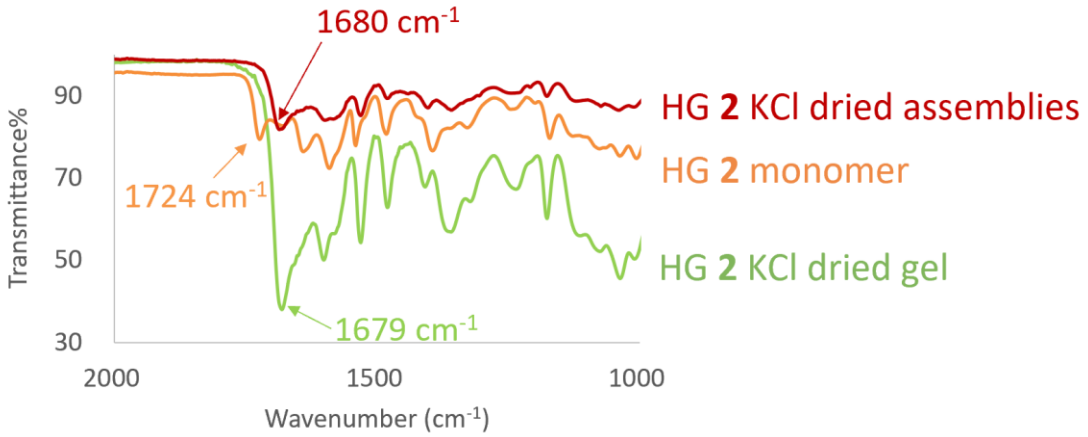

Figure 6.4: IR spectra show that the carbonyl wavenumber (red spectrum, 1680 cm^{-1}) of the freeze-dried assemblies colloidal assemblies made from addition of KCl to a saturated solution of HG **2** is similar to that for a dried powder from a 1 wt % HG **2**•KCl hydrogel (34 mM HG **2**, 17 mM KCl) (green spectrum, 1679 cm^{-1}).

Procedure for UV Quantification of Precipitation of Nucleoside by KCl: Each vial depicted in **Figure 6.5A** was charged with 1 mL of a saturated solution of G **1** (2.17 mM) or HG **2** (14.53 mM), and a specified amount of a 4 M KCl stock solution was added to each vial. The resulting solutions were mixed well and allowed to sit at rt for 1 h. Then, the vials were ultracentrifuged to remove any insoluble particles and 10 μL of supernatant was pipetted into a vial containing 3 mL of deionized water. The sample was well-mixed and the amount of G species in solution was quantified using UV spectroscopy by measuring the guanine absorbance at λ= 254 nm. These A_{254} measurements are plotted below in **Figure 6.5B**.

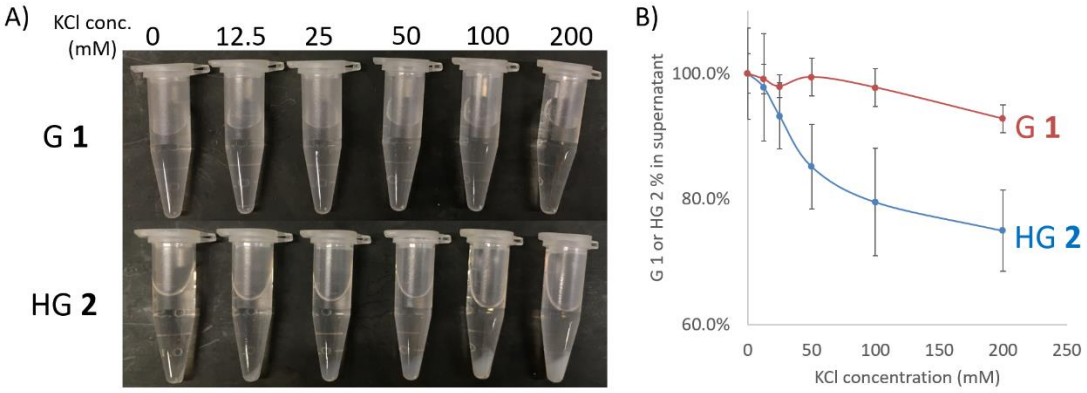

Figure 6.5: A) Photos showing that addition of higher concentrations of KCl generates more solid phase on the bottom of the vials for HG **2**, whereas G **1** shows no obvious precipitation. B) UV-Vis quantification of G concentration in the supernatant decreases more for HG **2** with increasing addition of KCl, indicating that HG **2** is more effective generation of assemblies than G **1** (at 200 mM KCl: 93% G **1** vs 75% HG **2** in supernatant).

Qualitative Dye Binding Procedure: Two different HG **2**•KCl hydrogel (2 wt %, 68 mM, 2 eq KCl) were prepared, one containing the cationic dye CV and one containing the anionic dye NBB. While the solution of HG **2**•KCl was still hot, 200 μM final concentration of CV or 200 μM of NBB dye solution was added to each solution and the vials were shaken. Then the solutions were immediately transferred to a mold made from parafilm and gels were allowed to form. After cooling for 1 hour at rt, the gel cubes were placed into a vial containing 5 mL of 155 mM KCl solution. The vials were gently shaken after 1 hour and the pictures were taken.

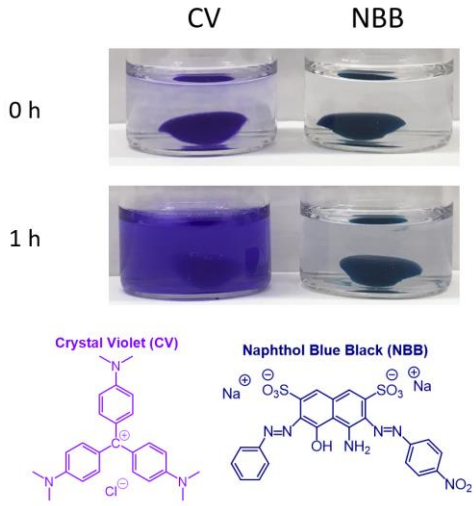

Figure 6.6: The HG **2**•KCl hydrogel (2 wt %, 68 mM, 2 eq KCl) binds anionic NBB while releasing cationic CV into 155 mM KCl. The selective binding indicates that the cationic G_4•K^+ hydrogel is selective for electrostatic binding of anions vs. cationic dyes.

Procedure for gas-phase uptake of propionaldehyde: The small vial (no cap) containing 0.5 mL of a hydrogel made from HG **2**•KCl or hydrazideG **3**•KCl (2 wt %, 68 mM, 0.5 eq KCl) was placed in the large vial, and a 1.0 equiv of neat propionaldehyde was pipetted into the outside vial. The large vial was immediately capped and sealed with parafilm. The small vial was taken out 2 days later and lyophilized to give a white powder, which was dissolved in 0.6 mL of DMSO-d_6 and the reaction products were analyzed by ^{1}H and ^{13}C NMR.

Figure 6.7: Experimental setup for gas phase uptake of propionaldehyde by HG **2**•KCl hydrogel.

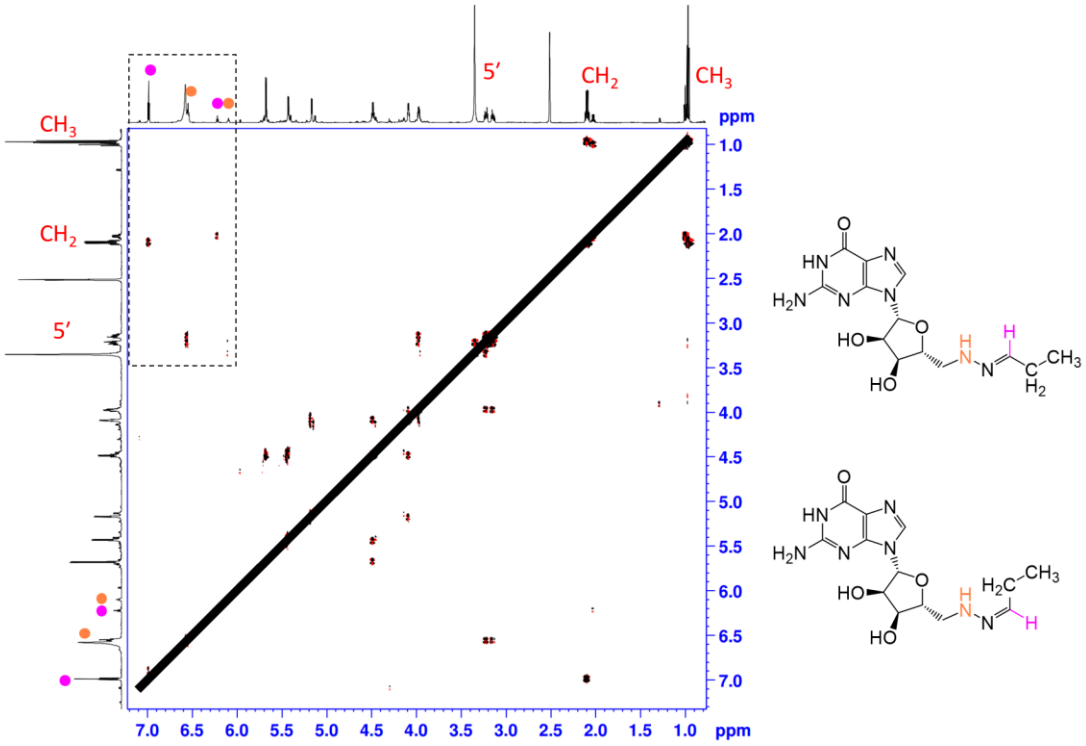

Figure 6.8: ^{1}H-^{1}H COSY 2D NMR showing assignments for hydrazone products trans-PG **7** (major) and cis-PG **7** (minor) from the gas phase reaction of HG **2**•KCl hydrogel with propionaldehyde. The box highlights ^{3}J coupling correlations between the imino protons (pink) and NH (orange) with 5'-CH_2 and the –CH_2- group originally from propionaldehyde.

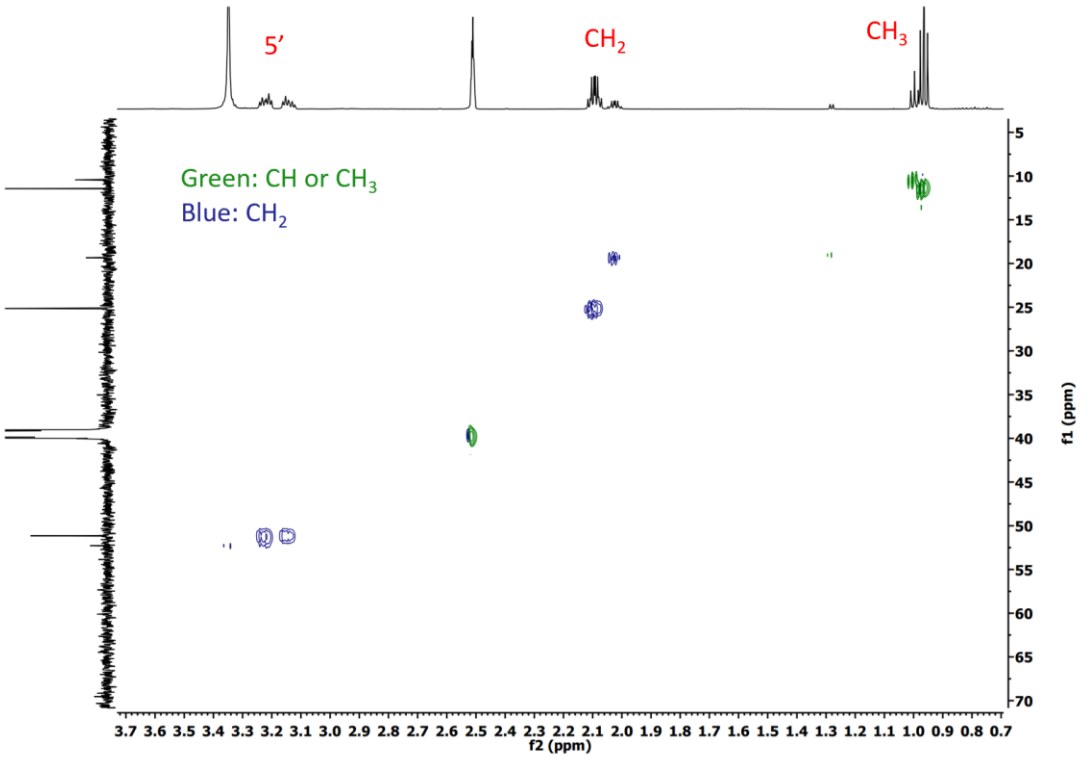

Figure 6.9: ^{1}H-^{13}C HSQC 2D NMR showing 2 sets of correlations for the hydrazone products trans-PG **7** (major) and cis-PG **7** (minor) from the gas phase reaction of HG **2**•KCl hydrogel with propionaldehyde.

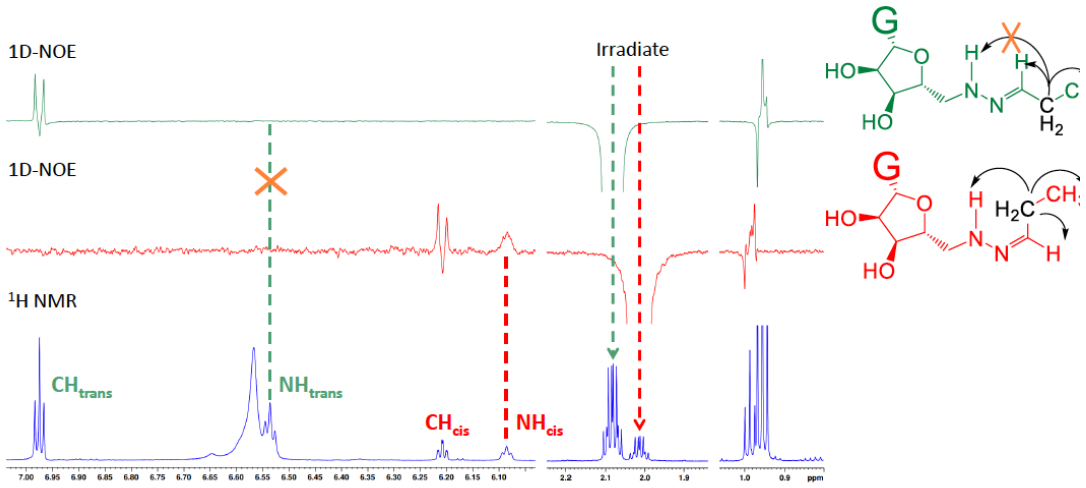

Figure 6.10: 1D NOE experiments that confirm assignment of hydrazone products trans-PG **7** (green structure) as the major product and cis-PG **7** (red structure) as the minor product from the gas phase reaction of HG **2**•KCl hydrogel with propionaldehyde.

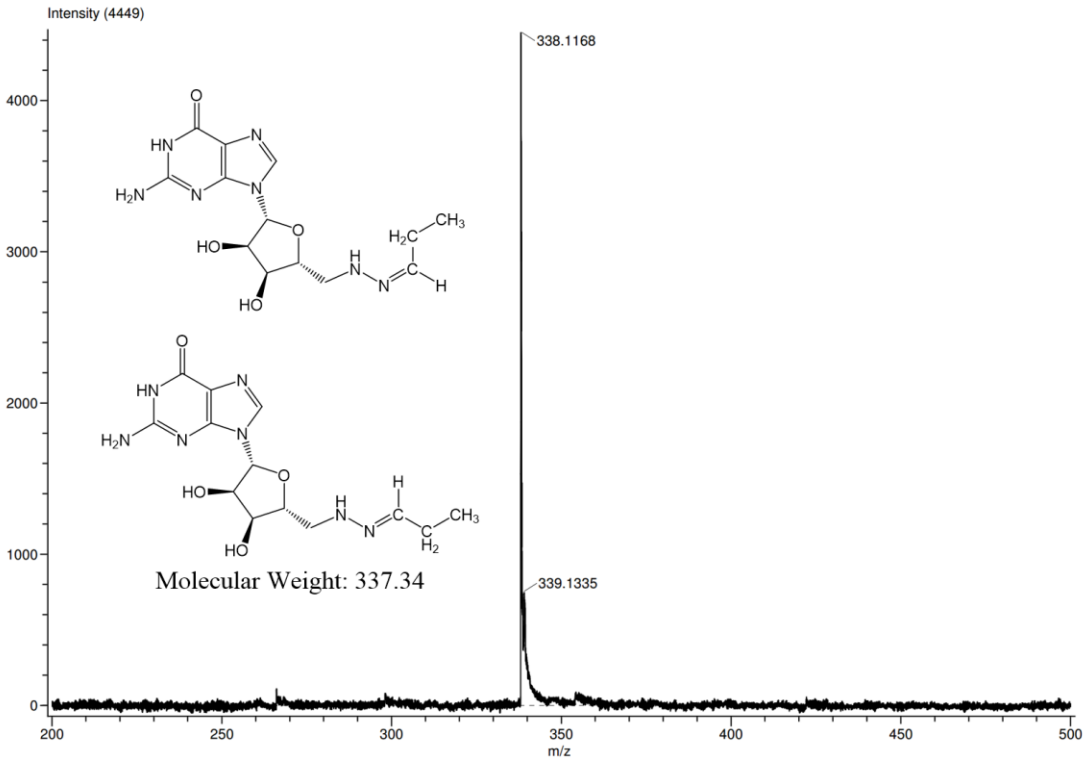

Figure 6.11: ESI-MS analysis of products from the gas phase reaction of HG **2**•KCl hydrogel with propionaldehyde.

6.4 Supporting information for Chapter 4

General Procedure for Preparation of G_4•K^+ hydrogels: The desired amount of guanosine derivatives **2** or **3** was weighed into a vial and the appropriate amount of deionized water was added (e.g. 2 wt% hydrazine **2** (68 mM), 0.5 eq KCl (34 mM)). The resulting suspension was sonicated until large aggregates were broken up to give a fine suspension. The suspension was then heated to boil with a heat gun until a clear solution resulted. The vial was removed from the heat and the appropriate amount of KCl was immediately added to the hot solution. The mixture was then vigorously shaken and heated to boil again. The mixture was then allowed to cool at room temperature.

Mass Spectrometry Procedure: 0.1 mL DMSO-d_6 solution of the freeze-dried hydrazine **2** or hydrazide **3** hydrogel (2 wt%, 0.5 eq KCl) after uptake of electrophile was diluted with 0.5 mL H_2O and then injected into the JEOL AccuTOF-CS Spectrometer.

Procedure for gas phase uptake of α,β-unsaturated carbonyls by G_4•K^+ hydrogels: A small vial, without a cap, containing 0.5 mL of a G_4•K^+ hydrogel made from either 5′-hydrazidoguanosine **3** or 5′-hydrazinoguanosine **2** (2 wt%, 0.5 eq KCl) was placed inside the larger vial, and 1.0 equiv of neat α,β-UC (either **AC**, **MVK** or **MA**) was added to the outside, larger vial (see **Figure 6.14**). The large vial was immediately capped and sealed with parafilm and the reaction mixture was allowed to stand at RT. The small vial was removed after 2 days, the hydrogel was lyophilized to give a white powder, which was dissolved in 0.6 mL of DMSO-d_6 and analyzed by ^{1}H and ^{13}C NMR and by ESI-MS.

Figure 6.12: The experimental setup for gas phase uptake of α,β-UC by G_4•K^+ hydrogels.

Preparation of 5′-deoxy-5′-pyrazolinoguanosine (4).

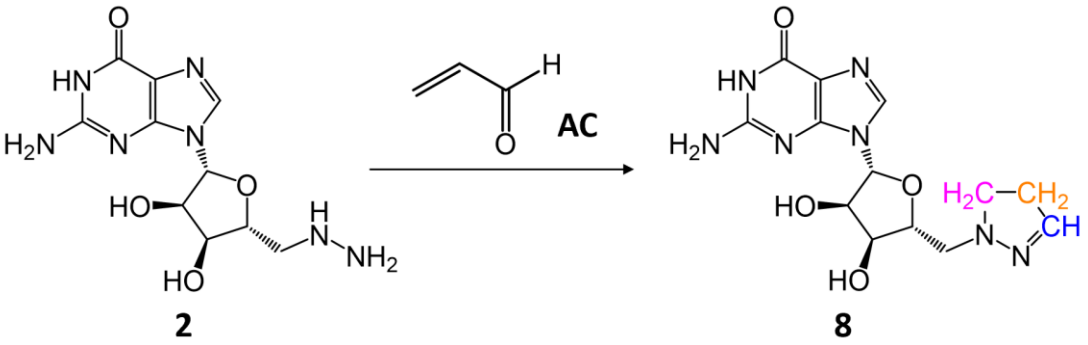

5′-deoxy-5′-pyrazolinoguanosine **8**. Using the experimental protocol for gas phase uptake described above, pyrazoline **8** was prepared from AC and 5′-deoxy-5′-hydrazinoguanosine **2**.[2] The lyophilized hydrogel, a white powder containing **8**, was analyzed by ^{1}H and ^{13}C NMR and by ESI-MS.

^{1}H NMR (DMSO-d_6) δ: 2.51-2.56 (2 H, m, yellow CH_2), 2.84-2.98 (2 H, m, pink CH_2), 3.02-3.08 (1 H, dd, 5′-CH_2, J=6.5 Hz, J=6.7 Hz), 3.21-3.26 (1 H, dd, 5′′-CH_2, J=8.3 Hz, J=5.0 Hz), 4.07 (1 H, m, 4′-CH), 4.12 (1 H, m, 3′-CH), 4.50 (1 H, m, 2′-CH), 5.22 (1 H, d, J=5.0 Hz, 3′-OH), 5.45 (1 H, d, J=6.0 Hz, 2′-OH), 5.68 (1 H, d, J=6.0 Hz, 1′-CH), 6.61 (2 H, s, NH_2), 6.81 (1 H, t, J=1.6 Hz, blue CH), 7.91 (1 H, s, 8-CH), 10.77 (1 H, s, br, N1H);

^{13}C NMR (DMSO-d_6) δ: 33.90 (yellow CH_2), 55.23 (pink CH_2), 58.36 (C5′), 71.55 (C4′), 72.73 (C2′), 82.51 (C3′), 86.35 (C1′), 116.69 (C5), 135.60 (C8), 142.81 (blue CH), 151.39 (C4), 153.75 (C2), 156.66 (C6);

ESI-MS m/z=335.98 (MW of **8**: 335.32)

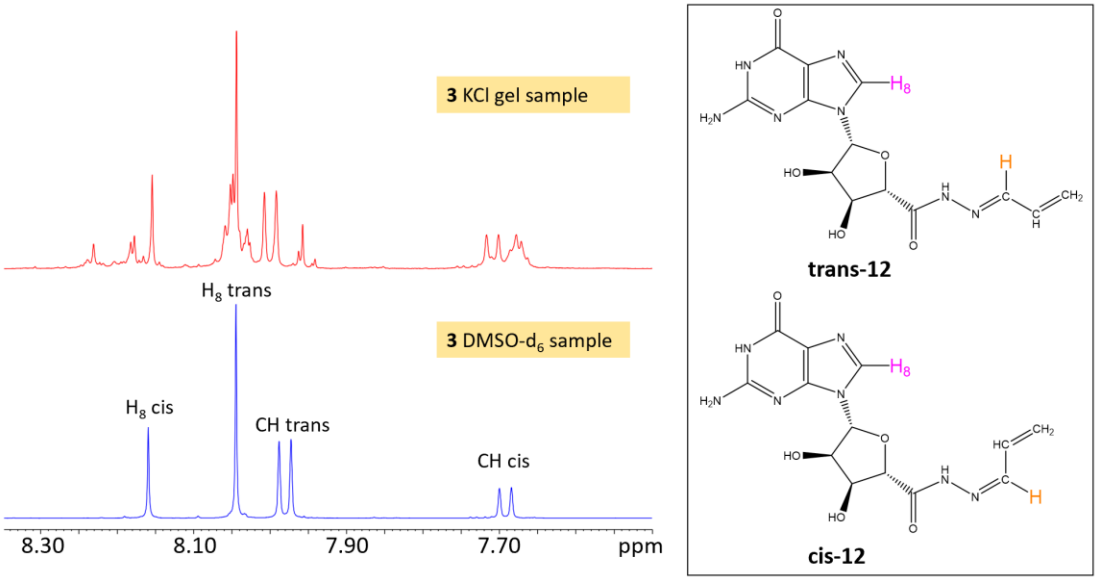

Figure 6.13: Top: A region of the ^{1}H NMR spectrum of reaction products formed by gas phase uptake of 1.0 eq of AC by the G_4•K^+ hydrogel made from 5′-hydrazidoguanosine **3** (2 wt%, 65 mM, 0.5 eq KCl) shows formation of a cis/trans mixture of acylhydrazones **12** and some cyclic adduct **13** (see also **Figure 6.16**). The region of the spectrum shown contains H_8 (pink) and the acylhydrazone CH (orange) in the acylhydrazones **12**. Bottom: The spectrum of a sample obtained by performing a gas phase uptake of 1.0 eq of AC with a 2 wt% solution of **3** in DMSO-d_6 for 2 days at RT. This sample gives a cleaner spectrum that shows formation of only cis/trans hydrazones **12**. All NMR signals were unambiguously assigned using 2D ^{1}H, ^{1}H-COSY and ^{1}H, ^{13}C-HSQC spectra (not shown).

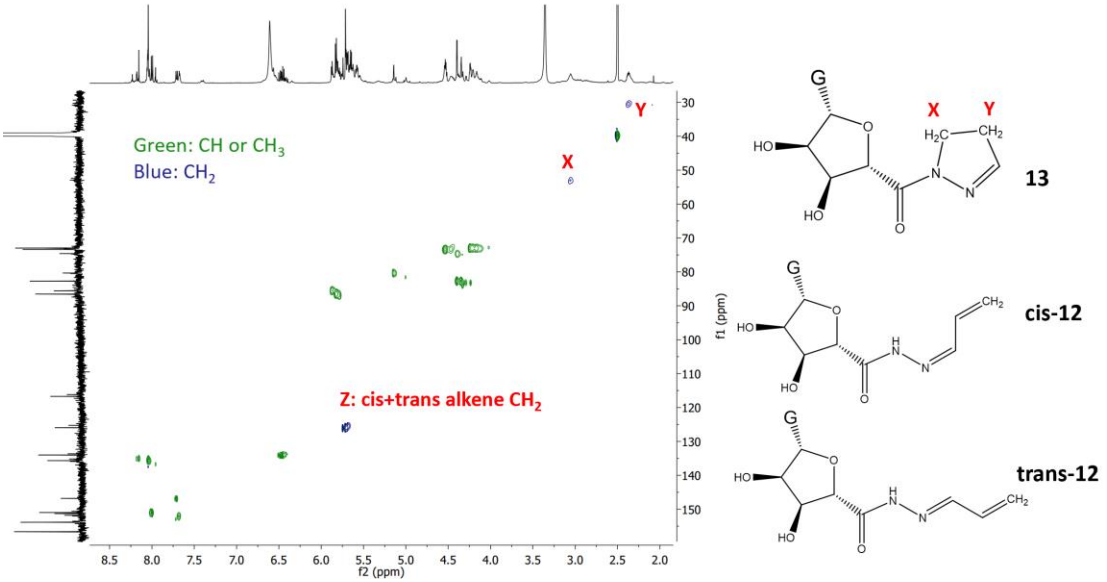

Figure 6.14: ^{1}H-^{13}C HSQC spectrum of reaction products formed by gas phase uptake of 1.0 eq of AC by the $G_4 \bullet K^+$ hydrogel made from 5′-hydrazidoguanosine **3** (2 wt%, 65 mM, 0.5 eq KCl) shows formation of a cis/trans mixture of acylhydrazones **12** and some cyclic adduct **13**. Blue crosspeaks represent CH_2 groups while green crosspeaks represent CH or CH_3 groups. Three CH_2 signals are identified: X and Y result from a CH_2-CH_2 linkage in the cyclic adduct **13** (a crosspeak is observed between X and Y in the ^{1}H, ^{1}H-COSY spectrum in **Figure 6.17**), while the crosspeak Z represents 2 different terminal alkenes, namely the acylhydrazones cis-**12** and trans-**12**, which show 2 separate ^{13}C signals peaks (f1) at ~126 ppm.

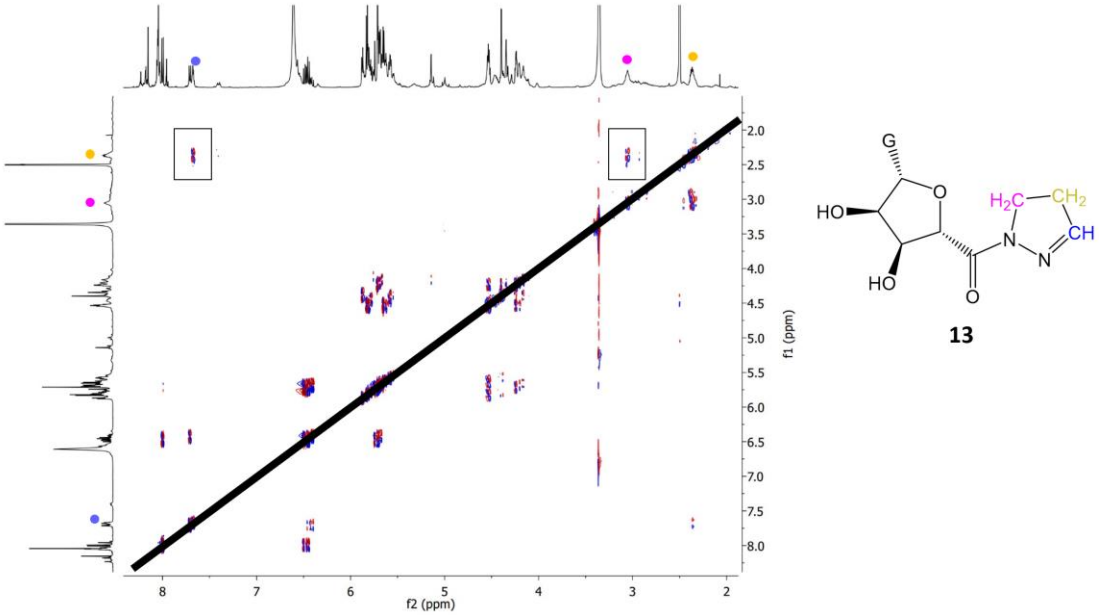

Figure 6.15: ^{1}H-^{1}H COSY spectrum of reaction products formed by gas phase uptake of 1.0 eq of AC by the $G_4 \bullet K^+$ hydrogel made from 5′-hydrazidoguanosine **3** (2 wt%, 65 mM, 0.5 eq KCl) shows a CH_2-CH_2-CH linkage (yellow CH_2 has crosspeaks with both pink CH_2 and blue CH), indicating formation of cyclic acylhydrazone **13**.

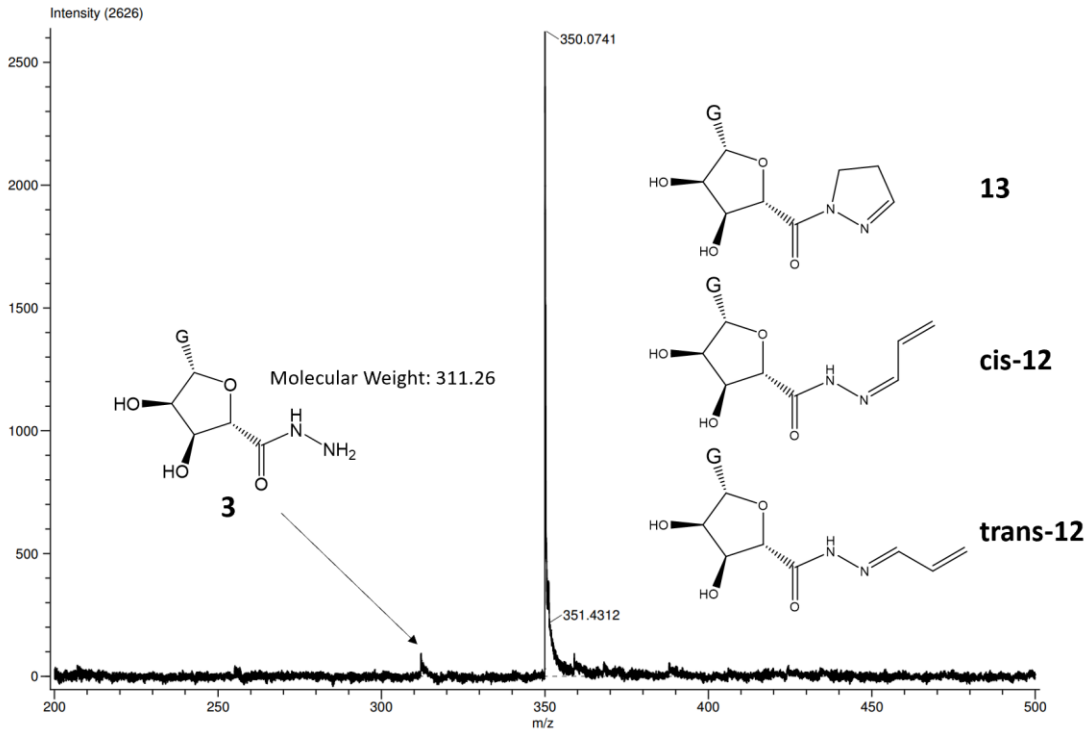

Figure 6.16: ESI-MS shows dehydration products formed between 1.0 eq of AC and the $G_4 \bullet K^+$ hydrogel made from 5′-hydrazidoguanosine **3** (2 wt%, 65 mM, 0.5 eq KCl). The major signal at m/z=350.07 is consistent with the structures of the 2 acyclic acylhydrazones (cis/trans-**12**) and the cyclic acylhydrazones **13**. A small amount of unreacted hydrazide **3** is also found at m/z=312.13.

This following experiment shows that AC in the solution is taken up ***from the solution***:

Procedure for aqueous phase uptake of AC by G_4•K^+ hydrogels: Hydrogels made from either 5′-hydrazidoguanosine **3** or 5′-hydrazinoguanosine **2** (2 wt%, 0.5 eq KCl) in D_2O were prepared according to the general preparation method. The G_4•K^+ hydrogel made from guanosine **1** (2 wt%, 72 mM) and $KB(OH)_4$ (0.5 equiv) was prepared according to literature procedure.[78] After heating the mixtures to boiling we then added 0.5 mL of the hot solutions into a parafilm-lined mold and allowed the solution to cool at RT for 1 h. The resulting hydrogels were then placed into a vial containing 5 mL of 155 mM KCl in D_2O that contained AC (3.37 mM, overall 0.5 eq of AC relative to the amount of nucleoside **1**-**3** in the hydrogel). Aliquots of the solution (0.6 mL) were removed periodically into a small vial and 10 µL of a 200 mM internal standard (3-(trimethylsilyl)propionic-2,2,3,3-d_4 acid sodium salt in D_2O) was added to each vial. These solutions were well mixed and transferred to NMR tubes after which ^{1}H NMR spectra were acquired (32 scans). The integration of the internal standard was set to 1.0 and the integration of the three olefin peaks in the AC (~ 6.5 ppm) was used for quantification. Experiments were done in triplicate. The amount of AC in solution at ***t*** hour was determined according to the following equation:

$$\frac{\text{AC } integration(\boldsymbol{t})}{\text{AC } integration(\mathbf{0}\ \boldsymbol{h})} \times 100\%$$

This following experiment shows that AC in the solution is ***taken up into the 3•KCl hydrogel:***

Procedure for AC Binding with 2•KCl Hydrogel in Aqueous Phase: 2 wt% hydrazine **2** (68 mM) hydrogels with 2.0 eq KCl were prepared according to the general gel preparation method in H_2O. 0.5 mL of the hot gels were then pipetted into a parafilm mold and allowed to cool at room temperature for 1 h. The hydrogels were then placed into a vial containing 5 mL of freshly prepared H_2O solution of AC (3.37 mM, overall 0.5 eq relative to the amount of hydrazine **2** in the gel) in 155 mM KCl. After 4 hours, the vial was gently shaken and the outside solution was removed. Then another 5 mL of 155 mM KCl solution was added to the vial in order to rinse the hydrogel. The solution was completely removed and the remaining hydrogel was lyophilized, dissolved in DMSO-d_6 and studied by ^{1}H NMR.

Preparation of 5′-deoxy-5′-methylpyrazolinoguanosine (9).

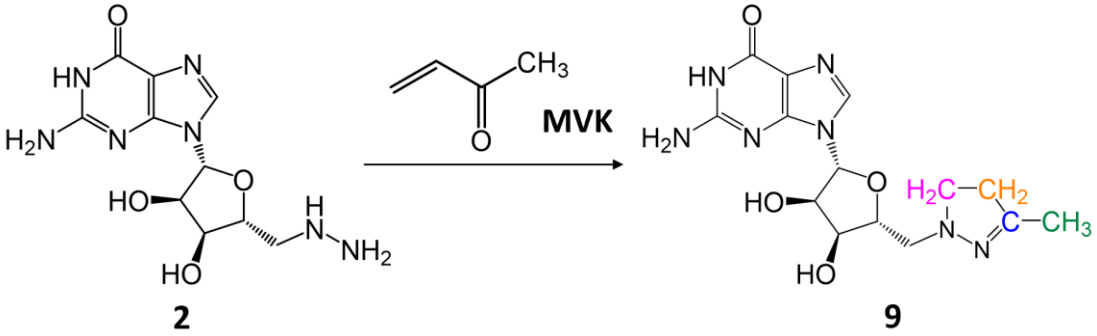

5′-deoxy-5′-methylpyrazolinoguanosine **9**.

^{1}H NMR (DMSO-d_6): δ 1.86 (3 H, s, green CH_3), 2.45-2.50 (2 H, m, CH_2), 2.84-2.98 (2 H, m, CH_2), 2.91-2.98 (1 H, dd, 5′-CH_2), 3.10-3.16 (1 H, dd, 5′′-CH_2, J=7.7 Hz, J=5.3 Hz), 4.05 (1 H, m, 4′-CH), 4.11 (1 H, m, 3′-CH), 4.50 (1 H, m, 2′-CH), 5.20 (1 H, d, J=5.0 Hz, 3′-OH), 5.43 (1 H, d, J=6.0 Hz, 2′-OH), 5.67 (1 H, d, J=6.0 Hz, 1′-CH), 6.60 (2 H, s, NH_2), 7.91 (1 H, s, 8-CH), 10.76 (1 H, s, br, N1H)

^{13}C NMR (DMSO-d_6) δ: 15.70 (green CH_3), 36.61 (yellow CH_2), 55.00 (pink CH_2), 58.84 (C5′), 71.61 (C4′), 72.74 (C2′), 82.59 (C3′), 86.23 (C1′), 116.68 (C5), 135.63 (C8), 151.44 (C4 or blue carbon), 151.45 (C4 or blue carbon), 153.75 (C2), 156.69 (C6)

ESI-MS m/z=350.13 (MW of **9**: 349.35)

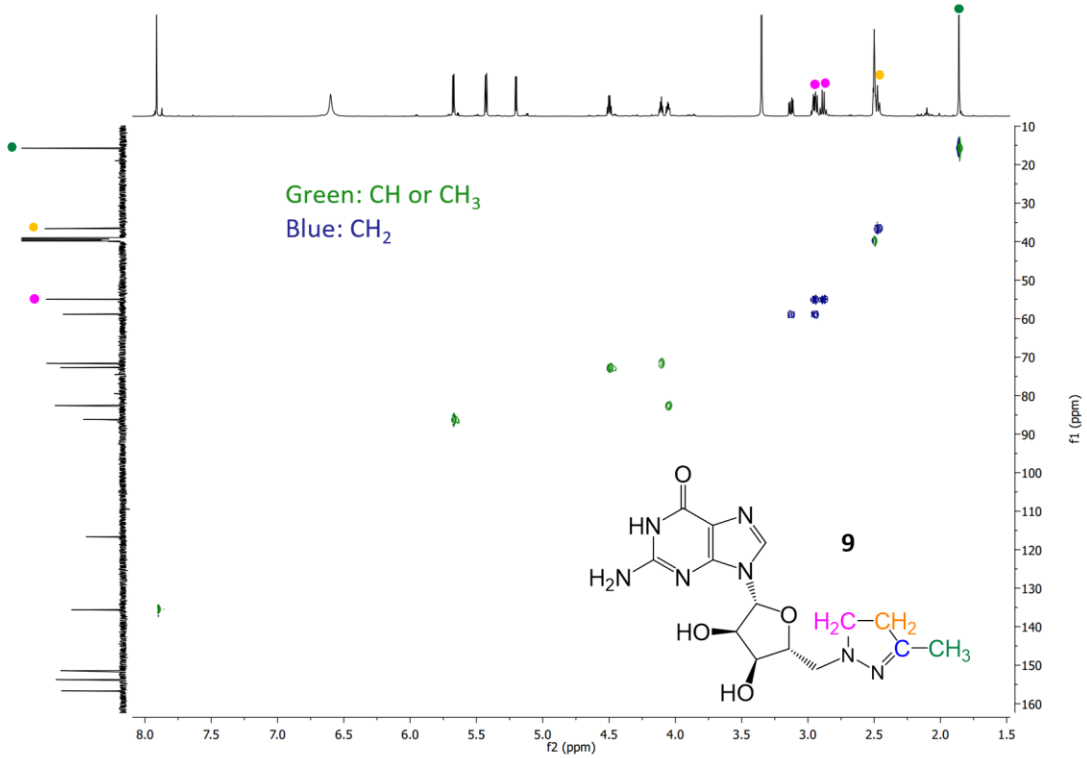

Figure 6.17: ^{1}H-^{13}C HSQC spectrum of methylpyrazoline **9**. The blue crosspeaks represent CH_2 groups while green crosspeaks represent CH or CH_3 groups. NMR signals for the CH_2 groups in the 5′-pyrazoline ring are indicated by colored dots (pink and orange).

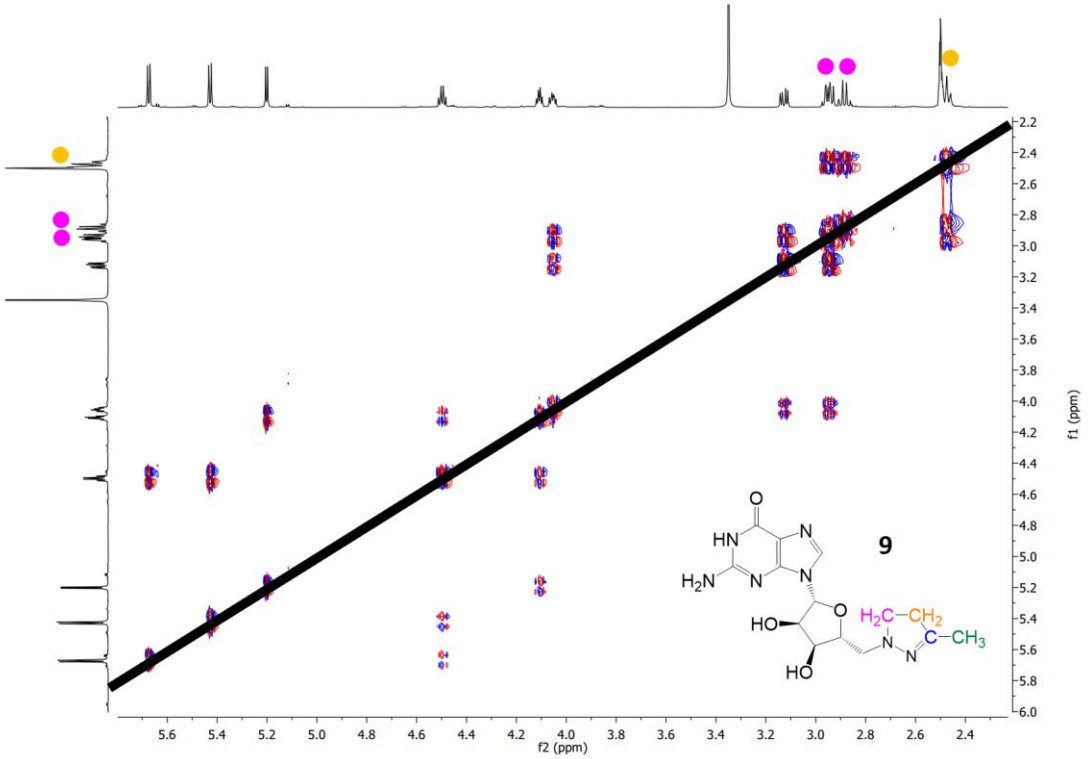

Figure 6.18: ^{1}H-^{1}H COSY spectrum of methylpyrazoline **9**. Combining this data with the HSQC spectrum in **Figure 6.19**, a CH_2-CH_2 linkage (pink and yellow) for the pyrazoline ring can be identified.

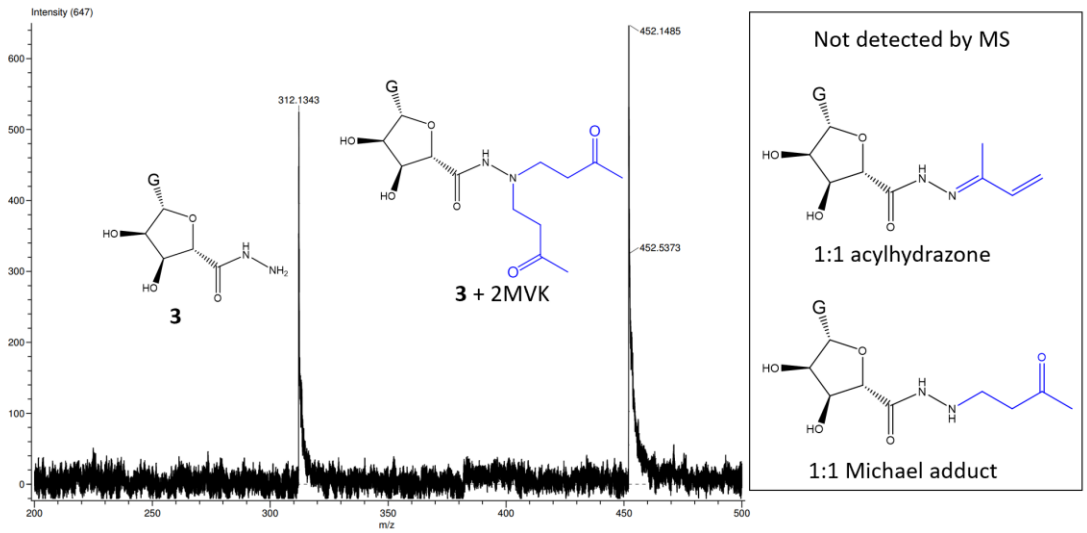

Figure 6.19: ESI-MS of gas-phase uptake reaction between 1.0 eq of MVK and the G_4•K^+ hydrogel containing hydrazide **3** (2 wt%, 65 mM, 0.5 eq KCl). Only peaks for unreacted **3** (m/z=312.13) and 1:2 Michael adduct (m/z=452.15) are observed. Signals for the 1:1 Michael adduct and 1:1 acylhydrazone adduct are not observed. A putative structure is shown for the 1:2 adduct. Addition of the first MVK molecule would likely increase the nucleophilicity of the terminal nitrogen, leading to a second Michael addition.

This following experiment shows that MVK in the solution is taken up ***from the solution***:

Procedure for aqueous phase uptake of MVK by G_4•K^+ hydrogels: Hydrogels made from either 5′-hydrazidoguanosine **3** or 5′-hydrazinoguanosine **2** (2 wt%, 0.5 eq KCl) in D_2O were prepared according to the general preparation method. The G_4•K^+ hydrogel made from guanosine **1** (2 wt%, 72 mM) and $KB(OH)_4$ (0.5 equiv) was prepared according to literature procedure.[78] After heating the mixtures to boiling we then added 0.5 mL of the hot solutions into a parafilm-lined mold and allowed the solution to cool at RT for 1 h. The resulting hydrogels were then placed into a vial containing 5 mL of 155 mM KCl in D_2O that contained MVK (3.37 mM, overall 0.5 eq of MVK relative to the amount of nucleoside **1-3** in the hydrogel). Aliquots of the solution (0.6 mL) were removed periodically into a small vial and 10 μL of a 200 mM internal standard (3-(trimethylsilyl)propionic-2,2,3,3-d_4 acid sodium salt in D_2O) was added to each vial. These solutions were well mixed and transferred to NMR tubes after which ^{1}H NMR spectra were acquired (32 scans). The integration of the internal standard was set to 1.0 and the integration of the three olefin peaks in the MVK (~ 6.5 ppm) was used for quantification. Experiments were done in triplicate. The amount of MVK in solution at ***t*** hour was determined according to the following equation:

$$\frac{\text{MVK } integration(\boldsymbol{t})}{\text{MVK } integration(\mathbf{0}\ \boldsymbol{h})} \times 100\%$$

This following experiment shows that MVK in the solution is taken up ***into 2•KCl hydrogel***:

Procedure for MVK Binding with 2•KCl Hydrogel in Aqueous Phase: 2 wt% hydrazine **2** (68 mM) hydrogels with 2.0 eq KCl were prepared according to the general gel preparation method in H_2O. 0.5 mL of the hot gels were then pipetted into a parafilm mold and allowed to cool at room temperature for 1 h. The hydrogels were then placed into a vial containing 5 mL of freshly prepared H_2O solution of MVK (3.37 mM, overall 0.5 eq relative to the amount of hydrazine **2** in the gel) in 155 mM KCl. After 4 hours, the vial was gently shaken and the outside solution was removed. Then another 5 mL of 155 mM KCl solution was added to the vial in order to rinse the hydrogel. The solution was completely removed and the remaining hydrogel was lyophilized, dissolved in DMSO-d_6 and studied by ^{1}H NMR.

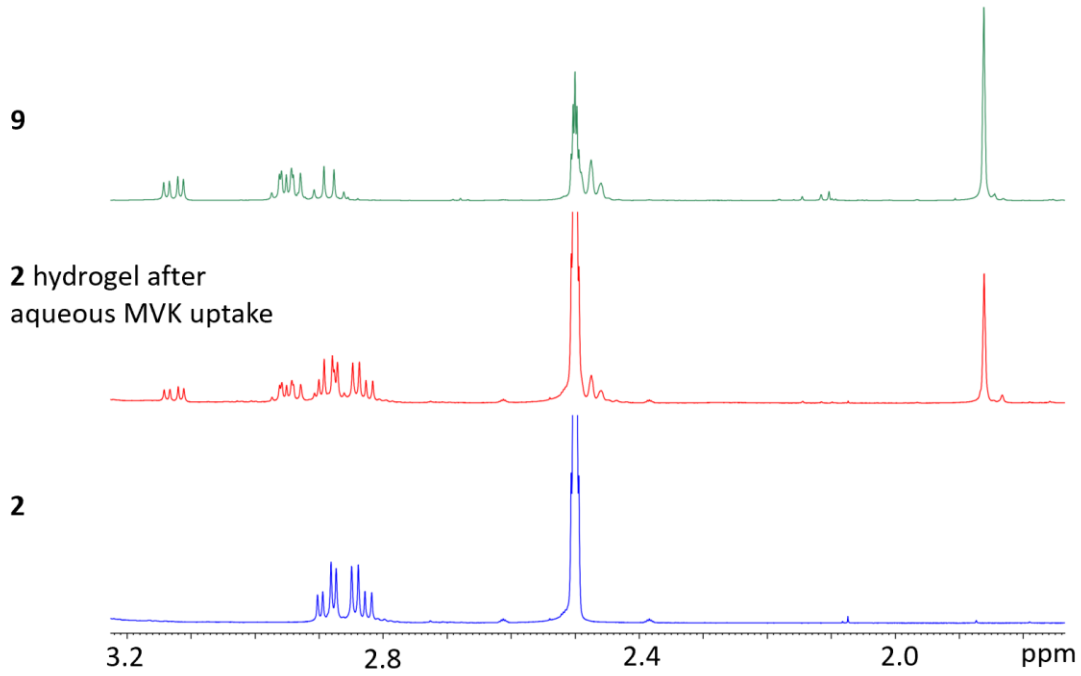

Figure 6.20: Methyl vinyl ketone (MVK) reacts with the $G_4 \bullet K^+$ hydrogel containing hydrazine **2** (2 wt%, 68 mM, 2 eq KCl) in aqueous solution by forming the cyclic pyrazoline **9**. ^1H NMR of the lyophilized gel (middle) shows peaks for both methylpyrazoline **5** (top) and unreacted hydrazine **2** (bottom).

Procedure for aqueous phase uptake of MA by G_4•K^+ hydrogels: 2 wt% G **2** (68 mM) and G **3** (65 mM) hydrogels with 2.0 eq KCl were prepared according to the general gel preparation method in D_2O. 0.5 mL of the hot gels were then pipetted into a parafilm lined mold and allowed to cool at room temperature for 1 h. A MA solution in 155 mM D_2O solution without any hydrogels served as a blank control. The hydrogels were then placed into a vial containing 5.5 mL of freshly prepared D_2O solution of MA (3.37 mM, overall 0.5 eq relative to the amount of G **2** in the gel) in 155 mM KCl. Before the addition of hydrogels (t=0 h), 0.5 mL of MA solution was pipetted into a vial which was used for NMR experiments at t=0 h. After 24 h of incubation at room temperature, the vials were gently shaken before 0.5 mL of the outside solution (0.5 mL) were removed into a small vial and 10 μL of a 200 mM internal standard (3-(trimethylsilyl)propionic-2,2,3,3-d_4 acid sodium salt in D_2O) was added to each vial. The solutions were well mixed and transferred to NMR tubes after which ^{1}H NMR spectra were acquired (16 scans). The integration of internal standard was set to 1.0 and the integration of three olefin peaks (~ 6.5 ppm) was used for quantification. Experiments were done in triplicates. The amount of MA in solution at 24 h was determined according to the following equation:

$$\frac{\text{MA } integration(\mathbf{24}\ \boldsymbol{h})}{\text{MA } integration(\mathbf{0}\ \boldsymbol{h})} \times 100\%$$

The % MA that disappeared in the blank is subtracted from samples containing G **2** and G **3** hydrogels.

6.5 Supporting information for Chapter 5

General Procedure for Preparation of G_4•K^+ hydrogels: The desired amount of guanosine derivatives was weighed into a vial and the appropriate amount of deionized water was added. The resulting suspension was sonicated until large aggregates were broken down to give a fine suspension. An appropriate amount of K^+ solution (either KCl and/or KOH) was added to the mixture, followed by manually shaking of the vial. The suspension was then heated with a heat gun until a clear solution resulted. The vial was removed from the heat and allowed to cool at rt.

Experimental and Summary of Crystal Structure Data for CAG 2•H_2O. A suitable single crystal of $C_{10}H_{13}N_5O_7$ (UM3107) was selected and measured on a Bruker APEX 2 SMART diffractometer. The crystal was kept at 200(2) K during data collection. The integral intensity was corrected for absorption using SADABS software[a] via the multi-scan method. Resulting minimum and maximum transmission are 0.893 and 0.979 respectively. The structure was solved with the ShelXT-2014 program,[b] and refined with the ShelXL-2015 program,[c] and least-square minimization using ShelX software.[b] Number of restraints used = 0. The H atoms were located from difference Fourier maps and freely refined. Crystal structure data for the monohydrate CAG **2**•H_2O have been deposited with Cambridge Crystallographic Data Centre as CCDC-1946227.

[a] Krause, L.; Herbst-Irmer, R.; Sheldrick, G.M.; Stalke, D. Comparison of silver and molybdenum microfocus X-ray sources for single-crystal structure determination. *J. Appl. Cryst.* **2015**, *48*, 3-10.

[b] Sheldrick, G. M. *SHELXT* – Integrated space-group and crystal-structure determination.

Acta Cryst. **2015**, *A71*, 3-8.

[c] Sheldrick, G. M. Crystal Structure Refinement with *SHELXL*. *Acta Cryst.* **2015**, *C71*, 3-8.

Table 6.2 Crystal and Structure Refinement Data for UM3107

Identification code	UM3107
Empirical formula	$C_{10}H_{13}N_5O_7$
Formula weight	315.25
Temperature/K	200(2)
Crystal system	orthorhombic
Space group	$P2_12_12_1$
a/Å	7.5544(5)
b/Å	10.4716(6)
c/Å	15.9670(10)
α/°	90
β/°	90
γ/°	90
Volume/Å^3	1263.10(14)
Z	4
ρ_{calc}g/cm^3	1.658
μ/mm^{-1}	0.142
F(000)	656.0
Crystal size/mm^3	0.28 × 0.22 × 0.15
Radiation	MoKα (λ = 0.71073)
2Θ range for data collection/°	4.652 to 53
Index ranges	$-9 \le h \le 9$, $-13 \le k \le 13$, $-20 \le l \le 20$
Reflections collected	12354
Independent reflections	2614 [R_{int} = 0.0223, R_{sigma} = 0.0197]
Data/restraints/parameters	2614/0/252
Goodness-of-fit on F^2	0.999
Final R indexes [I>=2σ (I)]	R_1 = 0.0263, wR_2 = 0.0493
Final R indexes [all data]	R_1 = 0.0291, wR_2 = 0.0499
Largest diff. peak/hole / e Å^{-3}	0.19/-0.15
Flack parameter	0.2(4)

Circular Dichroism Procedure: A 2 wt % HAG **15**/G **1** hydrogel (1:1 mixture, 64 mM nucleoside overall, 2 eq KCl) was prepared using the general procedure and allowed to stand at rt for 1 day. The CD spectra were recorded at 25 °C using a Hellma 106-QS quartz cell with an optical path length of 0.01 mm (scanning speed 200 nm/min; response time 2 s). The experiment was repeated at least 3 times, and the curves were smoothed and averaged.

***NMR Procedure for Determining Concentration of Nucleosides in the Sol and Gel Phases*:** Gels (0.5 mL, 2 wt %, 64 mM 1:1 HAG **15**/G **1** with 2 eq salt) were formed following the general procedure in D_2O. A 5μL aliquot of DMSO-h_6 was added to each sample as an internal standard. The hot gel solutions were immediately pipetted into hot NMR tubes and allowed to sit at rt for 1 day. ^{1}H NMR spectra were recorded on a Bruker AVIII-600 spectrometer. The HOD peak was set to δ 4.8 ppm and the DMSO-h_6 signal was integrated to 1.00. The H1′ peaks for G **1** and HAG **15** were integrated in comparison with the DMSO-h_6 peak. After the experiment, 20 μL of conc. DCl was added to the NMR tube to destroy the gel network and get everything into solution. Upon dissolution, new ^{1}H NMR spectra were obtained. The DMSO-h_6 peak was again set to 1.00 and the H1′ peaks for G **1** and HAG **15** in the DCl solution were integrated in comparison to the DMSO-h_6 peak. The amounts of G **1** and HAG **15** in the gel and the sol were then calculated. All experiments were done in triplicate.

Determination of aqueous solubility of CAG 14 or HAG 15 by UV-Vis Spectroscopy:

Working curve: Aqueous solutions of different concentrations of CAG **14** or HAG **15** were prepared (0, 0.005, 0.01, 0.02, 0.03 g/L). The absorbance of each sample was determined by UV-VIS spectroscopy. The experiments were done in triplicate and the absorbance at 254 nm (A_{254nm}) was plotted against CAG **14** or HAG **15** concentration (g/L) to give working curves.

Solubility determination: CAG **14** or HAG **15** (4 mg) was added to deionized water (1 mL) to give a suspension. The suspension was sonicated and stirred at rt for 1 h before ultracentrifugation was performed to remove insoluble particles. The supernatant (10 μL) was then diluted with 3 mL of deionized water. The solutions were then measured by UV-Vis spectroscopy. Experiments were done in triplicate and the absorbance at 254 nm was used to calculate the concentration of a saturated solution of CAG **14** or HAG **15**.

Rheology procedure: Gels were made following the general procedure. All rheology was done 1 day after the gels had been prepared. Experiments were performed on an AR2000 stress-controlled rheometer from TA Instruments at 20 °C with a 20 mm diameter parallel plate geometry. Strain sweeps on a hydrogel made from 1:1 HAG **15**/G **1** (2 wt %, 64 mM) and containing different amounts of KCl and/or KOH were taken at a constant angular frequency of 10 rad/s.

SEM procedure: A portion of the hydrogel was taken from the sample with a spatula and placed on a pre-cleaned Si chip that was attached on a SEM stub. A drop (3 μL) of 3% ionic liquid solution (Hitachi HILEM1000, $C_7H_{19}NO_4S$) in water was pipetted onto the sample immediately. Samples soaked with ionic liquid were set in air for 5-10 min. Excess ionic liquid was carefully absorbed by a filter paper. The sample was allowed to sit in air overnight (~ 20 h) with a cover glass to prevent possible contamination. Samples were examined with a Hitachi SU-70 high resolution analytical SEM.

Hydrogel molding procedure: HAG **15**/G **1** hydrogels (64 mM, 2 wt %, 2 eq K^+) were made following the general procedure. The hot gel solutions were immediately transferred to an ice cube tray or a mold made from parafilm and were allowed to sit at rt and solidify. After cooling for 1 h, the gels were carefully removed from the mold for future experiments.

Procedures for determination of the pK_a for 5'-HA sidechain:

Sample preparation: A suspension of D_2O containing 10 mg/mL HAI **17** and 0.5 mg/mL TMSP-d_4 (3-(trimethylsilyl)propionic-2,2,3,3-d_4 acid sodium salt) was prepared and 0.5 mL of that suspension was then transferred to glass vials labeled with target pD values (pD = 5, 6, 7, 7.5, 8, 8.5, 9, 9.5, 10, 11, 12). The pH values of the suspensions were adjusted using the following D_2O stock solutions: 0.1 M DCl, 1 M DCl, 0.1 M KOH and 1 M KOH. Each pD value was determined in triplicate. The resulting suspension/solution was then transferred to NMR tubes.

Data acquisition and processing: ^{13}C NMR spectra (1000 scans) were acquired for each sample. TMSP-d_4 was used as chemical shift standard and the chemical shift for the methyl carbons in TMSP-d_4 were set at δ 0 ppm.

***Procedure for measuring the pH-dependent binding of TO to the hydrogels*:** HAG **15**/G **1** hydrogels (1 mL, 12.8 mM, 0.4 wt %, 2 eq K^+) containing 5 μM of thiazole orange (TO) were made following the general procedure. Each gel contained 0 eq to 2 eq of KOH with KOH added in increments of 0.1 eq, while maintaining the overall 2 eq of K^+ by adding the appropriate amount of KCl. The gels were allowed to cool for 3 h at rt before the pH values of the gel samples were measured. The samples were then pipetted into a 2 mm x 10 mm fluorescence quartz cuvette (excitation path 10 mm and emission path 2 mm). Fluorescence spectra were then acquired at a scanning speed of 2400 nm/min with an excitation slit width of 10 nm and an emission slit width of 2.5 nm. Emission response was recorded from 515 to 700 nm after exciting at 500 nm.

Fluorescence intensities at 535 nm were plotted against pH value of the sample to obtain the curve. All experiments were performed in triplicate.

Procedure for writing on hydrogel with fluorescent thiazole orange as ink: Binary hydrogels (1 mL, 2 wt % of a 1:1 mix of HAG **15** and G **1**, 1.5 eq KCl & 0.5 eq KOH, pH 9.5) were made following the general procedure. The hot gel solution was then transferred to a polyethylene vial cap, which was sealed with parafilm and allowed to cool at rt for 1 h. To draw patterns on the gel, a melting tube was repeatedly dipped into a 1 mM solution of thiazole orange (TO) solution and then applied onto the gel surface, which was illuminated under a 365 nm UV lamp to visualize the drawing.

Procedure for Preparation of G_4•K^+ hydrogels containing $FeCl_3$: A 1:1 mixture of HAG **15** and G **1** was added into a vial and the appropriate amount of deionized water was added. The resulting suspension was sonicated until large aggregates were broken down to give a fine suspension. A small amount of a stock solution of $FeCl_3$ (0.33 eq relative to HAG **15**) was added to the mixture and the suspension turned red instantaneously. The mixture was sonicated before an appropriate amount of KCl (2 eq to total nucleoside) was added. The vial was then heated with a heat gun until a clear solution resulted. The vial was removed from the heat and allowed to cool at rt to give a self-standing red hydrogel.

Procedure for mass spectrometry characterization of HAG 15 Fe^{3+} adducts

Sample preparation: HAG **15** (20 mg, 64 mM) was added to 1 mL of deionized water. The mixture was sonicated before 2 eq of NEt_3 was added. While stirring, 0.33 eq of $FeCl_3$ was added to the mixture to give a red suspension. Another equivalent of NEt_3 was added to fully solubilize the resulting adduct resulting in a dark red solution.

HPLC-MS procedure: For the HPLC elution, the mobile phase was composed of 0.1 % formic acid solution (A) and methanol (B). The elution was performed as follows: the concentration of solvent B started at 10 % from 0 to 2.0 min, linearly increased to 75 % at 7.0 min, then increased to and was kept at 100 % from 9.0 to 12.0 min, and then decreased to and kept at 10 % from 13.0 to 15.0 min. A reversed-phase Imtakt Cadenza-C_{18} column (2.0 x 50 mm, particle size 3 μm) was used in the LC experiments, and the flow rate was set to 0.25 mL/min. The HPLC module was coupled with a JEOL AccuTOF spectrometer.

Procedure for drawing by hand with $FeCl_3$: Hydrogels (2 wt % nucleoside, 2 wt % Aga, 2 eq KCl) were made following the general procedure. The hot gel solution was then transferred to a polyethylene vial cap. The vial cap was sealed with parafilm and allowed to cool at rt for 1 h. The vial cap was unsealed and then a melting tube was repeatedly dipped into a 100 mM $FeCl_3$ solution and that solution was applied onto the gel surface to draw the desired patterns.

Procedure for Patterning Hydrogels Using a 3D-printer:

Model creation and path generation: Bitmap images were vectorized in Inkscape (https://inkscape.org/), and imported into Blender (https://blender.org) as scalar vector graphics (SVG). Vectors were extruded with Blender to a single layer height (0.2 mm) and exported as stereolithography (STL) files. Model paths were generated with Simplify3D slicing software (v 4.0.1). Concentric infill patterns were used on filled region. "Z-hopping" was used for travel moves between unconnected regions to prevent extraneous patterning from needle drag. Post-extrusion coasting moves of 8 mm were used to ensure connections between liquid extrusion start and end points.

Hydrogel sample preparation: Hydrogels (7 mL, 1 wt % of a 1:1 mixture of HAG **15** and G **1**, 1 wt % Aga, 1 eq KCl) were made following the general procedure. The hot hydrogel was then poured onto a hot glass plate (10 cm x 10 cm) placed on a flat surface. The gel was immediately spread all over the plate surface using a piece of hot

glass. The sample was allowed to cool to rt and gel patterning experiments were performed within 30 min of gel preparation.

Automated patterning: $FeCl_3$ (50 mM) patterning was performed using a custom designed and 3D-printed 12-channel syringe pump installed with a single 290 μL glass syringe with a 0.6 mm bore needle. The syringe pump was mounted on a RepRap Prusa i3-style 3D printer (Hictop 3DP11) running Marlin firmware with a BLTouch Z-leveling probe. The extruder motor default 151.79 steps/mm resulted in a volumetric conversion of 3.87 μL of liquid per mm of extrusion. HAG **15**/G **1**/Aga hydrogels (1 wt % nucleoside, 1 wt % Aga, 1 eq KCl) on 10 cm glass plates were centered manually on the build plate and adhered with a fine coating glue.

ICP-MS experiment procedure

Sample and standard preparation:

All samples and standards were doped with indium to give a uniform 10 ppb to monitor and correct for instrument drift and ionization efficiency changes that may have resulted from different solution matrices.

Blanks and standards of 1 ppb, 10 ppb, 50 ppb, 100 ppb, 250 ppb and 500 ppb Fe (derived by appropriate dilution from a single element 1000 ppm Specpure Alfa Aesar Fe plasma standard) were used to produce a calibration curve, which was then used to calculate the concentration of Fe in the solutions. All samples and standards were run in 5% nitric acid.

Fe release experiment setup:

Eight hydrogels (1 mL deionized water, 2 wt % Aga, 2 wt % 1:1 HAG **15**/G **1**, 2 eq KCl) were prepared according to the general procedure. The hot gel solutions were then transferred into polyethylene vial caps. The caps were sealed were parafilm and the hydrogel samples were allowed to cool at rt for 1 h. A stock solution of $FeCl_3$ in water (5 μL, 50 mM) was pipetted onto each gel surface and the solution was spread out on the surface by tilting the vial cap. The patterned samples were allowed to equilibrate for 10 min at rt before 1 mL of KCl solution (155 mM) was added to each sample. A stock solution of vitamin C (VC) was then added to 4 of the 8 samples to give a final VC concentration of 16 mM. After 45 min the samples containing VC lost the visible red patterns originally generated by addition of Fe^{3+}.

Iron released (x): Each supernatant was pipetted into a separate glass vial (overall 8 vials). Another 1 mL of 155 mM KCl solution was added to each gel sample to wash the surface and then combined with the corresponding supernatants.

Iron in hydrogel (y): The gel parts were then scooped into 8 new vials and the polyethylene caps were each rinsed with 1 mL of 155 mM KCl solution. The washes were combined with hydrogel chunks (another 8 vials).

All 16 samples were then lyophilized and dissolved in 5 mL of conc. HNO_3. The mixtures were allowed to sit at rt for 1 day to oxidize all organic components. Each sample was then diluted 12-fold so that each sample contains 10 ppb indium and 5% HNO_3.

Sample measurements:

Solutions were analyzed using a ThermoFinnigan Element 2 single collector Inductively Coupled Plasma Mass Spectrometer (ICPMS), fitted with aluminum sampler and skimmer cones. Solutions were run through an ESI Apex IR desolvating unit using a 50 mL min^{-1} uptake nebulizer.

Samples and standards were run in medium resolution (M/δM *ca*. 3000) in "Mass Accuracy" collection mode. Three iron isotopes (^{54}Fe, ^{57}Fe and ^{58}Fe) were measured in order to recognize possible molecular interferences from $^{40}Ar^{14}N^{+}$, ^{54}Cr (54), $^{40}Ar^{17}O^{+}$, $^{40}Ar^{16}O^{1}H^{+}$ (57) and $^{40}Ar^{18}O^{+}$, ^{58}Ni (58); ^{56}Fe was not measured due to the size of the $^{40}Ar^{16}O$ peak.

Each mass station was measured with a mass window of 150 % with 20 samples per peak, each monitored for 5 ms. An integration window of 60 % was used. All mass stations were measured in "Both" mode. Analyses consisted of 50 runs and a single pass. Total analysis time was 47 s, with a washout time of 2 min between each sample.

Fe% release calculation:

^{57}Fe count numbers were used for calculation. The intercept of the standard curve (1651.6) was subtracted from all data. For each set of samples, the following equation is used to calculate Fe% released:

$$\text{Fe \% released} = x/(x+y) * 100\%$$

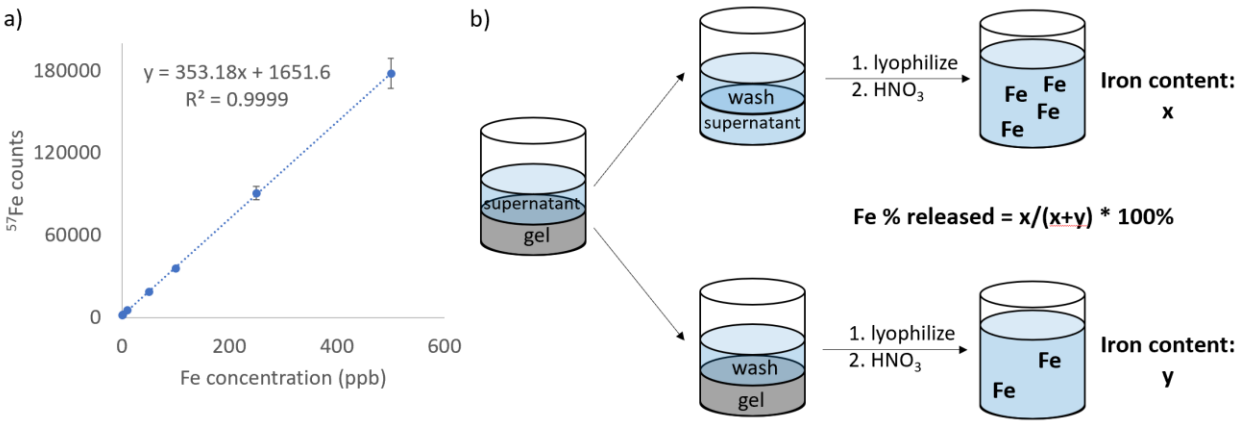

Figure 6.21: a) Calibration curve of ^{57}Fe count number. b) Schematic illustration of sample preparation and calculation of % Fe release from the hydrogel surface into the supernatant.

Procedure for hydrogel rewriting experiments: Hydrogels (2 wt % nucleoside, 2 wt % Aga, 2 eq KCl) were made following the general procedure. The hot gel solution was then transferred to a polyethylene vial cap. The cap was sealed with parafilm and allowed to cool at rt for 1 h. The vial cap was unsealed and then a melting tube was repeatedly dipped into a 50 mM $FeCl_3$ solution and that solution was applied onto the gel surface to draw the "+" pattern. The gel was allowed to sit for 1 min before 1 mL solution containing 155 mM KCl and 100 mM VC was added to the sample. The solution was removed after the pattern disappears and the surface was washed with 1 mL of 155 mM KCl. Another 1 mL of 155 mM KCl solution containing 100 mM H_2O_2 was added to remove any remaining VC. The solution was removed and the surface was carefully dried with Kim wipe before another writing experiment was performed.

6.6 Synthesis and characterization of guanosine and inosine analogs

D-guanosine (G **1**), GMP **6**, inosine **16**, ipG **19**, ipI **21**, 8-BrG **29**, 8-aminoG **31** and L-guanosine **40** were purchased from Sigma-Aldrich, Alfa Aesar, Carbosynth or Oakwood Chemical.

hydrazideG **3**,[80] 5′-aminoG **4**,[79] 5′-NHOHG **5**,[123] CAG **14**,[86,262] esterG **20**,[80] 5′-thiophosphoG **26**,[123] 8-IG **30**,[279] 8-morpholinoG **32**,[280] 8-thioG **37**[81] and 5′-IG **39**[79] were prepared based on literature procedures and their ^{1}H and ^{13}C NMR matched published values.

HG 2[123]

Hydrazine hydrate (30 mL of a 50 % NH_2NH_2 solution in water) was added to a 100 mL round-bottom flask containing 5′-deoxy-5′-iodoguanosine (5′-IG **39**)[79] (3.0 g, 7.5 mmol). The reaction mixture was stirred at 40 ^{o}C for 18 h. Methanol (75 mL) was added to the reaction mixture and the mixture was cooled on ice, causing precipitation of a white solid. The solid was collected by filtration and washed thoroughly with methanol. After methanol was removed by evaporation, the solid was heated in deionized water until a clear solution resulted and hot filtration was performed to remove any insoluble material. Then, methanol (50 mL) was added to the filtrate and cooled on ice for 30 min and the precipitate was collected by vacuum filtration and dried on a lyophilizer to afford HG **2** as an off-white solid (1.03 g, 45.4 %).

^{1}H NMR (600 MHz, DMSO-d_6) δ: 2.80-2.89 (2 H, m, 5′-CH_2), 3.94 (1 H, dd, 4′-CH), 4.05 (1 H, dd, 3′-CH), 4.45 (1 H, dd, 2′-CH), 5.64 (1 H, d, J=6.1 Hz 1′-CH), 6.46 (2 H, s, NH_2), 7.89 (1 H, s, 8-CH), 10.21 (1 H, s br, N1H).

^{13}C NMR (150 MHz, DMSO-d_6) δ: 57.00 (C5′), 71.62 (C3′), 72.87 (C2′), 82.62 (C4′), 86.75 (C1′), 116.90 (C5), 136.00 (C8), 151.19 (C4), 153.54 (C2), 156.72 (C6).

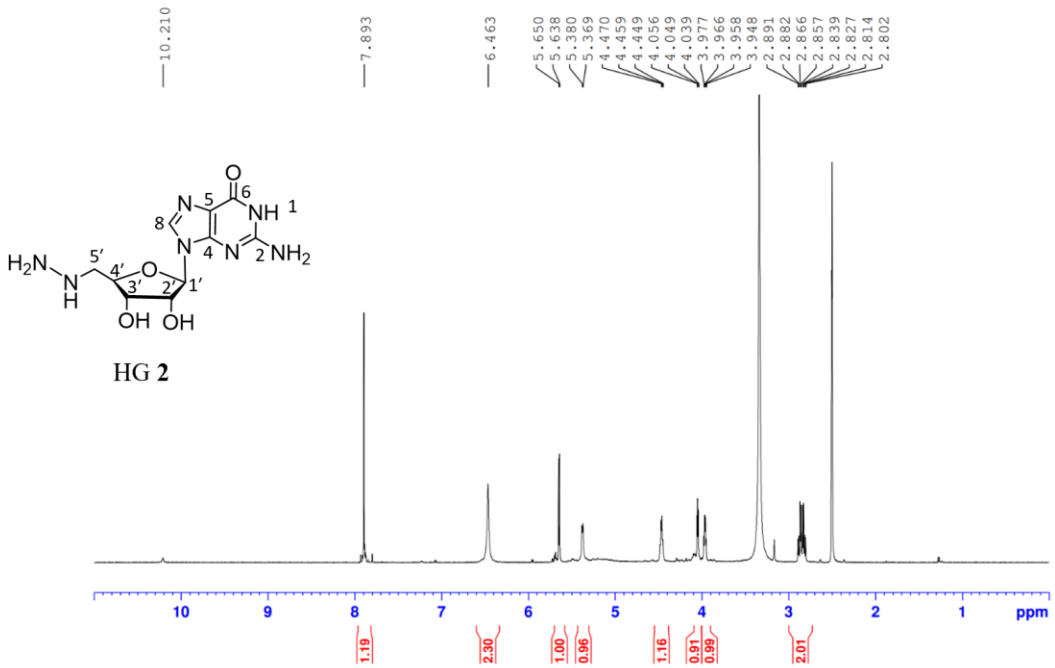

Figure 6.22: ^{1}H NMR spectrum of HG **2** in DMSO-d_6.

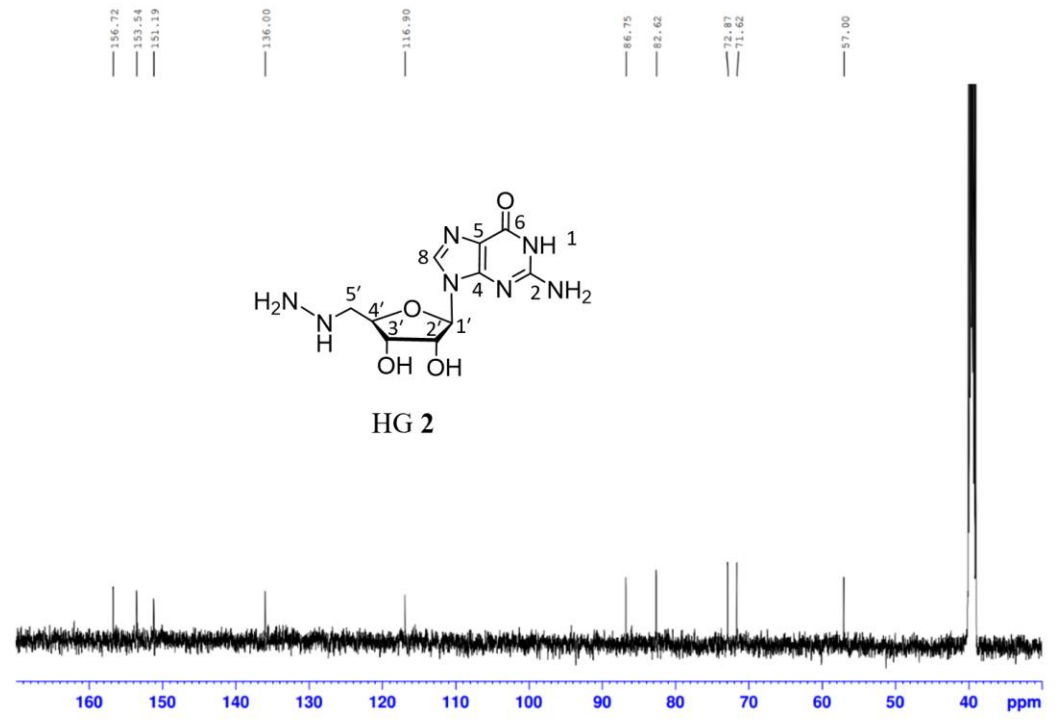

Figure 6.23: ^{13}C NMR spectrum of HG **2** in DMSO-d_6.

esterG 20[80]

Guanosine-5′-methylester (esterG **20**) was synthesized from 2′,3′-isopropylideneguanosine-5′-carboxylate (ipG **19**)[262] based on a literature procedure[80] with the following modifications: The resulting solid containing esterG **20** was thoroughly rinsed with cold water to remove NaCl. The filter cake was dried in air to give esterG **20** as a white solid. NMR data matched the literature.

Preparation of methanolic hydroxylamine solution

Hydroxylamine hydrochloride (6.0 g, 0.087 mol) was added to 20 mL of methanol. While stirring, triethylamine (12 mL, 0.087 mol) was slowly added to the mixture. White precipitates form immediately upon mixing. The resulting mixture was stirred at rt for another 5 min before cooling on ice for 1 h. The solids were filtered off and washed with 4 mL of methanol to give a methanolic solution of hydroxylamine (~25 mL, ~3.5 M) containing triethylammonium chloride.

HAG 15

EsterG **20** (200 mg, 0.64 mmol) was added to the methanolic hydroxylamine solution (25 mL). The mixture was sonicated to break apart any aggregates into a fine suspension and stirred vigorously at rt for 16 hr. Methanol was then removed under reduced pressure and the remaining solid was filtered. The solid was then suspended in deionized water (10 mL).With vigorous stirring, the mixture was acidified to pH~3 using 1 M HCl solution (a gel formed initially around pH 5-7, but with stirring and further acidifying, the aggregates broke apart). The resulting white suspension was filtered and washed with 5 mL of deionized water. The dried solid was recrystallized with a mixture of 10 mL of water and 1.5 mL of DMSO to give a white solid. The solid

was again washed with 5 mL of cold water to remove DMSO. The solid was then dried in air to afford HAG **15** as a white solid (122 mg, 61%).

^{1}H NMR (600 MHz, DMSO-d_6) δ: 4.14 (1 H, m, 3′-CH), 4.21 (1 H, d, J=2.4 Hz, 4′-CH), 4.47 (1 H, m, 2′-CH), 5.60 (1 H, d, J=6.2 Hz, 2′-OH), 5.66 (1 H, d, J=4.5 Hz, 3′-OH), 5.78 (1 H, d, J=6.6 Hz, 1′-CH), 6.40 (2 H, s, NH_2), 8.04 (1 H, s, 8-CH), 9.18 (1 H, s, 5′-NH), 10.74 (1 H, s, br, N1H), 11.28 (1 H, s, 5′-OH). A minor set of signals assigned to the trans-hydroxamic acid isomer was observed by NMR (1-2%).[281]

^{13}C NMR (150 MHz, DMSO-d_6) δ: 72.85 (C3′), 73.59 (C2′), 82.35 (C4′), 86.76 (C1′), 116.87 (C5), 136.03 (C8), 150.87 (C4), 153.70 (C2), 156.69 (C6), 166.08 (C5′).

ESI-MS m/z=313.04 (MW=312.24)

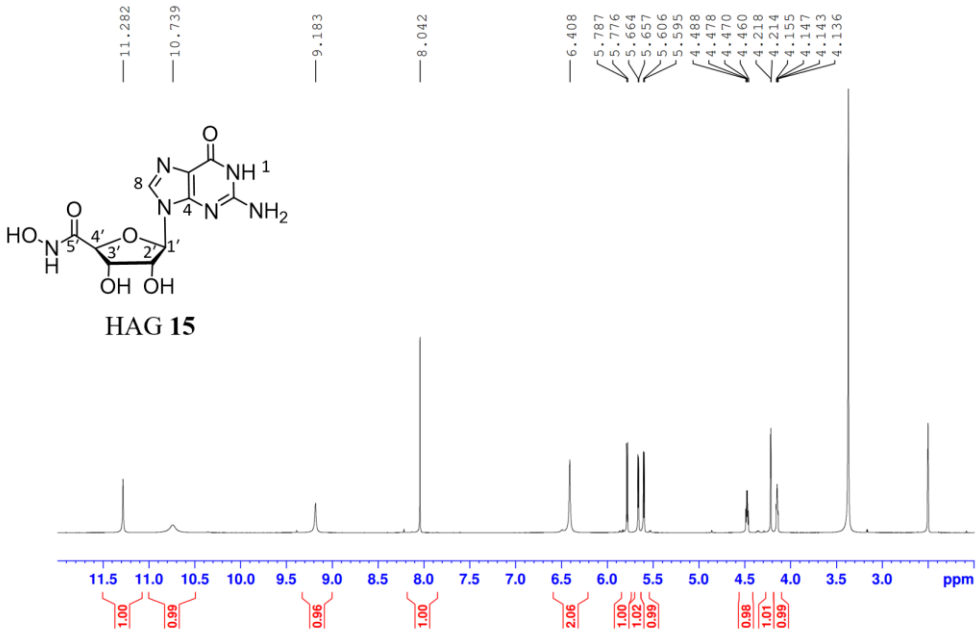

Figure 6.24: ^{1}H NMR spectrum of HAG **15** in DMSO-d_6.

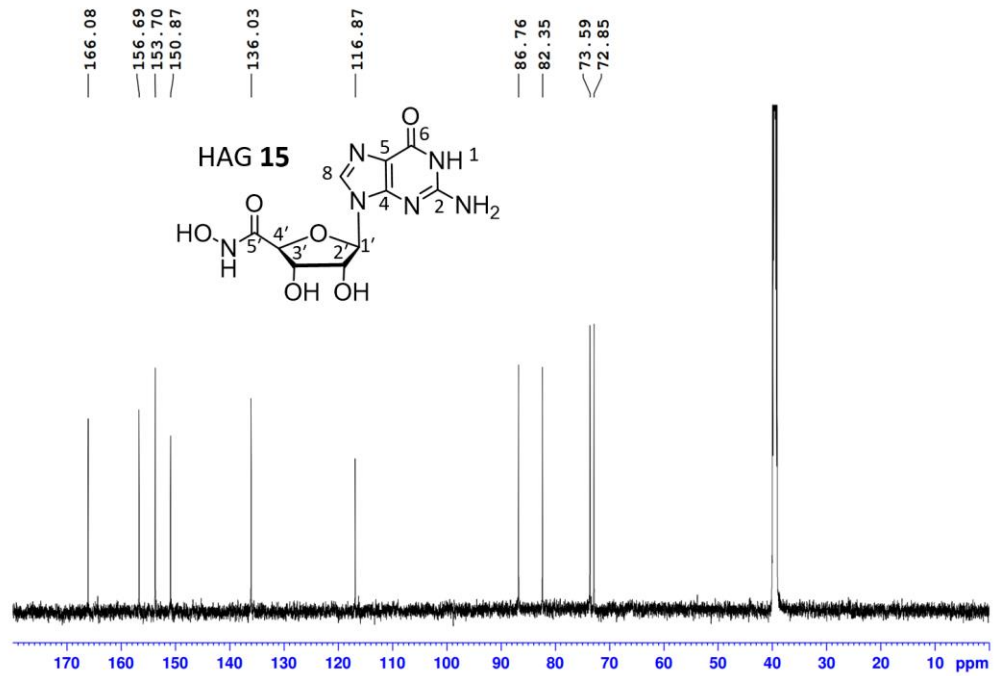

Figure 6.25: ^{13}C NMR spectrum of HAG **15** in DMSO-d_6.

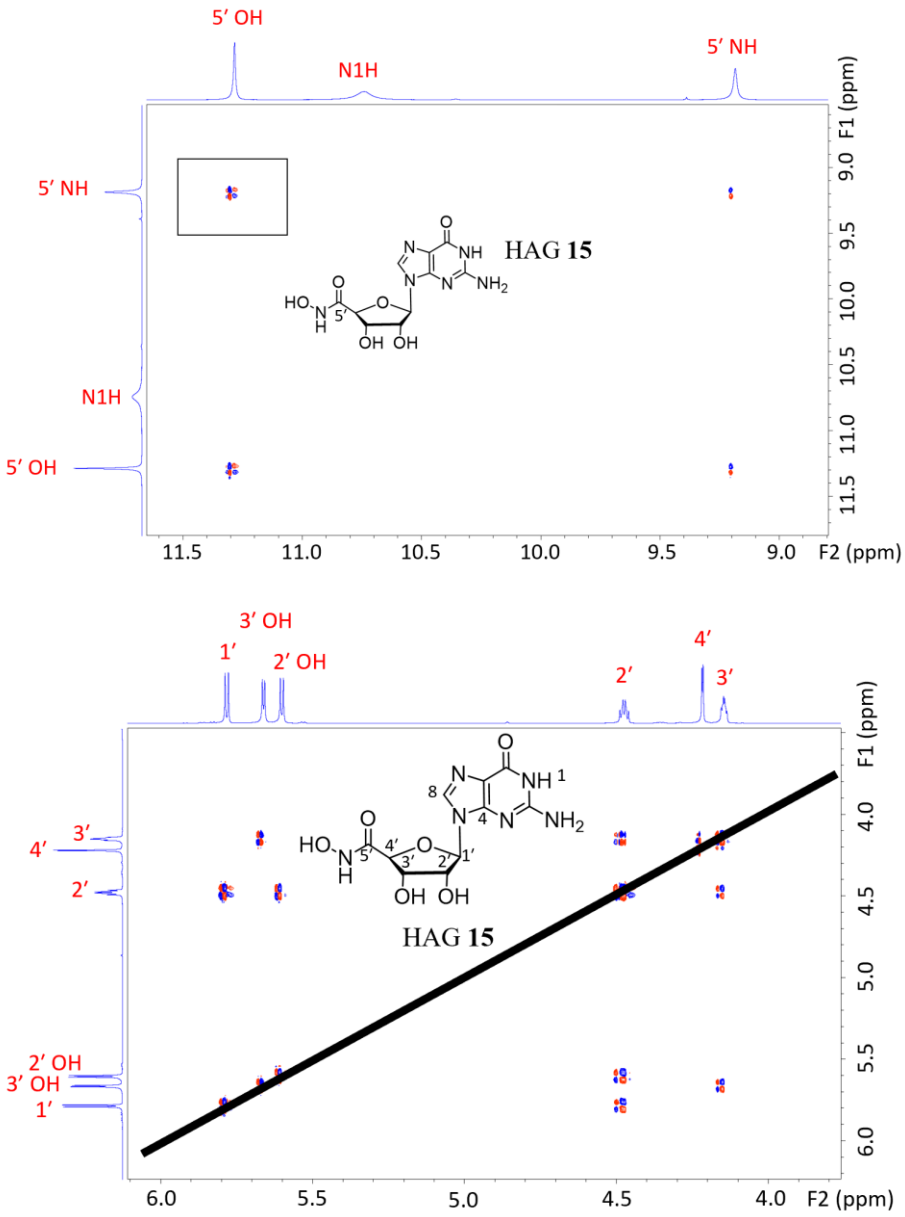

Figure 6.26: ^{1}H-^{1}H COSY spectra of HAG **15** in DMSO-d_6.

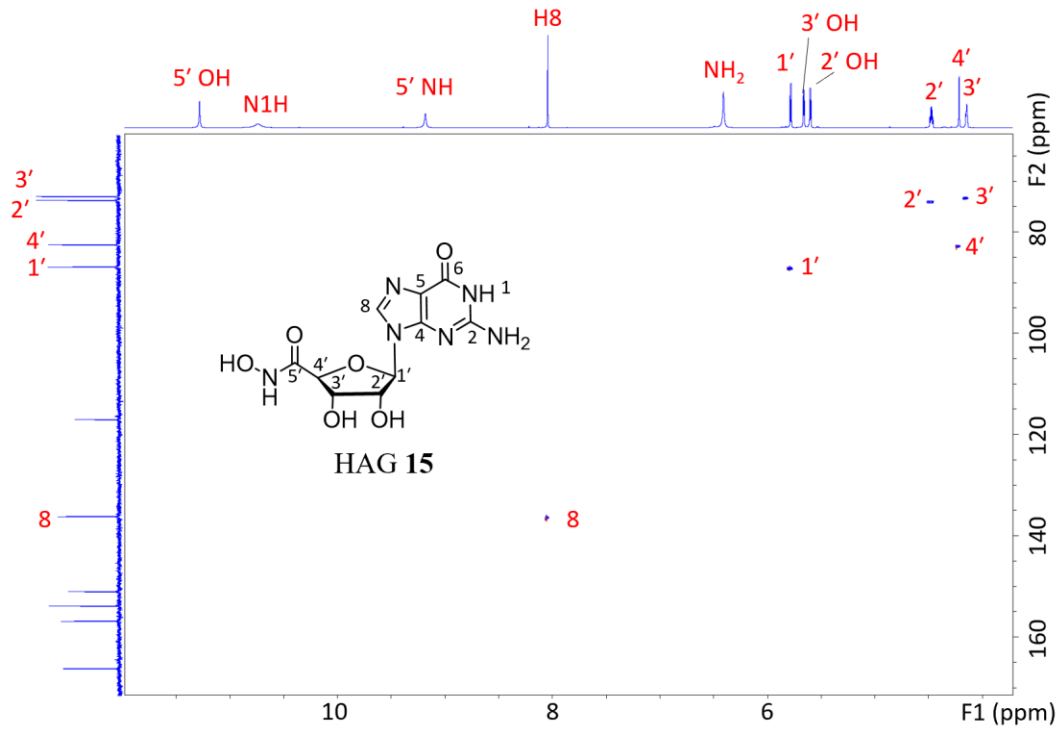

Figure 6.27: ^{1}H-^{13}C HSQC spectrum of HAG **15** in DMSO-d_6.

esterI 22

2′,3′-isopropylideneinosine-5′-carboxylic acid (ipI **21**)[282] (300 mg, 0.931 mmol) was suspended in 15 mL of methanol in a 50 mL roundbottom flask. Under vigorous stirring, thionyl chloride (0.7 mL, 9.6 mmol) was added to the solution within 5 min. The mixture was stirred at rt for 16 h before methanol was removed under reduced pressure. The remaining solid was filtered, washed with methanol (5 mL) and dried in air to afford esterI **22** as a white solid (255 mg, 92%)

^{1}H NMR (600 MHz, DMSO-d_6) δ: 3.72 (3 H, s, -OCH_3), 4.34 (1 H, dd, J=2.79 Hz, J=4.55 Hz, 3′-CH), 4.50 (1 H, d, J=2.61 Hz, 4′-CH), 4.55 (1 H, dd, J=6.45 Hz, J=4.55 Hz, 2′-CH), 6.02 (1 H, d, J=6.4 Hz, 1′-CH), 8.08 (1 H, s, 2-CH), 8.39 (1 H, s, 8-CH), 12.44 (1 H, s, br, N1H)

^{13}C NMR (150 MHz, DMSO-d_6) δ: 52.38 (-OCH_3), 73.15 (C3′), 73.95 (C2′), 82.54 (C4′), 87.46 (C1′), 123.34 (C5), 138.35 (C8), 146.51 (C2), 148.52 (C4), 156.21 (C6), 170.83 (C5′)

ESI-MS m/z=296.94 (MW=296.24)

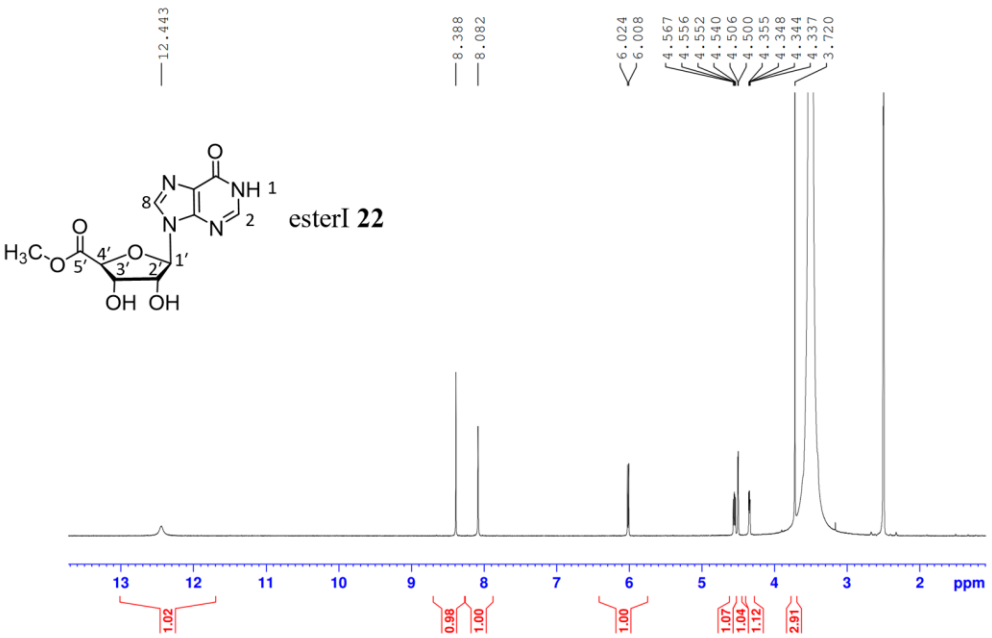

Figure 6.28: ^{1}H NMR spectrum of esterI **22** in DMSO-d_6.

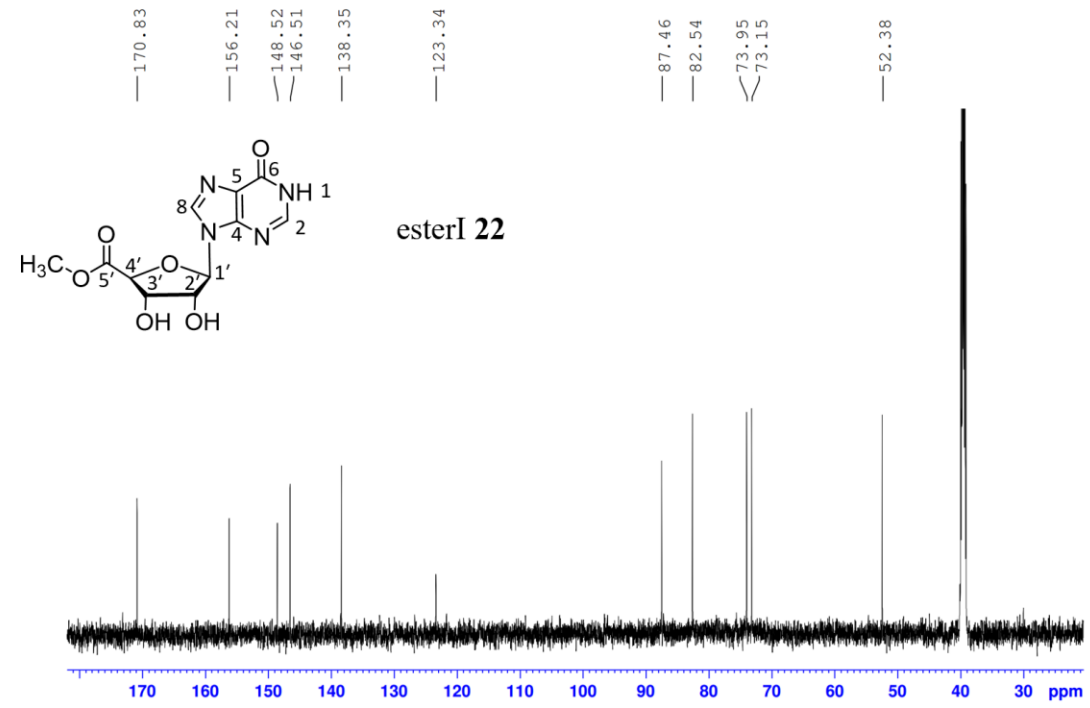

Figure 6.29: ^{13}C NMR spectrum of esterI **22** in DMSO-d_6.

Preparation of methanolic hydroxylamine solution[283]

Hydroxylamine hydrochloride (2.0 g, 0.029 mol) and 20 mL of methanol were added to a roundbottom flask in ice bath. With stirring, potassium hydroxide (1.61 g, 0.029 mol) was slowly added to the mixture. White precipitates form immediately upon mixing. The resulting mixture was stirred on ice for 1 h. The solid was filtered off to give methanolic hydroxylamine solution (~20 mL, ~1.5 M) containing potassium chloride.

Preparation of 5′-hydroxamic acid inosine (HAI 17)

Inosine-5′-methylester (esterI **22**) (200 mg, 0.675 mmol) was added to the methanolic hydroxylamine solution (20 mL). The mixture was sonicated to break apart any aggregates into a fine suspension and stirred vigorously at rt for 16 h. Methanol was then removed under reduced pressure and the remaining solid was filtered. The solid was then suspended in deionized water (4 mL) and the mixture was acidified to pH~3 using 1 M HCl solution. Acetone (50 mL) was then added to the solution to precipitate product. The solid was filtered and dried in air, which was recrystallized with 5 mL of DI water. Hot filtration was performed to remove insoluble particles. The filtrate was cooled on ice and filtered to afford HAI **17** as a white solid (106 mg, 53%).

^{1}H NMR (600 MHz, DMSO-d_6) δ: 4.19 (1 H, dd, J=3.2 Hz, J=4.76 Hz, 3′-CH), 4.27 (1 H, d, J=3.0 Hz, 4′-CH), 4.53 (1 H, dd, J=4.69 Hz, J=6.26 Hz , 2′-CH), 5.97 (1 H, d, J=6.1 Hz, 1′-CH), 8.08 (1 H, d, J=3.4 Hz, 2-CH), 8.49 (1 H, s, 8-CH), 9.18 (1 H, s, br, 5′-NH), 11.15 (1 H, s, 5′-OH), 12.49 (1 H, s, br, N1H). A minor set of signals assigned to the trans-hydroxamic acid isomer was observed by NMR (1-2%).[281]

^{13}C NMR (150 MHz, DMSO-d_6) δ: 72.80 (C3′), 74.54 (C2′), 82.20 (C4′), 87.47 (C1′), 124.26 (C5), 138.65 (C8), 146.09 (C2), 148.25 (C4), 156.52 (C6), 165.89 (C5′)

ESI-MS m/z=297.99 (MW=297.23)

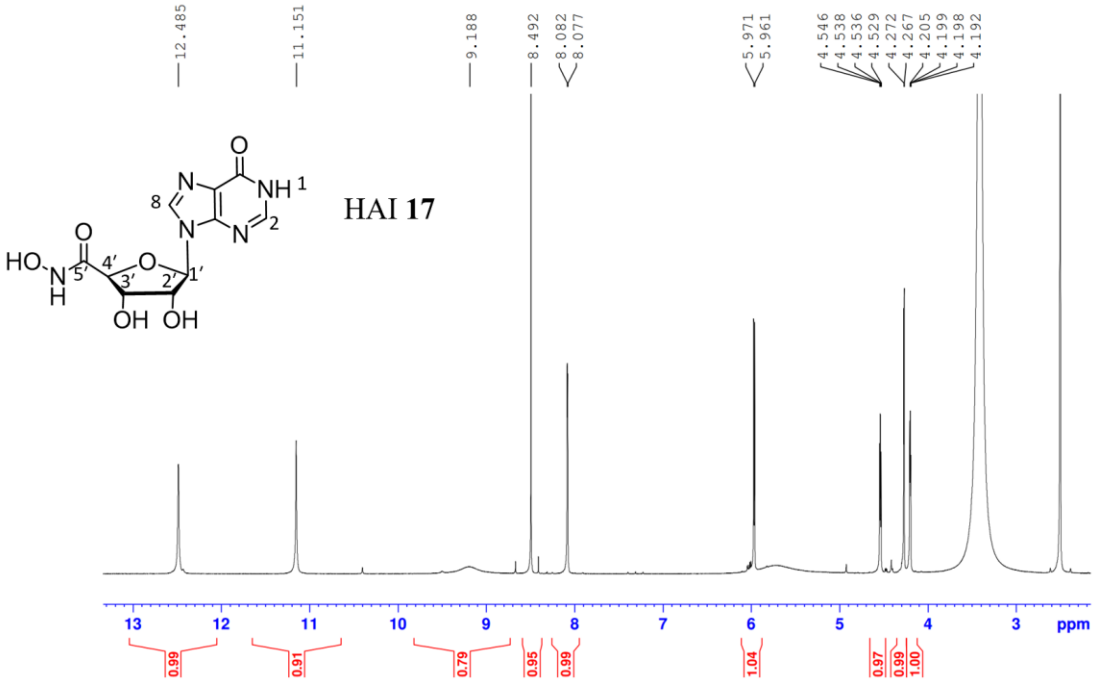

Figure 6.30: ^{1}H NMR spectrum of HAI **17** in DMSO-d_6.

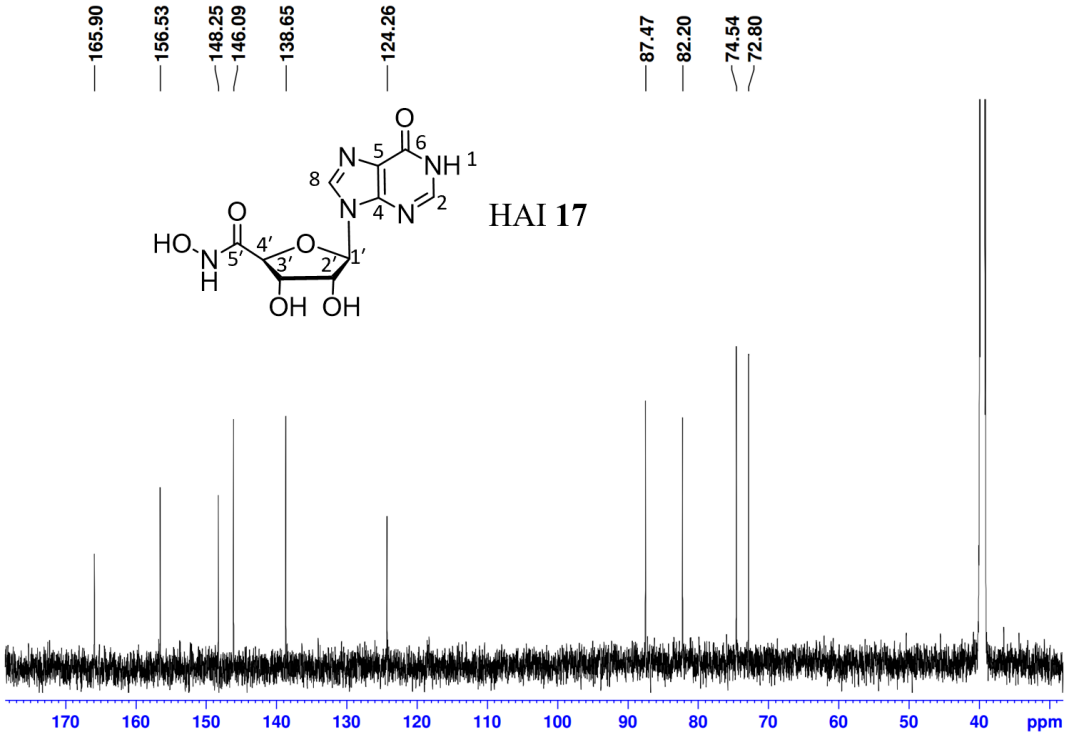

Figure 6.31: ^{13}C NMR spectrum of HAI **17** in DMSO-d_6.

5′-amideG 18

5′-esterG **20** (150 mg, 0.48 mmol) was heated in 5 mL of a methanolic ammonia (5 mL, 2 mol/L) under reflux for 18 h in a 10 mL microwave reaction vial. The mixture was allowed to cool to rt before the solvent was removed under reduced pressure. The residue was recrystallized from 5 mL water to give **18** as an off-white solid (118 mg, 0.40 mmol, 83%)

^{1}H NMR (600 MHz, DMSO-d_6) δ 10.72 (s, 1H, NH), 8.15 (s, 1H, 5′-NH_A), 7.98 (s, 1H), 7.26 (s, 1H, 5′-NH_B), 6.43 (s, 2H, N2H), 5.77 (d, J = 7.5 Hz, 1H, H1′), 5.65 (d, J = 4.2 Hz, 1H, 3′-OH), 5.52 (d, J = 6.4 Hz, 1H, 2′-OH), 4.46 (td, J = 7.0, 4.6 Hz, 1H, H2′), 4.22 (d, J = 1.7 Hz, 1H, H4′), 4.10 (td, J = 4.4, 1.7 Hz, 1H, H3′).

^{13}C NMR (151 MHz, DMSO-d_6) δ 171.77 (C5′), 156.65 (C6), 153.54 (C2), 150.76 (C4), 136.85 (C8), 117.30 (C5), 86.85 (C1′), 84.02 (C4′), 73.13 (C2′), 72.32 (C3′).

ESI-MS ($[M + H]^+$): m/z = 297.09 (MW=296.24)

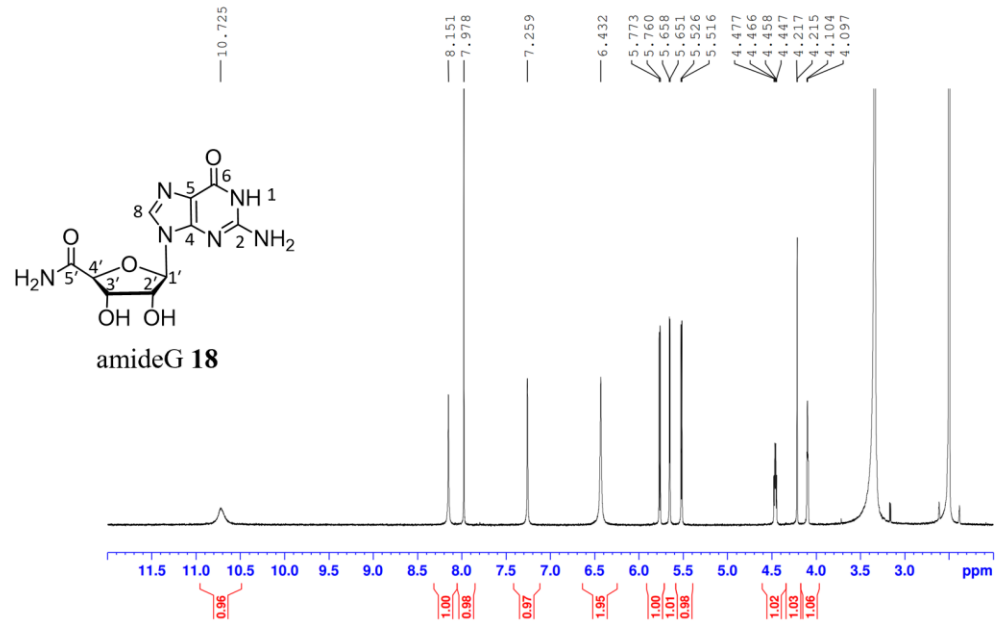

Figure 6.32: ^{1}H NMR spectrum of amideG **18** in DMSO-d_6.

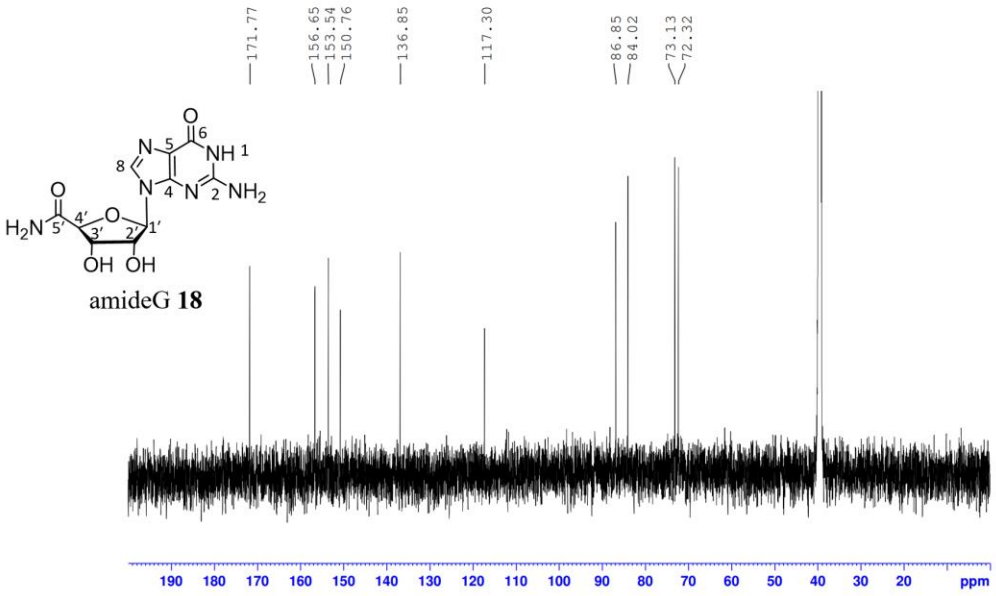

Figure 6.33: ^{13}C NMR spectrum of amideG **18** in DMSO-d_6.

5′-CAI 23

5′-esterI **22** (100 mg, 0.34 mmol) was heated at 75 °C in an aqueous NaOH solution (5 mL, 1 mol/L) for 2 h. The resulting solution was cooled down to rt before lyophilization to give a pink syrup. Conc. HCl was carefully added to adjust the solution to pH=2 and precipitates formed. The mixture was then cooled on ice for 1 h and the resulting solid was filtered, carefully rinsed with 0.5 mL of ice water to give **23** as a white powder (9.8 mg, 0.035 mmol, 10.3%).

^{1}H NMR (600 MHz, DMSO-d_6) δ 12.44 (s, 1H, N1H), 8.79 (s, 1H, C8H), 8.06 (s, 1H, C2H), 5.99 (d, J = 6.8 Hz, 1H, H1′), 5.68 (br), 4.41 (dd, J = 6.9, 4.3 Hz, 1H, H2′), 4.28 (d, J = 1.7 Hz, 1H, H4′), 4.19 (dd, J = 4.3, 1.8 Hz, 1H, H3′).

^{13}C NMR (151 MHz, DMSO-d_6) δ 173.05 (C5′), 156.67 (C6), 148.76 (C4), 145.89 (C2), 139.27 (C8), 123.85 (C5), 86.85 (C1′), 85.01 (C4′), 75.67 (C2′), 74.01 (C3′).

ESI-MS ($[M + H]^+$): m/z = 283.09 (MW=282.21)

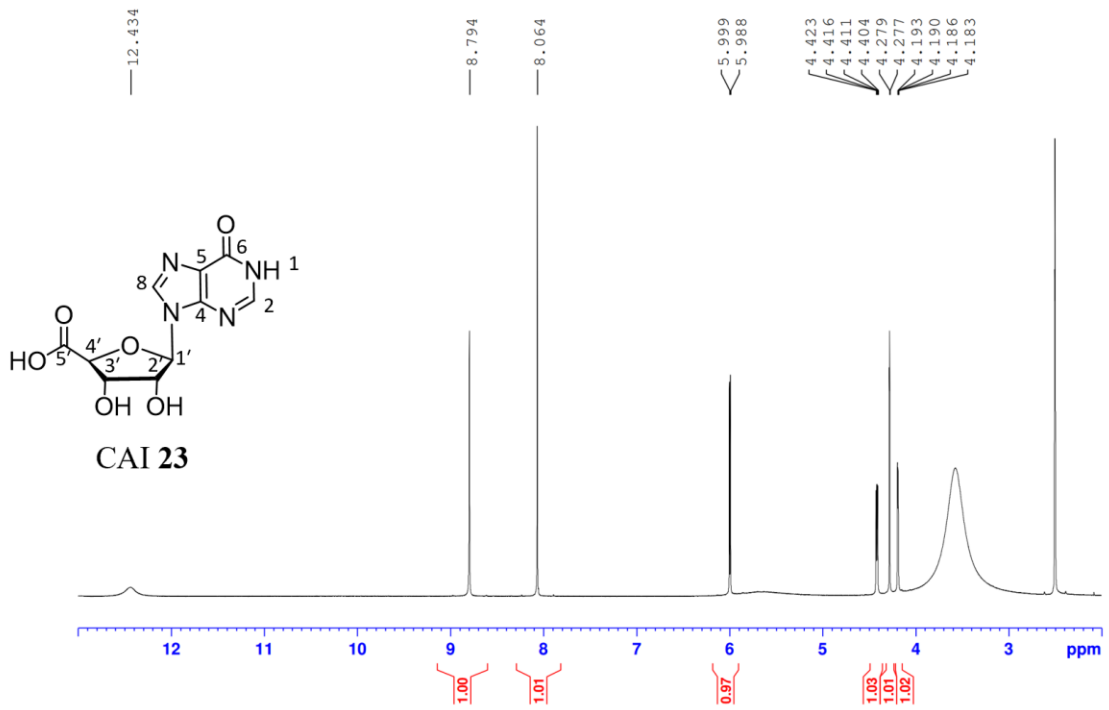

Figure 6.34: ^{1}H NMR spectrum of CAI **23** in DMSO-d_6.

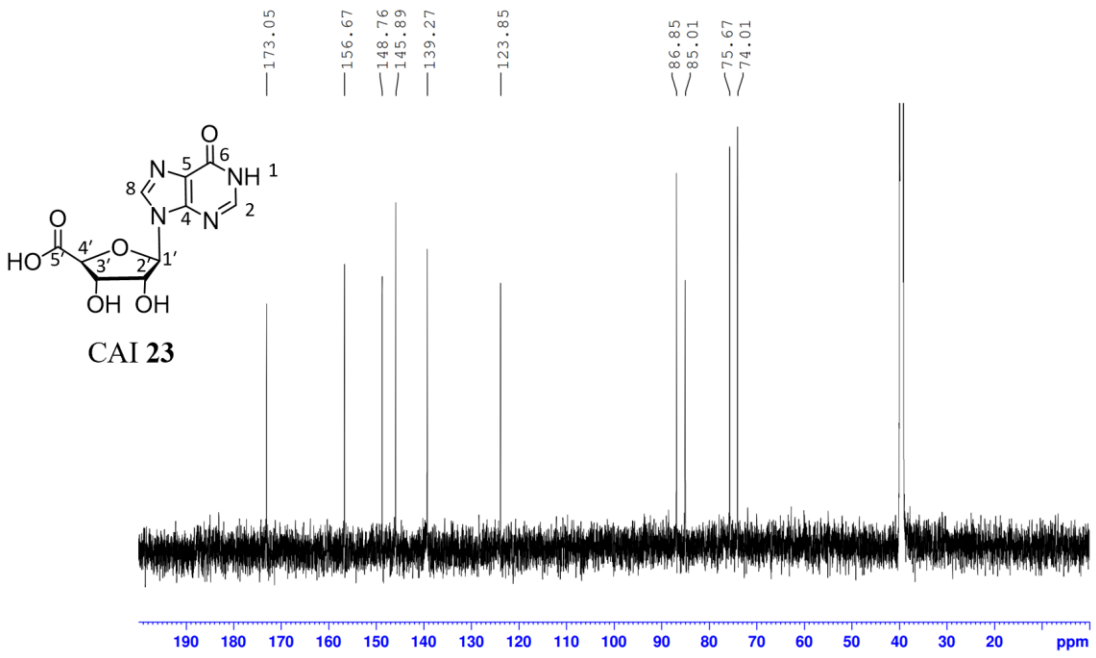

Figure 6.35: ^{13}C NMR spectrum of CAI **23** in DMSO-d_6.

5′-amideI 24

5′-esterI **22** (100 mg, 0.34 mmol) was heated in 5 mL of methanolic ammonia (5 mL, 2 mol/L) under reflux for 18 h in a 10 mL microwave reaction vial. The mixture was allowed to cool to rt before the solvent was removed under reduced pressure. The residue was recrystallized from 2 mL water to give **24** as a white solid (47.1 mg, 0.17 mmol, 50%)

^{1}H NMR (600 MHz, DMSO-d_6) δ 12.21 (s, 1H, N1H), 8.46 (s, 1H, C8H), 8.05 (s, 1H, C2H), 7.80 (s, 1H, 5′-NH_A), 7.42 (s, 1H, 5′-NH_B), 5.95 (d, J = 6.9 Hz, 1H, H1′), 5.70 (d, J = 4.7 Hz, 1H, 2′-OH), 5.63 (d, J = 6.3 Hz, 1H, 3′-OH), 4.53 (m, 1H, H2′), 4.30 (d, J = 2.2 Hz, 1H, H4′), 4.17 (m, 1H, H3′).

^{13}C NMR (151 MHz, DMSO-d_6) δ 171.71 (C5′), 156.55 (C6), 148.27 (C4), 145.96 (C2), 139.35 (C8), 124.60 (C5), 87.29 (C1′), 83.99 (C4′), 73.52 (C2′), 73.08 (C3′).

ESI-MS ($[M + H]^+$): m/z = 282.09 (MW=281.23)

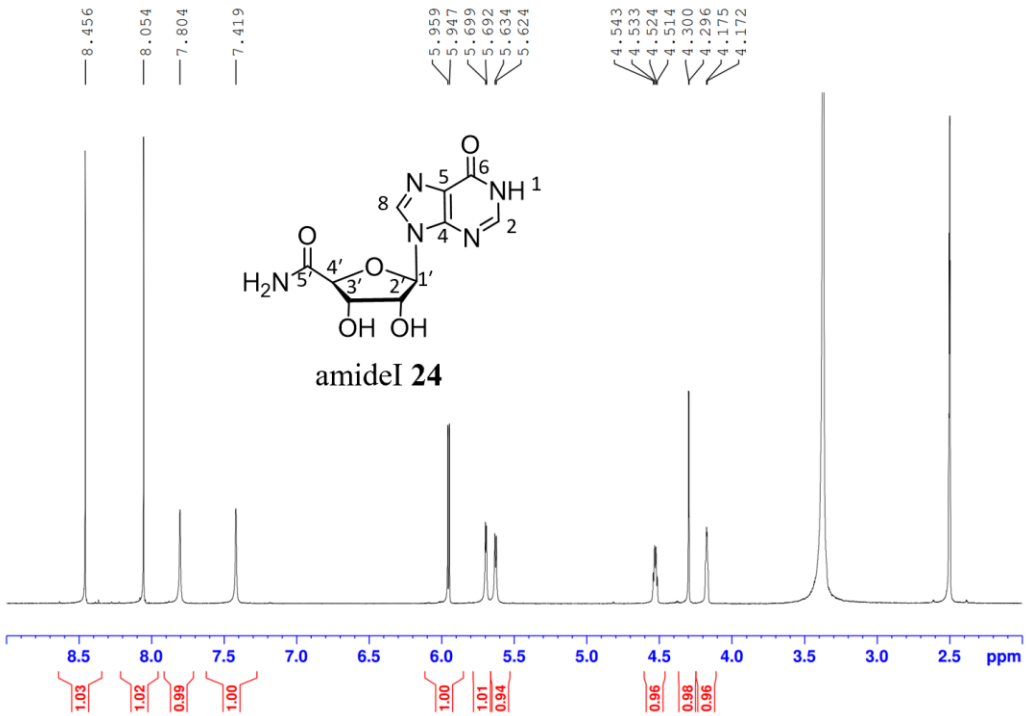

Figure 6.36: ^{1}H NMR spectrum of amideI **24** in DMSO-d_6.

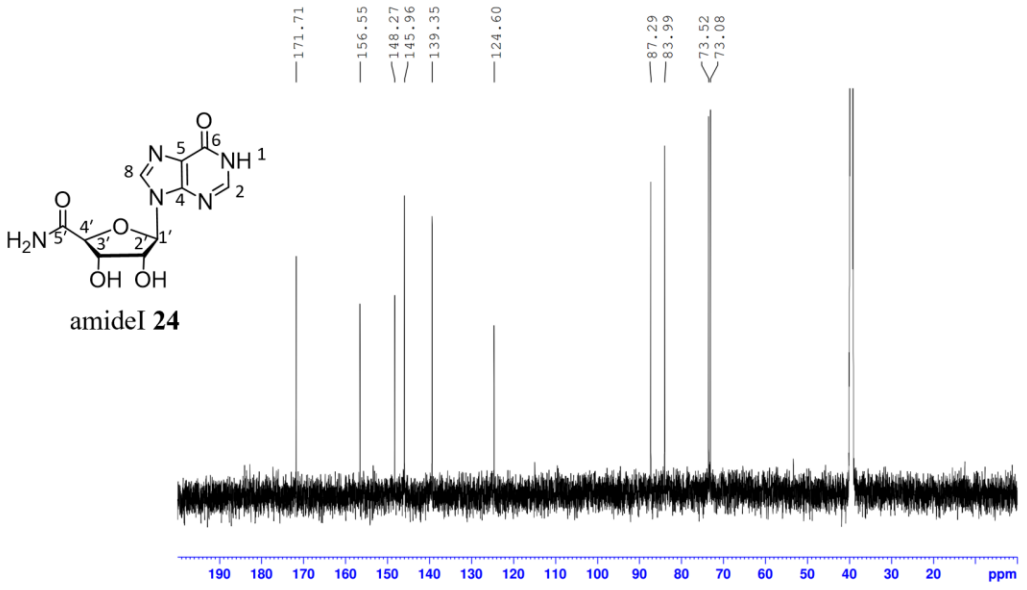

Figure 6.37: ^{13}C NMR spectrum of amideI **24** in DMSO-d_6.

5′-hydrazideI 25

5′-esterI **22** (100 mg, 0.34 mmol) was suspended in 5 mL ethanol and 0.14 mL hydrazine hydrate was added to the suspension. The mixture was heated under reflux for 18 h. The suspension was allowed to cool to rt before the solvent was removed under reduced pressure. The residue was thoroughly rinsed with ethanol to give **25** as a white solid (53 mg, 0.18 mmol, 53%)

^{1}H NMR (600 MHz, DMSO-d_6) δ 9.73 (s, 1H, 5′-NH), 8.47 (s, 1H, C8H), 8.08 (s, 1H, C2H), 5.96 (d, J = 6.4 Hz, 1H, H1′), 4.54 (dd, J = 6.4, 4.5 Hz, 1H, H2′), 4.43 (s, br, 2H, 5′-NH_2), 4.33 (d, J = 2.6 Hz, 1H, H4′), 4.17 (dd, J = 4.5, 2.6 Hz, 1H, H3′).

^{13}C NMR (151 MHz, DMSO-d_6) δ 168.10 (C5′), 156.89 (C6), 148.21 (C4), 146.29 (C2), 138.96 (C8), 124.48 (C5), 87.49 (C1′), 83.23 (C4′), 74.10 (C2′), 72.91 (C3′).

ESI-MS ($[M + H]^+$): m/z = 297.09 (MW=296.24)

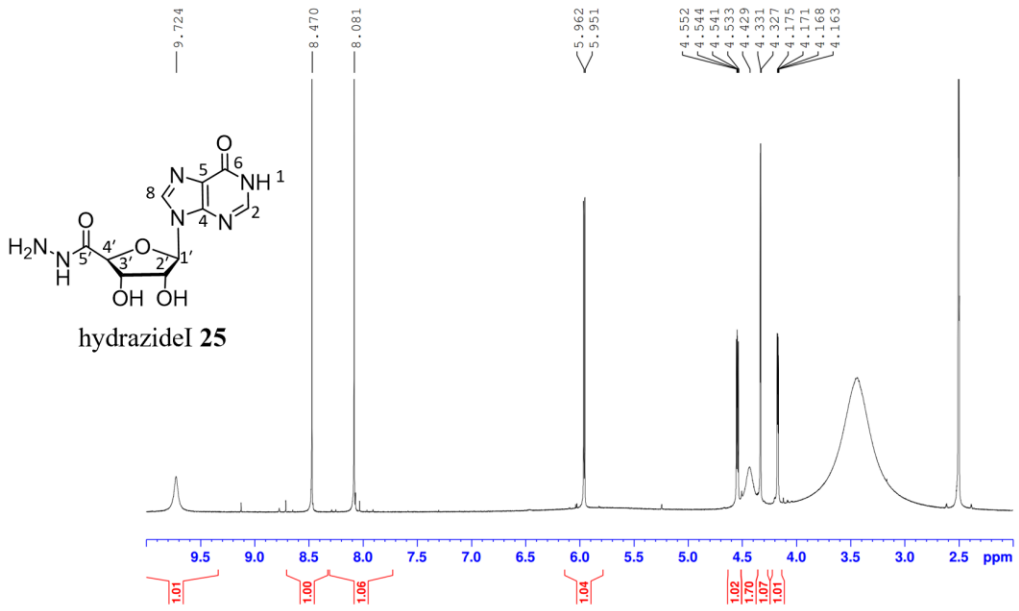

Figure 6.38: ^{1}H NMR spectrum of hydrazideI **25** in DMSO-d_6.

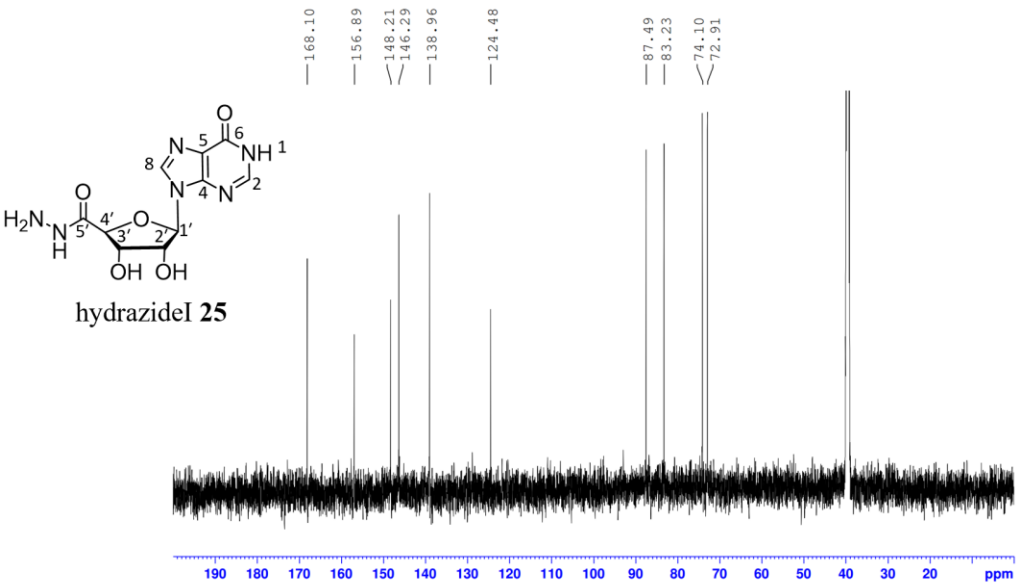

Figure 6.39: ^{13}C NMR spectrum of hydrazideI **25** in DMSO-d_6.

5′-SHG 27

A crude sample containing a mixture of 5′-SHG **27** (about 80%) and 5′-disulfideG **28** (about 20%) was prepared based on literature.[123] The solid (100 mg, 0.33 mmol) was ground to a fine powder and suspended in water (5 mL). Tris(2-carboxyethyl)phosphine (TCEP, 42 mg, 0.17 mmol) was added to the mixture, which was stirred at rt for 1 h The resulting fine suspension was ultracentrifuged and the solution was decanted. The residue was washed with 5 mL of water two times before drying in a lyophilizer to give **27** as a fine white powder (85 mg, 85%, 0.28 mmol)

^{1}H NMR (600 MHz, DMSO-d_6) δ 10.66 (s, 1H , N1H), 7.92 (s, 1H, C8H), 6.48 (s, 2H, N2H), 5.69 (d, J = 6.4 Hz, 1H, H1′), 5.48 (d, J = 6.2 Hz, 1H, 2′-OH), 5.25 (d, J = 4.7 Hz, 1H, 3′-OH), 4.57 (q, J = 5.8 Hz, 1H, H2′), 4.07 (q, J = 3.9 Hz, 1H, H3′), 3.89 (td, J = 6.3, 3.2 Hz, 1H, H4′), 2.82 (ddd, J = 13.7, 8.9, 6.3 Hz, 1H, H5′), 2.73 (ddd, J = 13.8, 7.8, 6.2 Hz, 1H, H5′′), 2.42 (t, J = 8.3 Hz, 1H, 5′-SH).

^{13}C NMR (151 MHz, DMSO-d_6) δ 156.77 (C6), 153.67 (C2), 151.48 (C4), 135.88 (C8), 116.78 (C5), 86.28 (C1′), 85.28 (C4′), 72.70 (C2′), 71.90 (C3′), 26.52 (C5′).

ESI-MS ($[M + H]^+$): m/z = 300.01 (MW=299.31)

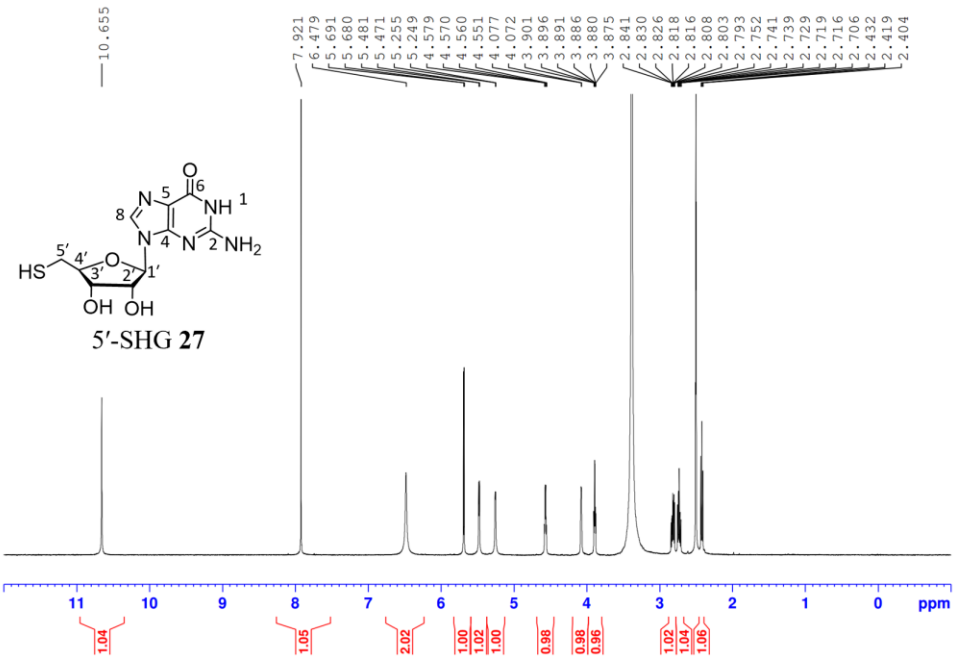

Figure 6.40: ^{1}H NMR spectrum of 5′-SHG **27** in DMSO-d_6.

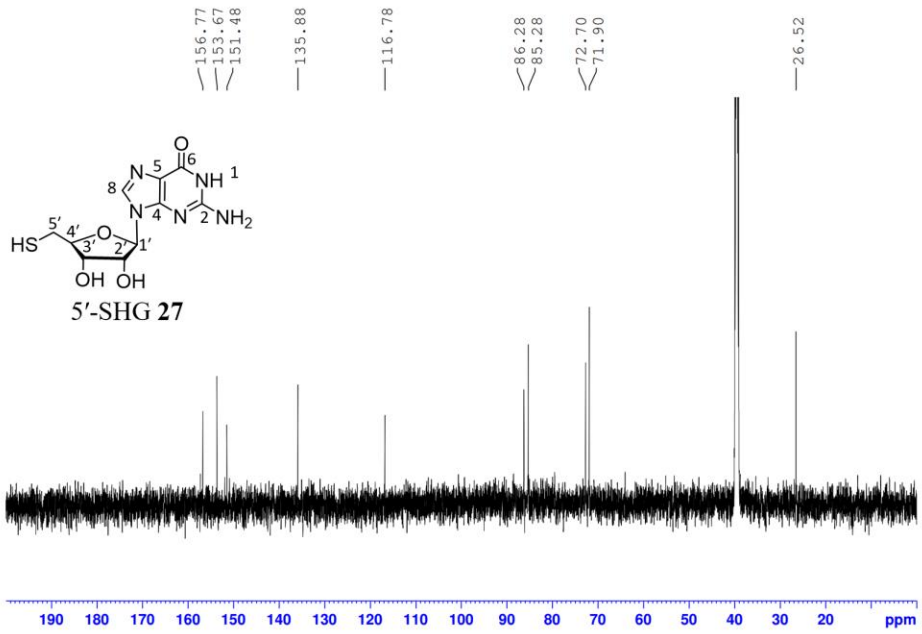

Figure 6.41: ^{13}C NMR spectrum of 5′-SHG **27** in DMSO-d_6.

5′-disulfideG 28

A crude sample containing a mixture of 5′-SHG **27** (about 80%) and 5′-disulfideG **28** (about 20%) was prepared based on literature.[123] The solid (100 mg, 0.33 mmol) was ground to fine powder and suspended in water (5 mL). A solution containing 20 mM NaI and 10 mM I_2 was added in 3 mL portions to the mixture under sonication until a yellow color from unreacted I_2 remain for 10 min. The mixture was then filtered and dried in air. The solid was then redissolved in about 3 mL DMSO to create a saturated solution. Any insoluble particles were filtered at this stage. Deionized water (15 mL) was added to precipitate the solid before filtration to give **28** as a light-yellow crystalline solid (88 mg, 0.15 mmol, 88%).

^{1}H NMR (600 MHz, DMSO-d_6) δ 10.68 (s, 2H, N1H), 7.91 (s, 2H, C8H), 6.50 (s, 4H, N2H), 5.70 (d, J = 6.4 Hz, 2H, H1′), 5.52 (d, J = 6.2 Hz, 2H, 2′-OH), 5.35 (s, 2H, 3′-OH), 4.61 (q, J = 5.0 Hz, 2H, H2′), 4.06 (m, 4H, H3′/ H4′), 3.12 (dd, J = 13.8, 5.8 Hz, 2H, H5′), 3.03 (dd, J = 13.8, 7.3 Hz, 2H, H5′′).

^{13}C NMR (151 MHz, DMSO-d_6) δ 156.81 (C6), 153.69 (C2), 151.48 (C4), 136.03 (C8), 116.83 (C5), 86.47 (C1′), 82.56 (C4′), 72.61 (C2′), 72.52 (C3′), 41.05 (C5′).

ESI-MS ($[M + H]^+$): m/z = 597.05 (MW=596.59)

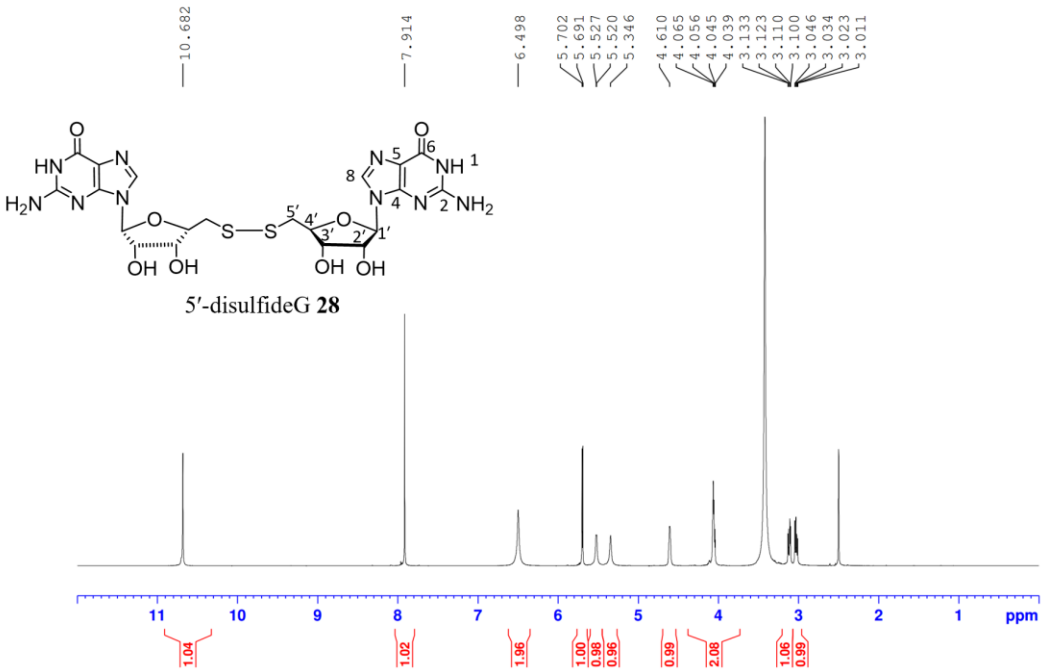

Figure 6.42: ^{1}H NMR spectrum of 5′-disulfideG **27** in DMSO-d_6.

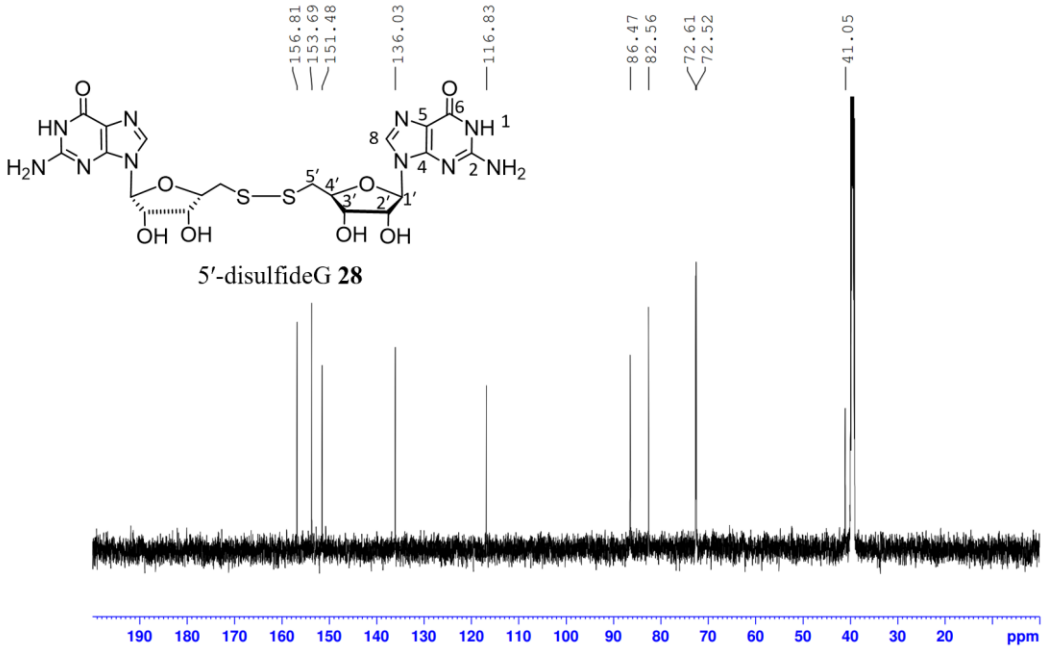

Figure 6.43: ^{13}C NMR spectrum of 5′-disulfideG **27** in DMSO-d_6.

8-thioG 37

8-bromoguanosine **29** (100 mg, 0.28 mmol) was heated with 1 mL of sodium thiomethoxide solution (21 wt%, 3 mmol) under reflux for 18 h. The resulting mixture was filtered to remove insoluble particles and cooled to rt. Under stirring, the filtrate was carefully acidified to pH=2 with concentrated HCl (in a good hood!). The suspension was cooled on ice and filtered. The solid was rinsed with 1 mL of cold water and 2 mL of acetone before recrystallization in water to give **37** as a white fine powder (81 mg, 0.257 mmol, 92%). ^{1}H and ^{13}C NMR spectra matched published values.

^{1}H NMR (600 MHz, DMSO-d_6) δ 12.91 (s, 1H, N7H), 11.03 (s, 1H, N1H), 6.54 (s, 2H, N2H), 6.24 (d, J = 5.5 Hz, 1H, H1′), 5.25 (d, J = 6.0 Hz, 1H, 2′-OH), 4.95 (q, J = 5.9 Hz, 1H, H2′), 4.88 (d, J = 5.7 Hz, 1H, 3′-OH), 4.77 (t, J = 5.9 Hz, 1H, 5′-OH), 4.21 (q, J = 5.4 Hz, 1H, H3′), 3.79 (q, J = 5.5, 4.5 Hz, 1H, H4′), 3.65 (m, 1H, H5′), 3.49 (m, 1H, H5″).

^{13}C NMR (151 MHz, DMSO-d_6) δ 165.71 (C8), 153.51 (C6), 150.90 (C2), 149.52 (C4), 104.08 (C5), 88.73 (C1′), 85.10 (C1′), 70.54 (C2′), 70.30 (C3′), 62.35 (C5′).

ESI-MS ($[M + H]^+$): m/z = 316.11 (MW=315.30)

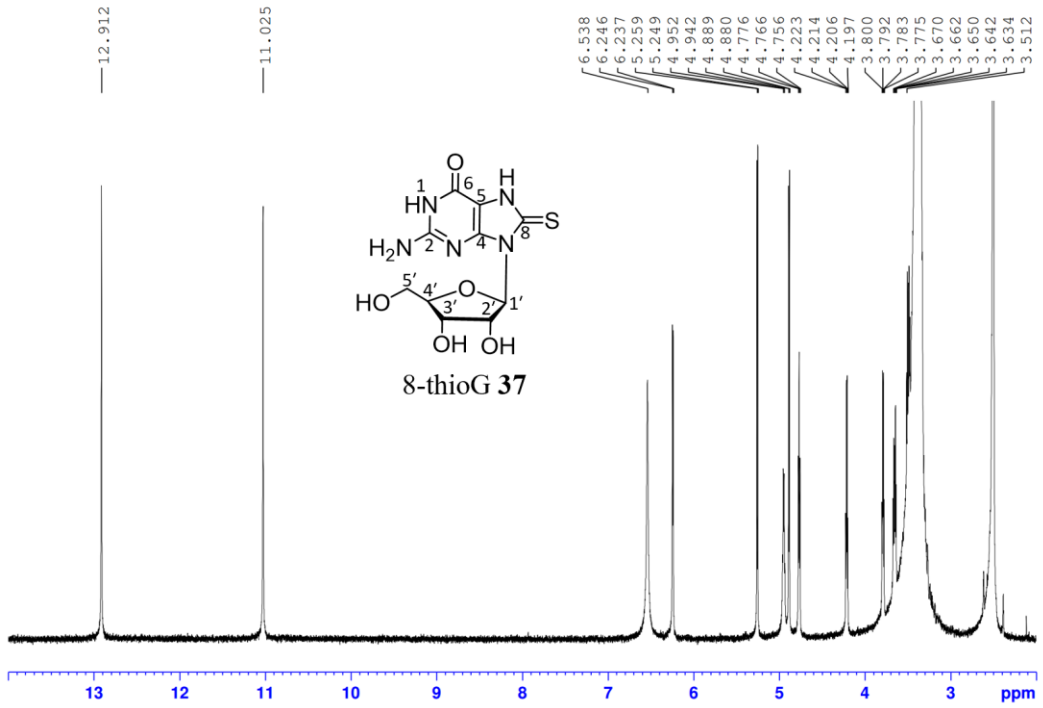

Figure 6.44: ^{1}H NMR spectrum of 8-thioG **37** in DMSO-d_6.

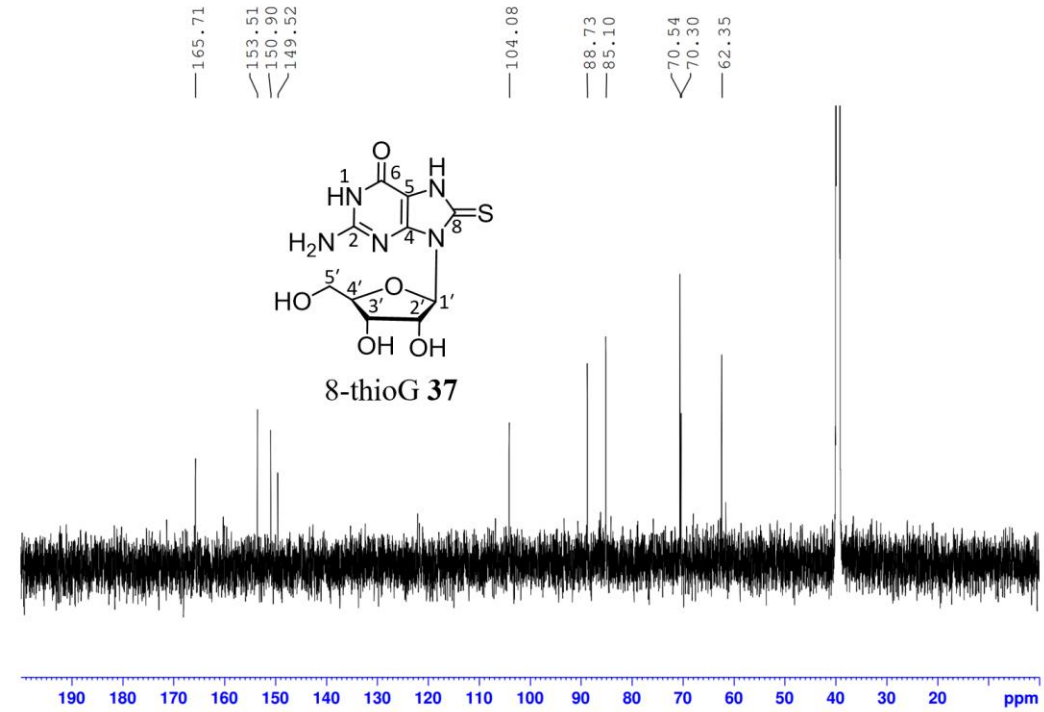

Figure 6.45: ^{13}C NMR spectrum of 8-thioG **37** in DMSO-d_6.

8-disulfideG 38

To a suspension of 8-thioG **37** (250 mg, 0.8 mmol) in a mixture of 2.5 mL methanol and 7.5 mL acetonitrile was added 180 μL I_2 solution (10 mol/L in DMSO). A dark and gelatinous mixture formed upon I_2 addition. The mixture was repeatedly shaken and sonicated until a red fine suspension resulted, which was stirred at rt for 12 h. The mixture was then diluted with dichloromethane (20 mL) and ultracentrifuged. The solid residue was washed with 30 mL of dichloromethane 5 more times. The residue was then stirred in diethyl ether (50 mL) until all solids had broken down to give fine solids. The solvent was removed *in vacuo* to afford **38** as a brown powder (221 mg, 0.35 mmol, 88%)

^{1}H NMR (600 MHz, DMSO-d_6) δ 10.91 (s, 2H, N1H), 6.60 (s, 4H, N2H), 5.93 (d, J = 6.2 Hz, 2H, H1′), 4.99 (t, J = 5.9 Hz, 2H, H2′), 4.18 (dd, J = 5.0, 3.7 Hz, 2H, H3′), 3.82 (dd, J = 4.8 Hz, J = 3.6 Hz, 2H, H4′), 3.66 (dd, J = 11.8, 4.9 Hz, 2H, H5′), 3.54 (dd, J = 11.8, 5.5 Hz, 2H, H5″).

^{13}C NMR (151 MHz, DMSO-d_6) δ 156.19 (C6), 153.82 (C2), 152.54 (C4), 139.41 (C8), 118.59 (C5), 88.77 (C1′), 85.69 (C4′), 71.08 (C2′), 70.60 (C3′), 61.96 (C5′).

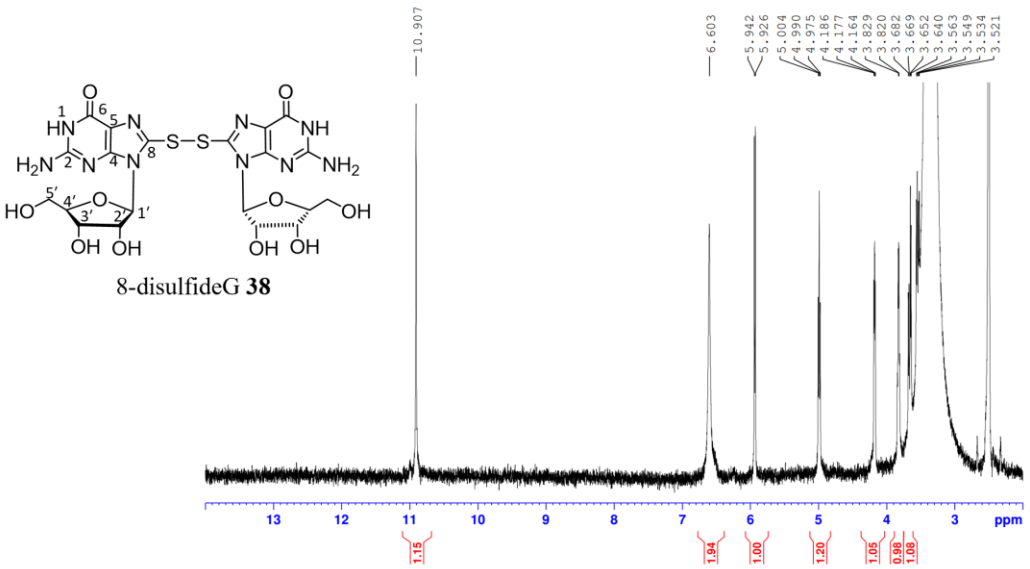

Figure 6.46: ^{1}H NMR spectrum of 8-disulfideG **38** in DMSO-d_6.

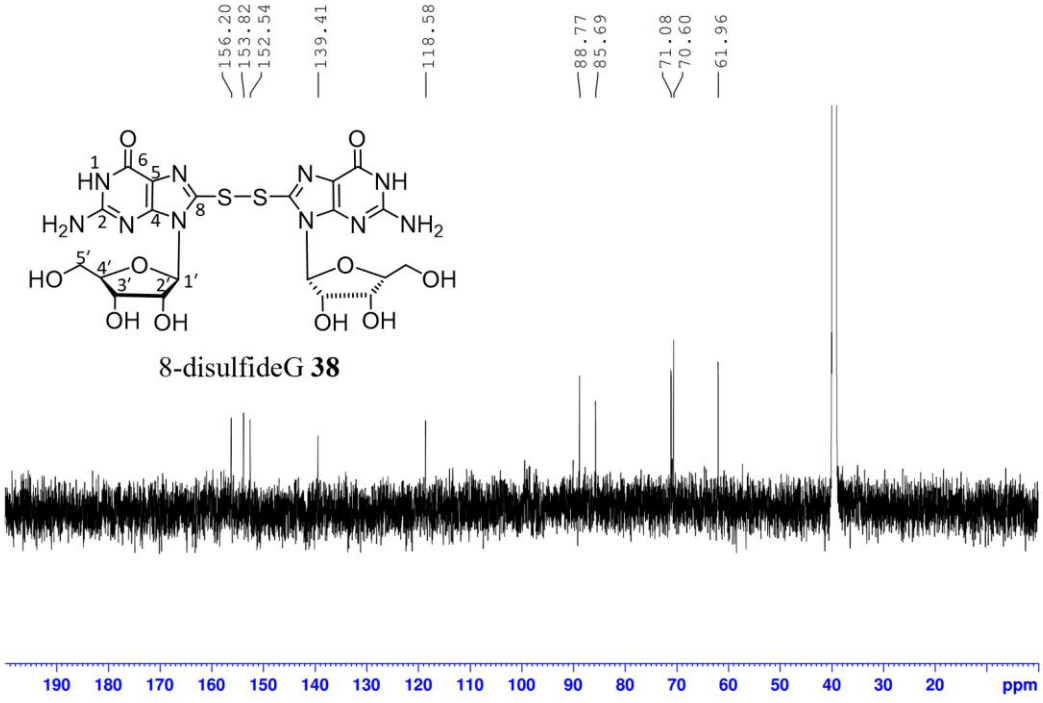

Figure 6.47: ^{13}C NMR spectrum of 8-disulfideG **38** in DMSO-d_6.

8-thiomorpholinoG 33

8-bromoguanosine **29** (100 mg, 0.28 mmol) was added to thiomorpholine (1 ml) and refluxed for 20 hours. The amine was removed under reduced pressure and the residue was sonicated in 2 mL water three times to give **33** as a light brown solid (86.7 mg, 0.23 mmol, 82%)

^{1}H NMR (600 MHz, DMSO-d_6) δ 10.45 (s, 1H, N1H), 6.25 (s, 2H, N2H), 5.52 (d, J = 6.6 Hz, 1H, H1′), 5.37 (d, J = 6.5 Hz, 1H, 2′-OH), 5.04 (m, 2H, 3′-OH/5′-OH), 4.94 (q, J = 6.1 Hz, 1H, H2′), 4.11 (td, J = 5.2, 3.2 Hz, 1H, H3′), 3.83 (td, J = 4.7, 3.1 Hz, 1H, H4′), 3.64 (m, 1H, H5′), 3.50 (m, 1H, H5″), 3.35 (m, 2H, H_A), 3.26 (m, 2H, $H_{A,A'}$), 2.74 (m, 4H, $H_{B,B'}$).

^{13}C NMR (151 MHz, DMSO-d_6) δ 156.00 (C6), 152.80 (C2), 151.95 (C4), 150.42 (C8), 113.68 (C5), 87.69 (C1′), 85.56 (C4′), 70.65 (C2′), 70.28 (C3′), 62.13 (C5′), 53.13 (C_A), 26.21 (C_B).

ESI-MS ($[M + H]^+$): m/z = 385.08 (MW=384.41)

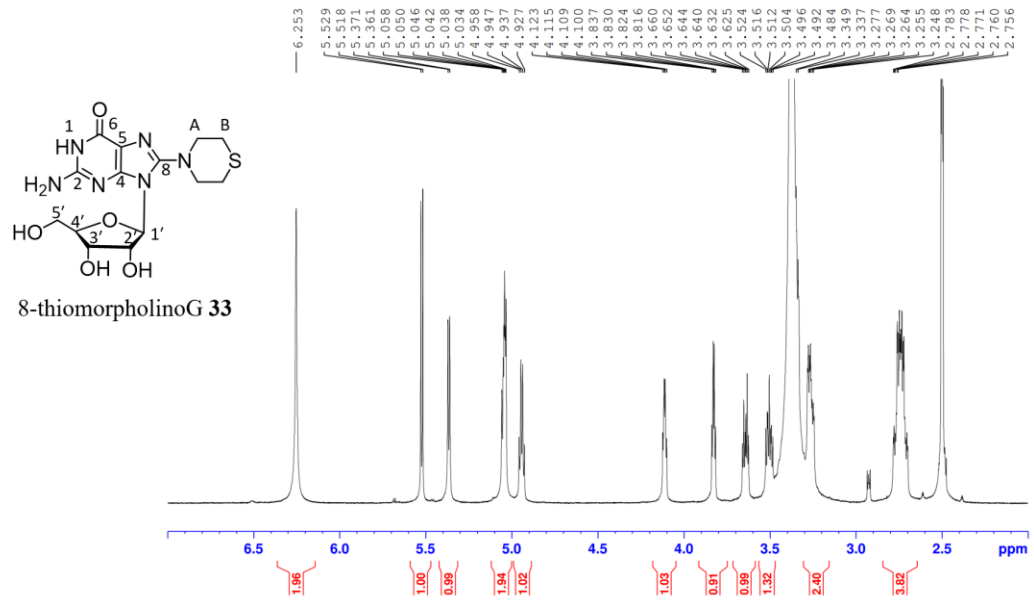

Figure 6.48: ^{1}H NMR spectrum of 8-thiomorpholinoG **33** in DMSO-d_6.

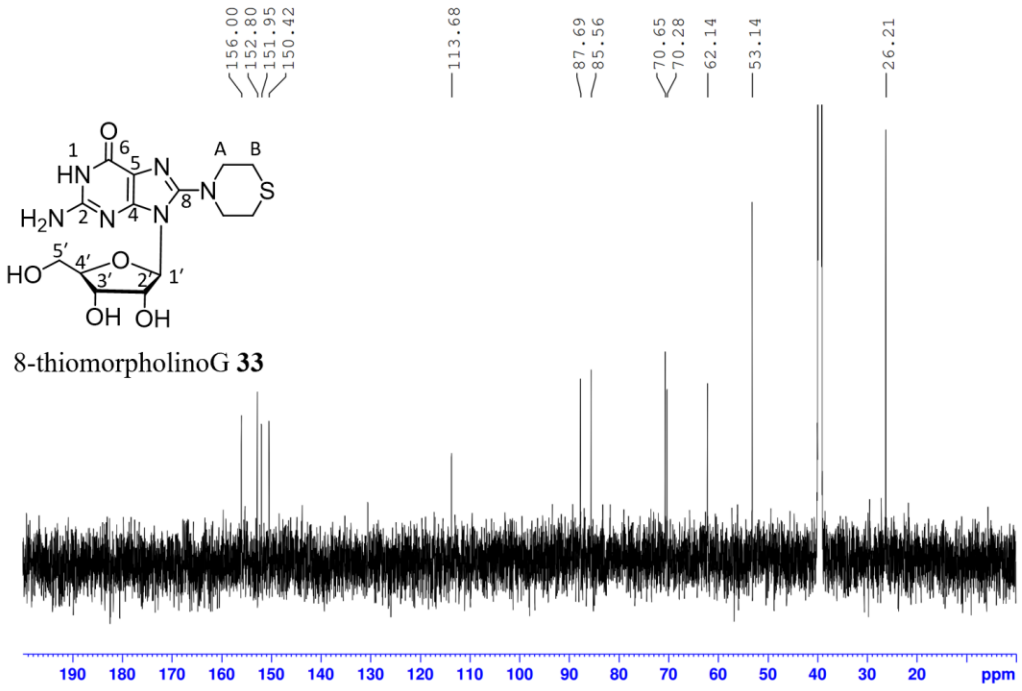

Figure 6.49: ^{13}C NMR spectrum of 8-thiomorpholinoG **33** in DMSO-d_6.

8-piperidinoG 34

8-bromoguanosine **29** (100 mg, 0.28 mmol) was added to piperidine (1 ml) and the mixture was heated under reflux for 20 h. The amine was removed under reduced pressure and the residue was sonicated in 2 mL water three times to give **34** as a white solid (84 mg, 0.23 mmol, 82%)

^{1}H NMR (600 MHz, DMSO-d_6) δ 10.53 (s, 1H, N1H), 6.22 (s, 2H, N2H), 5.54 (d, J = 6.5 Hz, 1H, H1′), 5.36 (d, J = 6.2 Hz, 1H, 2′-OH), 5.05 (dd, J = 7.3, 4.8 Hz, 1H, 5′-OH), 5.00 (d, J = 4.9 Hz, 1H, 3′-OH), 4.95 (q, J = 5.9 Hz, 1H, H2′), 4.12 (q, J = 4.5 Hz, 1H, H3′), 3.82 (m, 1H, H4′), 3.64 (m, 1H, H5′), 3.50 (m, 1H, H5″), 3.06 (m, 2H, H_A), 2.96 (m, 2H, H_A), 1.62 (m, 4H, H_B), 1.53 (m, 2H, H_C).

^{13}C NMR (151 MHz, DMSO-d_6) δ 156.00 (C6), 152.64 (C2 or C4), 152.64 (C4 or C2), 150.47 (C8), 113.60 (C5), 87.82 (C1′), 85.40 (C4′), 70.72 (C2′), 70.28 (C3′), 62.23 (C5′), 52.21 (C_A), 25.16 (C_B), 23.68 (C_C).

ESI-MS ($[M + H]^+$): m/z = 367.14 (MW=366.38)

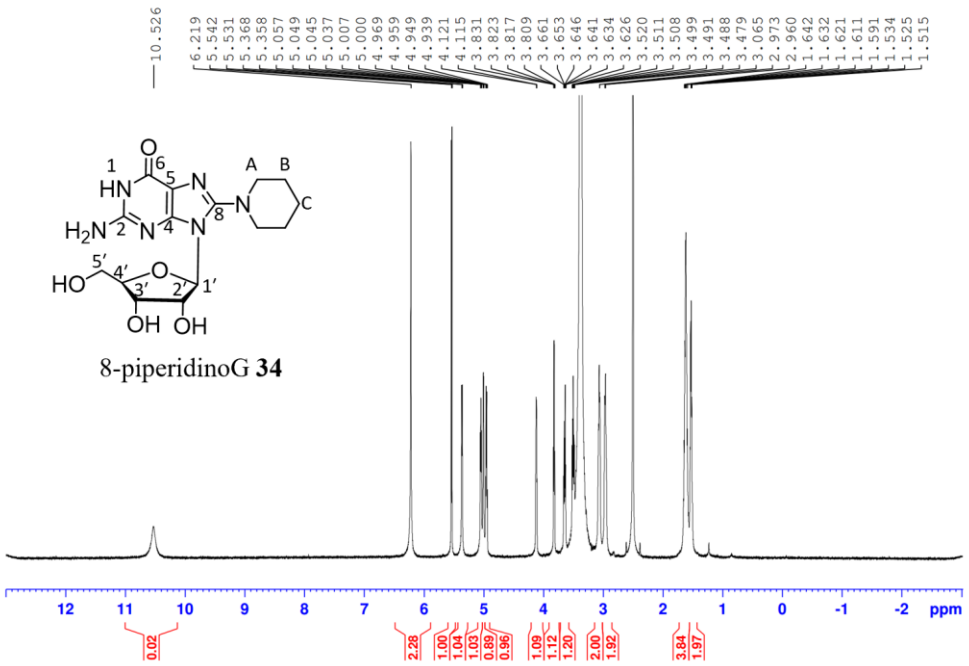

Figure 6.50: ^{1}H NMR spectrum of 8-piperidinoG **34** in DMSO-d_6.

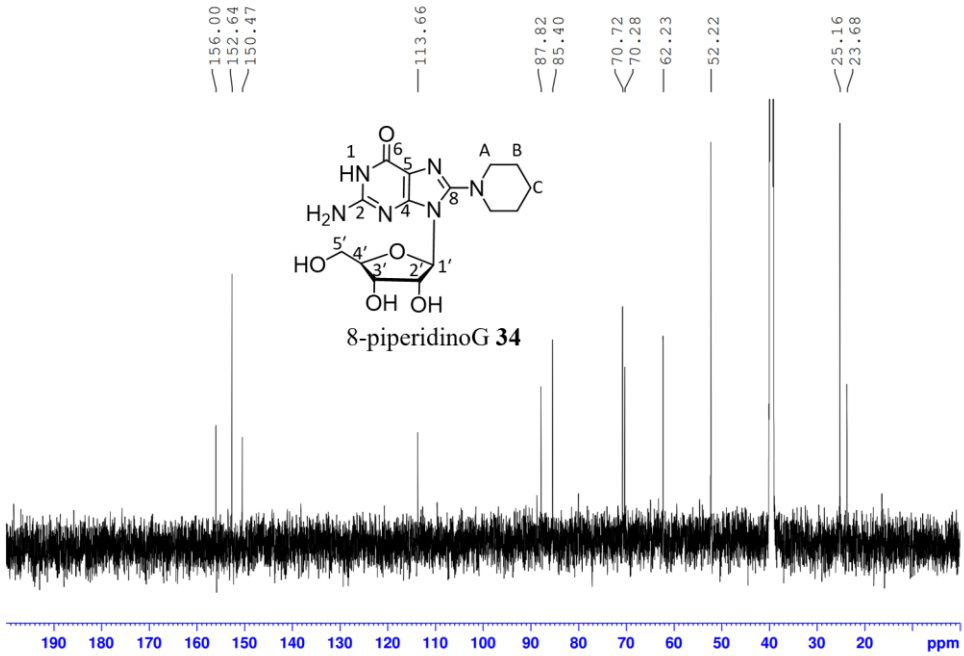

Figure 6.51: ^{13}C NMR spectrum of 8-piperidinoG **34** in DMSO-d_6.

8-pyrrolidinoG 35

8-bromoguanosine **29** (100 mg, 0.28 mmol) was added to pyrrolidine (1 ml) and refluxed for 20 hours. The amine was removed under reduced pressure and the residue was recrystallized from water to give **35** as a white solid (70.2 mg, 0.20 mmol, 71%)

^{1}H NMR (600 MHz, DMSO-d_6) δ 10.58 (s, 1H, N1H), 6.17 (s, 2H, N2H), 5.59 (d, J = 6.5 Hz, 1H, H1′), 5.34 (d, J = 6.4 Hz, 1H, 2′-OH), 5.13 (dd, J = 7.5, 4.6 Hz, 1H, 5′-OH), 5.04 (d, J = 5.1 Hz, 1H, 3′-OH), 4.98 (q, J = 6.2 Hz, 1H, H2′), 4.11 (m, J = 5.2, 3.1 Hz, 1H, H3′), 3.83 (m, J = 4.7, 3.1 Hz, 1H, H4′), 3.64 (m, 1H, H5′), 3.50 (m, 1H, H5″), 3.29 (m, 4H, H_A), 1.83 (m, 4H, H_B).

^{13}C NMR (151 MHz, DMSO-d_6) δ 156.06 (C6), 152.35 (C2), 152.01 (C4), 150.67 (C8), 113.84 (C5), 88.24 (C1′), 85.62 (C4′), 70.91 (C2′), 70.47 (C3′), 62.43 (C5′), 51.49 (C_A), 24.78 (C_B).

ESI-MS ($[M + H]^+$): m/z = 353.16 (MW=352.35)

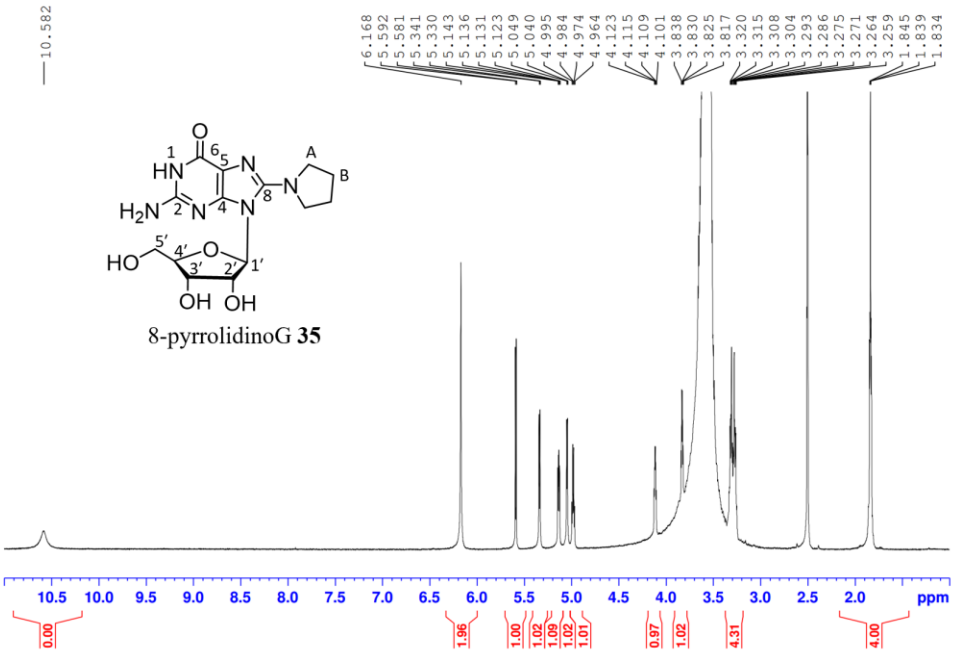

Figure 6.52: ^{1}H NMR spectrum of 8-pyrrolidinoG **35** in DMSO-d_6.

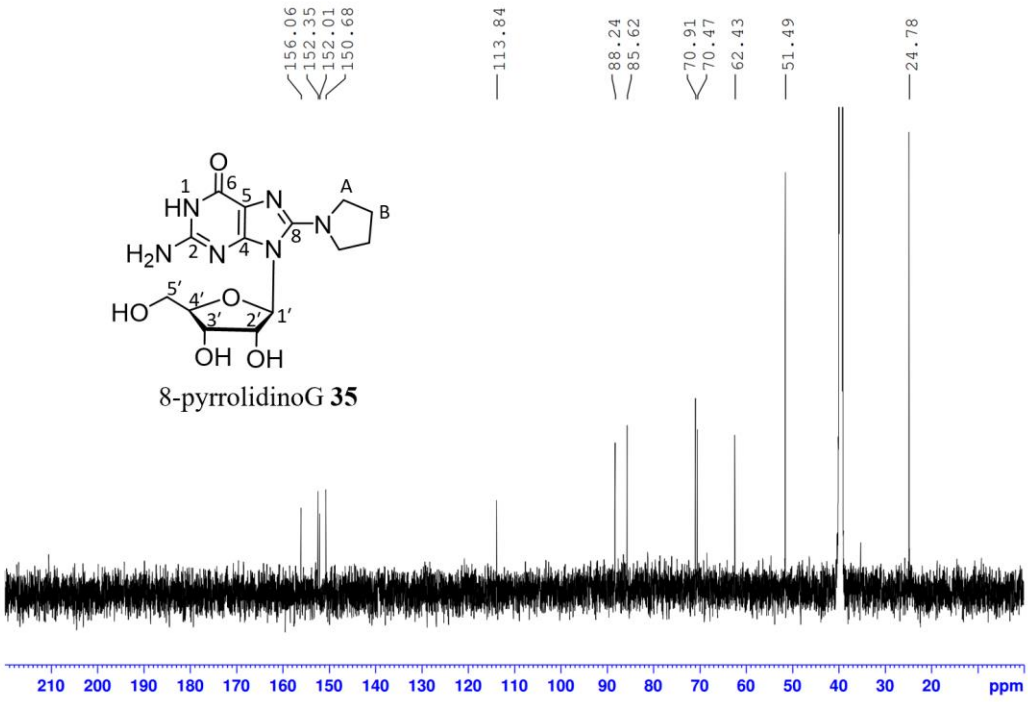

Figure 6.53: ^{13}C NMR spectrum of 8-pyrrolidinoG **35** in DMSO-d_6.

8-NMe_2G 36

8-bromoguanosine **29** (100 mg, 0.28 mmol) was added to a methanolic solution of dimethylamine (2 mol/L, 1.5 ml) and refluxed for 20 h in a 10 mL microwave reaction vial. The mixture was allowed to cool to rt before the solvent was removed under reduced pressure. The residue was recrystallized from water to give **36** as a shiny white solid (52.4 mg, 0.16 mmol, 57%)

^{1}H NMR (600 MHz, DMSO-d_6) δ 10.61 (s, 1H, N1H), 6.22 (s, 2H, N2H), 5.57 (d, J = 6.7 Hz, 1H, H1′), 5.35 (d, J = 6.4 Hz, 1H, 2′-OH), 5.11 (dd, J = 7.5, 4.6 Hz, 1H, 5′-OH), 5.05 (d, J = 4.9 Hz, 1H, 3′-OH), 4.96 (q, J = 6.2 Hz, 1H, H2′), 4.11 (m, 1H, H3′), 3.84 (q, J = 4.5 Hz, 1H, H4′), 3.40-3.70 (m, 2H, H5′, H5′′), 2.72 (s, 6H, 8-CH_3).

^{13}C NMR (151 MHz, DMSO-d_6) δ 156.19 (C6), 153.50 (C2), 152.75 (C4), 150.83 (C8), 113.67 (C5), 88.03 (C1′), 85.67 (C4′), 70.95 (C2′), 70.43 (C3′), 62.40 (C5′), 43.23 (C_A).

ESI-MS ($[M + H]^+$): m/z = 327.14 (MW=326.31)

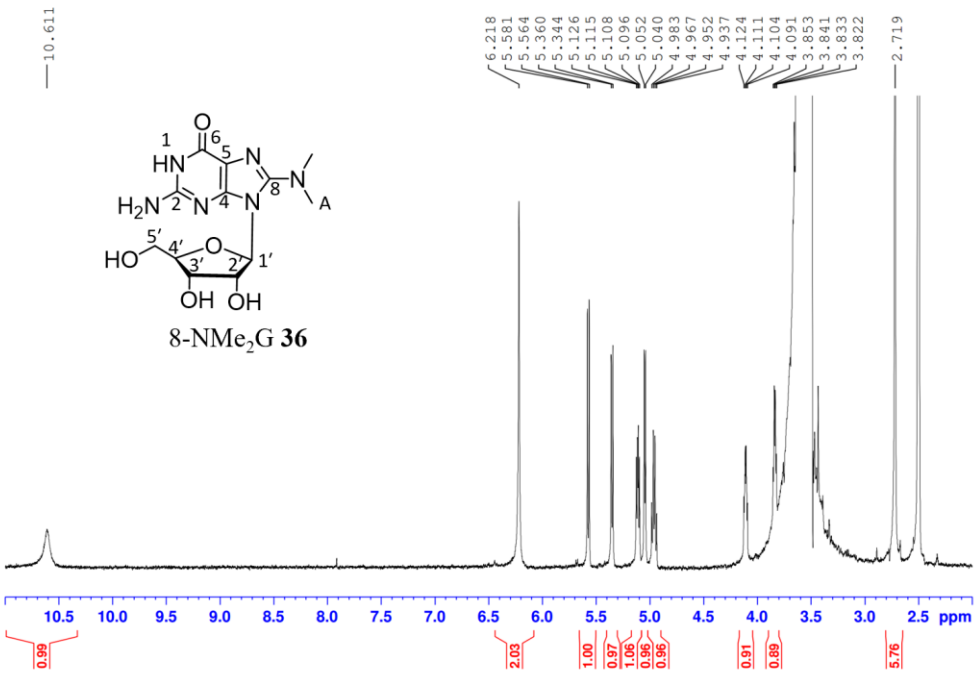

Figure 6.54: ^{1}H NMR spectrum of 8-NMe$_2$G **36** in DMSO-d$_6$.

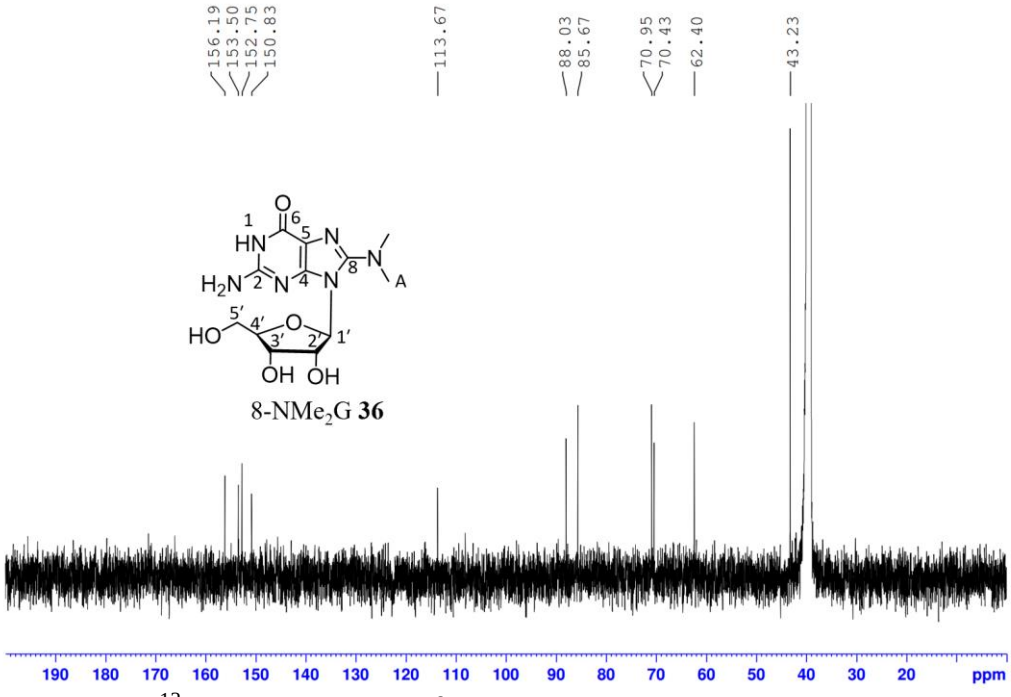

Figure 6.55: ^{13}C NMR spectrum of 8-NMe$_2$G **36** in DMSO-d$_6$.

6.7 NCI-60 screening results

General Description:[284]

As of early 2007 all compounds submitted to the NCI 60 Cell screen are tested initially at a single high dose (10^{-5} M) in the full NCI 60 cell panel. Only compounds which satisfy pre-determined threshold inhibition criteria in a minimum number of cell lines will progress to the full 5-dose assay. The threshold inhibition criteria for progression to the 5-dose screen was selected to efficiently capture compounds with anti-proliferative activity based on careful analysis of historical DTP screening data. The threshold criteria may be updated as additional data becomes available.

Interpretation of One-Dose Data:[284]

The One-dose data will be reported as a mean graph of the percent growth of treated cells and will be similar in appearance to mean graphs from the 5-dose assay. The number reported for the One-dose assay is growth relative to the no-drug control, and relative to the time zero number of cells. This allows detection of both growth inhibition (values between 0 and 100) and lethality (values less than 0). This is the same as for the 5-dose assay, described below. For example, a value of 100 means no growth inhibition. A value of 40 would mean 60% growth inhibition. A value of 0 means no net growth over the course of the experiment. A value of -40 would mean 40% lethality. A value of -100 means all cells are dead. Information from the One-dose mean graph is available for COMPARE analysis.

One-dose assays show that 8-thiomorpholinoG **33** has 25% inhibition against SNB-75 cell line (central nervous system cancer); 8-pyrrolidinoG **35** has 22% inhibition

against SNB-75 cell line (central nervous system cancer); aminoG **4** shows 23% inhibition against SNB-75 cell line (central nervous system cancer); thiophosphoG **26** shows 35% inhibition against UO-31 cell line (Renal cancer).

Developmental Therapeutics Program

One Dose Mean Graph

NSC: D-817320 / 1 | **Conc:** 1.00E-5 Molar | **Test Date:** Aug 05, 2019

Experiment ID: 1908OS48 | **Report Date:** Aug 29, 2019

Panel/Cell Line	Growth Percent
Leukemia	
CCRF-CEM	103.16
HL-60(TB)	105.45
K-562	119.74
MOLT-4	108.53
RPMI-8226	111.97
SR	124.34
Non-Small Cell Lung Cancer	
A549/ATCC	100.06
EKVX	100.23
HOP-62	101.32
HOP-92	102.11
NCI-H226	103.32
NCI-H23	99.29
NCI-H322M	103.81
NCI-H460	107.67
NCI-H522	92.31
Colon Cancer	
COLO 205	104.55
HCC-2998	100.14
HCT-116	107.31
HCT-15	100.57
HT29	101.24
KM12	104.09
SW-620	102.84
CNS Cancer	
SF-268	96.80
SF-539	102.98
SNB-19	103.92
SNB-75	85.49
U251	100.81
Melanoma	
LOX IMVI	98.34
MALME-3M	98.61
M14	107.31
MDA-MB-435	100.85
SK-MEL-2	107.51
SK-MEL-28	101.47
SK-MEL-5	101.33
UACC-257	98.40
UACC-62	99.52
Ovarian Cancer	
IGROV1	102.06
OVCAR-3	104.31
OVCAR-4	101.01
OVCAR-5	103.94
OVCAR-8	103.74
NCI/ADR-RES	103.60
SK-OV-3	101.25
Renal Cancer	
786-0	101.02
A498	107.45
ACHN	102.79
CAKI-1	97.16
RXF 393	103.70
SN12C	102.34
TK-10	94.81
UO-31	93.43
Prostate Cancer	
PC-3	99.58
DU-145	110.45
Breast Cancer	
MCF7	99.35
MDA-MB-231/ATCC	107.12
HS 578T	106.70
BT-549	104.61
MDA-MB-468	107.04
Mean	102.84
Delta	17.35
Range	38.85

Mean Growth Percent - Growth Percent

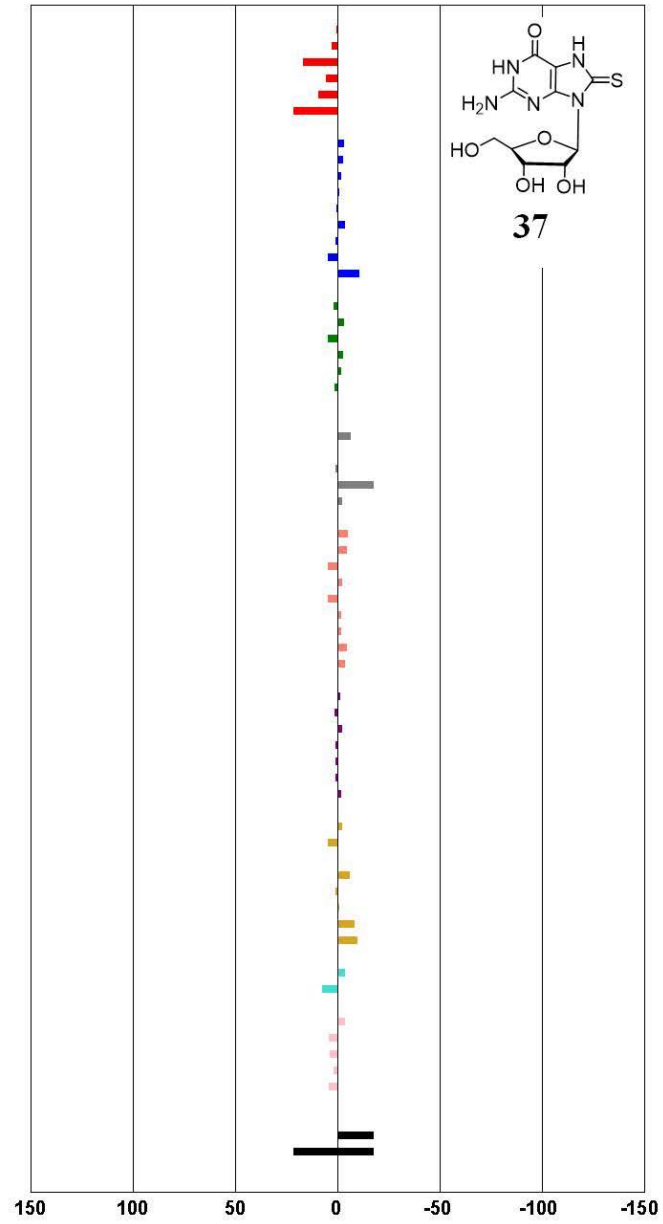

37

Developmental Therapeutics Program	NSC: D-817319 / 1	Conc: 1.00E-5 Molar	Test Date: Aug 05, 2019
One Dose Mean Graph	Experiment ID: 1908OS48		Report Date: Aug 29, 2019

Panel/Cell Line	Growth Percent
Leukemia	
CCRF-CEM	107.69
HL-60(TB)	111.98
K-562	119.88
MOLT-4	109.30
RPMI-8226	117.60
SR	121.40
Non-Small Cell Lung Cancer	
A549/ATCC	101.79
EKVX	100.63
HOP-62	97.77
HOP-92	105.15
NCI-H226	100.94
NCI-H23	97.69
NCI-H322M	97.60
NCI-H460	104.35
NCI-H522	91.95
Colon Cancer	
COLO 205	111.68
HCC-2998	98.72
HCT-116	100.56
HCT-15	98.71
HT29	101.14
KM12	100.14
SW-620	103.31
CNS Cancer	
SF-268	89.99
SF-539	98.29
SNB-19	97.66
SNB-75	74.60
U251	101.54
Melanoma	
LOX IMVI	96.79
MALME-3M	93.99
M14	102.70
MDA-MB-435	100.66
SK-MEL-2	107.61
SK-MEL-28	103.48
SK-MEL-5	102.24
UACC-257	101.82
UACC-62	98.17
Ovarian Cancer	
IGROV1	102.06
OVCAR-3	102.30
OVCAR-4	101.84
OVCAR-5	101.22
OVCAR-8	101.74
NCI/ADR-RES	98.28
SK-OV-3	106.84
Renal Cancer	
786-0	100.56
A498	113.12
ACHN	98.99
CAKI-1	96.00
RXF 393	115.76
SN12C	99.21
TK-10	98.28
UO-31	84.41
Prostate Cancer	
PC-3	99.68
DU-145	103.53
Breast Cancer	
MCF7	97.28
MDA-MB-231/ATCC	108.52
HS 578T	109.02
BT-549	100.50
MDA-MB-468	100.20
Mean	101.88
Delta	27.28
Range	46.80

Mean Growth Percent - Growth Percent

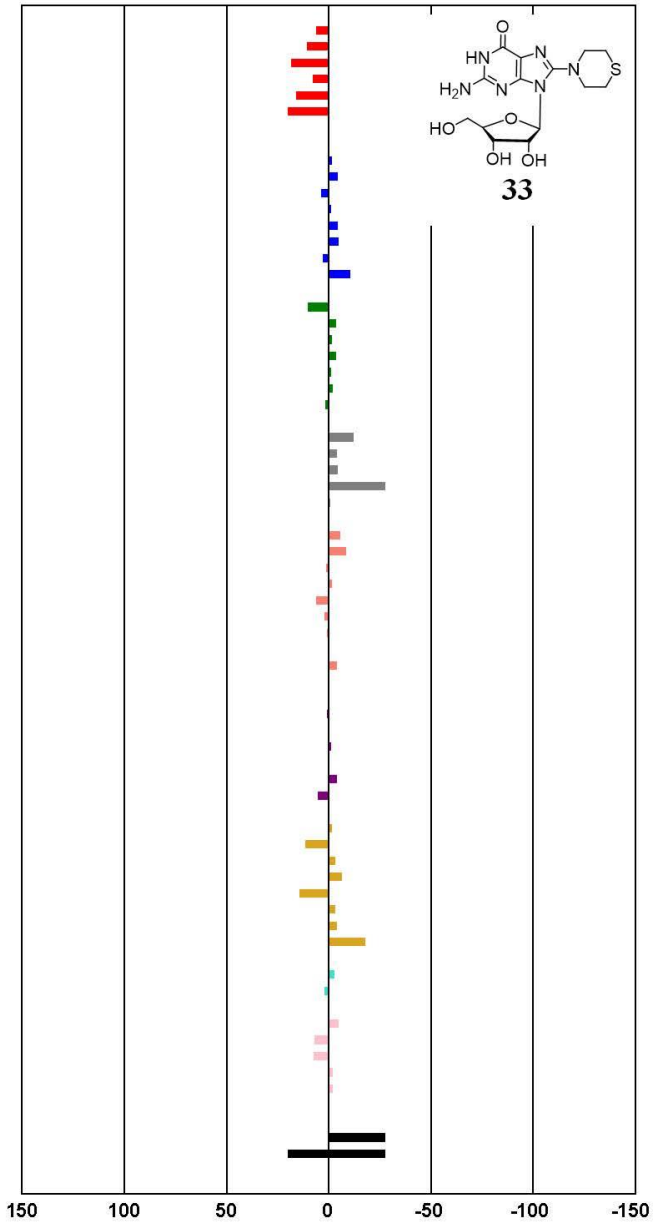

33

Developmental Therapeutics Program	NSC: D-817318 / 1	Conc: 1.00E-5 Molar	Test Date: Aug 05, 2019
One Dose Mean Graph	Experiment ID: 1908OS48		Report Date: Aug 29, 2019

Panel/Cell Line	Growth Percent
Leukemia	
CCRF-CEM	104.60
HL-60(TB)	104.13
K-562	105.29
MOLT-4	110.22
RPMI-8226	113.78
SR	119.22
Non-Small Cell Lung Cancer	
A549/ATCC	100.07
EKVX	100.61
HOP-62	104.96
HOP-92	104.77
NCI-H226	97.11
NCI-H23	100.35
NCI-H322M	97.95
NCI-H460	104.91
NCI-H522	92.90
Colon Cancer	
COLO 205	110.66
HCC-2998	105.74
HCT-116	106.04
HCT-15	99.01
HT29	107.98
KM12	102.96
SW-620	107.63
CNS Cancer	
SF-268	97.47
SF-539	102.07
SNB-19	103.31
SNB-75	89.00
U251	97.50
Melanoma	
LOX IMVI	97.32
MALME-3M	93.12
M14	104.01
MDA-MB-435	100.16
SK-MEL-2	109.82
SK-MEL-28	106.93
SK-MEL-5	100.29
UACC-257	100.13
UACC-62	97.25
Ovarian Cancer	
IGROV1	105.18
OVCAR-3	108.07
OVCAR-4	102.34
OVCAR-5	104.30
OVCAR-8	103.31
NCI/ADR-RES	99.72
SK-OV-3	110.15
Renal Cancer	
786-0	98.80
A498	98.58
ACHN	102.13
CAKI-1	100.79
RXF 393	113.95
SN12C	95.65
TK-10	90.81
UO-31	89.24
Prostate Cancer	
PC-3	99.67
DU-145	107.76
Breast Cancer	
MCF7	98.90
MDA-MB-231/ATCC	107.10
HS 578T	105.22
BT-549	105.03
MDA-MB-468	101.37
Mean	102.54
Delta	13.54
Range	30.22

Mean Growth Percent - Growth Percent

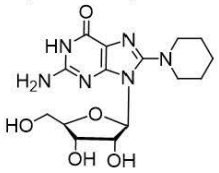

34

Developmental Therapeutics Program	NSC: D-817317 / 1	Conc: 1.00E-5 Molar	Test Date: Aug 05, 2019
One Dose Mean Graph	Experiment ID: 1908OS48		Report Date: Aug 29, 2019

Panel/Cell Line	Growth Percent
Leukemia	
CCRF-CEM	107.19
HL-60(TB)	107.21
K-562	105.01
MOLT-4	108.83
RPMI-8226	114.29
SR	114.40
Non-Small Cell Lung Cancer	
A549/ATCC	102.72
EKVX	103.62
HOP-62	93.85
HOP-92	102.34
NCI-H226	104.51
NCI-H23	100.71
NCI-H322M	98.94
NCI-H460	107.02
NCI-H522	92.41
Colon Cancer	
COLO 205	116.05
HCC-2998	102.72
HCT-116	101.12
HCT-15	100.46
HT29	109.94
KM12	104.49
SW-620	105.12
CNS Cancer	
SF-268	100.97
SF-539	99.23
SNB-19	103.14
SNB-75	78.29
U251	100.81
Melanoma	
LOX IMVI	99.55
MALME-3M	83.46
M14	103.10
MDA-MB-435	104.08
SK-MEL-2	103.71
SK-MEL-28	93.27
SK-MEL-5	99.37
UACC-257	98.27
UACC-62	94.94
Ovarian Cancer	
IGROV1	105.21
OVCAR-3	110.10
OVCAR-4	103.81
OVCAR-5	100.15
OVCAR-8	105.68
NCI/ADR-RES	103.04
SK-OV-3	100.41
Renal Cancer	
786-0	96.59
A498	95.06
ACHN	100.25
CAKI-1	99.47
RXF 393	108.45
SN12C	97.24
TK-10	90.38
UO-31	98.71
Prostate Cancer	
PC-3	101.62
DU-145	108.32
Breast Cancer	
MCF7	98.13
MDA-MB-231/ATCC	106.17
HS 578T	121.26
BT-549	102.50
MDA-MB-468	103.89
Mean	102.10
Delta	23.81
Range	42.97

Mean Growth Percent - Growth Percent

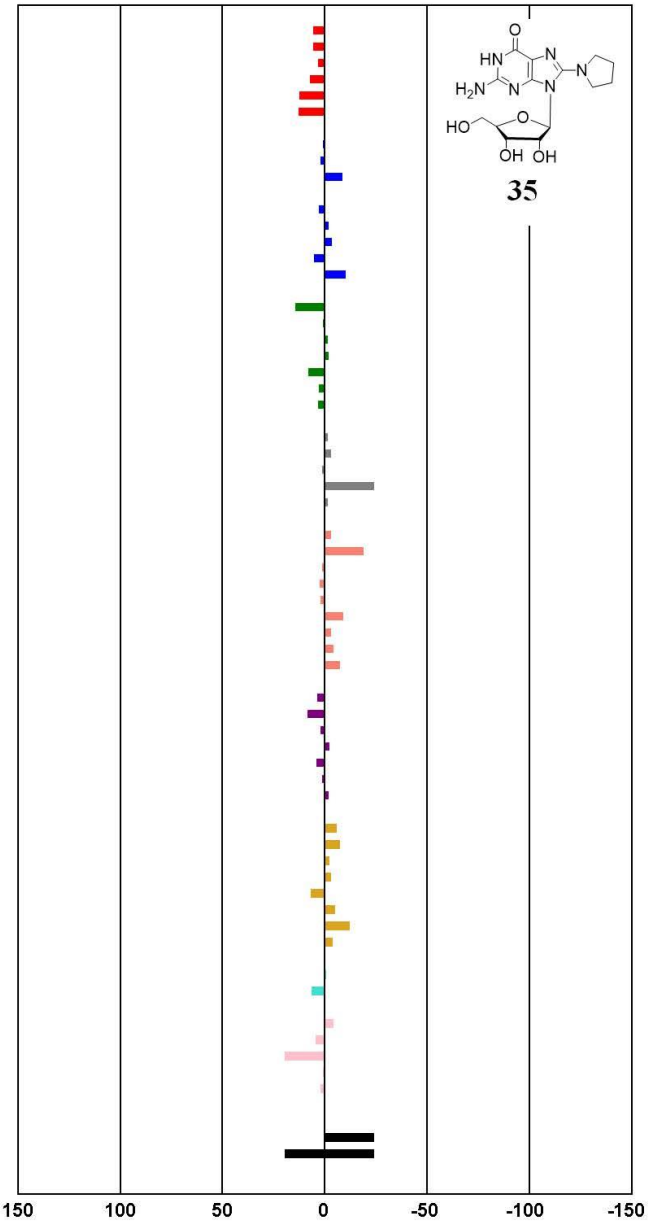

35

Developmental Therapeutics Program	NSC: D-817316 / 1	Conc: 1.00E-5 Molar	Test Date: Aug 05, 2019
One Dose Mean Graph	Experiment ID: 1908OS48		Report Date: Aug 29, 2019

Panel/Cell Line	Growth Percent
Leukemia	
CCRF-CEM	104.79
HL-60(TB)	99.25
K-562	109.43
MOLT-4	107.31
RPMI-8226	106.77
SR	109.29
Non-Small Cell Lung Cancer	
A549/ATCC	92.08
EKVX	104.85
HOP-62	105.99
HOP-92	90.96
NCI-H226	99.66
NCI-H23	100.60
NCI-H322M	99.71
NCI-H460	104.72
NCI-H522	84.14
Colon Cancer	
COLO 205	113.04
HCC-2998	101.26
HCT-116	113.15
HCT-15	103.23
HT29	96.76
KM12	107.46
SW-620	106.69
CNS Cancer	
SF-268	92.80
SF-539	95.71
SNB-19	100.62
SNB-75	89.53
U251	95.14
Melanoma	
LOX IMVI	95.65
MALME-3M	92.96
M14	108.96
MDA-MB-435	106.28
SK-MEL-2	98.80
SK-MEL-28	105.08
SK-MEL-5	96.29
UACC-257	95.52
UACC-62	98.03
Ovarian Cancer	
IGROV1	106.69
OVCAR-3	107.54
OVCAR-4	114.03
OVCAR-5	97.04
OVCAR-8	98.11
NCI/ADR-RES	100.62
SK-OV-3	105.30
Renal Cancer	
786-0	103.97
A498	107.09
ACHN	106.20
CAKI-1	97.76
RXF 393	102.36
SN12C	101.68
TK-10	94.70
UO-31	90.91
Prostate Cancer	
PC-3	96.97
DU-145	109.29
Breast Cancer	
MCF7	100.11
MDA-MB-231/ATCC	104.75
HS 578T	124.12
BT-549	104.85
MDA-MB-468	103.51
Mean	101.90
Delta	17.76
Range	39.98

Mean Growth Percent - Growth Percent

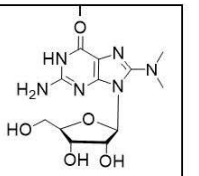

36

Developmental Therapeutics Program	NSC: D-816052 / 1	Conc: 1.00E-5 Molar	Test Date: Jun 03, 2019
One Dose Mean Graph	Experiment ID: 1906OS18		Report Date: Aug 29, 2019

Panel/Cell Line	Growth Percent
Leukemia	
CCRF-CEM	107.90
HL-60(TB)	100.25
K-562	95.63
MOLT-4	101.09
SR	99.88
Non-Small Cell Lung Cancer	
A549/ATCC	109.24
EKVX	101.92
HOP-62	105.81
HOP-92	138.40
NCI-H226	122.56
NCI-H23	114.24
NCI-H322M	109.46
NCI-H460	106.43
NCI-H522	104.94
Colon Cancer	
HCC-2998	110.80
HCT-116	107.28
HCT-15	102.30
HT29	104.40
KM12	107.88
SW-620	108.10
CNS Cancer	
SF-268	105.04
SF-295	108.33
SF-539	103.32
SNB-19	100.24
SNB-75	112.21
U251	109.31
Melanoma	
LOX IMVI	109.25
MALME-3M	105.15
M14	107.06
MDA-MB-435	106.29
SK-MEL-2	104.61
SK-MEL-28	104.08
SK-MEL-5	104.57
UACC-257	105.42
UACC-62	98.31
Ovarian Cancer	
IGROV1	109.62
OVCAR-3	109.01
OVCAR-4	108.02
OVCAR-5	107.40
OVCAR-8	104.23
NCI/ADR-RES	118.04
Renal Cancer	
786-0	103.92
ACHN	105.80
CAKI-1	98.46
RXF 393	112.44
SN12C	100.40
TK-10	112.18
UO-31	96.14
Prostate Cancer	
PC-3	110.69
DU-145	105.51
Breast Cancer	
MCF7	93.18
MDA-MB-231/ATCC	102.33
HS 578T	108.69
BT-549	127.71
T-47D	97.99
MDA-MB-468	110.87
Mean	106.86
Delta	13.68
Range	45.22

Mean Growth Percent - Growth Percent

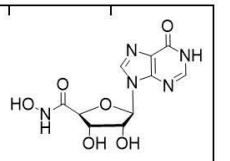

17

Developmental Therapeutics Program	NSC: D-816051 / 1	Conc: 1.00E-5 Molar	Test Date: Jun 03, 2019
One Dose Mean Graph	Experiment ID: 1906OS18		Report Date: Aug 29, 2019

Panel/Cell Line	Growth Percent
Leukemia	
CCRF-CEM	104.15
HL-60(TB)	108.38
K-562	97.97
MOLT-4	98.83
SR	114.82
Non-Small Cell Lung Cancer	
A549/ATCC	106.97
EKVX	111.58
HOP-62	107.21
HOP-92	131.29
NCI-H226	113.39
NCI-H23	114.97
NCI-H322M	112.85
NCI-H460	107.58
NCI-H522	100.78
Colon Cancer	
HCC-2998	112.54
HCT-116	102.22
HCT-15	103.68
HT29	98.96
KM12	104.74
SW-620	109.72
CNS Cancer	
SF-268	104.79
SF-295	112.56
SF-539	107.21
SNB-19	98.36
SNB-75	116.05
U251	111.79
Melanoma	
LOX IMVI	102.69
MALME-3M	113.77
M14	105.22
MDA-MB-435	108.29
SK-MEL-2	105.38
SK-MEL-28	107.98
SK-MEL-5	100.88
UACC-257	111.84
UACC-62	103.07
Ovarian Cancer	
IGROV1	113.10
OVCAR-3	105.48
OVCAR-4	109.41
OVCAR-5	109.47
OVCAR-8	105.20
NCI/ADR-RES	108.93
Renal Cancer	
786-0	108.18
ACHN	106.18
CAKI-1	104.46
RXF 393	130.04
SN12C	103.60
TK-10	112.60
UO-31	98.45
Prostate Cancer	
PC-3	113.03
DU-145	108.98
Breast Cancer	
MCF7	99.62
MDA-MB-231/ATCC	103.17
HS 578T	105.42
BT-549	116.96
T-47D	111.14
MDA-MB-468	116.68
Mean	108.26
Delta	10.29
Range	33.32

Mean Growth Percent - Growth Percent

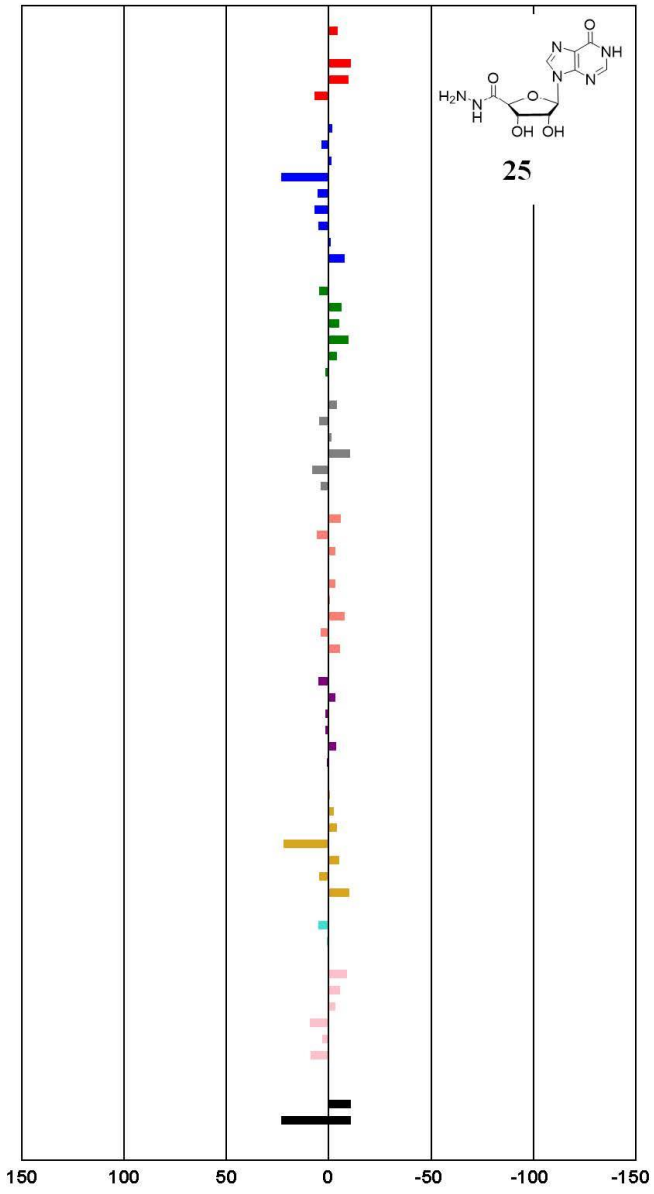

25

Developmental Therapeutics Program	NSC: D-816050 / 1	Conc: 1.00E-5 Molar	Test Date: Jun 03, 2019
One Dose Mean Graph	Experiment ID: 1906OS18		Report Date: Aug 29, 2019

Panel/Cell Line	Growth Percent
Leukemia	
CCRF-CEM	104.02
HL-60(TB)	105.58
K-562	100.30
MOLT-4	107.84
SR	110.97
Non-Small Cell Lung Cancer	
A549/ATCC	103.36
EKVX	107.98
HOP-62	96.72
HOP-92	115.03
NCI-H226	107.50
NCI-H23	108.10
NCI-H322M	113.57
NCI-H460	104.70
NCI-H522	102.37
Colon Cancer	
HCC-2998	108.84
HCT-116	111.78
HCT-15	103.77
HT29	104.44
KM12	104.74
SW-620	106.25
CNS Cancer	
SF-268	105.68
SF-295	110.91
SF-539	102.64
SNB-19	97.37
SNB-75	114.31
U251	98.61
Melanoma	
LOX IMVI	96.89
MALME-3M	111.42
M14	111.27
MDA-MB-435	104.51
SK-MEL-2	105.85
SK-MEL-28	103.05
SK-MEL-5	104.47
UACC-257	105.69
UACC-62	104.43
Ovarian Cancer	
IGROV1	110.12
OVCAR-3	104.26
OVCAR-4	106.36
OVCAR-5	108.08
OVCAR-8	107.71
NCI/ADR-RES	106.17
Renal Cancer	
786-0	104.86
ACHN	104.30
CAKI-1	101.68
RXF 393	129.89
SN12C	96.57
TK-10	112.08
UO-31	98.37
Prostate Cancer	
PC-3	104.51
DU-145	106.91
Breast Cancer	
MCF7	105.66
MDA-MB-231/ATCC	100.20
HS 578T	101.73
BT-549	114.46
T-47D	98.04
MDA-MB-468	110.96
Mean	106.03
Delta	9.46
Range	33.32

Mean Growth Percent - Growth Percent

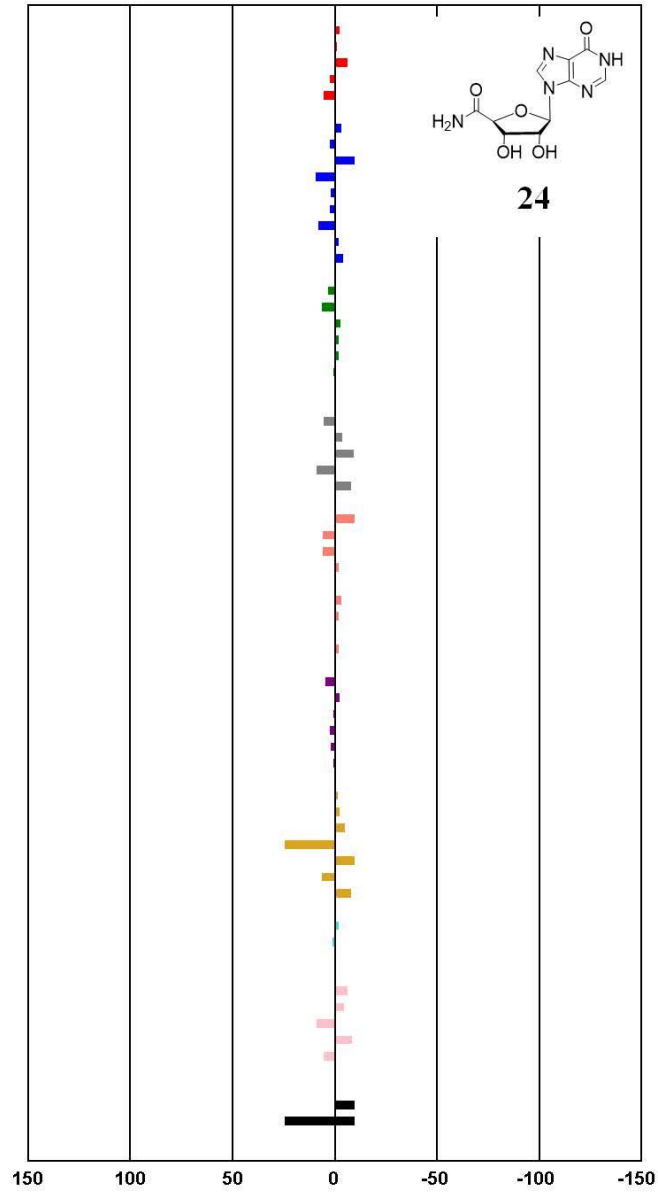

24

Developmental Therapeutics Program	NSC: D-816049 / 1	Conc: 1.00E-5 Molar	Test Date: Jun 03, 2019
One Dose Mean Graph	Experiment ID: 1906OS18		Report Date: Aug 29, 2019

Panel/Cell Line	Growth Percent
Leukemia	
CCRF-CEM	120.98
HL-60(TB)	108.21
K-562	97.11
MOLT-4	106.28
SR	111.15
Non-Small Cell Lung Cancer	
A549/ATCC	108.20
EKVX	106.88
HOP-62	103.45
HOP-92	121.69
NCI-H226	110.60
NCI-H23	107.24
NCI-H322M	120.11
NCI-H460	107.78
NCI-H522	103.50
Colon Cancer	
HCC-2998	103.01
HCT-116	103.40
HCT-15	103.65
HT29	105.71
KM12	107.00
SW-620	105.16
CNS Cancer	
SF-268	108.73
SF-295	112.20
SF-539	103.51
SNB-19	101.11
SNB-75	115.96
U251	111.85
Melanoma	
LOX IMVI	99.80
MALME-3M	119.03
M14	108.89
MDA-MB-435	105.58
SK-MEL-2	110.46
SK-MEL-28	102.70
SK-MEL-5	103.92
UACC-257	114.77
UACC-62	104.97
Ovarian Cancer	
IGROV1	114.07
OVCAR-3	107.70
OVCAR-4	104.34
OVCAR-5	106.68
OVCAR-8	104.70
NCI/ADR-RES	110.02
Renal Cancer	
786-0	104.81
ACHN	103.33
CAKI-1	102.88
RXF 393	127.05
SN12C	103.98
TK-10	108.89
UO-31	104.49
Prostate Cancer	
PC-3	103.54
DU-145	108.77
Breast Cancer	
MCF7	102.70
MDA-MB-231/ATCC	109.31
HS 578T	102.30
BT-549	115.58
T-47D	103.55
MDA-MB-468	111.05
Mean	107.94
Delta	10.83
Range	29.94

Mean Growth Percent - Growth Percent

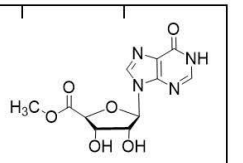

22

Developmental Therapeutics Program	NSC: D-816048 / 1	Conc: 1.00E-5 Molar	Test Date: Jun 03, 2019
One Dose Mean Graph	Experiment ID: 1906OS18		Report Date: Aug 29, 2019

Panel/Cell Line	Growth Percent
Leukemia	
CCRF-CEM	112.12
HL-60(TB)	102.37
K-562	96.91
MOLT-4	101.04
SR	99.60
Non-Small Cell Lung Cancer	
A549/ATCC	105.32
EKVX	107.19
HOP-62	105.48
HOP-92	132.60
NCI-H226	117.27
NCI-H23	108.21
NCI-H322M	113.59
NCI-H460	103.85
NCI-H522	104.27
Colon Cancer	
HCC-2998	104.11
HCT-116	105.29
HCT-15	106.84
HT29	107.48
KM12	104.56
SW-620	103.54
CNS Cancer	
SF-268	103.37
SF-295	107.03
SF-539	101.14
SNB-19	105.02
SNB-75	109.73
U251	104.33
Melanoma	
LOX IMVI	99.94
MALME-3M	108.87
M14	103.45
MDA-MB-435	103.49
SK-MEL-2	107.78
SK-MEL-28	107.74
SK-MEL-5	100.65
UACC-257	97.79
UACC-62	105.86
Ovarian Cancer	
IGROV1	113.27
OVCAR-3	110.53
OVCAR-4	104.95
OVCAR-5	109.94
OVCAR-8	101.77
NCI/ADR-RES	105.66
Renal Cancer	
786-0	105.84
ACHN	101.88
CAKI-1	100.80
RXF 393	122.16
SN12C	103.85
TK-10	107.04
UO-31	100.47
Prostate Cancer	
PC-3	104.13
DU-145	106.62
Breast Cancer	
MCF7	101.23
MDA-MB-231/ATCC	99.57
HS 578T	106.92
BT-549	107.81
T-47D	98.81
MDA-MB-468	107.72
Mean	105.87
Delta	8.96
Range	35.69

Mean Growth Percent - Growth Percent

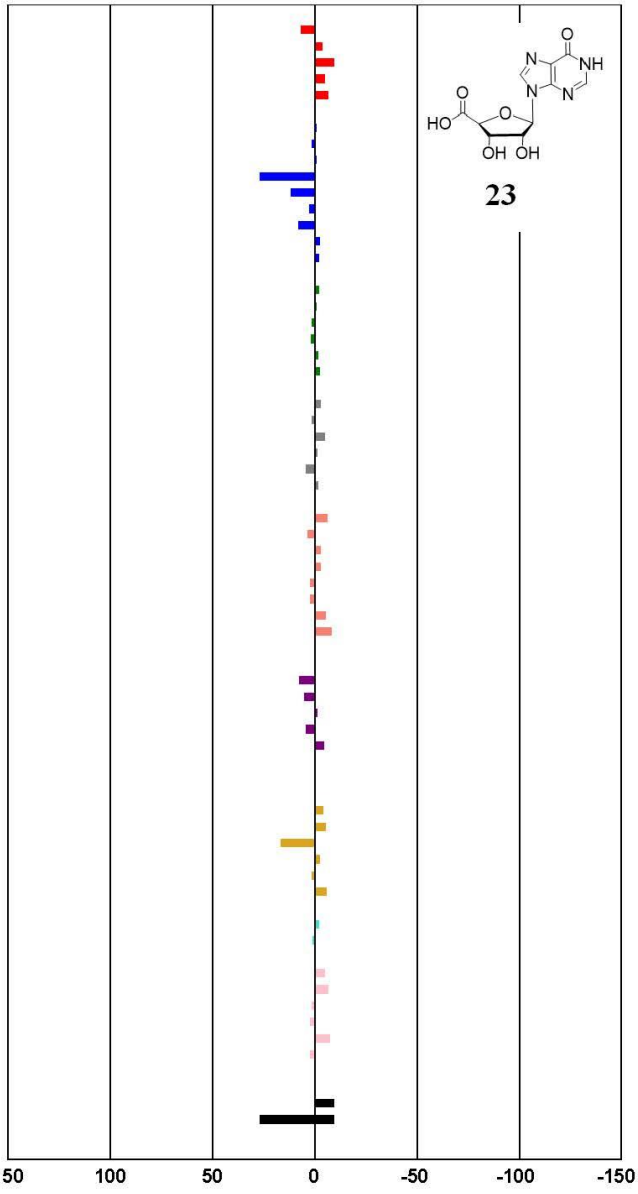

23

Developmental Therapeutics Program One Dose Mean Graph	NSC: D-816047 / 1	Conc: 1.00E-5 Molar	Test Date: Jun 03, 2019
	Experiment ID: 1906OS18		Report Date: Aug 29, 2019

Panel/Cell Line	Growth Percent
Leukemia	
CCRF-CEM	106.80
HL-60(TB)	99.24
K-562	97.35
MOLT-4	101.93
SR	107.88
Non-Small Cell Lung Cancer	
A549/ATCC	96.21
EKVX	105.70
HOP-62	105.56
HOP-92	131.84
NCI-H226	111.09
NCI-H23	104.27
NCI-H322M	110.89
NCI-H460	105.22
NCI-H522	99.70
Colon Cancer	
HCC-2998	104.14
HCT-116	112.82
HCT-15	103.49
HT29	107.70
KM12	106.69
SW-620	106.73
CNS Cancer	
SF-268	105.93
SF-295	116.54
SF-539	108.58
SNB-19	103.49
SNB-75	114.08
U251	103.67
Melanoma	
LOX IMVI	103.46
MALME-3M	116.84
M14	111.46
MDA-MB-435	108.49
SK-MEL-2	110.77
SK-MEL-28	107.03
SK-MEL-5	102.92
UACC-257	106.01
UACC-62	103.22
Ovarian Cancer	
IGROV1	111.12
OVCAR-3	105.36
OVCAR-4	107.06
OVCAR-5	111.94
OVCAR-8	104.01
NCI/ADR-RES	107.66
Renal Cancer	
786-0	103.84
ACHN	104.34
CAKI-1	102.39
RXF 393	131.18
SN12C	105.08
TK-10	113.40
UO-31	103.08
Prostate Cancer	
PC-3	107.04
DU-145	104.27
Breast Cancer	
MCF7	108.25
MDA-MB-231/ATCC	107.59
HS 578T	103.25
BT-549	115.37
T-47D	109.25
MDA-MB-468	108.71
Mean	107.53
Delta	11.32
Range	35.63

Mean Growth Percent - Growth Percent

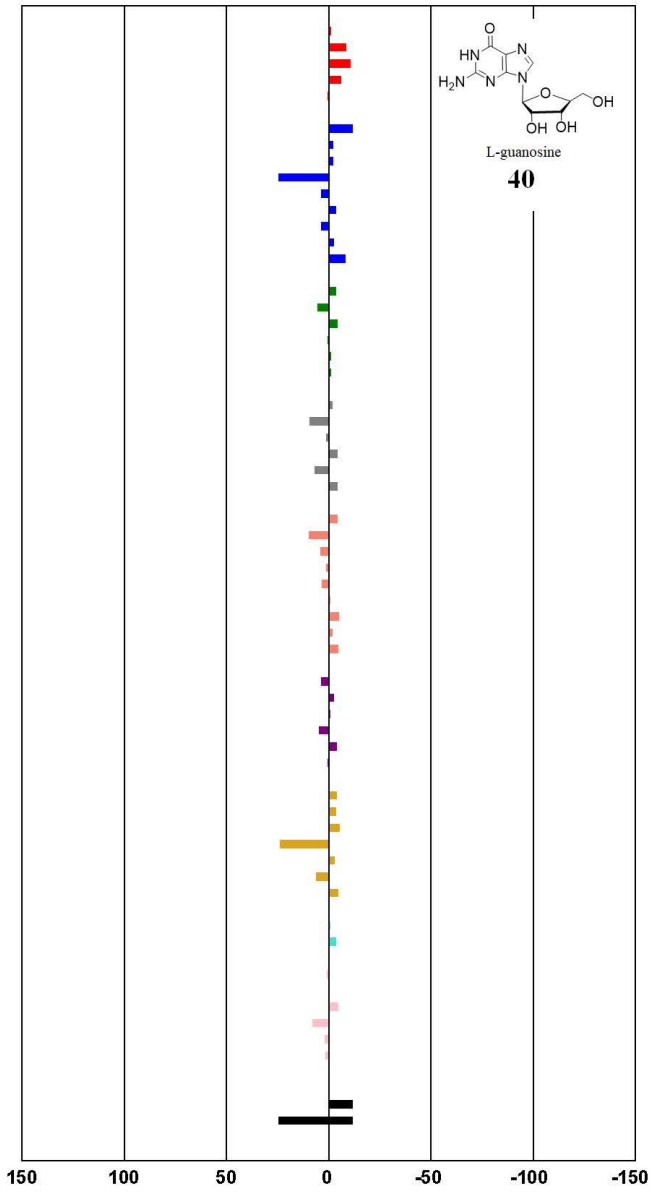

L-guanosine

40

Developmental Therapeutics Program	NSC: D-816046 / 1	Conc: 1.00E-5 Molar	Test Date: Jun 03, 2019
One Dose Mean Graph	Experiment ID: 1906OS18		Report Date: Aug 29, 2019

Panel/Cell Line	Growth Percent
Leukemia	
CCRF-CEM	108.64
HL-60(TB)	91.43
K-562	94.75
MOLT-4	95.65
SR	92.64
Non-Small Cell Lung Cancer	
A549/ATCC	98.49
EKVX	94.51
HOP-62	97.32
HOP-92	108.08
NCI-H23	103.54
NCI-H322M	113.22
NCI-H460	107.78
NCI-H522	95.03
Colon Cancer	
HCC-2998	112.46
HCT-116	103.22
HCT-15	98.81
HT29	106.74
KM12	104.79
SW-620	99.98
CNS Cancer	
SF-268	100.05
SF-295	97.65
SF-539	99.36
SNB-19	100.20
SNB-75	95.95
U251	105.18
Melanoma	
LOX IMVI	102.65
MALME-3M	99.35
M14	100.16
MDA-MB-435	94.53
SK-MEL-2	104.03
SK-MEL-28	100.19
SK-MEL-5	95.77
UACC-257	98.29
UACC-62	92.80
Ovarian Cancer	
IGROV1	107.05
OVCAR-3	107.07
OVCAR-4	98.94
OVCAR-5	101.42
OVCAR-8	103.20
NCI/ADR-RES	109.56
Renal Cancer	
786-0	102.46
ACHN	102.13
CAKI-1	96.84
RXF 393	98.78
SN12C	95.77
TK-10	103.85
UO-31	96.36
Prostate Cancer	
PC-3	105.81
DU-145	107.43
Breast Cancer	
MCF7	91.61
MDA-MB-231/ATCC	99.34
HS 578T	102.34
BT-549	111.57
T-47D	99.94
MDA-MB-468	95.88
Mean	100.92
Delta	9.49
Range	21.79

Mean Growth Percent - Growth Percent

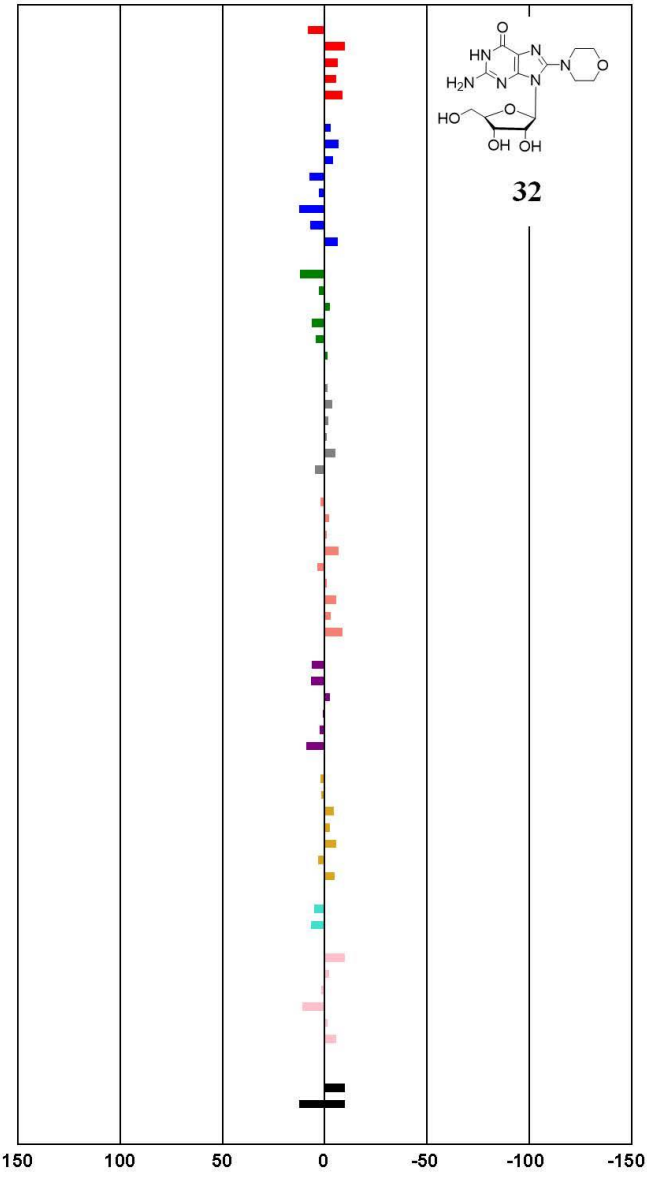

32

Developmental Therapeutics Program	NSC: D-816045 / 1	Conc: 1.00E-5 Molar	Test Date: Jun 03, 2019
One Dose Mean Graph	Experiment ID: 1906OS18		Report Date: Aug 29, 2019

Panel/Cell Line	Growth Percent
Leukemia	
CCRF-CEM	101.79
HL-60(TB)	93.91
K-562	96.33
MOLT-4	95.87
SR	87.19
Non-Small Cell Lung Cancer	
A549/ATCC	101.06
EKVX	100.74
HOP-62	91.54
HOP-92	100.67
NCI-H226	106.96
NCI-H23	108.17
NCI-H322M	111.67
NCI-H460	104.63
NCI-H522	95.39
Colon Cancer	
HCC-2998	106.58
HCT-116	102.20
HCT-15	100.23
HT29	109.65
KM12	103.21
SW-620	101.81
CNS Cancer	
SF-268	100.59
SF-295	98.16
SF-539	98.59
SNB-19	95.11
SNB-75	97.08
U251	105.81
Melanoma	
LOX IMVI	102.42
MALME-3M	102.74
M14	104.92
MDA-MB-435	103.07
SK-MEL-2	105.38
SK-MEL-28	102.13
SK-MEL-5	100.74
UACC-257	102.41
UACC-62	97.22
Ovarian Cancer	
IGROV1	107.08
OVCAR-3	110.96
OVCAR-4	102.46
OVCAR-5	101.36
OVCAR-8	106.40
NCI/ADR-RES	104.10
Renal Cancer	
786-0	100.77
ACHN	103.42
CAKI-1	95.36
RXF 393	102.75
SN12C	92.17
TK-10	103.77
UO-31	89.35
Prostate Cancer	
PC-3	105.07
DU-145	105.52
Breast Cancer	
MCF7	91.20
MDA-MB-231/ATCC	95.44
HS 578T	99.54
BT-549	116.51
T-47D	97.34
MDA-MB-468	101.92
Mean	101.22
Delta	14.03
Range	29.32

Mean Growth Percent - Growth Percent

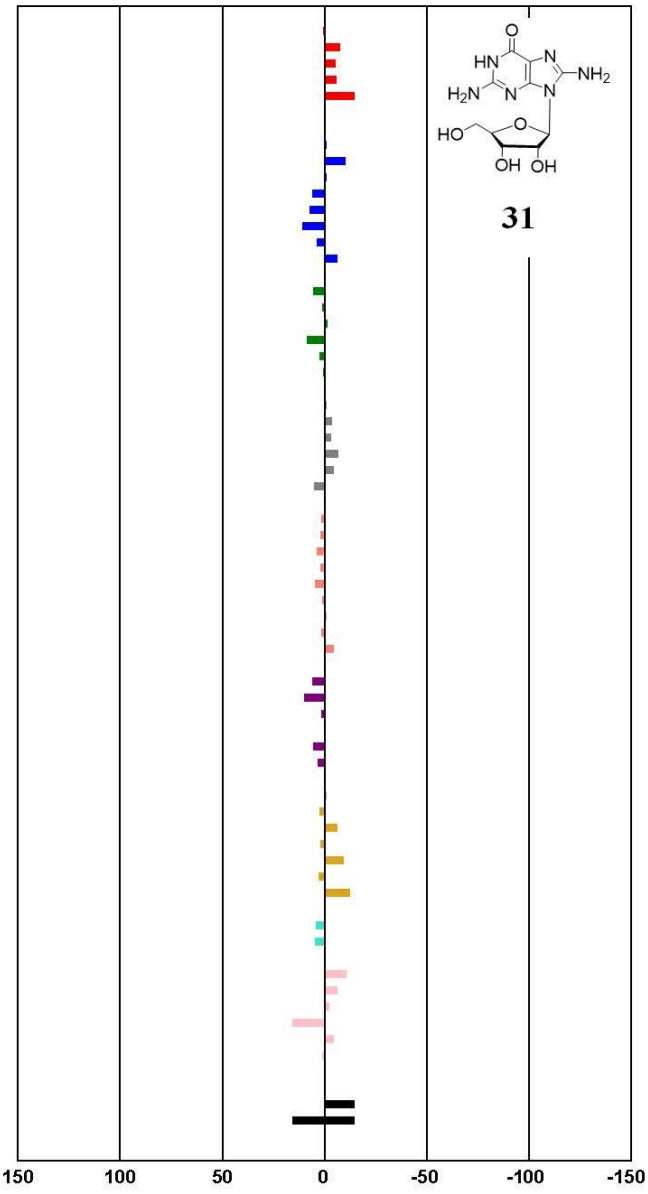

31

Developmental Therapeutics Program	NSC: D-816044 / 1	Conc: 1.00E-5 Molar	Test Date: Jun 03, 2019
One Dose Mean Graph	Experiment ID: 1906OS18		Report Date: Aug 29, 2019

Panel/Cell Line	Growth Percent
Leukemia	
CCRF-CEM	105.35
HL-60(TB)	100.61
K-562	97.07
MOLT-4	101.59
SR	91.16
Non-Small Cell Lung Cancer	
A549/ATCC	103.09
EKVX	97.24
HOP-62	98.70
HOP-92	117.70
NCI-H226	110.11
NCI-H23	111.64
NCI-H322M	107.12
NCI-H460	104.69
NCI-H522	96.10
Colon Cancer	
HCC-2998	110.13
HCT-116	103.88
HCT-15	96.34
HT29	101.77
KM12	103.42
SW-620	102.21
CNS Cancer	
SF-268	97.53
SF-295	100.05
SF-539	97.61
SNB-19	96.61
SNB-75	90.86
U251	109.28
Melanoma	
LOX IMVI	105.24
MALME-3M	98.67
M14	104.74
MDA-MB-435	100.16
SK-MEL-2	112.37
SK-MEL-28	100.49
SK-MEL-5	102.23
UACC-257	91.54
UACC-62	93.08
Ovarian Cancer	
IGROV1	108.75
OVCAR-3	101.87
OVCAR-4	97.85
OVCAR-5	96.42
OVCAR-8	102.70
NCI/ADR-RES	110.79
Renal Cancer	
786-0	101.17
ACHN	102.70
CAKI-1	93.08
RXF 393	97.35
SN12C	92.16
TK-10	104.53
UO-31	92.34
Prostate Cancer	
PC-3	103.27
DU-145	101.13
Breast Cancer	
MCF7	85.95
MDA-MB-231/ATCC	97.84
HS 578T	97.77
BT-549	118.53
T-47D	93.76
MDA-MB-468	101.09
Mean	101.10
Delta	15.15
Range	32.58

Mean Growth Percent - Growth Percent

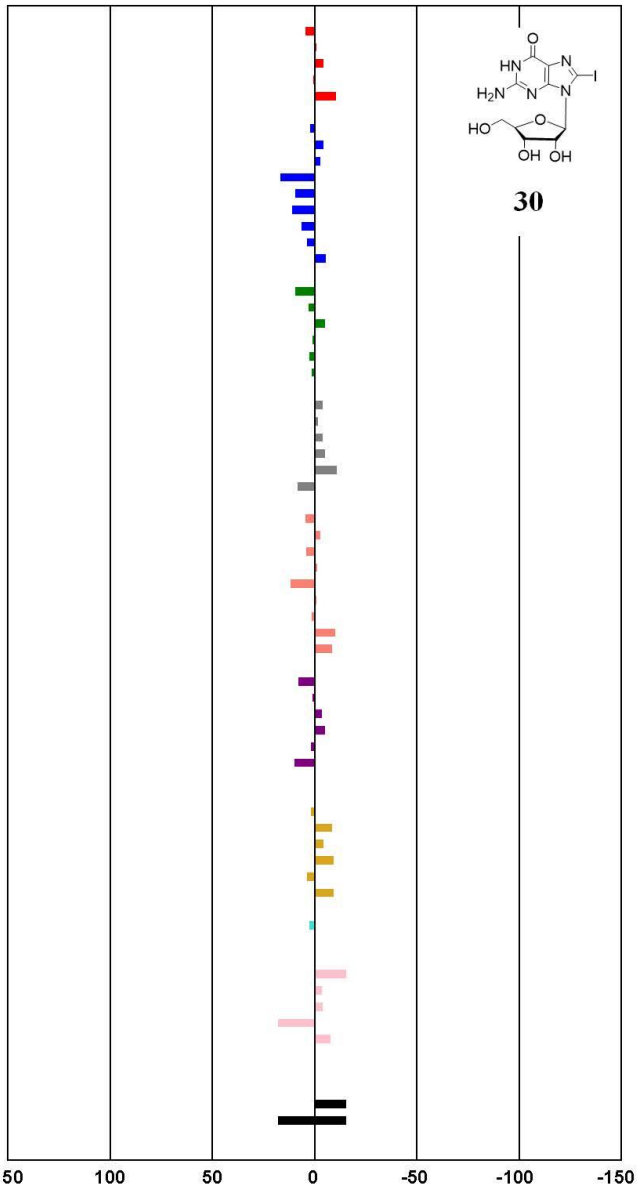

30

Developmental Therapeutics Program	NSC: D-816043 / 1	Conc: 1.00E-5 Molar	Test Date: Jun 03, 2019
One Dose Mean Graph	Experiment ID: 1906OS18		Report Date: Aug 29, 2019

Panel/Cell Line	Growth Percent
Leukemia	
CCRF-CEM	97.63
HL-60(TB)	98.84
K-562	98.66
MOLT-4	97.78
SR	98.55
Non-Small Cell Lung Cancer	
A549/ATCC	99.44
EKVX	101.67
HOP-62	100.32
HOP-92	111.64
NCI-H226	100.53
NCI-H23	109.81
NCI-H322M	110.76
NCI-H460	105.89
NCI-H522	87.48
Colon Cancer	
HCC-2998	112.29
HCT-116	102.97
HCT-15	101.14
HT29	101.29
KM12	100.94
SW-620	101.67
CNS Cancer	
SF-268	97.24
SF-295	97.87
SF-539	102.21
SNB-19	96.27
SNB-75	93.78
U251	108.26
Melanoma	
LOX IMVI	102.26
MALME-3M	103.42
M14	105.40
MDA-MB-435	97.18
SK-MEL-2	107.74
SK-MEL-28	102.45
SK-MEL-5	101.04
UACC-257	100.98
UACC-62	94.83
Ovarian Cancer	
IGROV1	110.18
OVCAR-3	102.24
OVCAR-4	98.11
OVCAR-5	102.10
OVCAR-8	107.15
NCI/ADR-RES	105.59
Renal Cancer	
786-0	102.25
ACHN	100.92
CAKI-1	91.82
RXF 393	113.08
SN12C	96.98
TK-10	107.28
UO-31	91.07
Prostate Cancer	
PC-3	107.44
DU-145	106.25
Breast Cancer	
MCF7	96.04
MDA-MB-231/ATCC	99.77
HS 578T	94.48
BT-549	113.96
T-47D	99.50
MDA-MB-468	107.18
Mean	101.85
Delta	14.37
Range	26.48

Mean Growth Percent - Growth Percent

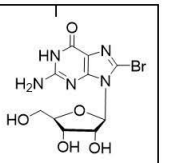

29

150 100 50 0 -50 -100 -150

Developmental Therapeutics Program	NSC: D-815026 / 1	Conc: 1.00E-5 Molar	Test Date: May 13, 2019
One Dose Mean Graph	Experiment ID: 1905OS06		Report Date: May 29, 2019

Panel/Cell Line	Growth Percent
Leukemia	
CCRF-CEM	107.39
HL-60(TB)	104.13
K-562	102.17
MOLT-4	101.70
RPMI-8226	104.19
SR	114.57
Non-Small Cell Lung Cancer	
A549/ATCC	97.27
EKVX	107.95
HOP-62	103.00
HOP-92	111.11
NCI-H23	103.86
NCI-H322M	101.86
NCI-H460	106.50
NCI-H522	98.30
Colon Cancer	
COLO 205	108.05
HCC-2998	103.61
HCT-116	102.65
HCT-15	100.51
HT29	103.90
KM12	104.39
SW-620	102.76
CNS Cancer	
SF-268	102.20
SF-295	98.18
SF-539	95.55
SNB-19	101.98
SNB-75	103.77
U251	106.03
Melanoma	
LOX IMVI	99.14
MALME-3M	105.80
M14	108.28
MDA-MB-435	103.84
SK-MEL-2	113.22
SK-MEL-28	102.69
SK-MEL-5	99.75
UACC-257	95.18
UACC-62	96.32
Ovarian Cancer	
IGROV1	108.48
OVCAR-3	108.84
OVCAR-4	108.44
OVCAR-5	101.18
OVCAR-8	102.14
NCI/ADR-RES	107.43
SK-OV-3	109.34
Renal Cancer	
786-0	108.59
A498	95.43
ACHN	108.77
CAKI-1	98.67
RXF 393	126.30
SN12C	100.57
TK-10	103.98
UO-31	91.17
Prostate Cancer	
PC-3	103.32
DU-145	106.80
Breast Cancer	
MCF7	98.96
MDA-MB-231/ATCC	108.23
HS 578T	109.50
BT-549	103.26
T-47D	106.06
MDA-MB-468	105.10
Mean	104.11
Delta	12.94
Range	35.13

Mean Growth Percent - Growth Percent

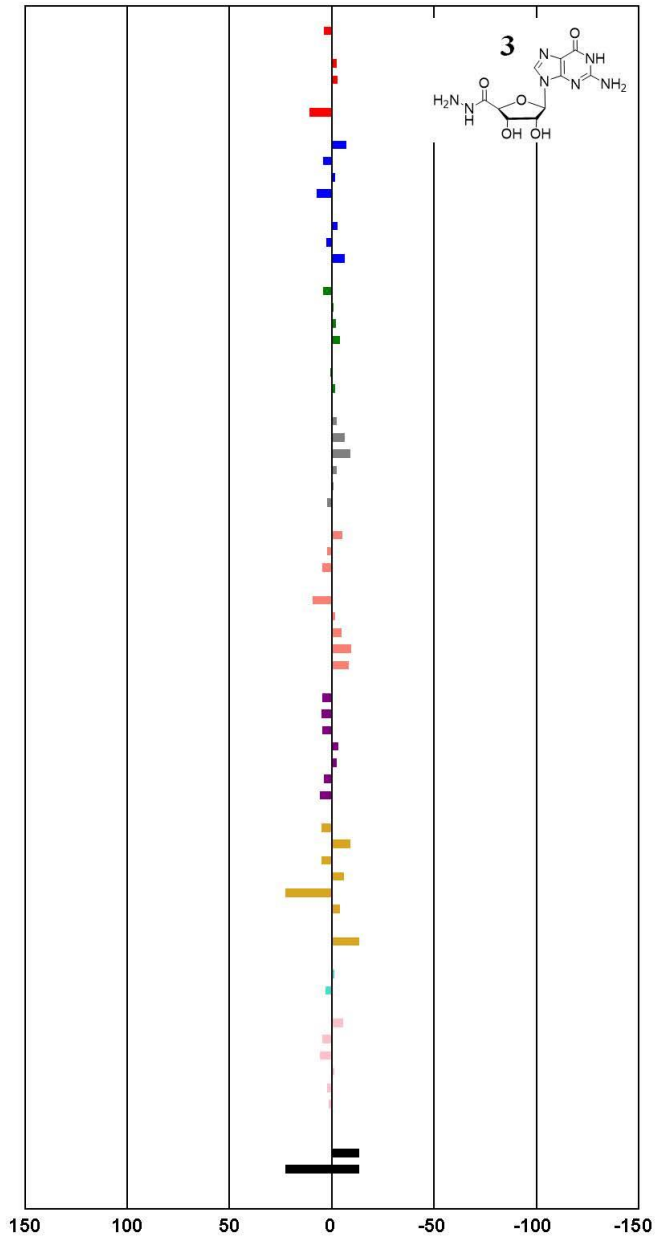

Developmental Therapeutics Program	NSC: D-815025 / 1	Conc: 1.00E-5 Molar	Test Date: May 13, 2019
One Dose Mean Graph	Experiment ID: 1905OS06		Report Date: May 29, 2019

Panel/Cell Line	Growth Percent
Leukemia	
CCRF-CEM	107.72
HL-60(TB)	103.88
K-562	102.57
MOLT-4	100.16
RPMI-8226	104.05
SR	102.19
Non-Small Cell Lung Cancer	
A549/ATCC	102.94
EKVX	109.83
HOP-62	98.81
HOP-92	107.61
NCI-H23	104.43
NCI-H322M	110.20
NCI-H460	104.74
NCI-H522	102.19
Colon Cancer	
COLO 205	107.28
HCC-2998	112.22
HCT-116	107.84
HCT-15	107.49
HT29	102.39
KM12	107.54
SW-620	106.94
CNS Cancer	
SF-268	106.98
SF-295	103.36
SF-539	102.56
SNB-19	99.49
SNB-75	118.48
U251	103.89
Melanoma	
LOX IMVI	105.67
MALME-3M	109.22
M14	107.64
MDA-MB-435	108.35
SK-MEL-2	106.55
SK-MEL-28	107.21
SK-MEL-5	104.41
UACC-257	99.60
UACC-62	104.54
Ovarian Cancer	
IGROV1	108.59
OVCAR-3	110.51
OVCAR-4	108.19
OVCAR-5	104.53
OVCAR-8	100.42
NCI/ADR-RES	107.40
SK-OV-3	95.33
Renal Cancer	
786-0	107.29
A498	107.22
ACHN	109.12
CAKI-1	102.60
RXF 393	127.53
SN12C	99.89
TK-10	101.98
UO-31	103.65
Prostate Cancer	
PC-3	99.43
DU-145	107.37
Breast Cancer	
MCF7	110.74
MDA-MB-231/ATCC	108.84
HS 578T	104.63
BT-549	113.30
T-47D	93.31
MDA-MB-468	113.66
Mean	105.87
Delta	12.56
Range	34.22

Mean Growth Percent - Growth Percent

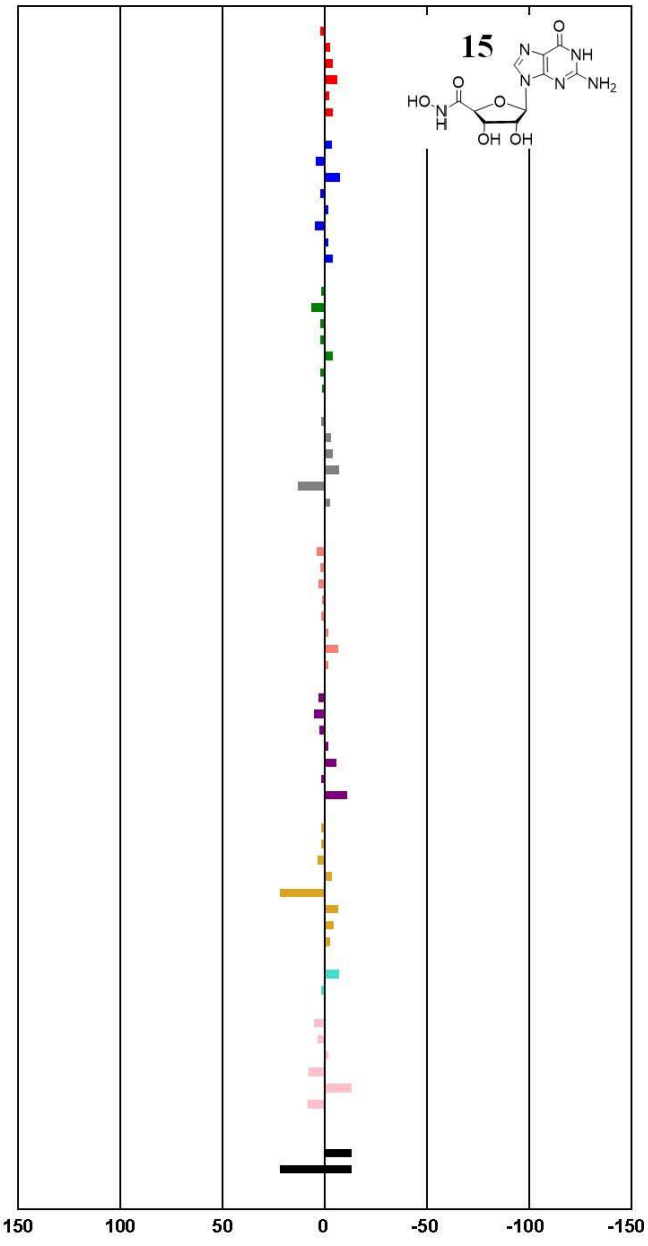

Developmental Therapeutics Program	NSC: D-815024 / 1	Conc: 1.00E-5 Molar	Test Date: May 13, 2019
One Dose Mean Graph	Experiment ID: 1905OS06		Report Date: May 29, 2019

Panel/Cell Line	Growth Percent
Leukemia	
CCRF-CEM	104.64
HL-60(TB)	102.85
K-562	105.82
MOLT-4	106.28
RPMI-8226	105.85
SR	110.15
Non-Small Cell Lung Cancer	
A549/ATCC	108.03
EKVX	103.66
HOP-62	99.74
HOP-92	112.74
NCI-H23	102.42
NCI-H322M	99.41
NCI-H460	107.12
NCI-H522	98.43
Colon Cancer	
COLO 205	105.17
HCC-2998	114.81
HCT-116	102.45
HCT-15	101.01
HT29	106.82
KM12	108.57
SW-620	103.28
CNS Cancer	
SF-268	104.87
SF-295	98.67
SF-539	96.70
SNB-19	103.08
SNB-75	101.20
U251	106.06
Melanoma	
LOX IMVI	100.13
MALME-3M	105.68
M14	106.65
MDA-MB-435	99.98
SK-MEL-2	108.80
SK-MEL-28	105.93
SK-MEL-5	101.26
UACC-257	105.35
UACC-62	99.12
Ovarian Cancer	
IGROV1	108.91
OVCAR-3	113.16
OVCAR-4	109.86
OVCAR-5	99.99
OVCAR-8	104.03
NCI/ADR-RES	108.65
SK-OV-3	105.39
Renal Cancer	
786-0	107.13
A498	99.99
ACHN	104.87
CAKI-1	94.90
RXF 393	117.55
SN12C	100.85
TK-10	105.72
UO-31	100.78
Prostate Cancer	
PC-3	99.88
DU-145	106.54
Breast Cancer	
MCF7	97.60
MDA-MB-231/ATCC	108.73
HS 578T	106.14
BT-549	101.12
T-47D	100.22
MDA-MB-468	108.80
Mean	104.47
Delta	9.57
Range	22.65

Mean Growth Percent - Growth Percent

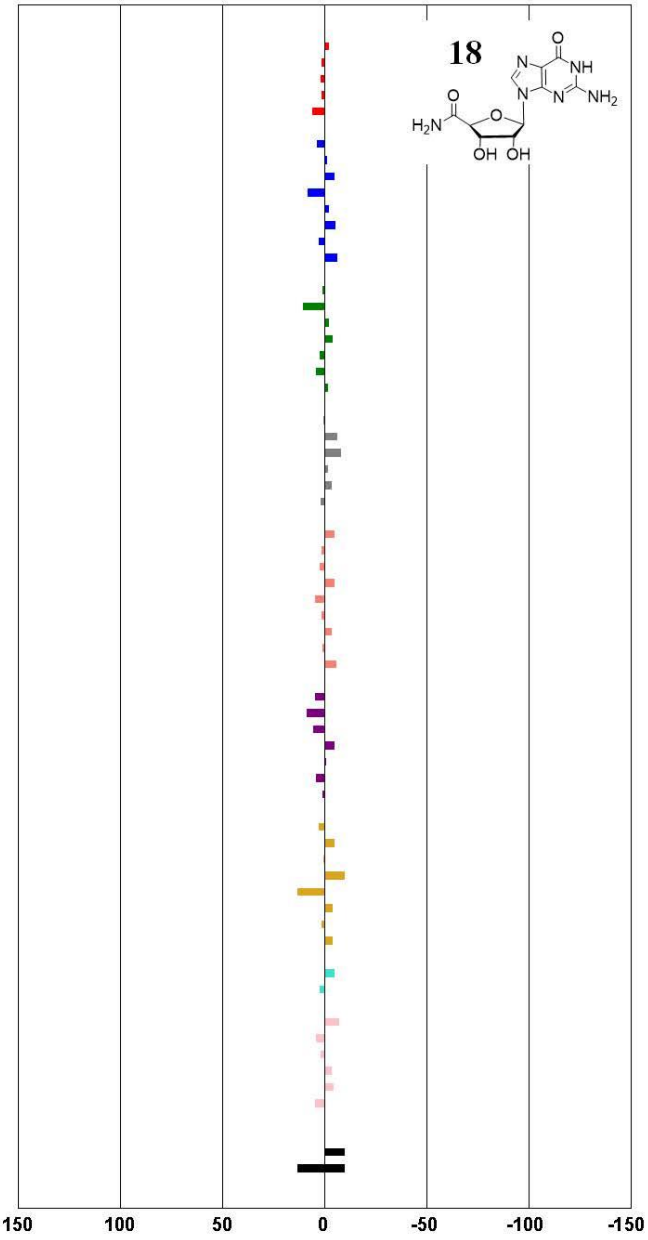

Developmental Therapeutics Program	NSC: D-815023 / 1	Conc: 1.00E-5 Molar	Test Date: May 13, 2019
One Dose Mean Graph	Experiment ID: 1905OS06		Report Date: May 29, 2019

Panel/Cell Line	Growth Percent
Leukemia	
CCRF-CEM	102.08
HL-60(TB)	102.58
K-562	107.36
MOLT-4	102.39
RPMI-8226	100.88
SR	115.84
Non-Small Cell Lung Cancer	
A549/ATCC	96.05
EKVX	105.31
HOP-62	99.79
HOP-92	119.79
NCI-H23	101.38
NCI-H322M	103.75
NCI-H460	107.17
NCI-H522	97.13
Colon Cancer	
COLO 205	116.17
HCC-2998	111.04
HCT-116	102.50
HCT-15	101.84
HT29	105.68
KM12	97.98
SW-620	104.06
CNS Cancer	
SF-268	101.19
SF-295	100.19
SF-539	101.27
SNB-19	101.73
SNB-75	101.19
U251	102.10
Melanoma	
LOX IMVI	97.67
MALME-3M	102.89
M14	108.09
MDA-MB-435	104.42
SK-MEL-2	114.41
SK-MEL-28	103.55
SK-MEL-5	101.59
UACC-257	96.25
UACC-62	99.92
Ovarian Cancer	
IGROV1	105.15
OVCAR-3	109.84
OVCAR-4	103.55
OVCAR-5	106.25
OVCAR-8	101.69
NCI/ADR-RES	106.07
SK-OV-3	108.31
Renal Cancer	
786-0	103.72
A498	102.34
ACHN	103.49
CAKI-1	97.28
RXF 393	117.54
SN12C	100.03
TK-10	97.54
UO-31	93.68
Prostate Cancer	
PC-3	102.36
DU-145	106.99
Breast Cancer	
MCF7	100.25
MDA-MB-231/ATCC	101.15
HS 578T	104.50
BT-549	106.26
T-47D	100.44
MDA-MB-468	107.04
Mean	103.77
Delta	10.09
Range	26.11

Mean Growth Percent - Growth Percent

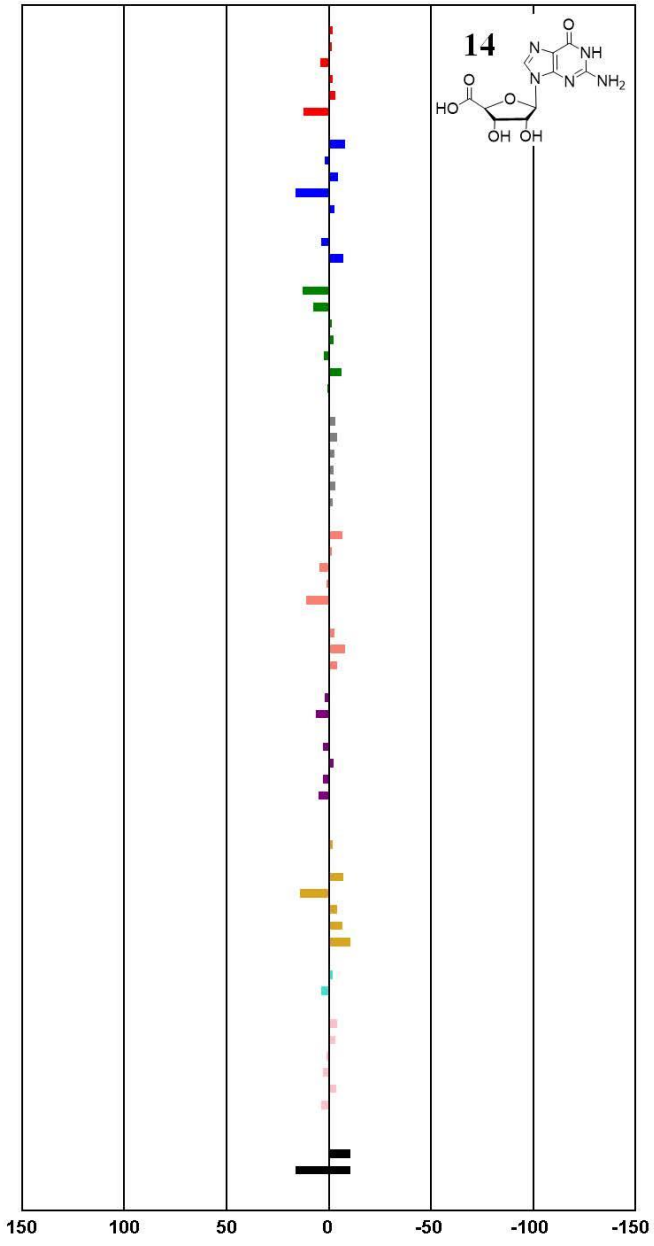

Developmental Therapeutics Program	NSC: D-815022 / 1	Conc: 1.00E-5 Molar	Test Date: May 13, 2019
One Dose Mean Graph	Experiment ID: 1905OS06		Report Date: May 29, 2019

Panel/Cell Line	Growth Percent
Leukemia	
CCRF-CEM	108.10
HL-60(TB)	102.34
K-562	102.67
MOLT-4	101.65
RPMI-8226	106.22
SR	101.20
Non-Small Cell Lung Cancer	
A549/ATCC	94.71
EKVX	101.34
HOP-62	103.57
HOP-92	132.35
NCI-H23	103.52
NCI-H322M	102.73
NCI-H460	107.76
NCI-H522	100.23
Colon Cancer	
COLO 205	114.34
HCC-2998	104.63
HCT-116	104.00
HCT-15	102.56
HT29	106.32
KM12	111.08
SW-620	103.94
CNS Cancer	
SF-268	102.97
SF-295	99.14
SF-539	97.18
SNB-19	105.34
SNB-75	94.28
U251	102.39
Melanoma	
LOX IMVI	98.32
MALME-3M	101.97
M14	104.83
MDA-MB-435	100.09
SK-MEL-2	109.38
SK-MEL-28	107.25
SK-MEL-5	101.43
UACC-257	81.54
UACC-62	99.21
Ovarian Cancer	
IGROV1	108.50
OVCAR-3	112.94
OVCAR-4	103.40
OVCAR-5	101.26
OVCAR-8	102.16
NCI/ADR-RES	104.69
SK-OV-3	110.01
Renal Cancer	
786-0	102.06
A498	101.00
ACHN	113.06
CAKI-1	98.98
RXF 393	122.20
SN12C	100.11
TK-10	104.29
UO-31	97.00
Prostate Cancer	
PC-3	105.32
DU-145	110.98
Breast Cancer	
MCF7	97.29
MDA-MB-231/ATCC	106.10
HS 578T	105.18
BT-549	106.40
T-47D	103.71
MDA-MB-468	106.04
Mean	104.12
Delta	22.58
Range	50.81

Mean Growth Percent - Growth Percent

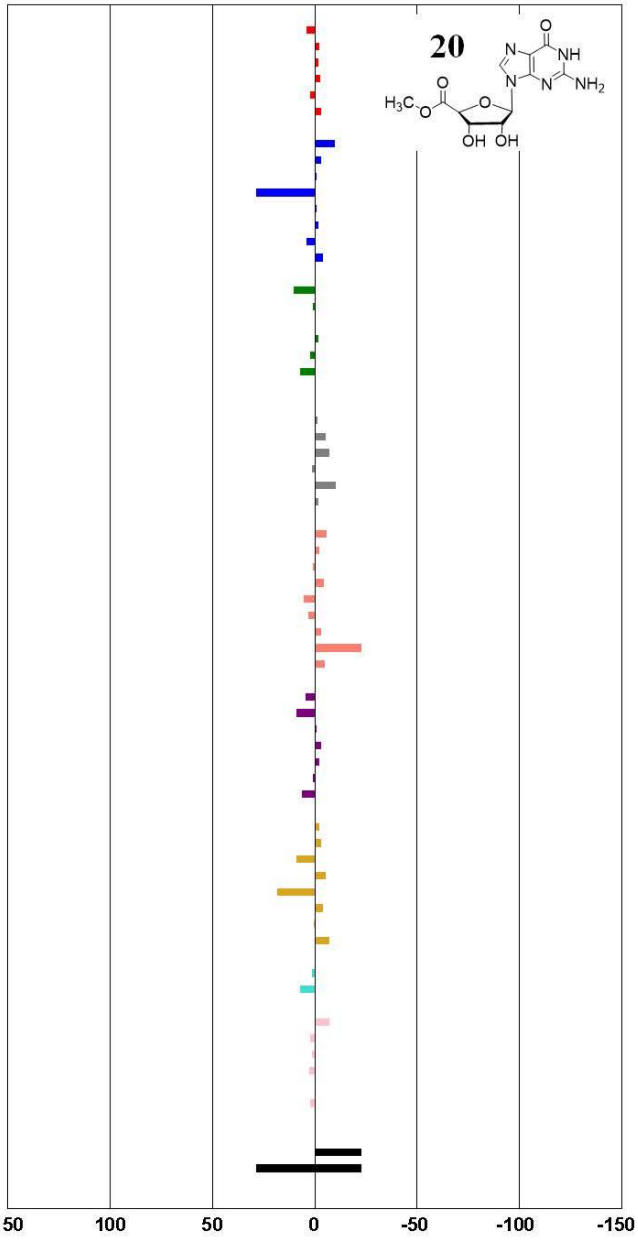

Developmental Therapeutics Program	NSC: D-815021 / 1	Conc: 1.00E-5 Molar	Test Date: May 13, 2019
One Dose Mean Graph	Experiment ID: 1905OS06		Report Date: May 29, 2019

Panel/Cell Line	Growth Percent
Leukemia	
CCRF-CEM	103.24
HL-60(TB)	103.45
K-562	101.65
MOLT-4	100.68
RPMI-8226	105.91
SR	110.42
Non-Small Cell Lung Cancer	
A549/ATCC	98.62
EKVX	102.84
HOP-62	98.79
HOP-92	116.70
NCI-H23	105.16
NCI-H322M	103.33
NCI-H460	106.59
NCI-H522	99.56
Colon Cancer	
COLO 205	111.95
HCC-2998	117.32
HCT-116	103.41
HCT-15	100.03
HT29	108.48
KM12	112.36
SW-620	107.12
CNS Cancer	
SF-268	102.22
SF-295	100.43
SF-539	103.03
SNB-19	102.46
SNB-75	96.66
U251	102.17
Melanoma	
LOX IMVI	98.53
MALME-3M	106.11
M14	106.21
MDA-MB-435	102.60
SK-MEL-2	112.21
SK-MEL-28	109.80
SK-MEL-5	101.67
UACC-257	102.09
UACC-62	101.29
Ovarian Cancer	
IGROV1	106.44
OVCAR-3	118.43
OVCAR-4	107.73
OVCAR-5	104.58
OVCAR-8	99.63
NCI/ADR-RES	108.62
SK-OV-3	99.51
Renal Cancer	
786-0	103.59
A498	102.33
ACHN	104.18
CAKI-1	96.82
RXF 393	127.15
SN12C	97.91
TK-10	106.33
UO-31	100.25
Prostate Cancer	
PC-3	104.96
DU-145	108.54
Breast Cancer	
MCF7	98.60
MDA-MB-231/ATCC	105.02
HS 578T	105.35
BT-549	104.92
T-47D	96.87
MDA-MB-468	110.77
Mean	104.81
Delta	8.15
Range	30.49

Mean Growth Percent - Growth Percent

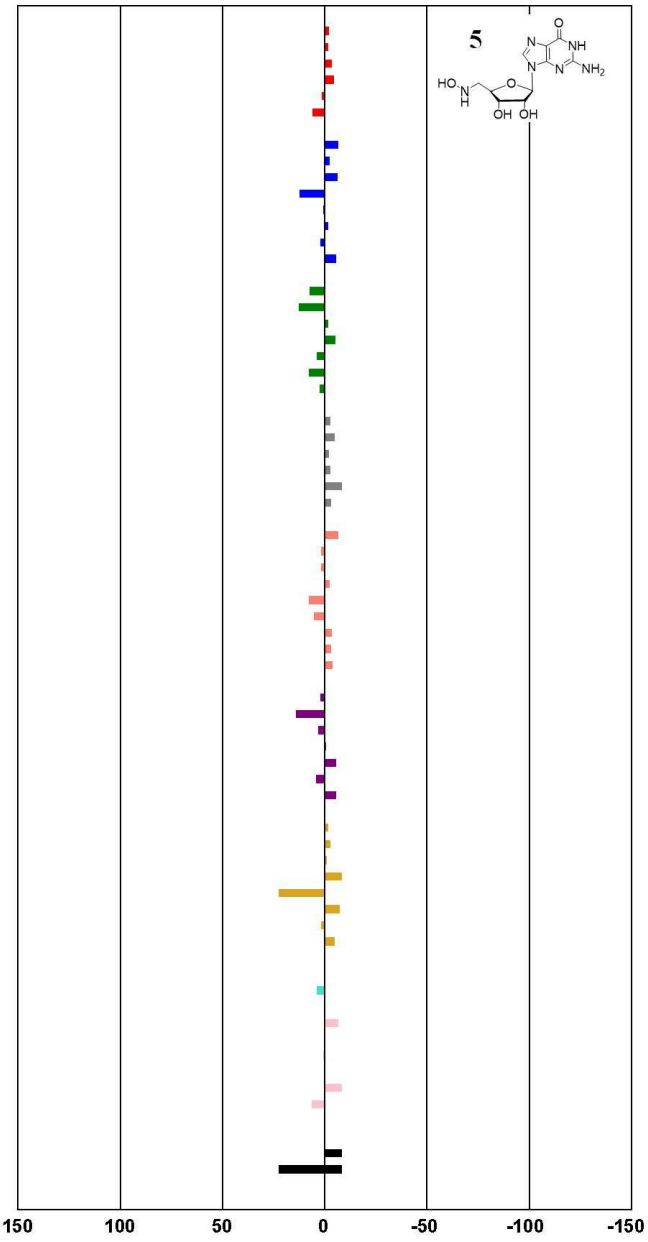

Developmental Therapeutics Program	NSC: D-815020 / 1	Conc: 1.00E-5 Molar	Test Date: May 13, 2019
One Dose Mean Graph	Experiment ID: 1905OS06		Report Date: May 29, 2019

Panel/Cell Line	Growth Percent
Leukemia	
CCRF-CEM	98.65
HL-60(TB)	104.74
K-562	106.05
MOLT-4	99.29
RPMI-8226	100.23
SR	97.03
Non-Small Cell Lung Cancer	
A549/ATCC	101.38
EKVX	98.47
HOP-62	102.35
HOP-92	94.16
NCI-H23	97.45
NCI-H322M	94.43
NCI-H460	103.31
NCI-H522	97.17
Colon Cancer	
COLO 205	105.06
HCC-2998	110.83
HCT-116	103.36
HCT-15	104.72
HT29	104.70
KM12	102.62
SW-620	98.19
CNS Cancer	
SF-268	98.58
SF-295	97.56
SF-539	100.10
SNB-19	100.04
SNB-75	76.93
U251	102.35
Melanoma	
LOX IMVI	95.52
MALME-3M	101.67
MDA-MB-435	98.46
SK-MEL-2	105.38
SK-MEL-28	101.52
SK-MEL-5	100.96
UACC-257	99.41
UACC-62	91.86
Ovarian Cancer	
IGROV1	102.68
OVCAR-3	107.67
OVCAR-4	105.37
OVCAR-5	92.63
OVCAR-8	101.67
NCI/ADR-RES	101.26
SK-OV-3	102.90
Renal Cancer	
786-0	102.26
A498	91.46
ACHN	98.69
CAKI-1	90.41
RXF 393	113.06
SN12C	98.58
TK-10	106.45
UO-31	89.37
Prostate Cancer	
PC-3	100.67
DU-145	108.43
Breast Cancer	
MCF7	93.20
MDA-MB-231/ATCC	101.92
HS 578T	98.24
BT-549	102.04
T-47D	97.81
MDA-MB-468	100.90
Mean	100.04
Delta	23.11
Range	36.13

Mean Growth Percent - Growth Percent

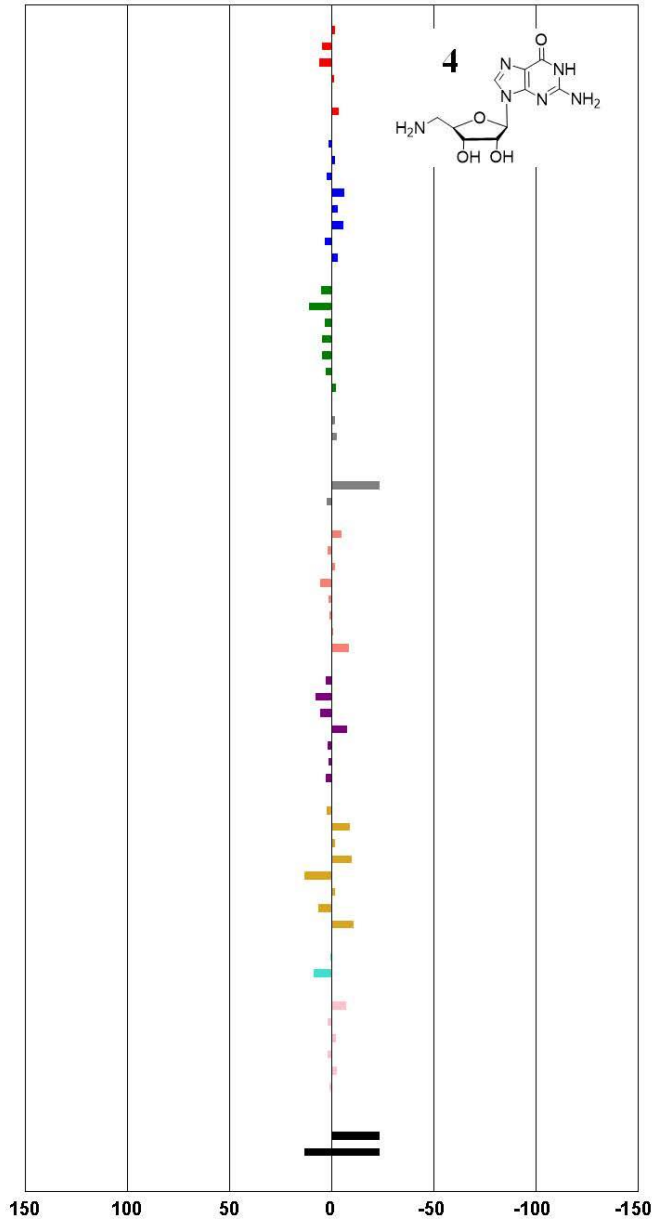

Developmental Therapeutics Program	NSC: D-815019 / 1	Conc: 1.00E-5 Molar	Test Date: May 13, 2019
One Dose Mean Graph	Experiment ID: 1905OS06		Report Date: May 29, 2019

Panel/Cell Line	Growth Percent
Leukemia	
CCRF-CEM	103.22
HL-60(TB)	100.58
K-562	101.20
MOLT-4	100.32
RPMI-8226	102.54
SR	88.49
Non-Small Cell Lung Cancer	
A549/ATCC	99.90
EKVX	94.94
HOP-62	93.34
HOP-92	97.06
NCI-H23	99.49
NCI-H322M	94.61
NCI-H460	104.26
NCI-H522	97.92
Colon Cancer	
COLO 205	100.23
HCC-2998	109.67
HCT-116	102.51
HCT-15	98.62
HT29	104.71
KM12	104.52
SW-620	94.65
CNS Cancer	
SF-268	97.66
SF-295	99.36
SF-539	99.39
SNB-19	98.10
SNB-75	93.72
U251	104.41
Melanoma	
LOX IMVI	97.83
MALME-3M	97.88
M14	104.73
MDA-MB-435	99.22
SK-MEL-2	117.30
SK-MEL-28	101.91
SK-MEL-5	98.80
UACC-257	97.72
UACC-62	96.19
Ovarian Cancer	
IGROV1	106.14
OVCAR-3	113.21
OVCAR-4	100.39
OVCAR-5	93.29
OVCAR-8	99.11
NCI/ADR-RES	100.07
SK-OV-3	107.28
Renal Cancer	
786-0	104.91
A498	89.09
ACHN	100.14
CAKI-1	95.77
RXF 393	107.30
SN12C	97.62
TK-10	98.90
UO-31	88.57
Prostate Cancer	
PC-3	101.96
DU-145	105.13
Breast Cancer	
MCF7	95.64
MDA-MB-231/ATCC	100.04
HS 578T	98.79
BT-549	101.47
T-47D	105.10
MDA-MB-468	99.86
Mean	100.12
Delta	11.63
Range	28.81

Mean Growth Percent - Growth Percent

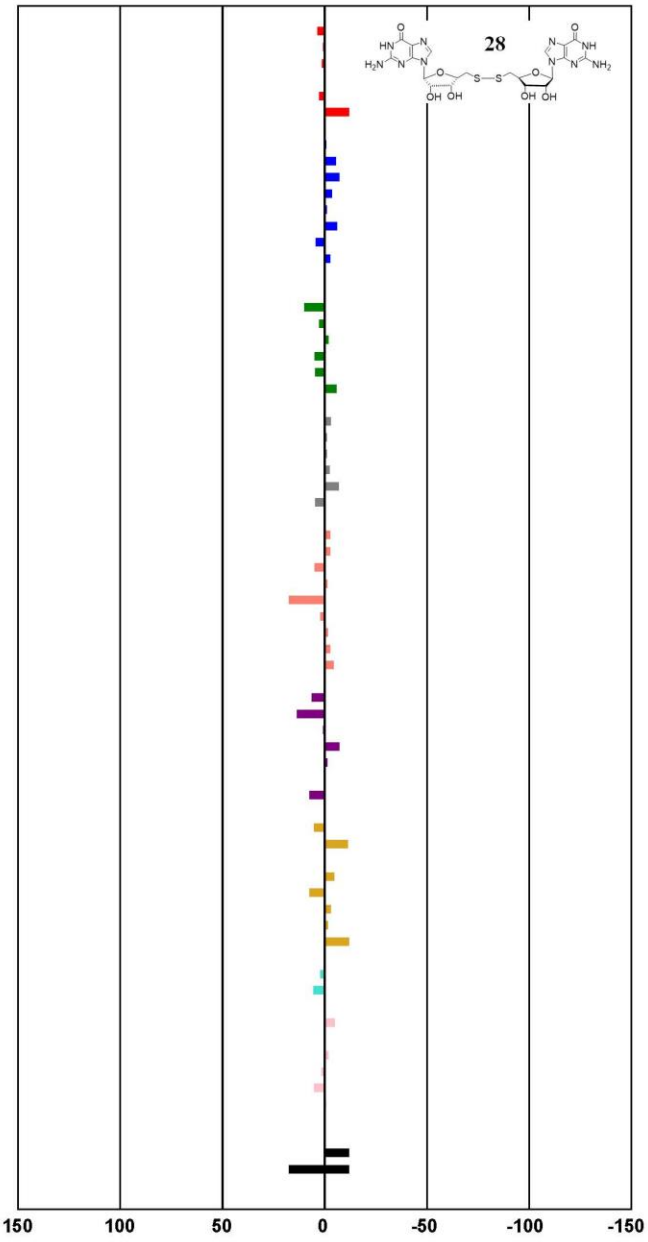

Developmental Therapeutics Program	NSC: D-815017 / 1	Conc: 1.00E-5 Molar	Test Date: May 13, 2019
One Dose Mean Graph	Experiment ID: 1905OS06		Report Date: May 29, 2019

Panel/Cell Line	Growth Percent
Leukemia	
CCRF-CEM	99.98
HL-60(TB)	100.69
K-562	97.18
MOLT-4	99.03
RPMI-8226	94.90
SR	100.86
Non-Small Cell Lung Cancer	
A549/ATCC	96.64
EKVX	95.77
HOP-62	100.46
HOP-92	103.14
NCI-H23	102.13
NCI-H322M	93.34
NCI-H460	101.90
NCI-H522	97.37
Colon Cancer	
COLO 205	99.13
HCC-2998	103.60
HCT-116	101.89
HCT-15	100.76
HT29	99.90
KM12	100.54
SW-620	95.96
CNS Cancer	
SF-268	99.66
SF-295	98.24
SF-539	102.33
SNB-19	95.30
SNB-75	92.61
U251	99.32
Melanoma	
LOX IMVI	96.87
MALME-3M	97.48
M14	101.54
MDA-MB-435	99.84
SK-MEL-2	119.97
SK-MEL-28	98.64
SK-MEL-5	96.95
UACC-257	94.66
UACC-62	93.58
Ovarian Cancer	
IGROV1	103.18
OVCAR-3	103.57
OVCAR-4	99.13
OVCAR-5	93.26
OVCAR-8	99.24
NCI/ADR-RES	103.83
SK-OV-3	105.10
Renal Cancer	
786-0	105.58
A498	99.92
ACHN	99.77
CAKI-1	94.53
RXF 393	111.15
SN12C	97.21
TK-10	96.25
UO-31	92.96
Prostate Cancer	
PC-3	100.67
DU-145	105.31
Breast Cancer	
MCF7	100.77
MDA-MB-231/ATCC	99.30
HS 578T	99.61
BT-549	100.13
T-47D	106.88
MDA-MB-468	97.81
Mean	99.79
Delta	7.18
Range	27.36

Mean Growth Percent - Growth Percent

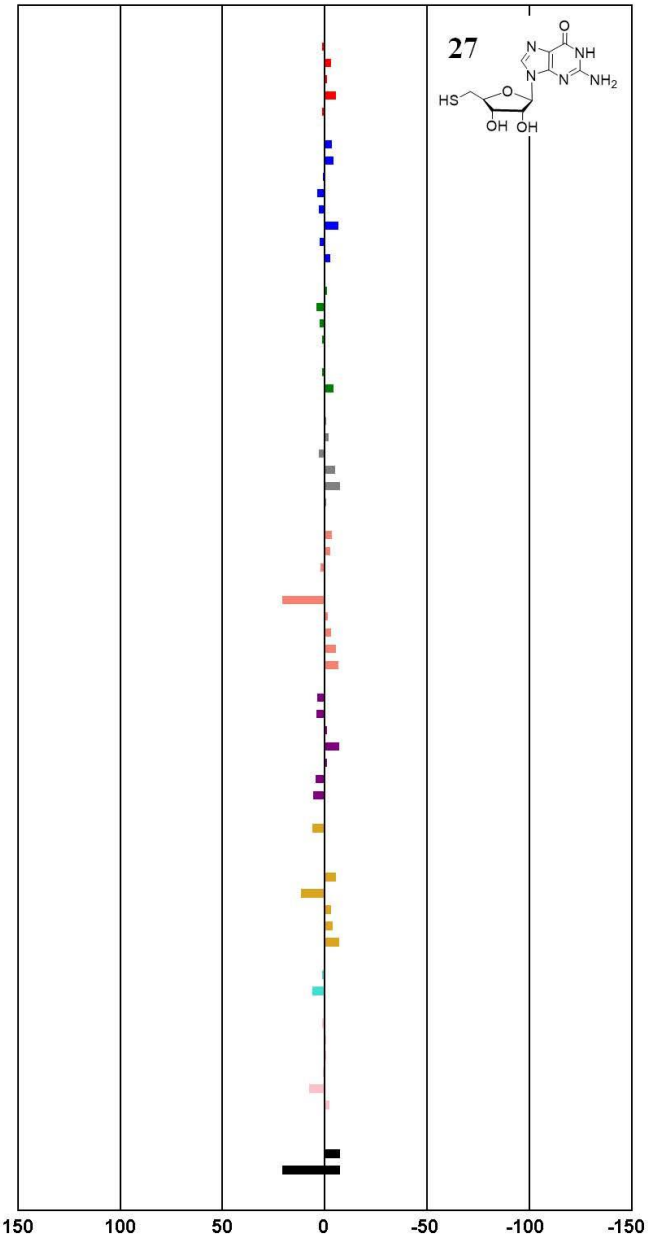

Developmental Therapeutics Program	NSC: D-815018 / 1	Conc: 1.00E-5 Molar	Test Date: May 13, 2019
One Dose Mean Graph	Experiment ID: 1905OS06		Report Date: May 29, 2019

Panel/Cell Line	Growth Percent
Leukemia	
CCRF-CEM	107.72
HL-60(TB)	103.45
K-562	94.68
MOLT-4	101.58
RPMI-8226	106.66
SR	92.57
Non-Small Cell Lung Cancer	
A549/ATCC	95.98
EKVX	102.21
HOP-62	96.57
HOP-92	119.03
NCI-H23	100.66
NCI-H322M	108.46
NCI-H460	101.67
NCI-H522	98.57
Colon Cancer	
COLO 205	110.18
HCC-2998	102.63
HCT-116	98.23
HCT-15	103.21
HT29	105.77
KM12	107.49
SW-620	106.06
CNS Cancer	
SF-268	100.16
SF-295	100.32
SF-539	88.43
SNB-19	101.62
SNB-75	94.60
U251	98.62
Melanoma	
LOX IMVI	95.69
MALME-3M	101.59
M14	94.49
MDA-MB-435	106.11
SK-MEL-2	108.70
SK-MEL-28	105.05
SK-MEL-5	100.25
UACC-257	102.75
UACC-62	101.79
Ovarian Cancer	
IGROV1	99.11
OVCAR-3	107.23
OVCAR-4	98.27
OVCAR-5	107.02
OVCAR-8	98.78
NCI/ADR-RES	100.92
SK-OV-3	107.19
Renal Cancer	
786-0	97.79
A498	115.90
ACHN	90.89
CAKI-1	94.56
RXF 393	118.19
SN12C	98.51
TK-10	108.18
UO-31	64.96
Prostate Cancer	
PC-3	100.70
DU-145	104.26
Breast Cancer	
MCF7	101.41
MDA-MB-231/ATCC	96.07
HS 578T	108.13
BT-549	97.43
T-47D	96.35
MDA-MB-468	103.75
Mean	101.34
Delta	36.38
Range	54.07

Mean Growth Percent - Growth Percent

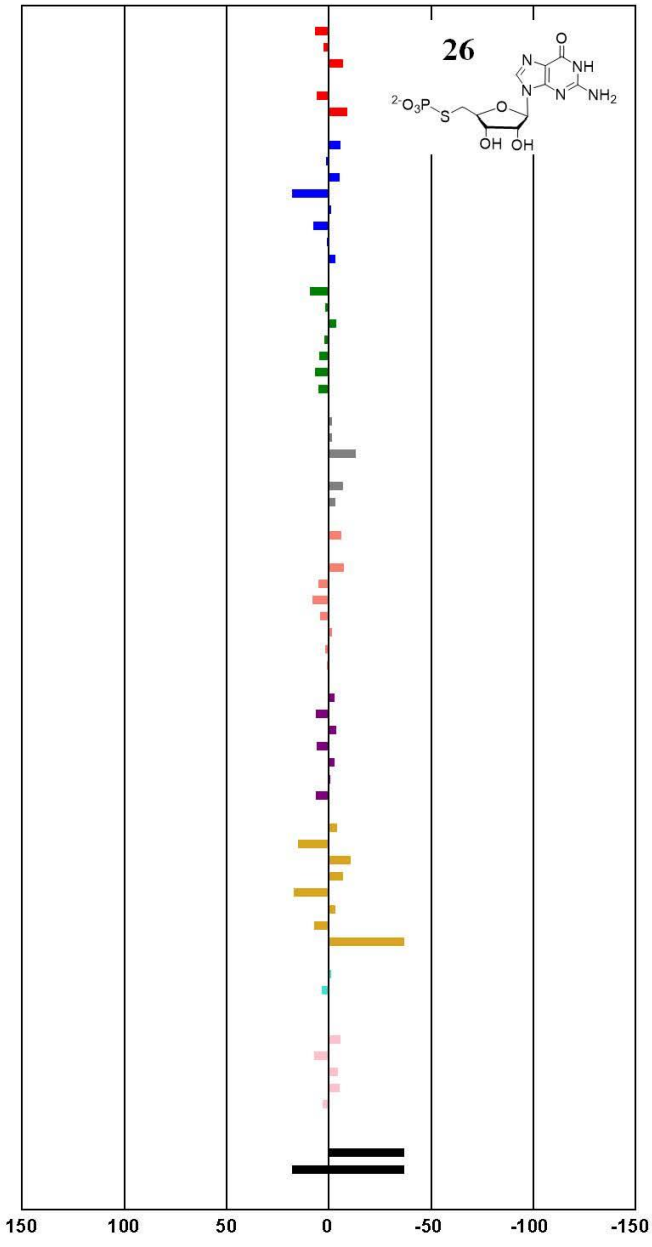

Bibliography

(1) Peters, G. M.; Davis, J. T. Supramolecular Gels Made from Nucleobase, Nucleoside and Nucleotide Analogs. *Chem. Soc. Rev.* **2016**, *45* (11), 3188–3206.

(2) Davis, J. T. G-Quartets 40 Years Later: From 5′-GMP to Molecular Biology and Supramolecular Chemistry. *Angew. Chemie - Int. Ed.* **2004**, *43* (6), 668–698.

(3) Bang, I. Untersuchungen Uber Die Guanylsaure. *Biochem. Zeitschrift* **1910**, *26*, 293–311.

(4) Bhattacharyya, T.; Saha, P.; Dash, J. Guanosine-Derived Supramolecular Hydrogels: Recent Developments and Future Opportunities. *ACS Omega* **2018**, *3* (2), 2230–2241.

(5) Xiao, S.; Davis, J. T. G 4 -Quartet Hydrogels from 5′-Hydrazino-Guanosine for the Non-Covalent and Covalent Remediation of Contaminants from Water. *Faraday Discuss.* **2018**, *209*, 97–112.

(6) Xiao, S.; Davis, J. T. A G 4 ·K + Hydrogel Made from 5′-Hydrazinoguanosine for Remediation of α,β-Unsaturated Carbonyls. *Chem. Commun.* **2018**, *54* (80), 11300–11303.

(7) Xiao, S.; Paukstelis, P. J.; Ash, R. D.; Zavalij, P. Y.; Davis, J. T. Drawing with Iron on a Gel Containing a Supramolecular Siderophore. *Angew. Chemie - Int. Ed.* **2019**, *58* (51), 18434–18437.

(8) Alemán, J.; Chadwick, A. V.; He, J.; Hess, M.; Horie, K.; Jones, R. G.;

Kratochvíl, P.; Meisel, I.; Mita, I.; Moad, G.; et al. Definitions of Terms Relating to the Structure and Processing of Sols, Gels, Networks, and Inorganic-Organic Hybrid Materials (IUPAC Recommendations 2007). *Pure Appl. Chem.* **2007**, *79* (10), 1801–1829.

(9) Hoffman, A. S. Hydrogels for Biomedical Applications. *Adv. Drug Deliv. Rev.* **2012**, *64*, 18–23.

(10) Slaughter, B. V.; Khurshid, S. S.; Fisher, O. Z.; Khademhosseini, A.; Peppas, N. A. Hydrogels in Regenerative Medicine. *Adv. Mater.* **2009**, *21* (32–33), 3307–3329.

(11) Peppas, N. A.; Hilt, J. Z.; Khademhosseini, A.; Langer, R. Hydrogels in Biology and Medicine: From Molecular Principles to Bionanotechnology. *Adv. Mater.* **2006**, *18* (11), 1345–1360.

(12) Weiss, R. G.; Terech, P. *Molecular Gels: Materials with Self-Assembled Fibrillar Networks*; Weiss, R. G., Terech, P., Eds.; Springer Netherlands: Dordrecht, 2006.

(13) Du, X.; Zhou, J.; Shi, J.; Xu, B. Supramolecular Hydrogelators and Hydrogels: From Soft Matter to Molecular Biomaterials. *Chem. Rev.* **2015**, *115* (24), 13165–13307.

(14) Du, X.; Zhou, J.; Shi, J.; Xu, B. Supramolecular Hydrogelators and Hydrogels: From Soft Matter to Molecular Biomaterials. *Chem. Rev.* **2015**, *115* (24), 13165–13307.

(15) Ji, X.; Ahmed, M.; Long, L.; Khashab, N. M.; Huang, F.; Sessler, J. L. Adhesive Supramolecular Polymeric Materials Constructed from Macrocycle-

Based Host-Guest Interactions. *Chem. Soc. Rev.* **2019**, *48* (10), 2682–2697.

(16) Appel, E. A.; Del Barrio, J.; Loh, X. J.; Scherman, O. A. Supramolecular Polymeric Hydrogels. *Chem. Soc. Rev.* **2012**, *41* (18), 6195–6214.

(17) Liu, J.; Scherman, O. A. Cucurbit[n]Uril Supramolecular Hydrogel Networks as Tough and Healable Adhesives. *Adv. Funct. Mater.* **2018**, *28* (21), 1800848.

(18) Harada, A.; Takashima, Y.; Nakahata, M. Supramolecular Polymeric Materials via Cyclodextrin-Guest Interactions. *Acc. Chem. Res.* **2014**, *47* (7), 2128–2140.

(19) Zhang, J.; Ma, P. X. Cyclodextrin-Based Supramolecular Systems for Drug Delivery: Recent Progress and Future Perspective. *Adv. Drug Deliv. Rev.* **2013**, *65* (9), 1215–1233.

(20) Qin, J.; Dong, B.; Cao, L.; Wang, W. Photonic Hydrogels for the Ultratrace Sensing of Divalent Beryllium in Seawater. *J. Mater. Chem. C* **2018**, *6* (15), 4234–4242.

(21) Yu, H. R.; Hu, J. Q.; Liu, Z.; Ju, X. J.; Xie, R.; Wang, W.; Chu, L. Y. Ion-Recognizable Hydrogels for Efficient Removal of Cesium Ions from Aqueous Environment. *J. Hazard. Mater.* **2017**, *323* (24), 632–640.

(22) Yan, P. J.; He, F.; Wang, W.; Zhang, S. Y.; Zhang, L.; Li, M.; Liu, Z.; Ju, X. J.; Xie, R.; Chu, L. Y. Novel Membrane Detector Based on Smart Nanogels for Ultrasensitive Detection of Trace Threat Substances. *ACS Appl. Mater. Interfaces* **2018**, *10* (42), 36425–36434.

(23) Ji, X.; Wu, R. T.; Long, L.; Ke, X. S.; Guo, C.; Ghang, Y. J.; Lynch, V. M.; Huang, F.; Sessler, J. L. Encoding, Reading, and Transforming Information Using Multifluorescent Supramolecular Polymeric Hydrogels. *Adv. Mater.*

2018, *30* (11), 1–6.

(24) Qi, Z.; Schalley, C. A. Exploring Macrocycles in Functional Supramolecular Gels: From Stimuli Responsiveness to Systems Chemistry. *Acc. Chem. Res.* **2014**, *47* (7), 2222–2233.

(25) Dong, S.; Zheng, B.; Wang, F.; Huang, F. Supramolecular Polymers Constructed from Macrocycle-Based Host-Guest Molecular Recognition Motifs. *Acc. Chem. Res.* **2014**, *47* (7), 1982–1994.

(26) Xue, M.; Yang, Y.; Chi, X.; Zhang, Z.; Huang, F. Pillararenes, A New Class of Macrocycles for Supramolecular Chemistry. *Acc. Chem. Res.* **2012**, *45* (8), 1294–1308.

(27) Lagona, J.; Mukhopadhyay, P.; Chakrabarti, S.; Isaacs, L. The Cucurbit[n]Uril Family. *Angew. Chemie Int. Ed.* **2005**, *44* (31), 4844–4870.

(28) Rebek Jr., J. Host–Guest Chemistry of Calixarene Capsules. *Chem. Commun.* **2000**, No. 8, 637–643.

(29) Cafferty, B. J.; Gállego, I.; Chen, M. C.; Farley, K. I.; Eritja, R.; Hud, N. V. Efficient Self-Assembly in Water of Long Noncovalent Polymers by Nucleobase Analogues. *J. Am. Chem. Soc.* **2013**, *135* (7), 2447–2450.

(30) Corbett, P. T.; Leclaire, J.; Vial, L.; West, K. R.; Wietor, J.; Sanders, J. K. M.; Otto, S. Dynamic Combinatorial Chemistry. *Chem. Rev.* **2006**, *106* (August), 3652–3711.

(31) Lehn, J. M. Dynamic Combinatorial Chemistry and Virtual Combinatorial Libraries. *Chem. - A Eur. J.* **1999**, *5* (9), 2455–2463.

(32) Corbett, P. T.; Leclaire, J.; Vial, L.; West, K. R.; Wietor, J.; Sanders, J. K. M.;

Otto, S. Dynamic Combinatorial Chemistry Dynamic Combinatorial Chemistry. *Chem. Rev.* **2006**, *106* (August), 3652–3711.

(33) Black, S. P.; Sanders, J. K. M.; Stefankiewicz, A. R. Disulfide Exchange: Exposing Supramolecular Reactivity through Dynamic Covalent Chemistry. *Chem. Soc. Rev.* **2014**, *43* (6), 1861–1872.

(34) Li, J.; Carnall, J. M. A.; Stuart, M. C. A.; Otto, S. Hydrogel Formation upon Photoinduced Covalent Capture of Macrocycle Stacks from Dynamic Combinatorial Libraries. *Angew. Chemie - Int. Ed.* **2011**, *50* (36), 8384–8386.

(35) Carnall, J. M. A.; Waudby, C. A.; Belenguer, A. M.; Stuart, M. C. A.; Peyralans, J. J. P.; Otto, S. Mechanosensitive Self-Replication Driven by Self-Organization. *Science (80-.).* **2010**, *327* (5972), 1502–1506.

(36) Li, J.; Cvrtila, I.; Colomb-Delsuc, M.; Otten, E.; Otto, S. An "Ingredients" Approach to Functional Self-Synthesizing Materials: A Metal-Ion-Selective, Multi-Responsive, Self-Assembled Hydrogel. *Chem. - A Eur. J.* **2014**, *20* (48), 15709–15714.

(37) Cook, T. R.; Zheng, Y. R.; Stang, P. J. Metal-Organic Frameworks and Self-Assembled Supramolecular Coordination Complexes: Comparing and Contrasting the Design, Synthesis, and Functionality of Metal-Organic Materials. *Chem. Rev.* **2013**, *113* (1), 734–777.

(38) Chakrabarty, R.; Mukherjee, P. S.; Stang, P. J. Supramolecular Coordination: Self-Assembly of Finite Two- and Three-Dimensional Ensembles. *Chem. Rev.* **2011**, *111* (11), 6810–6918.

(39) Yan, X.; Li, S.; Cook, T. R.; Ji, X.; Yao, Y.; Pollock, J. B.; Shi, Y.; Yu, G.; Li,

J.; Huang, F.; et al. Hierarchical Self-Assembly: Well-Defined Supramolecular Nanostructures and Metallohydrogels via Amphiphilic Discrete Organoplatinum(II) Metallacycles. *J. Am. Chem. Soc.* **2013**, *135* (38), 14036–14039.

(40) Zheng, W.; Chen, L. J.; Yang, G.; Sun, B.; Wang, X.; Jiang, B.; Yin, G. Q.; Zhang, L.; Li, X.; Liu, M.; et al. Construction of Smart Supramolecular Polymeric Hydrogels Cross-Linked by Discrete Organoplatinum(II) Metallacycles via Post-Assembly Polymerization. *J. Am. Chem. Soc.* **2016**, *138* (14), 4927–4937.

(41) Zheng, W.; Yang, G.; Shao, N.; Chen, L. J.; Ou, B.; Jiang, S. T.; Chen, G.; Yang, H. B. CO 2 Stimuli-Responsive, Injectable Block Copolymer Hydrogels Cross-Linked by Discrete Organoplatinum(II) Metallacycles via Stepwise Post-Assembly Polymerization. *J. Am. Chem. Soc.* **2017**, *139* (39), 13811–13820.

(42) Perry VI, J. J.; Perman, J. A.; Zaworotko, M. J. Design and Synthesis of Metal-Organic Frameworks Using Metal-Organic Polyhedra as Supermolecular Building Blocks. *Chem. Soc. Rev.* **2009**, *38* (5), 1400–1417.

(43) Foster, J. A.; Parker, R. M.; Belenguer, A. M.; Kishi, N.; Sutton, S.; Abell, C.; Nitschke, J. R. Differentially Addressable Cavities within Metal-Organic Cage-Cross-Linked Polymeric Hydrogels. *J. Am. Chem. Soc.* **2015**, *137* (30), 9722–9729.

(44) Sutar, P.; Suresh, V. M.; Jayaramulu, K.; Hazra, A.; Maji, T. K. Binder Driven Self-Assembly of Metal-Organic Cubes towards Functional Hydrogels. *Nat.*

Commun. **2018**, *9* (1), 1–12.

(45) Qin, Y.; Chen, L. L.; Pu, W.; Liu, P.; Liu, S. X.; Li, Y.; Liu, X. L.; Lu, Z. X.; Zheng, L. Y.; Cao, Q. E. A Hydrogel Directly Assembled from a Copper Metal-Organic Polyhedron for Antimicrobial Application. *Chem. Commun.* **2019**, *55* (15), 2206–2209.

(46) Sakai, N.; Kamikawa, Y.; Nishii, M.; Matsuoka, T.; Kato, T.; Matile, S. Dendritic Folate Rosettes as Ion Channels in Lipid Bilayers. *J. Am. Chem. Soc.* **2006**, *128* (7), 2218–2219.

(47) Xing, P.; Chu, X.; Ma, M.; Li, S.; Hao, A. Supramolecular Gel from Folic Acid with Multiple Responsiveness, Rapid Self-Recovery and Orthogonal Self-Assemblies. *Phys. Chem. Chem. Phys. Phys. Chem. Chem. Phys* **2014**, *16* (16), 8346–8359.

(48) Chakraborty, P.; Roy, B.; Bairi, P.; Nandi, A. K. Improved Mechanical and Photophysical Properties of Chitosan Incorporated Folic Acid Gel Possessing the Characteristics of Dye and Metal Ion Absorption. *J. Mater. Chem.* **2012**, *22* (38), 20291–20298.

(49) Panja, A.; Das, S.; Chakraborty, A.; Chakraborty, P.; Pal, S.; Nandi, A. K. Injectable Hydrogel of Vitamin B9 for the Controlled Release of Both Hydrophilic and Hydrophobic Anticancer Drugs. *ChemMedChem* **2018**, *13* (22), 2427–2436.

(50) Liu, K.; Zang, S.; Xue, R.; Yang, J.; Wang, L.; Huang, J.; Yan, Y. Coordination-Triggered Hierarchical Folate/Zinc Supramolecular Hydrogels Leading to Printable Biomaterials. *ACS Appl. Mater. Interfaces* **2018**, *10* (5),

4530–4539.

(51) Ren, C.; Song, Z.; Zheng, W.; Chen, X.; Wang, L.; Kong, D.; Yang, Z. Disulfide Bond as a Cleavable Linker for Molecular Self-Assembly and Hydrogelation. *Chem. Commun.* **2011**, *47* (5), 1619–1621.

(52) Li, X.; Yang, C.; Zhang, Z.; Wu, Z.; Deng, Y.; Liang, G.; Yang, Z.; Chen, H. Folic Acid as a Versatile Motif to Construct Molecular Hydrogelators through Conjugations with Hydrophobic Therapeutic Agents. *J. Mater. Chem.* **2012**, *22* (41), 21838–21840.

(53) Yang, C.; Li, D.; Fengzhao, Q.; Wang, L.; Wang, L.; Yang, Z. Disulfide Bond Reduction-Triggered Molecular Hydrogels of Folic Acid-Taxol Conjugates. *Org. Biomol. Chem.* **2013**, *11* (40), 6946–6951.

(54) Li, H.; Gao, J.; Shang, Y.; Hua, Y.; Ye, M.; Yang, Z.; Ou, C.; Chen, M. Folic Acid Derived Hydrogel Enhances the Survival and Promotes Therapeutic Efficacy of IPS Cells for Acute Myocardial Infarction. *ACS Appl. Mater. Interfaces* **2018**, *10* (29), 24459–24468.

(55) Wang, H.; Yang, C.; Wang, L.; Kong, D.; Zhang, Y.; Yang, Z. Self-Assembled Nanospheres as a Novel Delivery System for Taxol: A Molecular Hydrogel with Nanosphere Morphology. *Chem. Commun.* **2011**, *47* (15), 4439–4441.

(56) Cai, M.; Shi, X.; Sidorov, V.; Fabris, D.; Lam, Y. F.; Davis, J. T. Cation-Directed Self-Assembly of Lipophilic Nucleosides: The Cation's Central Role in the Structure and Dynamics of a Hydrogen-Bonded Assembly. *Tetrahedron* **2002**, *58* (4), 661–671.

(57) Cai, M.; Marlow, A. L.; Fettinger, J. C.; Fabris, D.; Haverlock, T. J.; Moyer, B.

A.; Davis, J. T. Binding Cesium Ions with Nucleosides: Templated Self-Assembly of Isoguanosine Pentamers. *Angew. Chemie - Int. Ed.* **2000**, *39* (7), 1283–1285.

(58) Tirumala, S.; Davis, J. T. Self-Assembled Ionophores. An Isoguanosine-K+ Octamer. *J. Am. Chem. Soc.* **1997**, *119* (12), 2769–2776.

(59) Davis, J. T.; Tirumala, S.; Jenssen, J. R.; Radler, E.; Fabris, D. Self-Assembled Ionophores From Isoguanosine. *J. Org. Chem.* **1995**, *60* (13), 4167–4176.

(60) Van Leeuwen, F. W. B. B.; Verboom, W.; Shi, X.; Davis, J. T.; Reinhoudt, D. N. Selective 226Ra2+ Ionophores Provided by Self-Assembly of Guanosine and Isoguanosine Derivatives. *J. Am. Chem. Soc.* **2004**, *126* (50), 16575–16581.

(61) Chantot, J. F.; Sarocchi, M.-T.; Guschlbauer, W. Physico-Chemical Properties of Nucleosides. *Biochimie* **1971**, *53*, 347–354.

(62) Zhao, H.; Schäfer, A. H.; Seela, F. Supramolecular Isoguanosine Assemblies Form Hydrogels with Excellent Long-Term Stability. *Chempluschem* **2017**, *82* (6), 826–833.

(63) Tang, F.; Feng, H.; Du, Y.; Xiao, Y.; Dan, H.; Zhao, H.; Chen, Q. Developing a Self-Healing Supramolecular Nucleoside Hydrogel Based on Guanosine and Isoguanosine. *Chem. - An Asian J.* **2018**, *13* (15), 1962–1971.

(64) Zhao, H.; Jiang, D.; Schäfer, A. H.; Seela, F. 8-Aza-2′-Deoxyisoguanosine Forms Fluorescent Hydrogels Whereas 8-Aza-2′-Deoxyguanosine Assembles into Nucleoside Nanotubes. *Chempluschem* **2017**, *82* (5), 778–784.

(65) Chen, M. C.; Cafferty, B. J.; Mamajanov, I.; Gállego, I.; Khanam, J.;

Krishnamurthy, R.; Hud, N. V. Spontaneous Prebiotic Formation of a β-Ribofuranoside That Self-Assembles with a Complementary Heterocycle. *J. Am. Chem. Soc.* **2014**, *136* (15), 5640–5646.

(66) Li, C.; Cafferty, B. J.; Karunakaran, S. C.; Schuster, G. B.; Hud, N. V. Formation of Supramolecular Assemblies and Liquid Crystals by Purine Nucleobases and Cyanuric Acid in Water: Implications for the Possible Origins of RNA. *Phys. Chem. Chem. Phys.* **2016**, *18* (30), 20091–20096.

(67) Karunakaran, S. C.; Cafferty, B. J.; Weigert-Muñoz, A.; Schuster, G. B.; Hud, N. V. Spontaneous Symmetry Breaking in the Formation of Supramolecular Polymers: Implications for the Origin of Biological Homochirality. *Angew. Chemie - Int. Ed.* **2019**, *58* (5), 1453–1457.

(68) Karunakaran, S. C.; Cafferty, B. J.; Peláez-Fernández, M.; Neselu, K.; Schmidt-Krey, I.; Fernandez-Nieves, A.; Schuster, G. B.; Hud, N. V. Exquisite Regulation of Supramolecular Equilibrium Polymers in Water: Chain Stoppers Control Length, Polydispersity and Viscoelasticity. *Polym. Chem.* **2018**, *9* (43), 5268–5277.

(69) Cafferty, B. J.; Avirah, R. R.; Schuster, G. B.; Hud, N. V. Ultra-Sensitive PH Control of Supramolecular Polymers and Hydrogels: PKa Matching of Biomimetic Monomers. *Chem. Sci.* **2014**, *5* (12), 4681–4686.

(70) Green, M. M.; Peterson, N. C.; Sato, T.; Teramoto, A.; Cook, R.; Lifson, S. A Helical Polymer with a Cooperative Response to Chiral Information. *Science (80-.).* **1995**, *268* (5219), 1860–1866.

(71) Gellert, M.; Lipsett, M. N.; Davies, D. R. Helix Formation By Guanylic Acid.

Proc. Natl. Acad. Sci. **1962**, *48* (12), 2013–2018.

(72) Pinnavaia, T. J.; Marshall, C. L.; Mettler, C. M.; Fisk, C. L.; Miles, H. T.; Becker, E. D. Alkali Metal Ion Specificity in the Solution Ordering of a Nucleotide, 5'-Guanosine Monophosphate. *J. Am. Chem. Soc.* **1978**, *100* (5), 3625–3627.

(73) Laughlan, G.; Murchie, A.; Norman, D.; Moore, M.; Moody, P.; Lilley, D.; Luisi, B. The High-Resolution Crystal Structure of a Parallel-Stranded Guanine Tetraplex. *Science (80-.).* **1994**, *265* (5171).

(74) Forman, S. L.; Fettinger, J. C.; Pieraccini, S.; Gottarelli, G.; Davis, J. T. Toward Artificial Ion Channels: A Lipophilic G-Quadruplex. *J. Am. Chem. Soc.* **2000**, *122* (17), 4060–4067.

(75) Kotch, F. W.; Fettinger, J. C.; Davis, J. T. A Lead-Filled G-Quadruplex: Insight into the G-Quartet's Selectivity for Pb(2+) over K(+). *Org Lett* **2000**, *2* (21), 3277–3280.

(76) Sutyak, K. B.; Zavalij, P. Y.; Robinson, M. L.; Davis, J. T. Controlling Molecularity and Stability of Hydrogen Bonded G-Quadruplexes by Modulating the Structure's Periphery. *Chem. Commun.* **2016**, *40* (74), 2382.

(77) Shi, X.; Fettinger, J. C.; Davis, J. T. Ion-Pair Recognition by Nucleoside Self-Assembly: Guanosine Hexadecamers Bind Cations and Anions. *Angew. Chemie - Int. Ed.* **2001**, *40* (15), 2827–2831.

(78) Peters, G. M.; Skala, L. P.; Plank, T. N.; Hyman, B. J.; Manjunatha Reddy, G. N.; Marsh, A.; Brown, S. P.; Davis, J. T. A G4·K+ Hydrogel Stabilized by an Anion. *J. Am. Chem. Soc.* **2014**, *136* (36), 12596–12599.

(79) Dean, D. K. An Improved Synthesis of 5′-Amino-5′-Deoxyguanosine. *Synth. Commun.* **2002**, *32* (10), 1517–1521.

(80) Buchs, B.; Fieber, W.; Vigouroux-Elie, F.; Sreenivasachary, N.; Lehn, J.-M.; Herrmann, A. Release of Bioactive Volatiles from Supramolecular Hydrogels: Influence of Reversible Acylhydrazone Formation on Gel Stability and Volatile Compound Evaporation. *Org. Biomol. Chem.* **2011**, *9* (8), 2906–2919.

(81) Holmes, R. E.; Robins, R. K. Purine Nucleosides. VII. Direct Bromination of Adenosine, Deoxyadenosine, Guanosine, and Related Purine Nucleosides. *J. Am. Chem. Soc.* **1964**, *86* (6), 1242–1245.

(82) Case, W. S.; Glinert, K. D.; LaBarge, S.; McGown, L. B. Guanosine Gel for Sequence-Dependent Separation of Polymorphic SsDNA. *Electrophoresis* **2007**, *28* (17), 3008–3016.

(83) Cassidy, L. M.; Burcar, B. T.; Stevens, W.; Moriarty, E. M.; McGown, L. B. Guanine-Centric Self-Assembly of Nucleotides in Water: An Important Consideration in Prebiotic Chemistry. *Astrobiology* **2014**, *14* (10), 876–886.

(84) Pu, F.; Wu, L.; Ran, X.; Ren, J.; Qu, X. G-Quartet-Based Nanostructure for Mimicking Light-Harvesting Antenna. *Angew. Chemie - Int. Ed.* **2015**, *54* (3), 892–896.

(85) Buerkle, L. E.; Li, Z.; Jamieson, A. M.; Rowan, S. J. Tailoring the Properties of Guanosine-Based Supramolecular Hydrogels. *Langmuir* **2009**, *25* (15), 8833–8840.

(86) Way, A. E.; Korpusik, A. B.; Dorsey, T. B.; Buerkle, L. E.; von Recum, H. A.; Rowan, S. J. Enhancing the Mechanical Properties of Guanosine-Based

Supramolecular Hydrogels with Guanosine-Containing Polymers. *Macromolecules* **2014**, *47* (5), 1810–1818.

(87) Adhikari, B.; Shah, A.; Kraatz, H.-B. Self-Assembly of Guanosine and Deoxy-Guanosine into Hydrogels: Monovalent Cation Guided Modulation of Gelation, Morphology and Self-Healing Properties. *J. Mater. Chem. B* **2014**, *2* (30), 4802.

(88) Ghosh, A.; Parasar, B.; Bhattacharyya, T.; Dash, J. Chiral Carbon Dots Derived from Guanosine 5′-Monophosphate Form Supramolecular Hydrogels. *Chem. Commun.* **2016**, *52* (74), 11159–11162.

(89) Wu, G.; Wong, A. Direct Detection of the Bound Sodium Ions in Self-Assembled 5′-GMP Gels: A Solid-State 23Na NMR ApproachElectronic Supplementary Information (ESI) Available: 31P CPMAS Spectra of Na Gel, Cs–Na Gel and Na2(5′-GMP)·7H2O. See Http://Www.Rsc.Org/Suppdata/Cc/B. *Chem. Commun.* **2001**, No. 24, 2658–2659.

(90) Wong, A.; Wu, G. Selective Binding of Monovalent Cations to the Stacking G-Quartet Structure Formed by Guanosine 5′-Monophosphate: A Solid-State NMR Study. *J. Am. Chem. Soc.* **2003**, *125* (45), 13895–13905.

(91) Kwan, I. C. M.; Mo, X.; Wu, G.; Kl, C. Probing Hydrogen Bonding and Ion - Carbonyl Interactions By. *J. Am. Chem. Soc.* **2007**, *129* (5), 2398–2407.

(92) Carducci, F.; Yoneda, J. S.; Itri, R.; Mariani, P. On the Structural Stability of Guanosine-Based Supramolecular Hydrogels. *Soft Matter* **2018**, *14* (15), 2938–2948.

(93) Zhang, J.; Li, X.; Sun, X.; Song, A.; Tan, Y.; Hao, J. GMP-Quadruplex-Based Hydrogels Stabilized by Lanthanide Ions. *Sci. China Chem.* **2018**, *61* (5), 604–612.

(94) Yu, E.; Nakamura, D.; DeBoyace, K.; Neisius, A. W.; McGown, L. B. Tunable Thermoassociation of Binary Guanosine Gels. *J. Phys. Chem. B* **2008**, *112* (4), 1130–1134.

(95) Peters, G. M.; Skala, L. P.; Davis, J. T. A Molecular Chaperone for G4-Quartet Hydrogels. *J. Am. Chem. Soc.* **2016**, *138* (1), 134–139.

(96) Venkatesh, V.; Mishra, N. K.; Romero-Canelón, I.; Vernooij, R. R.; Shi, H.; Coverdale, J. P. C.; Habtemariam, A.; Verma, S.; Sadler, P. J. Supramolecular Photoactivatable Anticancer Hydrogels. *J. Am. Chem. Soc.* **2017**, *139* (16), 5656–5659.

(97) Sreenivasachary, N.; Lehn, J.-M. M. Gelation-Driven Component Selection in the Generation of Constitutional Dynamic Hydrogels Based on Guanine-Quartet Formation. *Proc. Natl. Acad. Sci.* **2005**, *102* (17), 5938–5943.

(98) Plank, T. N.; Davis, J. T. A G 4 ·K + Hydrogel That Self-Destructs. *Chem. Commun.* **2016**, *52* (28), 5037–5040.

(99) Plank, T. N.; Skala, L. P.; Davis, J. T. Supramolecular Hydrogels for Environmental Remediation: G 4 -Quartet Gels That Selectively Absorb Anionic Dyes from Water. *Chem. Commun.* **2017**, *53* (28 mM), 6235–6238.

(100) Plank, T. PhD Thesis: Tailoring Guanosine Hydrogels for Various Applications, 2018.

(101) Oae, S.; Doi, J. Organic Sulfur Chemistry. **1991**.

(102) Loudon, G. M.; Parise, J. *Organic Chemistry*, 6th ed.; W.H. Freeman: New York, 2016.

(103) Bondi, A. Van Der Waals Volumes and Radii. *J. Phys. Chem.* **1964**, *68* (3), 441–451.

(104) Nair, D. P.; Podgórski, M.; Chatani, S.; Gong, T.; Xi, W.; Fenoli, C. R.; Bowman, C. N. The Thiol-Michael Addition Click Reaction: A Powerful and Widely Used Tool in Materials Chemistry. *Chem. Mater.* **2014**, *26* (1), 724–744.

(105) Tang, W.; Becker, M. L. "Click" Reactions: A Versatile Toolbox for the Synthesis of Peptide-Conjugates. *Chem. Soc. Rev.* **2014**, *43* (20), 7013–7039.

(106) Iha, R. K.; Wooley, K. L.; Nyström, A. M.; Burked, D. J.; Kade, M. J.; Hawker, C. J. Applications of Orthogonal "Click" Chemistries in the Synthesis of Functional Soft Materials. *Chem. Rev.* **2009**, *109* (11), 5620–5686.

(107) Buller, A. R.; Townsend, C. A. Intrinsic Evolutionary Constraints on Protease Structure, Enzyme Acylation, and the Identity of the Catalytic Triad. *Proc. Natl. Acad. Sci. U. S. A.* **2013**, *110* (8), E653-61.

(108) Singh, S.; Topuz, F.; Hahn, K.; Albrecht, K.; Groll, J. Embedding of Active Proteins and Living Cells in Redox-Sensitive Hydrogels and Nanogels through Enzymatic Cross-Linking. *Angew. Chemie - Int. Ed.* **2013**, *52* (10), 3000–3003.

(109) Burns, J. A.; Butler, J. C.; Moran, J.; Whitesides, G. M. Selective Reduction of Disulfides by Tris(2-Carboxyethyl)Phosphine. *J. Org. Chem.* **1991**, *56* (8), 2648–2650.

(110) Lukesh, J. C.; Palte, M. J.; Raines, R. T. A Potent, Versatile Disulfide-

Reducing Agent from Aspartic Acid. *J. Am. Chem. Soc.* **2012**, *134* (9), 4057–4059.

(111) Singh, R.; Whitesides, G. M. *Thiol-Disulfide Interchange*; John Wiley & Sons, Ltd: Hoboken, New Jersey, 1993.

(112) Singh, R.; Whitesides, G. M. Comparisons of Rate Constants for Thiolate-Disulfide Interchange in Water and in Polar Aprotic Solvents Using Dynamic 1H NMR Line Shape Analysis. *J. Am. Chem. Soc.* **1990**, *112* (3), 1190–1197.

(113) Azcune, I.; Odriozola, I. Aromatic Disulfide Crosslinks in Polymer Systems: Self-Healing, Reprocessability, Recyclability and More. *Eur. Polym. J.* **2016**, *84*, 147–160.

(114) Caraballo, R.; Rahm, M.; Vongvilai, P.; Brinck, T.; Ramström, O. Phosphine-Catalyzed Disulfide Metathesis. *Chem. Commun.* **2008**, No. 48, 6603–6605.

(115) Caraballo, R.; Sakulsombat, M.; Ramström, O. Phosphine-Mediated Disulfide Metathesis in Aqueous Media. *Chem. Commun.* **2010**, *46* (44), 8469–8471.

(116) Arisawa, M.; Yamaguchi, M. Rhodium-Catalyzed Disulfide Exchange Reaction. *J. Am. Chem. Soc.* **2003**, *125* (22), 6624–6625.

(117) Dénès, F.; Pichowicz, M.; Povie, G.; Renaud, P. Thiyl Radicals in Organic Synthesis. *Chem. Rev.* **2014**, *114* (5), 2587–2693.

(118) Fritze, U. F.; Von Delius, M. Dynamic Disulfide Metathesis Induced by Ultrasound. *Chem. Commun.* **2016**, *52* (38), 6363–6366.

(119) Gorman, C. B.; Folkers, J. P.; Nuzzo, R. G.; Whitesides, G. M.; Buchholz, S.; Laibinis, P. E. Self-Assembled Monolayers of Long-Chain Hydroxamic Acids on the Native Oxide of Metals. *Langmuir* **2005**, *11* (3), 813–824.

(120) Mercier, L.; Pinnavaia, T. J. Access in Mesoporous Materials: Advantages of a Uniform Pore Structure in the Design of a Heavy Metal Ion Adsorbent for Environmental Remediation. *Adv. Mater.* **1997**, *9* (6), 500–503.

(121) Sato, K.; Hosokawa, K.; Maeda, M. Rapid Aggregation of Gold Nanoparticles Induced by Non-Cross-Linking DNA Hybridization. *J. Am. Chem. Soc.* **2003**, *125* (27), 8102–8103.

(122) Merí-Bofí, L.; Royuela, S.; Zamora, F.; Ruiz-González, M. L.; Segura, J. L.; Muñoz-Olivas, R.; Mancheño, M. J. Thiol Grafted Imine-Based Covalent Organic Frameworks for Water Remediation through Selective Removal of Hg(II). *J. Mater. Chem. A* **2017**, *5* (34), 17973–17981.

(123) Brear, P.; Freeman, G. R.; Shankey, M. C.; Trmcić, M.; Hodgson, D. R. W. Aqueous Methods for the Preparation of 5′-Substituted Guanosine Derivatives. *Chem. Commun.* **2009**, No. 33, 4980–4981.

(124) Marriott, J. H.; Mottahedeh, M.; Reese, C. B. 9-(4-Methoxyphenyl)Xanthen-9-Thiol: A Useful Reagent for the Preparation of Thiols. *Tetrahedron Lett.* **1990**, *31* (51), 7485–7488.

(125) Reist, E. J.; Benitez, A.; Goodman, L. The Synthesis of Some 5′-Thiopentofuranosylpyrimidines. *J. Org. Chem.* **1964**, *29* (3), 554–558.

(126) Li, N. S.; Frederiksen, J. K.; Koo, S. C.; Lu, J.; Wilson, T. J.; Lilley, D. M. J.; Piccirilli, J. A. A General and Efficient Approach for the Construction of RNA Oligonucleotides Containing a 5′-Phosphorothiolate Linkage. *Nucleic Acids Res.* **2011**, *39* (5), e31–e31.

(127) Peters, G. M.; Skala, L. P.; Plank, T. N.; Oh, H.; Manjunatha Reddy, G. N.;

Marsh, A.; Brown, S. P.; Raghavan, S. R.; Davis, J. T. G4-Quartet·M^+ Borate Hydrogels. *J. Am. Chem. Soc.* **2015**, *137* (17), 5819–5827.

(128) Manso, J. A.; Céspedes Camacho, I. F.; Calle, E.; Casado, J. Alkylating Potential of α,β-Unsaturated Compounds. *Org. Biomol. Chem.* **2011**, *9* (18), 6226.

(129) Rinaldi, R.; Branca, E.; Cingolani, R.; Masiero, S.; Spada, G. P.; Gottarelli, G. Photodetectors Fabricated from a Self-Assembly of a Deoxyguanosine Derivative. *Appl. Phys. Lett.* **2001**, *78* (22), 3541–3543.

(130) Randazzo, A.; Spada, G. P.; Da Silva, M. W. Circular Dichroism of Quadruplex Structures. In *Topics in Current Chemistry*; Springer, Berlin, Heidelberg, 2013; Vol. 330, pp 67–86.

(131) Peters, G. M.; Skala, L. P.; Plank, T. N.; Oh, H.; Manjunatha Reddy, G. N.; Marsh, A.; Brown, S. P.; Raghavan, S. R.; Davis, J. T. G4-Quartet·M+ Borate Hydrogels. *J. Am. Chem. Soc.* **2015**, *137* (17), 5819–5827.

(132) Cadet, J.; Douki, T.; Gasparutto, D.; Ravanat, J. L. Oxidative Damage to DNA: Formation, Measurement and Biochemical Features. *Mutat. Res. - Fundam. Mol. Mech. Mutagen.* **2003**, *531* (1–2), 5–23.

(133) Cho, B. P.; Kadlubar, F. F.; Culp, S. J.; Evans, F. E. 15N Nuclear Magnetic Resonance Studies on the Tautomerism of 8-Hydroxy-2'-Deoxyguanosine, 8-Hydroxyguanosine, and Other Os-Substituted Guanine Nucleosides. *Chem. Res. Toxicol.* **1990**, *3* (5), 445–452.

(134) Giorgi, T.; Lena, S.; Mariani, P.; Cremonini, M. A.; Masiero, S.; Pieraccini, S.; Rabe, J. P.; Samori, P.; Spada, G. P.; Gottarelli, G. Supramolecular Helices via

Self-Assembly of 8-Oxoguanosines. *J. Am. Chem. Soc.* **2003**, *125* (48), 14741–14749.

(135) Giorgio, S.; Barão, S. C.; Augusto, O.; Kwee, J. K. Leishmania Amazonensis Infection Is Reduced in Macrophages Treated with Guanine Ribonucleosides. *Acta Trop.* **1998**, *70* (1), 119–122.

(136) Hikida, M.; Takai, T.; Ohmori, H. Requirements of a Costimulus for IL-4-Induced IgE Class Switching in Murine B Cells Activated via Antigen Receptors: Effectiveness of 8-Mercaptoguanosine. *J. Immunol.* **1996**, *156* (8), 2730–2736.

(137) Goodman, M. G.; Weigle, W. O. Derivatized Guanine Nucleosides: A New Class of Adjuvant for in Vitro Antibody Responses. *J. Immunol.* **1983**, *130* (6), 2580–2585.

(138) Tsukamoto, Y.; Uehara, S.; Mizoguchi, C.; Sato, A.; Horikawa, K.; Takatsu, K. Requirement of 8-Mercaptoguanosine as a Costimulus for IL-4-Dependent μ to Γ1 Class Switch Recombination in CD38-Activated B Cells. *Biochem. Biophys. Res. Commun.* **2005**, *336* (2), 625–633.

(139) Nishida, M.; Sawa, T.; Kitajima, N.; Ono, K.; Inoue, H.; Ihara, H.; Motohashi, H.; Yamamoto, M.; Suematsu, M.; Kurose, H.; et al. Hydrogen Sulfide Anion Regulates Redox Signaling via Electrophile Sulfhydration. *Nat. Chem. Biol.* **2012**, *8* (8), 714–724.

(140) Ida, T.; Sawa, T.; Ihara, H.; Tsuchiya, Y.; Watanabe, Y.; Kumagai, Y.; Suematsu, M.; Motohashi, H.; Fujii, S.; Matsunaga, T.; et al. Reactive Cysteine Persulfides and S-Polythiolation Regulate Oxidative Stress and Redox

Signaling. *Proc. Natl. Acad. Sci. U. S. A.* **2014**, *111* (21), 7606–7611.

(141) Sawa, T.; Zaki, M. H.; Okamoto, T.; Akuta, T.; Tokutomi, Y.; Kim-Mitsuyama, S.; Ihara, H.; Kobayashi, A.; Yamamoto, M.; Fujii, S.; et al. Protein S-Guanylation by the Biological Signal 8-Nitroguanosine 3′,5′-Cyclic Monophosphate. *Nat. Chem. Biol.* **2007**, *3* (11), 727–735.

(142) Saito, Y.; Taguchi, H.; Fujii, S.; Sawa, T.; Kida, E.; Kabuto, C.; Akaike, T.; Arimoto, H. 8-Nitroguanosines as Chemical Probes of the Protein S-Guanylation. *Chem. Commun.* **2008**, No. 45, 5984–5986.

(143) Hwu, J. R.; Huang, W. C.; Lin, S. Y.; Tan, K. T.; Hu, Y. C.; Shieh, F. K.; Bachurin, S. O.; Ustyugov, A.; Tsay, S. C. Chikungunya Virus Inhibition by Synthetic Coumarin–Guanosine Conjugates. *Eur. J. Med. Chem.* **2019**, *166*, 136–143.

(144) Abbott, D. W.; Woods, C. Carbon-13, Phosphorus-31, and Proton Nmr Studies of the Interactions of the Carbonyibis(Triphenyiphosphine) Rhodium (I) Cation with Base Pairs of 6-Mercaptoguanosine and 8-Mercaptoguanosine with Cytidine. *Inorg. Chem.* **1984**, *23* (22), 3626–3629.

(145) Norris, A. R.; Kumar, R.; Buncel, E. Metal Ion-Biomolecule Interactions. VIII. Methylmercury(II) Complexes of 8-Thioguanosine. Synthesis and Spectroscopic Investigations. *J. Inorg. Biochem.* **1984**, *22* (1), 11–20.

(146) Aragoni, M. C.; Arca, M.; Demartin, F.; Devillanova, F. A.; Garau, A.; Isaia, F.; Lippolis, V.; Veranit, G. Anti-Thyroid Drug Methimazole: X-Ray Characterization of Two Novel Ionic Disulfides Obtained from Its Chemical Oxidation by I2. *J. Am. Chem. Soc.* **2002**, *124* (17), 4538–4539.

(147) Cheong, K. K.; Fu, Y. C.; Robins, R. K.; Eyring, H. Absorption, Optical Rotatory Dispersion, and Circular Dichroism Studies on Some Sulfur-Containing Ribonucleosides. *J. Phys. Chem.* **1969**, *73* (12), 4219–4227.

(148) Sugihara, A.; Uemura, K.; Matsuura, Y.; Tanaka, N.; Ashida, T.; Kakudo, M.; IUCr. The Crystal Structure of L-Ergothioneine Dihydrate, C9H15N3O2S.2H2O. *Acta Crystallogr. Sect. B Struct. Crystallogr. Cryst. Chem.* **1976**, *32* (1), 181–185.

(149) Elcombe, M. M.; Taylor, J. C. A Neutron Diffraction Determination of the Crystal Structures of Thiourea and Deuterated Thiourea above and below the Ferroelectric Transition. *Acta Crystallogr. Sect. A* **1968**, *24* (4), 410–420.

(150) Thewalt, U.; Bugg, C. E.; Marsh, R. E. The Crystal Structure of Guanosine Dihydrate and Inosine Dihydrate. *Acta Crystallogr. B.* **1970**, *26* (8), 1089–1101.

(151) Tavale, S. S.; Sobell, H. M. Crystal and Molecular Structure of 8-Bromoguanosine and 8-Bromoadenosine, Two Purine Nucleosides in the Syn Conformation. *J. Mol. Biol.* **1970**, *48* (1), 109–123.

(152) Birnbaum, G. I.; Lassota, P.; Shugar, D. 8-Chloroguanosine: Solid-State and Solution Conformations and Their Biological Implications. *Biochemistry* **1984**, *23* (21), 5048–5053.

(153) Buerkle, L. E.; von Recum, H. A.; Rowan, S. J. Toward Potential Supramolecular Tissue Engineering Scaffolds Based on Guanosine Derivatives. *Chem. Sci.* **2012**, *3* (2), 564.

(154) BielskutėĖ, S.; Plavec, J.; Podbevšek, P. Impact of Oxidative Lesions on the

Human Telomeric G-Quadruplex. *J. Am. Chem. Soc.* **2019**, *141* (6), 2594–2603.

(155) Abbott, D. W.; Woods, C. Carbon-13 and Phosphorus-31 NMR Studies of Interactions of Organorhodium Complexes with Guanosine, Inosme, 6-Mercaptoguanosine, and 8-Mercaptoguanosine in Neutral and Basic Dimethyl-D6 Sulfoxide Solutions. *Inorg. Chem.* **1983**, *22* (13), 1918–1924.

(156) Heitner, H. I.; Lippard, S. J.; Sunshine, H. R. Metal Binding by Thionucleosides. *J. Am. Chem. Soc.* **1972**, *94* (25), 8936–8937.

(157) Araki, K.; Takasawa, R.; Yoshikawa, I. Design, Fabrication, and Properties of Macroscale Supramolecular Fibers Consisted of Fully Hydrogen-Bonded Pseudo-Polymer Chains. *Chem. Commun.* **2001**, No. 18, 1826–1827.

(158) Sessler, J.; Sathiosatham, M.; Doerr, K.; Lynch, V.; Abboud, K. A G-Quartet Formed in the Absence of a Templating Metal Cation: A New 8-(N,N-Dimethylaniline)Guanosine Derivative This Work Was Supported by the Robert A. Welch Foundation. We Thank Dr. Ben Shoulders and the Staff at the NMR Facility at the University Of. *Angew. Chem. Int. Ed. Engl.* **2000**, *39* (7), 1300–1303.

(159) Boyle, P. D.; Godfrey, S. M. The Reactions of Sulfur and Selenium Donor Molecules with Dihalogens and Interhalogens. *Coord. Chem. Rev.* **2001**, *223* (1), 265–299.

(160) Freeman, F.; Ziller, J. W.; Po, H. N.; Keindl, M. C. Reactions of Imidazole-2-Thiones with Molecular Iodine and the Structures of Two Crystalline Modifications of the 1:1 1, 3-Dimethylimidazole-2-Thione-Diiodine Charge-

Transfer Complex (C 5 H 8 I 2 N 2 S). *J. Am. Chem. Soc.* **1988**, *110* (8), 2586–2591.

(161) Laurence, C.; El Ghomari, M. J.; Le Questel, J. Y.; Berthelot, M.; Mokhlisse, R. Structure and Molecular Interactions of Anti-Thyroid Drugs. Part 3. Methimazole: A Diiodine Sponge. *J. Chem. Soc. Perkin Trans. 2* **1998**, No. 7, 1545–1551.

(162) Ji, S.; Cao, W.; Yu, Y.; Xu, H. Dynamic Diselenide Bonds: Exchange Reaction Induced by Visible Light without Catalysis. *Angew. Chemie - Int. Ed.* **2014**, *53* (26), 6781–6785.

(163) Ji, S.; Cao, W.; Yu, Y.; Xu, H. Visible-Light-Induced Self-Healing Diselenide-Containing Polyurethane Elastomer. *Adv. Mater.* **2015**, *27* (47), 7740–7745.

(164) Cao, W.; Wang, L.; Xu, H. Selenium/Tellurium Containing Polymer Materials in Nanobiotechnology. *Nano Today* **2015**, *10* (6), 717–736.

(165) Chu, S. H.; Shiue, C. Y.; Chu, M. Y. Synthesis and Biological Activity of Some 8-Substituted Selenoguanosine Cyclic 3′,5′-Phosphates and Related Compounds. *J. Med. Chem.* **1975**, *18* (6), 559–564.

(166) Galmarini, C. M.; Mackey, J. R.; Dumontet, C. Nucleoside Analogues and Nucleobases in Cancer Treatment. *Lancet Oncol.* **2002**, *3* (7), 415–424.

(167) Balfour, H. H. Antiviral Drugs. *N. Engl. J. Med.* **1999**, *340* (16), 1255–1268.

(168) Shoemaker, R. H. The NCI60 Human Tumour Cell Line Anticancer Drug Screen. *Nat. Rev. Cancer* **2006**, *6* (10), 813–823.

(169) Hirst, A. R.; Escuder, B.; Miravet, J. F.; Smith, D. K. High-Tech Applications of Self-Assembling Supramolecular Nanostructured Gel-Phase Materials:

From Regenerative Medicine to Electronic Devices. *Angew. Chemie - Int. Ed.* **2008**, *47* (42), 8002–8018.

(170) Jones, C. D.; Steed, J. W. Gels with Sense: Supramolecular Materials That Respond to Heat, Light and Sound. *Chem. Soc. Rev.* **2016**, *45* (23), 6546–6596.

(171) Okesola, B. O.; Smith, D. K. Applying Low-Molecular Weight Supramolecular Gelators in an Environmental Setting – Self-Assembled Gels as Smart Materials for Pollutant Removal. *Chem. Soc. Rev.* **2016**, *45* (15), 4226–4251.

(172) Buerkle, L. E.; Rowan, S. J. Supramolecular Gels Formed from Multi-Component Low Molecular Weight Species. *Chem. Soc. Rev.* **2012**, *41* (18), 6089–6102.

(173) Santacroce, P. V.; Okunola, O. A.; Zavalij, P. Y.; Davis, J. T. A Transmembrane Anion Transporter Selective for Nitrate over Chloride. *Chem. Commun. (Camb).* **2006**, *0* (30), 3246–3248.

(174) Dash, J.; Saha, P. Functional Architectures Derived from Guanine Quartets. *Org. Biomol. Chem.* **2016**, *14* (7), 2157–2163.

(175) Mihai, S.; Le Duc, Y.; Cot, D.; Barboiu, M. Sol-Gel Selection of Hybrid G-Quadruplex Architectures from Dynamic Supramolecular Guanosine Libraries. *J. Mater. Chem.* **2010**, *20* (42), 9443–9448.

(176) Das, R. N.; Kumar, Y. P.; Pagoti, S.; Patil, A. J.; Dash, J. Diffusion and Birefringence of Bioactive Dyes in a Supramolecular Guanosine Hydrogel. *Chem. - A Eur. J.* **2012**, *18* (19), 6008–6014.

(177) Belda, R.; García-España, E.; Morris, G. A.; Steed, J. W.; Aguilar, J. A.

Guanosine-5′-Monophosphate Polyamine Hybrid Hydrogels: Enhanced Gel Strength Probed by z-Spectroscopy. *Chem. - A Eur. J.* **2017**, *23* (32), 7755–7760.

(178) Shi, X.; Fettinger, J. C.; Davis, J. T. Homochiral G-Quadruplexes with Ba^{2+} but Not with K^{+}: The Cation Programs Enantiomeric Self-Recognition. *J. Am. Chem. Soc.* **2001**, *123* (27), 6738–6739.

(179) Shi, X.; Mullaugh, K. M.; Fettinger, J. C.; Jiang, Y.; Hofstadler, S. a.; Davis, J. T. Lipophilic G-Quadruplexes Are Self-Assembled Ion Pair Receptors, and the Bound Anion Modulates the Kinetic Stability of These Complexes. *J. Am. Chem. Soc.* **2003**, *125* (36), 10830–10841.

(180) González-Rodríguez, D.; Van Dongen, J. L. J.; Lutz, M.; Spek, A. L.; Schenning, A. P. H. J.; Meijer, E. W. G-Quadruplex Self-Assembly Regulated by Coulombic Interactions. *Nat. Chem.* **2009**, *1* (2), 151–155.

(181) Betancourt, J. E.; Rivera, J. M. Tuning Thermoresponsive Supramolecular G-Quadruplexes. *Langmuir* **2015**, *31* (7), 2095–2103.

(182) Betancourt, J. E.; Rivera, J. M. Nonpolymeric Thermosensitive Supramolecules. *J. Am. Chem. Soc.* **2009**, *131* (46), 16666–16668.

(183) Plank, T. N.; Davis, J. T. A G4·K+ Hydrogel That Self-Destructs. *Chem. Commun.* **2016**, *52* (28), 5037–5040.

(184) Venkatesh, V.; Mishra, N. K.; Romero-Canelón, I.; Vernooij, R. R.; Shi, H.; Coverdale, J. P. C.; Habtemariam, A.; Verma, S.; Sadler, P. J. Supramolecular Photoactivatable Anticancer Hydrogels. *J. Am. Chem. Soc.* **2017**, *139* (16), 5656–5659.

(185) Rotaru, A.; Pricope, G.; Plank, T. N.; Clima, L.; Ursu, E. L.; Pinteala, M.; Davis, J. T.; Barboiu, M. G-Quartet Hydrogels for Effective Cell Growth Applications. *Chem. Commun.* **2017**, *53* (94), 12668–12671.

(186) Bhattacharyya, T.; Kumar, Y. P.; Dash, J. Supramolecular Hydrogel Inspired from DNA Structures Mimics Peroxidase Activity. *ACS Biomater. Sci. Eng.* **2017**, *3* (10), 2358–2365.

(187) Zhong, R.; Tang, Q.; Wang, S.; Zhang, H.; Zhang, F.; Xiao, M.; Man, T.; Qu, X.; Li, L.; Zhang, W.; et al. Self-Assembly of Enzyme-Like Nanofibrous G-Molecular Hydrogel for Printed Flexible Electrochemical Sensors. *Adv. Mater.* **2018**, *30* (12), 1706887.

(188) Buhler, E.; Sreenivasachary, N.; Candau, S. J.; Lehn, J. M. Modulation of the Supramolecular Structure of G-Quartet Assemblies by Dynamic Covalent Decoration. *J. Am. Chem. Soc.* **2007**, *129* (33), 10058–10059.

(189) Hinman, R. L. Base Strengths of Some Alkylhydrazines. *J. Org. Chem.* **1958**, *23* (10), 1587–1588.

(190) Edwards, J. O.; Pearson, R. G. The Factors Determining Nucleophilic Reactivities. *J. Am. Chem. Soc.* **1962**, *84*, 16–24.

(191) Jencks, W. P.; Gilchrist, M. General Base Catalysis of the Aminolysis of Phenyl Acetate by Primary Alkylamines [1]. *J. Am. Chem. Soc.* **1966**, *88* (1), 104–108.

(192) Jencks, W. P. Mechanism and Catalysis of Simple Carbonyl Group Reactions. In *Progress in Physical Organic Chemistry*; 1964; Vol. 2, pp 63–68.

(193) Kool, E. T.; Park, D. H.; Crisalli, P. Fast Hydrazone Reactants: Electronic and

Acid/Base Effects Strongly Influence Rate at Biological PH. *J. Am. Chem. Soc.* **2013**, *135* (47), 17663–17666.

(194) Hirst, A. R.; Coates, I. A.; Boucheteau, T. R.; Miravet, J. F.; Escuder, B.; Castelletto, V.; Hamley, I. W.; Smith, D. K. Low-Molecular-Weight Gelators: Elucidating the Principles of Gelation Based on Gelator Solubility and a Cooperative Self-Assembly Model. *J. Am. Chem. Soc.* **2008**, *130* (28), 9113–9121.

(195) Setnička, V.; Urbanová, M.; Volka, K.; Nampally, S.; Lehn, J. M. Investigation of Guanosine-Quartet Assemblies by Vibrational and Electronic Circular Dichroism Spectroscopy, a Novel Approach for Studying Supramolecular Entities. *Chem. - A Eur. J.* **2006**, *12* (34), 8735–8743.

(196) Mezzina, E.; Mariani, P.; Itri, R.; Masiero, S.; Pieraccini, S.; Spada, G. P.; Spinozzi, F.; Davis, J. T.; Gottarelli, G. The Self-Assembly of a Lipophilic Guanosine Nucleoside into Polymeric Columnar Aggregates: The Nucleoside Strucutre Contains Sufficient Information to Drive the Process towards a Strikingly Regular Polymer. *Chemistry* **2001**, *7* (2), 388–395.

(197) Gottarelli, G.; Masiero, S.; Spada, G. P. The Use of CD Spectroscopy for the Study of the Self-Assembly of Guanine Derivatives. *Enantiomer* **1998**, *3*, 429–438.

(198) Yu, G.; Yan, X.; Han, C.; Huang, F. Characterization of Supramolecular Gels. *Chem. Soc. Rev.* **2013**, *42* (16), 6697–6722.

(199) Parkinson, G. N.; Lee, M. P. H.; Neidle, S. Crystal Structure of Parallel Quadruplexes from Human Telomeric DNA. *Nature* **2002**, *417* (6891), 876–

880.

(200) Menger, F. M. Supramolecular Chemistry and Self-Assembly. *Proc. Natl. Acad. Sci.* **2002**, *99* (8), 4818–4822.

(201) Stupp, S. I.; Palmer, L. C. Supramolecular Chemistry and Self-Assembly in Organic Materials Design. *Chem. Mater.* **2014**, *26* (1), 507–518.

(202) Elacqua, E.; Zheng, X.; Shillingford, C.; Liu, M.; Weck, M. Molecular Recognition in the Colloidal World. *Acc. Chem. Res.* **2017**, *50* (11), 2756–2766.

(203) Brown, M. A.; De Vito, S. C. Predicting Azo Dye Toxicity. *Crit. Rev. Environ. Sci. Technol.* **1993**, *23* (3), 249–324.

(204) Proudfoot, A. T.; Bradberry, S. M.; Vale, J. A. Sodium Fluoroacetate Poisoning. *Toxicol. Rev.* **2006**, *25* (4), 213–219.

(205) Sreenivasachary, N.; Lehn, J. M. Structural Selection in G-Quartet-Based Hydrogels and Controlled Release of Bioactive Molecules. *Chem. - An Asian J.* **2008**, *3* (1), 134–139.

(206) Lopachin, R. M.; Gavin, T. Molecular Mechanisms of Aldehyde Toxicity: A Chemical Perspective. *Chem. Res. Toxicol.* **2014**, *27* (7), 1081–1091.

(207) Draper, E. R.; Adams, D. J. Low-Molecular-Weight Gels: The State of the Art. *Chem* **2017**, *3* (3), 390–410.

(208) Veits, G. K.; Carter, K. K.; Cox, S. J.; McNeil, A. J. Developing a Gel-Based Sensor Using Crystal Morphology Prediction. *J. Am. Chem. Soc.* **2016**, *138* (37), 12228–12233.

(209) Basak, S.; Nandi, N.; Paul, S.; Hamley, I. W.; Banerjee, A. A Tripeptide-Based

Self-Shrinking Hydrogel for Waste-Water Treatment: Removal of Toxic Organic Dyes and Lead (Pb 2+) Ions. *Chem. Commun.* **2017**, *53* (43), 5910–5913.

(210) Wang, Y.; Zhu, Y.; Hu, Y.; Zeng, G.; Zhang, Y.; Zhang, C.; Feng, C. How to Construct DNA Hydrogels for Environmental Applications: Advanced Water Treatment and Environmental Analysis. *Small* **2018**, *14* (17), 1703305.

(211) Pu, F.; Ren, J.; Qu, X. Nucleobases, Nucleosides, and Nucleotides: Versatile Biomolecules for Generating Functional Nanomaterials. *Chem. Soc. Rev.* **2018**, *47* (4), 1285–1306.

(212) Biswas, A.; Malferrari, S.; Kalaskar, D. M.; Das, A. K. Arylboronate Esters Mediated Self-Healable and Biocompatible Dynamic G-Quadruplex Hydrogels as Promising 3D-Bioinks. *Chem. Commun.* **2018**, *54* (14), 1778–1781.

(213) Zhong, R.; Xiao, M.; Zhu, C.; Shen, X.; Tang, Q.; Zhang, W.; Wang, L.; Song, S.; Qu, X.; Pei, H.; et al. Logic Catalytic Interconversion of G-Molecular Hydrogel. *ACS Appl. Mater. Interfaces* **2018**, *10* (5), 4512–4518.

(214) Enders, D.; Kirchhoff, J. H.; Köbberling, J.; Peiffer, T. H. Asymmetric Synthesis of α-Branched Primary Amines on Solid Support via Novel Hydrazine Resins. *Org. Lett.* **2001**, *3* (8), 1241–1244.

(215) Baxendale, I. R.; Ley, S. V.; Sneddon, H. F. A Clean Conversion of Aldehydes to Nitriles Using a Solid-Supported Hydrazine. *Synlett* **2002**, *2002* (05), 0775–0777.

(216) Zhu, M.; Ruijter, E.; Wessjohann, L. A. New Scavenger Resin for the Reversible Linking and Monoprotection of Functionalized Aromatic

Aldehydes. *Org. Lett.* **2004**, *6* (22), 3921–3924.

(217) Kecili, R.; Nivhede, D.; Billing, J.; Leeman, M.; Sellergren, B.; Yilmaz, E. Removal of Acrolein from Active Pharmaceutical Ingredients Using Aldehyde Scavengers. *Org. Process Res. Dev.* **2012**, *16* (6), 1225–1229.

(218) Kalia, J.; Raines, R. T. Reactivity of Intein Thioesters: Appending a Functional Group to a Protein. *ChemBioChem* **2006**, *7* (9), 1375–1383.

(219) Varghese, B.; Al-Busafi, S. N.; Suliman, F. O.; Al-Kindy, S. M. Z. Unveiling a Versatile Heterocycle: Pyrazoline-a Review. *RSC Adv.* **2017**, *7* (74), 46999–47016.

(220) Lou, J.; Liu, F.; Lindsay, C. D.; Chaudhuri, O.; Heilshorn, S. C.; Xia, Y. Dynamic Hyaluronan Hydrogels with Temporally Modulated High Injectability and Stability Using a Biocompatible Catalyst. *Adv. Mater.* **2018**, *30* (22), 1705215.

(221) Azagarsamy, M. A.; Marozas, I. A.; Spaans, S.; Anseth, K. S. Photoregulated Hydrazone-Based Hydrogel Formation for Biochemically Patterning 3D Cellular Microenvironments. *ACS Macro Lett.* **2016**, *5* (1), 19–23.

(222) Purcell, B. P.; Lobb, D.; Charati, M. B.; Dorsey, S. M.; Wade, R. J.; Zellars, K. N.; Doviak, H.; Pettaway, S.; Logdon, C. B.; Shuman, J. A.; et al. Injectable and Bioresponsive Hydrogels for On-Demand Matrix Metalloproteinase Inhibition. *Nat. Mater.* **2014**, *13* (6), 653–661.

(223) Zhu, Q.; Sun, Z.; Jiang, Y.; Chen, F.; Wang, M. Acrolein Scavengers: Reactivity, Mechanism and Impact on Health. *Mol. Nutr. Food Res.* **2011**, *55* (9), 1375–1390.

(224) Burcham, P. C. Acrolein and Human Disease: Untangling the Knotty Exposure Scenarios Accompanying Several Diverse Disorders. *Chem. Res. Toxicol.* **2017**, *30* (1), 145–161.

(225) Burcham, P. C. Carbonyl Scavengers as Pharmacotherapies in Degenerative Disease: Hydralazine Repurposing and Challenges in Clinical Translation. *Biochem. Pharmacol.* **2018**, *154*, 397–406.

(226) Park, J.; Muratori, B.; Shi, R. Acrolein as a Novel Therapeutic Target for Motor and Sensory Deficits in Spinal Cord Injury. *Neural Regen. Res.* **2014**, *9* (7), 677–683.

(227) Fox, R. J.; Markwalter, C. E.; Lawler, M.; Zhu, K.; Albrecht, J.; Payack, J.; Eastgate, M. D. Development of Scalable Processes for the Preparation of N-Methyl-3-Bromo-5-Methyl Pyrazole. *Org. Process Res. Dev.* **2017**, *21* (5), 754–762.

(228) Chouhan, G.; Alper, H. Synthesis of Ring-Fused Oxazolo- and Pyrazoloisoquinolinones by a One-Pot Pd-Catalyzed Carboxamidation and Aldol-Type Condensation Cascade Process. *J. Org. Chem.* **2009**, *74* (16), 6181–6189.

(229) LoPachin, R. M.; Gavin, T.; Petersen, D. R.; Barber, D. S. Molecular Mechanisms of 4-Hydroxy-2-Nonenal and Acrolein Toxicity: Nucleophilic Targets and Adduct Formation. *Chem. Res. Toxicol.* **2009**, *22* (9), 1499–1508.

(230) Kozekov, I. D.; Nechev, L. V.; Moseley, M. S.; Harris, C. M.; Rizzo, C. J.; Stone, M. P.; Harris, T. M. DNA Interchain Cross-Links Formed by Acrolein and Crotonaldehyde. *J. Am. Chem. Soc.* **2003**, *125* (1), 50–61.

(231) Li, H.; Wang, J.; Kaphalia, B. S.; Ansari, G. A. S.; Khan, M. F. Quantitation of Acrolein–Protein Adducts: Potential Biomarker of Acrolein Exposure. *J. Toxicol. Environ. Heal. - Part A* **2004**, *67* (6), 513–524.

(232) Feng, Z.; Hu, W.; Hu, Y.; Tang, M. S. Acrolein Is a Major Cigarette-Related Lung Cancer Agent: Preferential Binding at P53 Mutational Hotspots and Inhibition of DNA Repair. *Proc. Natl. Acad. Sci.* **2006**, *103* (42), 15404–15409.

(233) Chen, W. Y.; Zhang, J.; Ghare, S.; Barve, S.; McClain, C.; Joshi-Barve, S. Acrolein Is a Pathogenic Mediator of Alcoholic Liver Disease and the Scavenger Hydralazine Is Protective in Mice. *Cmgh* **2016**, *2* (5), 685–700.

(234) Karabatsos, G. J.; Taller, R. A. Structural Studies by Nuclear Magnetic Resonance. V. Phenylhydrazones. *J. Am. Chem. Soc.* **1963**, *85* (22), 3624–3629.

(235) Allgäuer, D. S.; Jangra, H.; Asahara, H.; Li, Z.; Chen, Q.; Zipse, H.; Ofial, A. R.; Mayr, H. Quantification and Theoretical Analysis of the Electrophilicities of Michael Acceptors. *J. Am. Chem. Soc.* **2017**, *139* (38), 13318–13329.

(236) Yoshii, E. Cytotoxic Effects of Acrylates and Methacrylates: Relationships of Monomer Structures and Cytotoxicity. *J. Biomed. Mater. Res.* **1997**, *37* (4), 517–524.

(237) Reininghaus, W.; Koestner, A.; Klimisch, H. J. Chronic Toxicity and Oncogenicity of Inhaled Methyl Acrylate and N-Butyl Acrylate in Sprague-Dawley Rats. *Food Chem. Toxicol.* **1991**, *29* (5), 329–339.

(238) Nigst, T. A.; Ammer, J.; Mayr, H. Ambident Reactivities of Methylhydrazines.

Angew. Chemie - Int. Ed. **2012**, *51* (6), 1353–1356.

(239) Amabilino, D. B.; Smith, D. K.; Steed, J. W. Supramolecular Materials. *Chem. Soc. Rev.* **2017**, *46* (9), 2404–2420.

(240) Chivers, P. R. A.; Smith, D. K. Shaping and Structuring Supramolecular Gels. *Nat. Rev. Mater.* **2019**, *4* (7), 463–478.

(241) Matsumoto, S.; Yamaguchi, S.; Ueno, S.; Komatsu, H.; Ikeda, M.; Ishizuka, K.; Iko, Y.; Tabata, K. V.; Aoki, H.; Ito, S.; et al. Photo Gel-Sol/Sol-Gel Transition and Its Patterning of a Supramolecular Hydrogel as Stimuli-Responsive Biomaterials. *Chem. - A Eur. J.* **2008**, *14* (13), 3977–3986.

(242) Maity, C.; Hendriksen, W. E.; Van Esch, J. H.; Eelkema, R. Spatial Structuring of a Supramolecular Hydrogel by Using a Visible-Light Triggered Catalyst. *Angew. Chemie - Int. Ed.* **2015**, *54* (3), 998–1001.

(243) Draper, E. R.; Eden, E. G. B.; McDonald, T. O.; Adams, D. J. Spatially Resolved Multicomponent Gels. *Nat. Chem.* **2015**, *7* (10), 848–852.

(244) Wang, Y.; Oldenhof, S.; Versluis, F.; Shah, M.; Zhang, K.; van Steijn, V.; Guo, X.; Eelkema, R.; van Esch, J. H. Controlled Fabrication of Micropatterned Supramolecular Gels by Directed Self-Assembly of Small Molecular Gelators. *Small* **2019**, *15* (8), 1804154.

(245) Peng, X.; Liu, T.; Zhang, Q.; Shang, C.; Bai, Q. W.; Wang, H. Surface Patterning of Hydrogels for Programmable and Complex Shape Deformations by Ion Inkjet Printing. *Adv. Funct. Mater.* **2017**, *27* (33), 1701962.

(246) Arnal-Hérault, C.; Banu, A.; Barboiu, M.; Michau, M.; Van Der Lee, A.; van der Lee, A. Amplification and Transcription of the Dynamic Supra-Molecular

Chirality of the Guanine Quadruplex. *Angew. Chemie - Int. Ed.* **2007**, *46* (23), 4268–4272.

(247) Howe, R. C. T.; Smalley, A. P.; Guttenplan, A. P. M.; Doggett, M. W. R.; Eddleston, M. D.; Tan, J. C.; Lloyd, G. O. A Family of Simple Benzene 1,3,5-Tricarboxamide (BTA) Aromatic Carboxylic Acid Hydrogels. *Chem. Commun.* **2013**, *49* (39), 4268–4270.

(248) Zhang, S.; Bellinger, A. M.; Glettig, D. L.; Barman, R.; Lee, Y. A. L.; Zhu, J.; Cleveland, C.; Montgomery, V. A.; Gu, L.; Nash, L. D.; et al. A PH-Responsive Supramolecular Polymer Gel as an Enteric Elastomer for Use in Gastric Devices. *Nat. Mater.* **2015**, *14* (10), 1065–1071.

(249) Monzyk, B.; Crumbliss, A. L. Acid Dissociation Constants (Ka) and Their Temperature Dependencies (AHa, ASa) for a Series of Carbon- and Nitrogen-Substituted Hydroxamic Acids in Aqueous Solution. *J. Org. Chem.* **1980**, *45* (23), 4670–4675.

(250) Ventura, O. N.; Rama, J. B.; Turi, L.; Dannenberg, J. J. Acidity of Hydroxamic Acids: An Ab Initio and Semiempirical Study. *J. Am. Chem. Soc.* **1993**, *115* (13), 5754–5761.

(251) Codd, R. Traversing the Coordination Chemistry and Chemical Biology of Hydroxamic Acids. *Coord. Chem. Rev.* **2008**, *252* (12–14), 1387–1408.

(252) Abu-Dari, K.; Cooper, S. R.; Raymond, K. N. Coordination Chemistry of Microbial Iron Transport Compounds. 15. Electrochemistry and Magnetic Susceptibility of Iron(III)-Hydroxamate and -Thiohydroxamate Complexes. *Inorg. Chem.* **1978**, *17* (12), 3394–3397.

(253) Powell, P. E.; Cline, G. R.; Reid, C. P. P.; Szaniszlo, P. J. Occurrence of Hydroxamate Siderophore Iron Chelators in Soils. *Nature* **1980**, *287* (5785), 833–834.

(254) Raymond, K. N.; Allred, B. E.; Sia, A. K. Coordination Chemistry of Microbial Iron Transport. *Acc. Chem. Res.* **2015**, *48* (9), 2496–2505.

(255) Cooper, S. R.; McArdle, J. V.; Raymond, K. N. Siderophore Electrochemistry: Relation to Intracellular Iron Release Mechanism. *Proc. Natl. Acad. Sci. U. S. A.* **1978**, *75* (8), 3551–3554.

(256) Crumbliss, A. L.; Boukhalfa, H. Chemical Aspects of Siderophore Mediated Iron Transport. *Biometals* **2002**, *15* (4), 325–339.

(257) Ponce, A.; Brostoff, L. B.; Gibbons, S. K.; Zavalij, P.; Viragh, C.; Hooper, J.; Alnemrat, S.; Gaskell, K. J.; Eichhorn, B. Elucidation of the Fe(III) Gallate Structure in Historical Iron Gall Ink. *Anal. Chem.* **2016**, *88* (10), 5152–5158.

(258) Dai, Q.; Yu, Q.; Tian, Y.; Xie, X.; Song, A.; Caruso, F.; Hao, J.; Cui, J. Advancing Metal–Phenolic Networks for Visual Information Storage. *ACS Appl. Mater. Interfaces* **2019**, *11* (32), 29305–29311.

(259) Polomoscanik, S. C.; Cannon, C. P.; Neenan, T. X.; Holmes-Farley, S. R.; Mandeville, W. H.; Dhal, P. K. Hydroxamic Acid-Containing Hydrogels for Nonabsorbed Iron Chelation Therapy: Synthesis, Characterization, and Biological Evaluation. *Biomacromolecules* **2005**, *6* (6), 2946–2953.

(260) Liu, Z.; Wang, Y.; Purro, M.; Xiong, M. P. Oxidation-Induced Degradable Nanogels for Iron Chelation. *Sci. Rep.* **2016**, *6* (1), 20923.

(261) Johann, T.; Kemmer-Jonas, U.; Barent, R. D.; Frey, H. Multifunctional Fe(III)-

Binding Polyethers from Hydroxamic Acid-Based Epoxide Monomers. *Macromol. Rapid Commun.* **2019**, 1900282.

(262) Epp, J. B.; Widlanski, T. S. Facile Preparation of Nucleoside-5'-Carboxylic Acids. *J. Org. Chem.* **1999**, *64* (1), 293–295.

(263) Isono, Y.; Sudo, T.; Hoshino, M. Properties of a New Enzyme, Nucleoside Oxidase, from Pseudomonas Maltophilia Lb-86. *Agric. Biol. Chem.* **1989**, *53* (6), 1671–1677.

(264) Skene, W. G.; Lehn, J.-M. P. Dynamers: Polyacylhydrazone Reversible Covalent Polymers, Component Exchange, and Constitutional Diversity. *Proc. Natl. Acad. Sci.* **2004**, *101* (22), 8270–8275.

(265) Monchaud, D.; Allain, C.; Bertrand, H.; Smargiasso, N.; Rosu, F.; Gabelica, V.; De Cian, A.; Mergny, J. L.; Teulade-Fichou, M. P. Ligands Playing Musical Chairs with G-Quadruplex DNA: A Rapid and Simple Displacement Assay for Identifying Selective G-Quadruplex Binders. *Biochimie* **2008**, *90* (8), 1207–1223.

(266) Yang, P.; De Cian, A.; Teulade-Fichou, M. P.; Mergny, J. L.; Monchaud, D. Engineering Bisquinolinium/Thiazole Orange Conjugates for Fluorescent Sensing of G-Quadruplex DNA. *Angew. Chemie - Int. Ed.* **2009**, *48* (12), 2188–2191.

(267) Nakayama, S.; Kelsey, I.; Wang, J.; Roelofs, K.; Stefane, B.; Luo, Y.; Lee, V. T.; Sintim, H. O. Thiazole Orange-Induced c-Di-GMP Quadruplex Formation Facilitates a Simple Fluorescent Detection of This Ubiquitous Biofilm Regulating Molecule. *J. Am. Chem. Soc.* **2011**, *133* (13), 4856–4864.

(268) Chiang, Y.; Kresge, A. J. Alkylation of Guanosine and 2′-Deoxyguanosine by o-Quinone α-(p-Anisyl)Methide in Aqueous Solution. *Org. Biomol. Chem.* **2004**, *2* (7), 1090–1092.

(269) Okesola, B. O.; Smith, D. K. Versatile Supramolecular PH-Tolerant Hydrogels Which Demonstrate PH-Dependent Selective Adsorption of Dyes from Aqueous Solution. *Chem. Commun.* **2013**, *49* (95), 11164–11166.

(270) Dhungana, S.; Harrington, J. M.; Gebhardt, P.; Möllmann, U.; Crumbliss, A. L. Iron Chelation Equilibria, Redox, and Siderophore Activity of a Saccharide Platform Ferrichrome Analogue. *Inorg. Chem.* **2007**, *46* (20), 8362–8371.

(271) Hu, K.; Sun, J.; Guo, Z.; Wang, P.; Chen, Q.; Ma, M.; Gu, N. A Novel Magnetic Hydrogel with Aligned Magnetic Colloidal Assemblies Showing Controllable Enhancement of Magnetothermal Effect in the Presence of Alternating Magnetic Field. *Adv. Mater.* **2015**, *27* (15), 2507–2514.

(272) Wang, C. Y.; Lee, L. H. Mutagenicity and Antibacterial Activity of Hydroxamic Acids. *Antimicrob. Agents Chemother.* **1977**, *11* (4), 753–755.

(273) Winston, A.; Kirchner, D. Hydroxamic Acid Polymers. Effect of Structure on the Selective Chelation of Iron in Water. *Macromolecules* **1978**, *11* (3), 597–603.

(274) Waite, J. H.; Birkedal, H.; Holten-Andersen, N.; Harrington, M. J.; Messersmith, P. B.; Lee, K. Y. C.; Lee, B. P. PH-Induced Metal-Ligand Cross-Links Inspired by Mussel Yield Self-Healing Polymer Networks with near-Covalent Elastic Moduli. *Proc. Natl. Acad. Sci.* **2011**, *108* (7), 2651–2655.

(275) Okesola, B. O.; Suravaram, S. K.; Parkin, A.; Smith, D. K. Selective

Extraction and in Situ Reduction of Precious Metal Salts from Model Waste to Generate Hybrid Gels with Embedded Electrocatalytic Nanoparticles. *Angew. Chemie - Int. Ed.* **2016**, *55* (1), 183–187.

(276) Slavík, P.; Kurka, D. W.; Smith, D. K. Palladium-Scavenging Self-Assembled Hybrid Hydrogels-Reusable Highly-Active Green Catalysts for Suzuki-Miyaura Cross-Coupling Reactions. *Chem. Sci.* **2018**, *9* (46), 8673–8681.

(277) Bannwarth, M. B.; Weidner, T.; Eidmann, E.; Landfester, K.; Crespy, D. Reversible Redox-Responsive Assembly/Disassembly of Nanoparticles Mediated by Metal Complex Formation. *Chem. Mater.* **2014**, *26* (3), 1300–1302.

(278) Wang, J.; Li, T.; Chen, F.; Zhou, D.; Li, B.; Zhou, X.; Gan, T.; Handschuh-Wang, S.; Zhou, X. Softening and Shape Morphing of Stiff Tough Hydrogels by Localized Unlocking of the Trivalent Ionically Cross-Linked Centers. *Macromol. Rapid Commun.* **2018**, *39* (12), 1800143.

(279) Lipkin, D.; Howard, F.; Nowotny, D.; Sano, M. The Iodination of Nucleosides and Nucleotides. *J. Biol. Chem.* **1963**, *238* (6), 2249–2251.

(280) Läppchen, T.; Pinas, V. A.; Hartog, A. F.; Koomen, G. J.; Schaffner-Barbero, C.; Andreu, J. M.; Trambaiolo, D.; Löwe, J.; Juhem, A.; Popov, A. V.; et al. Probing FtsZ and Tubulin with C8-Substituted GTP Analogs Reveals Differences in Their Nucleotide Binding Sites. *Chem. Biol.* **2008**, *15* (2), 189–199.

(281) Brown, D. A.; Glass, W. K.; Mageswaran, R.; Girmay, B. Cis-Trans Isomerism in Monoalkylhydroxamic Acids By1H,13C And15N NMR Spectroscopy.

Magn. Reson. Chem. **1988**, *26* (11), 970–973.

(282) Aurelio, L.; Baltos, J.-A.; Ford, L.; Nguyen, A. T. N.; Jörg, M.; Devine, S. M.; Valant, C.; White, P. J.; Christopoulos, A.; May, L. T.; et al. A Structure–Activity Relationship Study of Bitopic N^6 -Substituted Adenosine Derivatives as Biased Adenosine A_1 Receptor Agonists. *J. Med. Chem.* **2018**, *61* (5), 2087–2103.

(283) Gediya, L. K.; Chopra, P.; Purushottamachar, P.; Maheshwari, N.; Njar, V. C. O. A New Simple and High-Yield Synthesis of Suberoylanilide Hydroxamic Acid and Its Inhibitory Effect Alone or in Combination with Retinoids on Proliferation of Human Prostate Cancer Cells. *J. Med. Chem.* **2005**, *48* (15), 5047–5051.

(284) NCI-60 Screening Methodology https://dtp.cancer.gov/discovery_development/nci-60/methodology.htm.